PARAMETERS OF SELECTED CENTRAL STARS OF PLANETARY NEBULAE FROM CONSISTENT OPTICAL AND UV SPECTRAL ANALYSIS

Cornelius Bernhard Kaschinski

PARAMETERS OF SELECTED CENTRAL STARS OF PLANETARY NEBULAE FROM CONSISTENT OPTICAL AND UV SPECTRAL ANALYSIS

Dissertation
Ph.D. Thesis

an der Ludwig–Maximilians–Universität (LMU) München
at the Ludwig–Maximilians–University (LMU) Munich

für den Grad des
for the degree of

Doctor rerum naturalium

vorgelegt von
submitted by

Cornelius Bernhard Kaschinski

München, 2013

1st Evaluator: Prof. Dr. A. W. A. Pauldrach
2nd Evaluator: Prof. Dr. Barbara Ercolano
Date of oral exam: 25.4.2013

Contents

List of Figures

List of Tables

Zusammenfassung

Massearme Sterne haben Nullalter-Hauptreihenmassen von ungefähr 0.8-8.0 Sonnenmassen. Sobald ihr H und He erschöpft ist, haben massearme Sterne die Spitze des asymptotischen Riesenastes (AGB) erreicht und werden unter Abwurf ihrer Hüllen zu Zentralsternen Planetarischer Nebel (ZSPNs).

Der größte Teil dieser Arbeit befasst sich mit der Untersuchung der Sternparameter einer speziellen Auswahl von ZSPNs, um die Gültigkeit der allgemein akzeptierten Kern-Masse-Leuchtkraft Beziehung von ZSPNs weiterführend zu prüfen. Die Notwendigkeit einer solch kritischen Untersuchung wurde hervorgerufen durch eine Diskrepanz zwischen den bestimmten Sternparametern einer hydrodynamisch selbstkonsistenten UV-Analyse und den Sternparametern, die von planparallelen Modelllinienfits an photosphärische H und He Absorptionslinien bestimmt werden. Die konsistent bestimmten Massen der UV-Analyse wiesen eine größere Bandbreite auf als jene, die von der optischen Analyse unter zu Hilfenahme von theoretischen post-AGB Entwicklungsverläufen bestimmt wurden.

Die Untersuchung wurde unter Verwendung von "WM-basic", einem Code, der die Abweichungen vom lokalen thermodynamischen Gleichgewicht in den Atmosphären von heissen Sternen berücksichtigt, durchgeführt. Dieser Code diente zuvor als Basis für die frühere konsistente UV-Analyse von einer speziellen Auswahl von ZSPNs. Zuerst verbesserten wir den Code, indem wir den Starkverbreiterungseffekt einbauten, um damit optische H und He Linien gleichzeitig mit dem UV Spektrum rechnen zu können. Dies erlaubte eine selbstkonsistente Neuuntersuchung des masseärmsten sowie des massereichsten Zentralsterns der betrachteten ZSPNs.

Unter Verwendung des UV Parametersatzes konnten wir nicht nur das beobachtete UV Spektrum, sondern auch die optischen Linienprofile reproduzieren, die fast identisch waren mit den optischen Sternparametermodellen. Die konsistenten Modelle, basierend auf dem optischen Parametersatz, konnten keines der Spektren korrekt reproduzieren. Das Fehlen der Konsistenz zwischen den Stern-und Windparametern des optischen Parametersatzes wird auch deutlich, wenn man einen anderen Untersuchungsansatz verwendet, der auf den dynamischen Windparametern basiert.

In einer weiterführenden Studie verbesserten wir den WM-basic Code nochmals, indem wir das Klumpungsverfahren einbauten. Die Stärke der optischen Emissionslinien, von der die Massenverlustrate im Fall einer ausschliesslich optischen Analyse bestimmt wird, hängt vom Quadrat der Dichte ab. Ein mögliches Klumpen der Winde würde deshalb zu einer Messunsicherheit in der Bestimmung der atmosphärischen Massenverlustrate von der Stärke solcher optischen Linien führen. Da die Massenverlustrate kein freier Parameter ist, sondern vielmehr eine Funktion der anderen Sternparameter, könnte dies zu einer Messunsicherheit in der Bestimmung der Sternparameter führen. Wir verwendeten den verbesserten Code deshalb um unter hinzufgen der Klumpung das Erscheinungsbild des UV Spektrums des optischen Parametersatzes, neu bewerten zu können. Letzterer wurde in einer früheren Studie ermittelt wurde, die die Klumpung in ihren Modellen verwendete, um Fits an die optischen Linien zu erreichen. Wir fanden heraus, dass, mit oder ohne Berücksichtigung der Klumpung, Windstärken und Endgeschwindigkeiten, welche mit den Sternparametern aus der optischen Analyse übereinstimmen, Spektren liefern, die inkompatibel mit den optischen und UV Beobachtungen sind. Unsere selbstkonsistenten Modelle liefern dagegen gute Fits an beide Beobachtungen. Des weiteren stellte sich heraus, dass Klumpungswerte den gleichen Grad an Einfluss auf die optischen Rekombinationslinien aufweisen wie es die Dichte (das Geschwindigkeitsfeld) hat.
Innerhalb der gleichen Studie haben wir auch Schocktemperaturen und Verhältnisse von röntgen-zu bolometrischen Leuchtkräften bestimmt, die es uns ermöglichten, die hoch ionisierte O VI Linie, welche Teil des Spektralbereiches des *Far Ultraviolet Spectroscopic Explorers* ist, zu reproduzieren. Die erhaltenen Werte stimmen mit jenen überein, die bereits für O Sterne erlangt wurden. Dies bestätigt zum wiederholten Male die Ähnlichkeit der Atmosphären von massereichen O Sternen und O-Typ ZSPNs.

Basierend auf den von uns abgeleiteten Schockstrukturen unserer Auswahl von ZSPNs, untersuchten wir einen möglichen Einfluss der Schocks auf Studien von Emissionslinien von H II Regionen. Hierbei werden Verfahren zur Umrechnung von Linienverhältnissen in gewünschte physikalische Eigenschaften benötigt, die in Form von diagnostischen Linienverhältnissen oder Diagrammen vorkommen und die auf Gittern von Photoionisationsmodellen basieren. Wir berechneten solch ein Gitter von schockbeinflussten Ionisationsflüssen eines Zentralsterns und verwendeten diese verstärkten Flüsse als Eingabewert für den Photoionisationscode MOCASSIN. Dies ermöglichte es uns, den Einfluss der schockverstärkten Flüsse auf das den Stern umgebende Gas zu untersuchen. Die Effekte sind speziell wichtig für stellare Quellen mit effektiven Temperaturen kleiner als 30kK.

Zum Schluss untersuchten wir in zwei Studien einige der Eigenschaften von jungen, massereichen Sternhaufen (YMCs). In der ersten Studie widmeten wir uns der Frage, ob die anfängliche Massenfunktion der Sternhaufen ein zugrundeliegendes Limit bei hohen Massen aufweisst oder nicht. Wir verwendeten eine Methode, basierend auf den Leuchtkräften der YMCs, kombiniert mit deren Alter, wobei wir herausfanden, dass ein Abschneiden der Massenfunktion benötigt wird, um die Beobachtungen zu reproduzieren. Dies bestätigt frühere Untersuchungsergebnisse.

Die zweite Studie beschäftigte sich mit der radialen Verteilung von YMCs in einer Auswahl von nahegelegenen Spiralgalaxien. Wir suchten nach den charakteristischen Abständen zum galaktischen Zentrum, die die Entstehung und/oder das Überleben von den massereichsten Sternhaufen begünstigen. Wir verglichen daraufhin die beobachteten Daten mit einem einfachen theoretischen Modell, das auf der Stichprobengröße basiert. Letzteres ergibt sich aus der Sternentstehungsrate als Funktion des Radiuses, multipliziert mit der Fläche. Wir fanden heraus, dass solch ein Modell dazu in der Lage ist, die beobachteten Abstandsverteilungen der YMCs zu reproduzieren. Dies gelang ohne Zuhilfenahme einer bevorzugten Sternhaufenbildung oder einem Zerfall aufgrund einer erhöhten Anzahl an Riesenmolekülwolken in der Nähe von galaktischen Zentren.

Abstract

Low mass stars have zero age main sequence masses of roughly 0.8-8.0 solar masses. Once their H and He source is depleted, low mass stars reaching the tip of the asymptotic giant branch (AGB) eject their envelopes becoming Central Stars of Planetary Nebulae (CSPNs).

In the main part of this thesis we investigate the stellar parameters of a selected samples of CSPNS in order to further examine the validity of the commonly accepted core mass-luminosity relation of CSPNs. The necessity of such a critical examination was highlighted by a mismatch between the derived stellar parameters from hydrodynamical self-consistant UV analysis and those from a plane-parallel model fit to photospheric H and He absorption lines. The consistently derived masses from the UV analysis showed a wider spread than the masses derived from the optical analysis, which were obtained using theoretical post-AGB evolutionary tracks.

This investigation was carried out using the non-local thermodynamic equilibrium atmosphere code "WM-basic", which has been previously used as the basis for the earlier consistent UV analysis performed on the sample of selected CSPNs. First, we improved the code by implementing the Stark broadening effect, so as to model optical H and He lines simultaneously along with the UV spectrum. This allowed a self-consistent re-analysis of the most and least massive of the CSPNs sampled.

Using the UV parameter set we then reproduced not only the observed UV spectra but also produced optical line profiles which are nearly identical to those from optical stellar parameter models. The consistent models using the optical parameter set reproduce neither spectrum accurately. The lack of consistency between stellar and wind parameters of the optical parameter set is also evident from a different approach based on an investigation of the dynamical wind parameters.

In a subsequent study, we further improved the WM-basic code by implementing the treatment of clumping. The strength of optical emission lines, from which the mass loss rate is determined in case of a purely optical based analysis, depends on the square of the density. A possible clumpiness in the winds would thus lead to an uncertainty in the determination of atmospheric mass loss rates from the strength of such optical recombination lines. Since the mass loss rate is not a free parameter, but is rather a function of the other stellar parameters, this may lead to an uncertainty in the determination of the stellar parameters. We used the improved code to re-evaluate, with respect to the influence of clumping on the appearance of the UV spectra, the optical parameter set determined in an earlier study that employed clumping in its models to achieve fits to the observed optical lines. We found that, with and without clumping, wind strengths and terminal velocities in accordance to their stellar parameters from the optical analysis yield spectra which are incompatible with the optical and UV observations, whereas our self-consistent models achieve good fits to both observations. Moreover, moderate clumping factors are found to have the same order of influence on the optical recombination lines as the density (velocity field) has.

During the same study we also derived shock temperatures and ratios of X-ray to bolometric luminosities so as to reproduce the highly ionized O VI line in the Far Ultraviolet Spectroscopic Explorer spectral range. These values agree with those derived for O stars, again confirming the similarity of massive O type CSPN and massive O star atmospheres.

Based on the derived shock structures of our sample of CSPNs we investigated the possible influence of shocks on emission line studies from H II regions. Here, tools for the inversion of line ratios into desired physical properties are required and come in the form of diagnostic ratios or diagrams which are based on grids of photoionization models. We calculated such a grid of shock influenced ionizing fluxes from a central star and used these enhanced fluxes as an input to the photoionization code MOCASSIN. This allowed us to investigate the impact of shock enhanced fluxes on the gas surrounding the star. These effects are particularly important for stellar sources with effective temperatures lower than 30kK.

Finally, we investigated some properties of young massive clusters (YMCs) over two studies. In the first study we addressed the question of whether the initial cluster mass function has a fundamental limit at high masses. We used a method based on the luminosities of YMCs combined with their age, and found that a truncation in the mass function is required to reproduce the observations. This confirms previous findings.

The second study concerns the radial distribution of YMCs in a sample of nearby spiral galaxies. We searched for the characteristic galactocentric radii that are favorable to the formation and/or survival of the most massive YMCs. We then compared the observed data to a simple theoretical model based on the sample size, that is, the star formation rate as a function of radius multiplied by the area. We found that such a model is able to reproduce the observed YMC radial distribution without the need to include preferential cluster formation or dissolution due to the increased density of giant molecular clouds near galactic centers.

Chapter 1

Introduction

1.1 Hot Stars

The term hot stars does not refer to a single group of stellar objects but rather to objects in various parts of the Hertzsprung-Russel diagram undergoing different stages of their stellar evolution. The most important groups among the Hot Stars are massive O/B stars, Supernovae (SN) of Type Ia and II, and O-type Central Stars of Planetary Nebulae (CSPNs). The final stage into which a main sequence (MS) star evolves to depends on the initial mass of the star. Therefore, during its lifetime the star evolves away from the MS, eventually becoming a member of one of these groups of hot stars (provided its initial mass is large enough). The members of these groups differ greatly in their characteristic attributes such as temperature, size, luminosity, mass, or abundances. Nonetheless, the basic physics of their expanding atmospheres is similar, which is thought to be subject to the same radiatively-driven wind theory. This is, however questinable since different hot stars display greatly differing stellar parameters, making a deeper knowledge of hot stars and their evolution a prerequisite for improving our understanding of stellar evolution models as a whole.

As this thesis focuses mainly on the analysis of CSPNs, below we provide a short review of the creation of the group of CSPNs.

1.1.1 Evolution of hot stars

In general, stellar evolution theory places the position of the observed stellar quantities - absolute magnitude and spectral type - in a diagram of analogous physical quantities, namely effective temperature $T_{\rm eff}$ vs. luminosity L (see Fig. 1.1). This diagram is called the Hertzsprung-Russell diagram (HRD) and is based on the work by Russell (1913) and Hertzsprung (1911).

The point at which MS stars begin to evolve away from the main sequence (point A in Fig. 1.1) is defined by the mass of the star. High-mass stars encompass a wide range of masses, from roughly 10 solar masses ($M_{\odot}$) up to a several hundred $M_{\odot}$. (The most massive star reported to date is R136a1, massing approximately 265 $M_{\odot}$, see Crowther et al. 2010). Low-mass hot stars are the offspring of intermediate-mass stars with zero age main sequence masses (ZAMS) between approximately 0.8 and 8 $M_{\odot}$. As with high mass stars, low mass stars have a core temperature that is hot enough to burn hydrogen into helium. Below 1.3 $M_{\odot}$ the protonproton chain reaction is the dominant mechanism for this fusion process. For stars with masses higher than 1.3. $M_{\odot}$ the CNO-cycle (carbon-nitrogen-oxygen–cycle) becomes the dominant energy mechanism. Hydrogen is continually consumed, and

once H levels are no longer sufficient to sustain the stellar structure in equilibrium, the star begins to contract until the core H-burning phase is over. H-burning then continues in a shell surrounding the core. The outer envelope expands while being heated by H-shell burning, but eventually cools. The resulting temperature gradient establishes a convective zone which extends as far down as the layers of the core burning. The so called "dredge up" effect kicks in where the H-burning products from the core are brought back to the surface via convection. The star now enters the Red Giant Branch (RGB, point B in Fig. 1.1). The compact H-core is now degenerate, where its pressure inside is independent of temperature, and remains idle until it reaches a temperature that is high enough to fuse helium. The amount of time required for the contraction of the core to reach the required temperature for helilum fusion is a function of the total mass of the star. In other words, the more massive a star is, the faster it reaches the required temperature. If the critical temperature is reached, He-burning begins with the the so-called He-flash, removing the degeneracy of the core which thus expands while the enveloppe shrinks simultaneously. At thus point the star enters the horizontal branch on the HRD (point C in Fig. 1.1). The He-core burning sequence is analogous to the former H-burning of the stars' core. When helium levels in the core are reduced beyond a critical point the star again mimics the H-shell burning process and begins burning helium in a shell. Some additional H-burning also occurs in an outer shell surrounding the inner He-shell. The star has now entered a double shell burning phase around a carbon core. As was the case during the pure H-shell burning, the carbon core contracts, becomes degenerate and sits idle while the envelope expands and the envelope layers become strongly convective again, dredging up material to the surface. The star has now moved on to the Asymptotic Giant Branch (AGB, point D in Fig. 1.1). Unlike low-mass evolution, high mass stars undergo further, similar evolutionary stages in which first carbon, then neon, oxygen and finally silicon become the main energy source throughout core burning. The former burning stages all continue burning in shells around the core, the so-called onion-like structure. After the silicon burning stage the core is primarily composed of iron which cannot be further merged as iron has the highest binding energy per nucleon. The core eventually collapses, resulting in a SN explosion or Gamma Ray Burst (GRB).

After a low-mass star has moved onto the AGB, the He-shell burning continues, merging helium into carbon which is dumped upon the idle core. Thus, the mass of the core increases, resulting in a luminosity increase of the star which then moves up on the AGB. This process is accompanied by an increase in the mass-loss rate. Once the star has reached the "tip" of the AGB the evolutionary stage is marked by the onset of thermal pulses (TP). For a more in depth discussion on TPs as well as on late thermal pulses (LTPs), very late thermal pulses (VLTP), AGB final thermal pulses (AFTPs), and differences amongst them see for example Herwig et al. (2006) and references therein. After the outer H-shell has burned for some time it cools, and eventually stops burning. However, the He-shell keeps burning and moves outwards until its hot, burning material meets the extinguished H-shell. The hot He-shell ($\sim 10^8\ K$) re-ignites the H-shell which leads to a thermal pulse in the star resulting in double shell burning. This process of a burning H-shell which then moves outwards, cools, becomes extinguished, and is re-ignited by the subsequent hot He-burning shell hence resulting again in a thermal pulse is repeated with a period of roughly 10^4 years. The constant mass-loss removes material from the outer layers whereas the continuous burning adds mass to the core. Thus, the mass of the envelope will eventually reach a critical, lower limit of roughly $10^{-3}\ M_\odot$. At this point there is not enough material to sustain the convection of the layers of the envelope and hence the star reverts to radiative equilibrium. The AGB phase is now at an end and the star moves to the left in the HRD initiating the PN phase (point E in Fig. 1.1). The central star has reached an effective temperature of at least 30 000 K and developed a fast line-driven wind that overtakes the

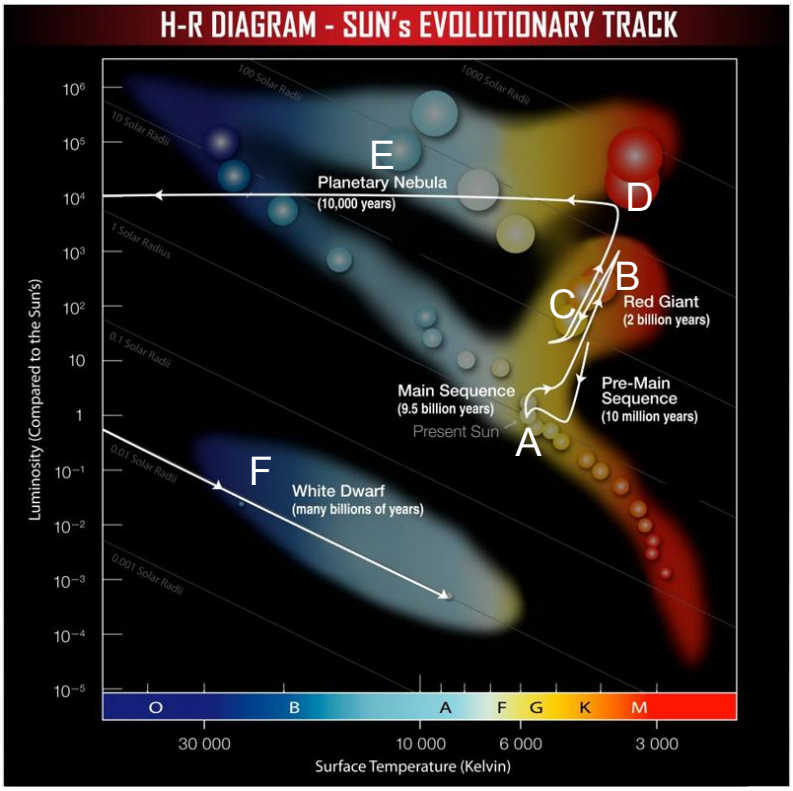

Figure 1.1: Evolution of a solar mass star which begins to move away from the main sequence at point A undergoing various evolutionary stages until the star finally becomes a White Dwarf indicated by point F in the HRD. (Original image credit: NASA/CXC/SAO, http://chandra.harvard.edu.)

much smaller wind from the AGB. The stellar remnant is now hot enough to emit photons able to ionize the surrounding gas. This will form the planetary nebula and its central star, which will evolve under constant luminosity toward higher effective temperatures. The CSPNs provide information about late evolutionary stages of sun-like stars, representing the connective link between Red Giants and White Dwarfs. As a consequence, their properties display different physical conditions depending on their original stellar masses. This makes CSPNs extremely important in the study of the chemical evolution of the Galaxy. Planetary nebulae nuclei are not located in a confined region of the HRD. This is due to their differing initial masses, which define the starting point at which the stars evolve away from the main sequence, resulting in a different end position of the planetary nebula phase in the HRD. The position also reflects the age of the star. Their optical spectra encompass all varieties known for hot stars, ranging from pure emission to emission-absorption mixtures, and from a nearly pure continuum to pure strong absorption. Mendez (1991) suggested that the majority of CSPN can be classified into two distinct categories: H-rich (O-type) central stars and H-poor, i.e. He-rich (Wolf-Rayet type central stars). The PN phase is followed by the White Dwarf phase (point F in Fig. 1.1) which is initiated after the radiatively-driven wind of the central star has dispersed its envelope mass to a level lower then $10^{-5}\ M_{\odot}$ at which point shell burning stops, and is followed by the cooling of the central star, resulting in it becoming a White Dwarf.

We will now give a quick overview of low-mass hot stars.

Miscellaneous types of low-mass (hot) stars

Young, cool central stars Young, cool central stars are on the lower end of the temperature spectrum typical for CSPNs, reaching about 35.000 K. They have just recently evolved off the asymptotic giant branch. The young CSPNs resemble stars of late Of-type spectra (i.e. H-rich atmospheres), with signs of mass loss and late-type WC spectra[1]. Their spectra feature C, O, and He emission lines which indicate intense, high-velocity winds. The CSPN He 2-131 is a good example of a late-Of-type star. Low temperature CSPN also include late-type Wolf-Rayet stars.

O-type Central stars As mentioned above, O-type central stars are H-rich CSPNs where hydrogen is the dominant element. Their main spectral types are O and Of and, to a lesser extent, early B (stars with $T_{\rm eff} < 20\,000$ K could not ionize the nebula).

Wolf-Rayet-type Central stars The stellar spectrum of H-poor CSPNs is almost free of hydrogen, with helium and carbon being the most prominent elements in their spectrum. Such stars are referred to as Wolf-Rayet Central stars. They exhibit in their spectra broad and strong emission lines of carbon, helium, and oxygen which is typical for Wolf-Rayet stars. Weidmann & Gamen (2011) and references therein state that there are several debatable galactic [WN] CSPN. However, [WC]-type CSPN show a broader range in temperature ($\sim$ 30kK-130kK) than WC stars. In spite of spectral similarities and comparable chemical composition, Todt et al. (2010) pointed out that the formation of the low-mass [WC] stars is very different from the formation of the massive WC stars. Stellar evolutionary models accounting for simultaneous burning and mixing explain the formation of a [WC] star by the occurrence of a thermal pulse at the very end or after the asymptotic giant branch phase of a H-normal low-mass star.

Very hot central stars The temperature range of very hot CSPNs lies between 80.000 K and 170.000 K (Werner et al. 1996). Even at these high temperatures the dichotomy between O and [WR] CSPNs is still evident. Some CSPNs (Mendez 1991) show very early O-type spectra (although they display strong C IV lines) whereas there are also [WC/WO] CSPNs showing Wolf-Rayet emission line spectra (Heap 1982, Feibelman 1996).

White Dwarfs (WD) After the PN phase, CSPNs evolve eventually into White Dwarfs. They have low luminosities (from $\sim 10^{-4}$ to 1 $L_{\odot}$) but still have high effective temperatures ($T_{\rm eff} = 6000 - 2 \times 10^4$ K). While their radii are small (roughly 0.1 $R_{\odot}$) their central densities are extremely high ($\sim 10^6 - 10^9$ $g\ cm^{-3}$). This leads to a completely electron degenerated core (expect in thin surface layers) where gas remains ionized independent of temperature. The WD is thus only supported by electron degeneracy pressure. The radii of WD decrease as a function of increasing mass with an upper limit, Chandrasekhar limit, which lies roughly at $\sim 1.4\ M_{\odot}$. Above that limit the star explodes in a Supernova Ia explosion. Examples of WDs are the Sirius B and 40 Eri B, which are known to have

[1] Wolf-Rayet stars (WR) stars are divided into classes such as WN and WC stars. WN describes a WR star where the dominant emission lines are from nitrogen. Similarly, WC stars have dominant carbon emission lines. This classification also holds true for [WR] Central stars although according to Heap (1997) their spectra only show [WC] or [WN/NC] spectra. Because their spectra resemble those of WR stars, they are called, for example, [WR] stars, with brackets to distinguish them from their massive counterparts.

masses and radii equal to $M = 1.05\ M_\odot$, $R = 7.4 \times 10^{-3}\ R_\odot$ and $M = 0.48\ M_\odot$, $R = 12.4 \times 10^{-3}\ R_\odot$ respectively.

1.2 Impact of massive stars on the evolution of stellar clusters

Although rare, massive stars dominate the life cycle of gas and dust in star forming regions and are responsible for the chemical enrichment of the interstellar medium (ISM) due to their relatively short lifetimes. The recycling of heavier elements has a significant impact on the chemical evolution of the host galaxy. Furthermore, due to the interaction of their fast stellar winds, which results in a vast amount of momentum and energy transfer in the ISM, massive stars control the dynamical evolution of the ISM which triggers new star formation. Massive stars are usually clustered, providing extreme energy input into the ISM to further nourish the creation of star forming regions around themselves. Stellar clusters can be separated into two groups: globular clusters (GCs) and young massive clusters (YMCs). The GCs are very old ($>$ 10 Gyr) massive and dense clusters with an average mass of $2 \times 10^5\ M_\odot$ (Brodie & Strader 2006). They are some of the oldest objects in the universe and are found around almost every galaxy. YMCs are thought to be the GC counterparts that are forming today. They are young ($<$ 1 Gyr), massive ($> 10^4\ M_\odot$) and generally dense ($> 10^3\ M_\odot\ pc^{-3}$, for a recent review on YMCs see Portegies Zwart et al. 2010).

Stellar clusters undergo various processes, gradually evolve, and eventually dissolve. In clusters that survive the early expulsion of their natal gas, the most important process is mass loss due to stellar evolution (Portegies Zwart et al. 2010). Furthermore, spectroscopic studies of galaxies with pronounced current star formation reveal the specific spectral signatures of massive stars (e.g., Pauldrach 2003). This demonstrates the fundamental influence of massive stars on the evolution of stellar clusters, which is reflected in the spectral appearance of star burst galaxies. It illustrates that the underlying physics is not only rooted in the atmospheric expansion of massive O stars, but also dominated by these objects (c.f. Pettini et al. 2000 and Conti et al. 1996).

While a stars' evolution is not dominated by its environment (with the exception of binaries) it is currently not known if the birth is environmentally dependent. Can massive stars form in all galaxies? Are there regions within the Milky Way that preferential form or inhibit massive star formation?

1.3 Motivation of this thesis

Accurate knowledge of the properties of CSPNs is crucial for understanding of the evolution of their progenitors on the ABG. Modeling a synthetic spectrum that can be compared to observations is the primary diagnostic tool for the determination of the fundamental stellar parameters. While determining the effective temperature $T_{\rm eff}$ and the surface gravity $\log g$ from the observed spectrum is an established procedure - using the ionization balance of He I and He II and the pressure-dependent Stark-broadening in hydrogen Blamer lines - the determination of the radii and masses from the spectrum alone is not so straight forward. Without knowledge of the distance to the star a quantity that is dependent on the absolute radius and that can be traced spectroscopically is required. Two approaches exist to tackle this problem. The first regards a property of O stars. O stars exhibit direct signatures of stellar winds in their spectra, with spectral lines formed out to several dozens of stellar radii. The link to the stellar radius is provided via self-consistent hydrodynamical modeling of the gravitational and radiative acceleration in the wind, allowing for a purely spectroscopic determination of the stellar

radius.
The second approach uses information provided by theoretical evolutionary models. For CSPNs these models predict surface gravities $\log g$ and effective temperatures $T_{\rm eff}$ as function of mass and age. By plotting the observed values in a log g - $T_{\rm eff}$ diagram and comparing these to the theoretical tracks allows reading off the stellar masses and thus radii. However, this method is not an independent test of the evolutionary tracks since their validity is assumed *a priori*.

A recent comparison of the results from two methods for a sample of CSPNs yielded severe discrepancies (Kudritzki et al. 1997,Pauldrach et al. 2004). This was surprising as the hydrodynamical method reported almost identical results to those from optical analyses for massive O stars. Pauldrach et al. (2001), Hoffmann & Pauldrach (2003), Pauldrach (2003), and Pauldrach et al. (2003) presented the self-consistent hydrodynamical models for a sample of massive O stars (e.g., HD 66811 (ζ Puppis)) confirming the parameters derived by Puls et al. (1996) from an optical analysis.

For CSPNs the hydrodynamical analysis yielded a much larger spread in reported masses compared to the ones derived from the optical analysis in conjunction with theoretical post-AGB evolutionary tracks. These evolutionary tracks suggested a narrow distribution around roughly 0.6 $M_{\odot}$ whereas the consistently derived masses based on the UV analysis showed a bigger spread in the stars masses. In fact, Pauldrach et al. (2004) found a number of CSPNs with masses around 1.3 to 1.4$M_{\odot}$, near the Chandrasekhar limit for white dwarfs (Chandrasekhar 1931). This might suggest that CSPNs could be possible progenitors for Supernova Ia events. However, one of the stars, NGC 2392, was found to have a surprisingly small mass of only 0.4$M_{\odot}$, thus excluding the possibility of a systematic overestimate of the masses by the hydrodynamical method. It is unclear whether these discrepancies in the determined masses of the two methods were the result of a weakness in the radiation driven wind models, of the evolutionary tracks, of as yet unrecognized difference in the behavior between UV and optical spectra. The hydrodynamical code ("WM-basic") that had been used in the UV analysis was at that point not able to correctly compute optical line profiles. Thus, the main aim of this thesis was to improve this code so as to allow simultaneous optical and UV analysis. A successful analysis of such an investigation that includes H and He lines has, as a combined analysis, a more convincing character. This will provide clues to the causes of the above mentioned discrepancies. To achieve this, implementing of the Stark broadening of H and He lines was necessary.

Moreover, in recent years evidence[2] has accumulated that winds of O-type stars might not be as smooth as previously assumed. This so-called clumping (e.g., Repolust et al. 2004) would lead to a systematic overestimation of mass loss rates, since the H_{α} line, which is used by the optical analysis as the primary diagnostic line to derive the mass loss rate, is a recombination line and depends on the square of the wind density. With this effect in mind, Kudritzki et al. (2006) reanalyzed the sample of CSPNs investigated by Kudritzki et al. (1997), adjusting clumping factors in the models to provide new fits to the optical emission lines. The newly derived mass loss rates for the sample of CSPNs were significantly reduced compared to the earlier optical analysis[3]. It is therefore important to further improve the atmosphere code used in our models with the addition of treatment for a clumped wind structure. The improved code must then be used to re-investigate the set of optical parameters with their reduced mass loss rates as well as the UV stellar parameters with their consistent mass loss

[2] It has long been known that the line-driving mechanism of the winds is intrinsically unstable (Milne 1926; Lucy & Solomon 1970), but it was not suspected that the fragmentation of the wind would already be significant in the lower regions where most of H_{α} is formed.

[3] Knowledge of the mass loss rates is principally important because the mass loss has a significant effect on the evolution of the star Meynet et al. (1994)

rates. Thus in this thesis we investigate whether the optical lines predicted by the two sets of stellar parameters using the suggested clumping factor from the revised analysis of Kudritzki et al. (2006) can match the observed lines, or whether the set of our UV parameters suggests different clumping factors. Moreover, we investigated whether the appearance of the consistently calculated UV spectra is influenced by the application of a clumped rather than a smooth atmosphere in respect to their compatibility with the observations.

In recent years, observations with Chandra and XMM have led to the detection of X-ray emission from CSPNs and their PNe (Guerrero 2006, Guerrero 2006 or for more recent work see Kastner et al. 2012). This X-ray emission is believed to result from shocks running through the stellar winds, which can provide further information about the nature of these winds. As in massive O star winds, small regions of the material in the wind is accelerated relative to the mean flow and eventually collides with other material producing shocked regions with temperatures of a few million Kelvins. The hot material cools radiatively, thereby emitting X-rays (Lucy & White 1980; Lucy 1982). The extra radiation from shocks produces highly ionized species such as N V, O VI, and S VI which are indeed observed in their far UV spectral range by the Far Ultraviolet Spectroscopic Explorer (FUSE). A successful modeling of these lines in the UV spectra of CSPNs would provide a corresponding structure of maximum shock temperatures and X-ray luminosities L_X. Extensive studies on massive O-stars have already been carried out in the past, yielding corresponding structures for maximum shock temperatures and L_X values. A comparison between massive O-stars and O-type CSPNs could therefore further ascertain whether CSPN winds are driven by the same mechanism as massive O-stars. To provide more insight into this matter we use FUSE data for several of our CSPNs to perform the investigation.

Closely related to the modeling of hot stars is the study of their emitted fluxes of ionizing radiation. Their ionizing fluxes may also be influenced by shock enhanced X-ray radiation. The resulting emission lines from H II regions that surround hot stars in our own and other galaxies are used for the determination of abundance gradients in galaxies, which are a crucial constraint for chemical evolution models (e.g., with implications for fundamental correlations, such as the relation of stellar effective temperatures and hardness of stellar spectrum and with galactocentric distance/metallicity (e.g. Campbell et al. 1988, Martín-Hernández et al. 2002, Giveon et al. 2002, Dors & Copetti 2003). This requires tools for determining physical properties from the observed line ratios. These tools generally come in the form of diagnostic ratios/diagrams that are based on grids from photoionization models. An important input to the photoionization models is the stellar atmosphere spectrum of the ionizing source. Many detailed models of either PNe or CSPNs have been developed separately, but few studies combine the investigation of the nebula with its central star. One such example is the unified study of the CSPN NGC 6826 and its PN described by Fierro et al. 2011. We therefore conducted an investigation of H II regions calculated with the photoionization code MOCASSIN (Ercolano et al. 2003, 2004, 2005) based on the input spectra of the ionizing central source computed using the stellar atmosphere code WM-basic.

The quality of diagnostics depends primarily on the input, i.e. the spectral energy distribution (SED). We computed a grid of ionizing fluxes on the basis of the consistent UV stellar parameters of the sample of CSPNs. The computed grid includes our derived shock structures and used them as input for the MOCASSIN models. Shocks are expected to have a stronger influence on the emitted flux the cooler the ionizing central source becomes. This is of particular interest as Pauldrach (2003) already pointed out that for most of the considered H II regions models indicated that the effective temperatures of the exciting stars lie in the range of 35 000 to 45 000 K. We were therefore interested in determining whether the effects of shock enhanced fluxes on the nebular emission lines can be

seen in stars with such a temperature range, or whether stars in that temperature range are already hot enough and the influence of the extra X-ray radiation due to shocks is negligible. Moreover, Pauldrach (2003) already showed that high excitation emission lines (e.g., [Ne III]) observed in H II regions were not reproduced by nebular calculations which made use of the ionizing fluxes of earlier stellar models. In Chapter 4 we test whether shock emission has a similar influence on the nebular spectra.

Massive stars have the largest influence on their interstellar environment when they appear in a stellar cluster. A better understanding of the evolution of massive stars will thus eventually contributes to a more detailed understanding of cluster formation, cluster age, and the impact of massive stars on the ambient environment. Unfortunately, the detailed process of cluster formation, its early evolution, and the role of the ambient environment is not well understood. There is still ongoing debate on some of the basic properties of cluster populations, such as the question of how long clusters live, whether the mass function of clusters is truncated at high masses or whether the power-law continues to the highest mass clusters? In Chapter 5 we investigate the form of the initial mass function of clusters within a single galaxy, NGC 2997, with particular attention to whether or not it is truncated at the high mass end.
We also investigate whether there is a characteristic galactocentric radius in which young massive clusters are more likely to be present in a second, photometric, observational based study of nearby spiral galaxies (survey presented in Larsen 2004).

1.4 Organization of this thesis

Chapter 2: Self-consistent, simultaneous modeling of optical and UV spectral lines with WM-basic

We describe the important implementation of the Stark broadening required for the modeling of optical H and He lines with WM-basic. We conduct a combined analysis of the two different sets of stellar parameters from a selected sample of Central Stars of Planetary Nebulae, one set derived on the basis of optical fits to H and He lines, the other one based on a hydrodynamical, self-consistent UV analysis.

Chapter 3: Consideration of wind inhomogeneities and their impact on optical and UV spectral features of a selected sample of CSPNs

In this chapter we examine the treatment of two different types of wind inhomogeneities (clumping and shocks). First, an extended UV analysis using the optical and UV sets of stellar parameters is presented along with the treatment of a shocked atmosphere. Using mainly the highly ionized O VI line we obtain shock structures for all CSPNs of the sample for which FUSE data was available. Comparing the derived structures to those obtained in the literature for O stars we investigate how similar the driving mechanisms of winds of CSPNs are compared to O stars. The clumping theory is then briefly outlined along with its implementation and testing in WM-basic. The consideration of different clumping factor values and its impact on the optical and UV spectra of the sample of selected CSPNs based on the optical and UV stellar parameter sets is shown.

Chapter 4: Shocks as enhancement for ionizing fluxes of stellar sources and the resulting impact on H II regions

The effect of a shocked atmosphere of stellar sources as an input for a grid of photoionizing models is explained. The derived shock structure and UV stellar parameters on the basis of the CSPN analyses was used to compute the ionizing fluxes with WM-basic which were then used as an input for the photoionization code MOCASSIN to calculated diagnostic line ratios/diagrams.

Chapter 5: Form of the stellar cluster mass function

In this chapter we investigate whether the initial mass function has a fundamental limit at high masses. To do this we perform an optical spectroscopy of twelve young stellar clusters in the spiral galaxy NGC 2997.

Chapter 6: Massive stars and their environment

In this chapter we investigate the radial distribution of young stellar clusters in nearby spiral galaxies. Specifically, we compare the galactocentric distances of young massive clusters in a sample of nearby spiral galaxies, which are then compared to stellar population model.

Chapter 7: Summary and Conclusions

In the last chapter we summarize the results obtained within the scope of this thesis.

Chapter 2

Radiation-driven winds of hot luminous stars

XVII. Parameters of selected central stars of PN from consistent optical and UV spectral analysis and the universality of the mass–luminosity relation

The contents of this chapter was published in Kaschinski et al. (2012), Astronomy & Astrophysics, 542A, 45K.

Abstract. The commonly accepted mass–luminosity relation of central stars of planetary nebulae (CSPNs) might not be universally valid. While the atmospheric parameters $T_{\rm eff}$, $\log g$, and the He abundances have in the past been determined using fits to photospheric H and He absorption lines from plane-parallel model atmospheres, the masses and luminosities could not be derived independently this way, and were instead taken from theoretical evolutionary models. Improvements in hydrodynamically selfconsistent modelling of the stellar atmospheric outflows now allow using fits to the wind-sensitive features in the UV spectra to consistently determine the stellar radii, masses, and luminosities without assuming a mass–luminosity relation. Recent application to a sample of CSPNs in an earlier paper of this series raised questions regarding the validity of the mass–luminosity relation of central stars of planetary nebulae.

The results of the earlier UV analysis are reassessed by means of a simultaneous comparison of both the observed optical and UV spectra with corresponding synthetic spectra. The synthetic optical and UV spectra are computed simultaneously from the same atmospheric models, using the same model atmosphere code. Synthetic spectra for the two central stars NGC 6826 and NGC 2392 are computed using parameter sets from two different published analyses to check their compatibility to the observations.

Using the different published stellar parameter sets, derived on the one hand by a consistent UV analysis, and on the other hand from fits to optical H and He lines, we calculate corresponding optical and UV spectra with our model atmosphere code. We have improved this model atmosphere code by

implementing Stark broadening for hydrogen and helium lines, thus allowing us to obtain consistent optical H and He line profiles simultaneously with our state-of-the-art modelling of the UV-spectrum.

Optical line profiles computed with the consistent parameter sets from the UV analysis yield line profiles with good agreement to the observations (with small discrepancies in the emission lines corresponding to about a factor of one half in the mass loss rate). Spectra computed with the stellar parameter sets from the optical analysis in the literature and corresponding *consistent* wind parameters, however, show large discrepancies to the observed spectra, in the optical as well as in the UV. We conclude that the published optical analyses give good fits to the observed spectrum only because the wind parameters assumed in these analyses are inconsistent to their stellar parameters. By enforcing consistency between stellar and wind parameters, stellar parameters are obtained which disagree with the core-mass–luminosity relation for the two objects analyzed. This disagreement is also evident from a completely different approach: an investigation of the dynamical wind parameters.

2.1 Introduction

In recent years there has been substantial progress in the modelling of expanding atmospheres of hot stars. Current state-of-the-art wind models dealing with homogeneous, stationary, spherically symmetric, radiatively driven, extended, outflowing atmospheres can now produce synthetic UV spectra of O stars that resemble the observed ones nearly perfectly. A complete model atmosphere calculation of this kind involves solving both the hydrodynamics and the so-called non-LTE problem,[1] comprising a simultaneous solution of the total interdependent system of the radiative transfer, the rate equations for all important elements, and the energy equation. The primary diagnostic output of such a computation is a predicted, or synthetic, spectrum, which can be compared to an observed UV spectrum. The fundamental stellar parameters are determined by varying the model parameters until a match to the observed spectrum is achieved. Using this new generation of realistic stellar model atmospheres, Pauldrach et al. (2001) and Pauldrach (2003) have already presented an analysis of the massive O supergiants HD 30614 (α Cam) and HD 66811 (ζ Pup) that provided good matches to the observable UV spectra, thereby determining the basic stellar parameter sets of these objects.

By solving the stationary hydrodynamic equations (in which the acceleration driving the outflow depends in turn on the occupation numbers and the radiation field) simultaneously with the non-LTE problem, a solution is obtained that is hydrodynamically consistent and provides the velocity law as well as the mass-loss rate, two key quantities determining the appearance of the UV spectrum. (For details of the physical and technical background see Pauldrach 1987, Pauldrach et al. 1994, and details in Pauldrach et al. 2004.) Such a consistent treatment has very important consequences for the analysis of the UV spectral features, since it provides information about the complete set of the basic stellar parameters: the effective temperature $T_{\rm eff}$, the radius R (or equivalently, the luminosity L), the mass M, the terminal wind velocity v_∞, and the mass loss rate $\dot{M}$. Thus, a purely spectroscopic method allowing the determination of L and M exists.

Pauldrach et al. (2004) have applied this method to O-type central stars of planetary nebulae, thus providing, for the first time, an *independent* test of the predictions from post-AGB evolutionary calculations (see, for instance, Blöcker 1995). This was not possible in the earlier work on CSPNs, which

[1] Due to the high radiation intensities and the low densities in hot star atmospheres, the ionic occupation numbers can deviate strongly from local thermodynamic equilibrium (LTE), and thus a much more general treatment is required. Our approach is described in Pauldrach et al. 2001.

was based on plane-parallel, non-LTE model atmospheres (e.g., Mendez et al. 1988a, Mendez et al. 1988b). Lacking a consistent solution of the hydrodynamics of the atmospheric outflow, the corresponding model fits to optical hydrogen and helium photospheric absorption lines could only provide information about surface temperature, helium abundance, and surface gravity ($\log g$), whereas stellar masses or luminosities could not be derived from the spectra, and additional observational data was needed to furnish information about the physical size of the stars, such as their distances. But for most CSPNs, unfortunately, reliable distance measurements are not available.

In the earlier work, therefore, the masses and luminosities of these objects were obtained from the positions of the CSPNs in the $\log g$–$\log T_{\rm eff}$ diagram (both the effective temperatures and the surface gravities being available from spectroscopic analysis) by comparing these with theoretical post-AGB tracks for given masses. This procedure to determine the CSPN masses is thus based entirely on the assumption that the evolutionary models give the correct relation between stellar mass and luminosity.

Kudritzki et al. (1997) performed such an analysis for a sample of 9 selected O-type CSPNs, additionally modeling the H_α line profiles to determine the mass loss rates, and found the O-type CSPNs to lie along the wind-momentum–luminosity relation defined by the massive O stars, albeit with a somewhat larger scatter. (The tight correlation between the so-called modified wind-momentum rate $D = \dot{M} v_\infty \sqrt{R}$ and the stellar luminosity L of massive O stars was found empirically by Kudritzki et al. (1995) and was subsequently explained by Puls et al. (1996) using the theory of radiatively driven winds.) This was a further indication that the winds of O-type CSPNs are radiatively driven and that the atmospheres of massive O stars and O-type CSPNs are governed by the same physics, confirming the work of Pauldrach et al. (1988). Nevertheless, one of the surprising results of Kudritzki et al. (1997) was the large fraction of high-mass CSPNs in their sample.

In another study, Napiwotzki et al. (1999) determined masses for a sample of 46 hot DA white dwarfs selected from the Extreme UV Explorer (EUVE) and the ROSAT Wide Field Camera bright source lists. They found a peak mass of 0.59 $M_\odot$, in agreement with many other studies, but also found a non-negligible fraction of white dwarfs with masses in excess of 1 $M_\odot$.

These surprising results prompted Tinkler & Lamers (2002) to check the consistency of stellar and wind parameters for a larger sample of CSPNs. As a result of scaling the distances and stellar parameters according to their method, however, they obtained no clear dependence of wind momentum on luminosity. This brought up a conflict between the predictions of post-AGB evolutionary theory and the theory of radiatively driven stellar winds.

The work of Pauldrach et al. (2004) compounded the situation further. The masses obtained from hydrodynamically consistent modelling of the UV spectra of the CSPNs of the particular sample that had already been analyzed by Kudritzki et al. (1997) were for the most part even larger than those determined by Kudritzki et al. Figure 2.1 shows that the luminosities derived from the UV analysis lie within the range expected from their prominent P-Cygni spectral features, but a much larger spread in the masses was obtained, up to the critical Chandrasekhar mass limit for white dwarfs.

This result was even more disturbing for the community. To clarify the situation, Napiwotzki (2006) investigated the kinematical properties of the sample stars of Kudritzki et al. (1997) and Pauldrach et al. (2004). He found NGC 6826, one of the sample stars, to be indeed close to the old thin disk, but not the young thin disk as Napiwotzki suspected. Apart from one star he found better – but still unsatisfactory – agreement with respect to the kinematical properties of his sample by arbitrarily assuming a mass of 0.565 $M_\odot$ for *all* CSPNs, ignoring the fact that Kudritzki et al. (1997), based on the core-mass–luminosity relation *and* well-established spectral analysis techniques, had found masses almost a factor of two larger for most objects of the sample. As these latter masses are not

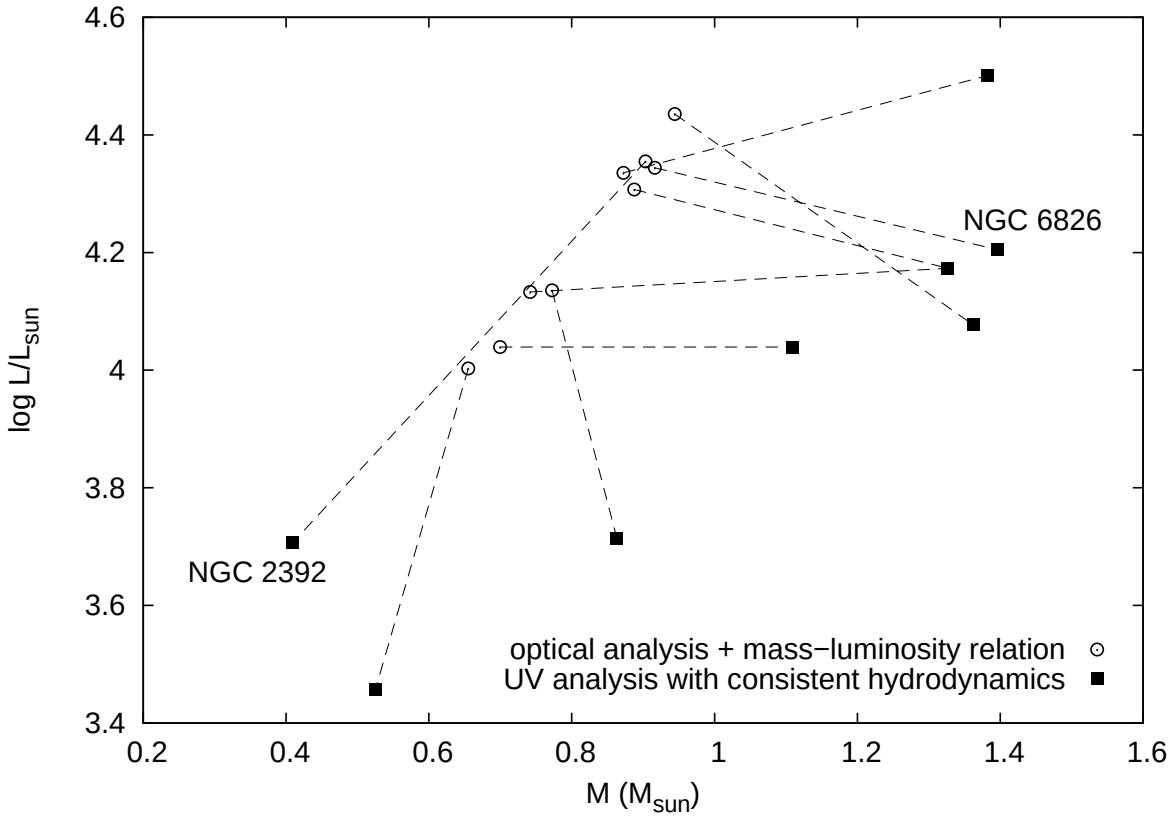

Figure 2.1: Luminosities vs. masses derived for a sample of CSPNs using a hydrodynamically consistent UV spectral analysis (filled squares; Pauldrach et al. 2004) vs. those obtained from an analysis of optical hydrogen and helium lines and assuming a mass–luminosity relation from theoretical post-AGB evolutionary tracks (open circles; Kudritzki et al. 1997). Although the luminosities derived with the UV analysis lie in the expected range, the obtained masses ($0.4\,M_{\odot}$ up to $1.4\,M_{\odot}$) deviate severely from the masses for the evolutionary tracks.

based on an arbitrary assumption, but on a sophisticated spectroscopic analysis, these masses are certainly to be preferred to those assumed by Napiwotzki. Although Napiwotzki did not show results for the Kudritzki et al. masses, interpolating between the positions for the Pauldrach et al. (2004) masses and for $0.565\,M_{\odot}$ in Napiwotzki's diagrams, we see that the masses of Kudritzki et al. also contradict the kinematical positions. Thus, the kinematic evolution of the selected group of CSPNs (which had been chosen for their pronounced wind spectra and their uncharacteristically very high luminosities) is obviously not as straightforward as one might think on basis of simple arguments. This clearly means that the kinematics of CSPN, at least for a statistically not representative sample such as this one, are much less reliable than the well-understood behavior of stellar atmospheres.[2]

Although the result of a much larger spread in the masses, up to the critical mass limit for white dwarfs, of the selected group of CSPNs might be of relevance for the controversially discussed pre-

[2] Moreover, Napiwotzki employed a circular argument by basing the primary assumption – the theoretical age of the sample – on the theory which has been shown not to work for the sub-sample of objects, in order to show that that theory cannot be wrong.

cursor scenarios of type Ia supernovae (cf. Pauldrach 2005), the discrepancy to the optical analysis of Kudritzki et al. (1997) is *still* surprising, since the same model atmospheres worked perfectly well for massive O stars, using exactly the same physics (cf. Pauldrach et al. 2011).

All this is a strong hint that there is something fundamental we do not yet understand about the formation of CSPNs. In this paper we try to provide further constraints to clarify the situation. We do this by testing whether, if both optical and UV analysis are based on an adequate consistent treatment of the expanding CSPN atmospheres, analyses from optical spectra necessarily yield different stellar parameters than analyses from UV-spectra, or whether the discrepancies between the analyses result as a consequence of the missing consistency between the stellar and the assumed wind parameters in the published optical analyses of Kudritzki et al. 1997 and Kudritzki et al. 2006.

In the following we will first outline the two different modeling techniques for deriving the stellar parameters (Section 2.2) and describe the implementation of the Stark broadening tables in our stellar atmosphere code and the test calculations performed using H and He lines (Section 2.3). After briefly identifying the optical and UV observations we have used in this study (Section 2.4) we describe the model runs performed using the published parameter sets for the two CSPNs selected from the sample previously studied by Pauldrach et al. (2004) and Kudritzki et al. (1997), NGC 6826 and NGC 2392, and discuss the resulting synthetic optical and UV spectra in comparison to the observed spectra (Section 2.5).

With regard to the stellar parameters – R, L and M – of a sample of CSPN stars with pronounced wind features we include in this section a discussion of the dynamical parameters as an additional point. This discussion should be considered as an extension to the investigation of Pauldrach et al. (1988) who showed that the calculated terminal wind velocities are in agreement with the observations and therefore allow an independent determination of stellar masses and radii. With respect to this result, different sets of stellar masses and radii applied to our sample of stars should therefore lead at least partly to an inconsistent behavior with regard to predictions of the radiation-driven wind theory.[3] Here, such an inconsistent behavior is realized by the ratios of the terminal wind velocities v_∞ and the escape velocities v_{esc} of the stars (cf. Pauldrach et al. 1988 and Pauldrach et al. 1990a). We compare our results of the v_∞/v_{esc} obtained with our improved models for the CSPN sample not just to the corresponding "observed ratios", which are based on the the mass–luminosity relation of CSPN, but also to the ratios of an O star sample and its corresponding observations. We interpret and summarize our results in Section 2.6.

2.2 Methods

2.2.1 Parameter determination using hydrodynamic models and the UV spectrum

The winds of O-type stars are driven by radiative absorption in spectral lines, a circumstance reflected in the existence of the wind-momentum–luminosity relation. This means that the velocity and strength of the wind are not free parameters, but instead explicit functions of the stellar parameters and the atmospheric chemical composition. This in turn implies that if the dependence is known or can be computed, then a measurement of the density and velocity structure of the atmospheric outflow will also yield the fundamental stellar parameters.

[3] Note that based on striking observational properties of CSPN winds Pauldrach et al. (1988) where able to show that the winds of CSPN are driven by radiation pressure.

The UV spectrum between 1000 and 2000 Å is well suited for this measurement. It contains P-Cygni-type profiles of resonance lines of several ions of C, N, O, Si, S, P, which remain strong until far out in the wind, as well as hundreds of strongly wind-contaminated lines of Fe IV, Fe V, Fe VI, Cr V, Ni IV, Ar V, and Ar VI, formed in a large range of depths from deep within the photosphere to the transition region into the "wind". But in order to extract the information about the abundances and wind parameters, and from these the stellar parameters, a sophisticated analysis is required.

Our method for modeling the atmosphere and computing the emergent UV spectrum in order to deduce the fundamental stellar parameters via a comparison with the observed spectrum is based on the premise that the winds are radiation-driven, homogeneous, stationary, and spherically symmetric. It incorporates a consistent treatment of the blocking and blanketing influence of all metal lines in the entire sub- and supersonically regions and a full non-LTE treatment of all level populations. Although a detailed description of the procedure is given by Pauldrach et al. (2001), Pauldrach (2003), Pauldrach et al. (2004), and Pauldrach et al. (2011), we will give here an overview of the physics to be treated.

The general concept. Although the basis of our approach in constructing detailed atmospheric models for hot stars is the concept of homogeneous, stationary, and spherically symmetric radiation-driven atmospheres, the method is not simple, since modeling the atmospheres of hot stars involves the replication of a tightly interwoven mesh of physical processes: the equations of radiation hydrodynamics including the energy equation, the statistical equilibrium for all important ions with detailed atomic physics (a detailed description of our atomic models is to be found in Sect. 3 and Table 1 of Pauldrach et al. (2001) and in Sect. 2 of Pauldrach et al. (1994) where several Tables and Figures illustrating and explaining the overall procedure are shown), and the radiative transfer equation at all transition frequencies have to be solved simultaneously.

The principal features of the method are:

- *The hydrodynamic equations* are solved. Here the crucial term is the radiative acceleration with minor contributions from continuous absorption and major contributions from scattering and line absorption (including the effects of line-overlap and multiple scattering, cf. Fig. 2.2). We note that the consistent treatment of the hydrodynamics is a crucial point, because the hydrodynamics affects the non-LTE model via the density structure and the velocity field, and the radiative transfer with respect to Doppler-shifted spectral lines, but in turn is controlled by the line force determined by the occupation numbers and the radiative transfer of the non-LTE model. Back reaction mechanisms are therefore inherently involved in the procedure.

- *The occupation numbers* are determined by the *rate equations* containing collisional and radiative transition rates. Low-temperature dielectronic recombination is included and Auger ionization due to K-shell absorption (essential for C, N, O, Ne, Mg, Si, and S) of soft X-ray radiation arising from shock-heated matter is taken into account using detailed atomic models for all important ions. Note that the hydrodynamical equations are coupled directly with the rate equations. The velocity field enters into the radiative rates via the Doppler shift, while the density is important for the collisional rates and the total number density.

- *The spherical transfer equation* which yields the radiation field at every depth point, including the thermalized layers where the diffusion approximation is used as inner boundary, is solved for the total opacities and source functions of all important ions. Hence, the influence of the spectral lines – the strong EUV *line blocking* including the effects of line-overlap (cf. Fig. 2.2) –

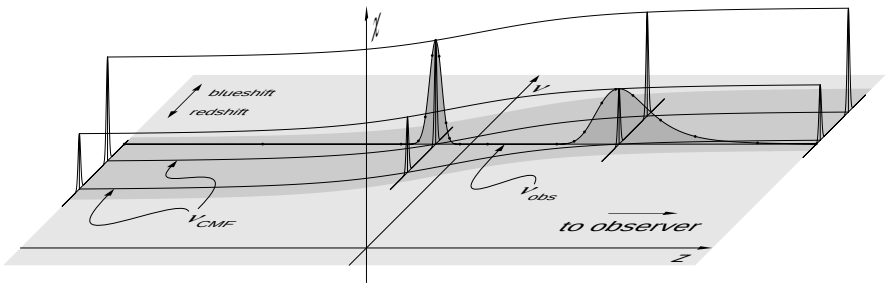

Figure 2.2: Diagram illustrating the basic relationship of the rest-frame frequencies of spectral lines ($\nu_{\rm CMF}$) to observer's frame frequency ($\nu_{\rm obs}$) for one particular (non-core) p-ray in the spherically symmetric geometry (p,z geometry). Shown are two spectral lines of different opacity χ which get shifted across the observer's frame frequency by the velocity field in the wind. The dots represent the stepping points of the adaptive microgrid used in solving the transfer equation in the radiative line transfer. The method employed is an integral formulation of the transfer equation using an adaptive stepping technique on every p-ray in which the radiation transfer in each micro-interval is solved as a weighted sum on the microgrid (cf. Pauldrach et al. 2001): $I(\tau_0(p,z)) = I(\tau_n)e^{-(\tau_n-\tau_0)} + \sum_{i=0}^{n-1}\left(e^{-(\tau_i-\tau_0)}\int_{\tau_i}^{\tau_{i+1}} S(\tau)e^{-(\tau-\tau_i)}\,{\rm d}\tau(p,z)\right)$ where I is the specific intensity, S is the source function and τ is the optical depth (increasing from τ_0 on the right to τ_n on the left in the figure). To accurately account for the variation of the line opacities and emissivities due to the Doppler shift, all line profile functions are evaluated correctly for the current microgrid-(z,p)-coordinate on the ray, thus effectively resolving individual line profiles. Based on that, application of the Sobolev technique gives for the radiative line acceleration (cf. Pauldrach et al. 2011): $g_{\rm lines}(r) = \frac{2\pi}{c}\frac{1}{\rho(r)}\sum_{\rm lines}\chi_{\rm line}(r)\int_{-1}^{+1} I_{\nu_0}(r,\mu)\frac{1-e^{-\tau_s(r,\mu)}}{\tau_s(r,\mu)}\mu\,{\rm d}\mu$ where $\tau_s(r,\mu) = \chi_{\rm line}(r)\frac{c}{\nu_0}\left[(1-\mu^2)\frac{v(r)}{r} + \mu^2\frac{{\rm d}v(r)}{{\rm d}r}\right]^{-1}$ is the Sobolev optical depth, and ν_0 is the frequency at the center of each line – thus, the effects of line-overlap and multiple scattering are naturally included ($\chi_{\rm line}(r)$ is the local line absorption coefficient, μ is the cosine of the angle between the ray direction and the outward normal on the spherical surface element, and c is the speed of light).[4]

which affects the ionizing flux that determines the ionization and excitation of levels, is naturally taken into account. This is also the case for the effect of Stark-broadening, which is essential for the diagnostic use of certain spectral lines. *Stark-broadening* has therefore, as a new feature, been included in our procedure (cf. Sect. 2.3). Moreover, the *shock source functions* produced by radiative cooling zones which originate from a simulation of shock heated matter, together with K-shell absorption, are also included in the radiative transfer (the shock source function is incorporated on the basis of an approximate calculation of the volume emission coefficient of the X-ray plasma in dependence of the velocity-dependent post-shock temperatures and a filling factor).

- *The temperature structure* is determined by the microscopic *energy equation* which, in principle, states that the luminosity must be conserved in the atmosphere. *Line blanketing* effects which reflect the influence of line blocking on the temperature structure are taken into account.

The iterative solution of the total system of equations yields the hydrodynamic structure of the wind (i.e., the *mass-loss rate* and the *velocity structure*) together with *synthetic spectra* and *ionizing fluxes*.

The analysis technique. In general, the analysis technique involves the following steps: first, a preliminary inspection of the UV and/or visual spectrum of the star gives a guess for $T_{\rm eff}$, and, together with a reasonable estimate of the mass M and radius R of the star, we use this to compute an initial atmospheric model and its emergent UV spectrum. Since the ionization balance in the wind depends strongly on the strength of the radiation field and thus on the effective temperature, we can then refine our value for $T_{\rm eff}$ by comparing the strengths of the lines of successive ionization stages of several elements.[5] Given the current set of stellar parameters, a consistent calculation of the hydrodynamics of the outflow yields the terminal velocity v_∞ of the wind, measurable from the blue edge of the P-Cygni profiles of strong resonance lines in the observed UV spectrum, and the mass loss rate $\dot{M}$, reflected mainly in the overall strength of the lines in the transition region. In case the calculated v_∞ of the model differs from the observed value, we need to modify the stellar mass until agreement is reached (since v_∞ depends sensitively on $(M/R)^{1/2}$ according to the theory of radiation-driven winds). If the overall fit of the spectrum is not satisfactory we must modify the mass loss rate $\dot{M}$ via a change of R (since $\log \dot{M} \sim \log L$, according to radiation-driven wind theory). The change in R forces us to change the mass, too, in order to keep v_∞ consistent with the observed value. (Additionally, we may correct the temperature slightly, if this improves the fit.) The new model is calculated and the process is repeated until we obtain a good simultaneous fit to all features in the observed spectrum. For a detailed description of the procedure used to derive all relevant parameters see Pauldrach et al. (2004) and Pauldrach et al. (2011).

2.2.2 Parameter determination using optical H and He lines

An alternative method which has been applied to the analysis of hot stars by other workers in the field is based on modelling the optical spectrum, in particular using the stellar Hα profile to determine the mass loss rate (see, for instance, Puls et al. 1996 and references therein): the strength of Hα, if in emission, reacts very sensitively to changes in the density (being a recombination line), and thus the mass loss rate. The outflow velocity is usually assumed to be a function of the radius as a so-called "beta velocity law," $v(r) = v_\infty (1 - R/r)^\beta$, where the shape of the velocity field is dependent on the arbitrary parameter β (the best-fit value of β to be determined as part of the analysis).

[4] Note that a comparison of the line acceleration of strong and weak lines evaluated with the comoving frame method and the Sobolev technique without consideration of the continuum acceleration is presented in Fig. 5 of Pauldrach et al. (1986), and with the comoving frame method and the Sobolev-with-continuum technique with consideration of the complete continuum acceleration in Fig. 3 of Puls & Hummer (1988), showing the excellent agreement of the two methods. It is thus important to realize that the accuracy of the calculation of the radiative acceleration is of the same quality as that of the synthetic spectrum, since the radiative acceleration is calculated analogously and in parallel to the synthetic spectrum. This means that the velocity field $v(r)$ and the mass loss rate $\dot{M}$, which are just functions of the basic stellar parameters and the radiative acceleration, are as realistic as the synthetic spectrum is. Finally, the hydrodynamics is solved by iterating the complete continuum acceleration $g_{\rm cont}(r)$ (which includes in our case the force of Thomson scattering and of the continuum opacities $\chi_\nu^{\rm cont}(r)$ – free-free and bound-free – of all important ions (cf. Pauldrach et al. 2001)) together with the line acceleration $g_{\rm lines}(r)$ – obtained from the spherical NLTE model – and the density $\rho(r)$, the velocity $v(r)$, and the temperature structure $T(r)$ (cf. Pauldrach et al. 2011 and references therein).

[5] Especially for effective temperatures in the range of 30 000 to 40 000 K we have found the Fe IV/Fe V ionization balance well suited for this purpose. The wavelength range from 1400 to 1550 Å is dominated by lines from Fe V, whereas Fe IV lines dominate in the range from 1550 to 1650 Å, and a comparison of the relative strengths of the lines in these wavelength ranges in the observed and the synthetic UV spectrum usually allows the effective temperature to be constrained to within $\pm$1000 K (see, for instance, Pauldrach et al. 2001).

Table 2.1: Parameters of the two test models used for comparing the resulting profile shapes of optical H and He lines computed with the two different stellar atmosphere codes WM-basic and FASTWIND.

Model	$T_{\rm eff}$ (K)	$\log g$	R ($R_\odot$)	$\dot{M}$ ($M_\odot$/yr)	v_∞ (km/s)
D30	30000	3.85	12	8×10^{-9}	1800
D45	45000	3.9	12	1.3×10^{-6}	3000

The fitting procedure is usually as follows (see also Kudritzki et al. 1997): by using fits to the optical hydrogen and helium stellar absorption lines with theoretical profiles computed from plane-parallel non-LTE models, preliminary estimates of $T_{\rm eff}$, the surface gravity $\log g$, and the He abundance $Y_{\rm He}$ are made. To calculate the H_α profile an estimate for the stellar mass M as well as for the terminal velocity v_∞ is needed in addition to the already estimated preliminary atmospheric parameters $T_{\rm eff}$, $\log g$, and $Y_{\rm He}$: the mass is derived from evolutionary tracks plotted in the $\log g$–$\log T_{\rm eff}$ diagram, assuming these to be correct, whereas v_∞ is measured directly from the bluest edge of the strongest resonance line in the observed UV spectrum. To fit the stellar H_α profile, different values for the parameter β and the mass loss rate are used. Having a first estimate for the mass loss rate, new "unified" models (comprising photosphere and wind, parametrizing the outflow velocity law with the fit parameter β) are calculated to obtain improved theoretical profiles for the other diagnostic lines. The procedure is iterated until adequate fits to most of the stellar absorption and emission lines are achieved. It must be stressed that in this procedure it is only possible to obtain values for the stellar mass and the luminosity by assuming that the evolutionary models give us the correct relation between the two.

2.2.3 Combined analysis

Given the differences between the parameter sets derived from UV vs. optical analyses published in the literature, the obvious question was whether there is an intrinsic discrepancy between modelling the UV and the optical spectra. Up to now we were unable to answer this question since our model atmosphere code did not compute the shapes of the optical lines correctly, due to the fact that Stark broadening was not included in the calculations. (This is quite unimportant for the atmospheric structure and the UV spectra, but crucial if one wants to determine atmospheric parameters from the optical lines.) With the inclusion of Stark broadening (see below) we can now compute UV and optical spectra consistently from the same atmospheric model. Having this tool at hand, we will in this paper apply it to the parameter sets for two CSPNs published by Pauldrach et al. (2004) (UV analysis) and Kudritzki et al. (1997) (optical analysis), and compare the results to the observations.

2.3 Implementation of Stark broadening in the model atmosphere code WM-basic

Depending on the physical environment, the shapes of line profiles are affected by different physical processes. Natural broadening, for instance, dominates the shapes of the profiles at large frequency

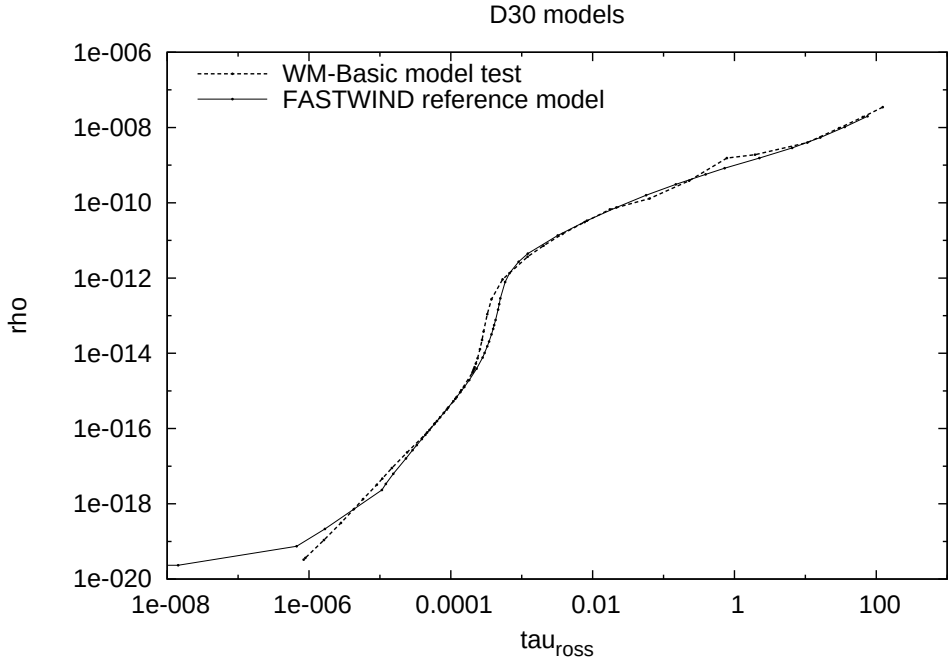

Figure 2.3: Density profiles for the D30 test model. The solid line shows the density structure used by the FASTWIND model, the dashed line shows the hydrodynamically calculated density structure of the WM-basic model, using a (not necessarily consistent) parametrization of the radiative force designed to approximate the density structure of the FASTWIND comparison model.

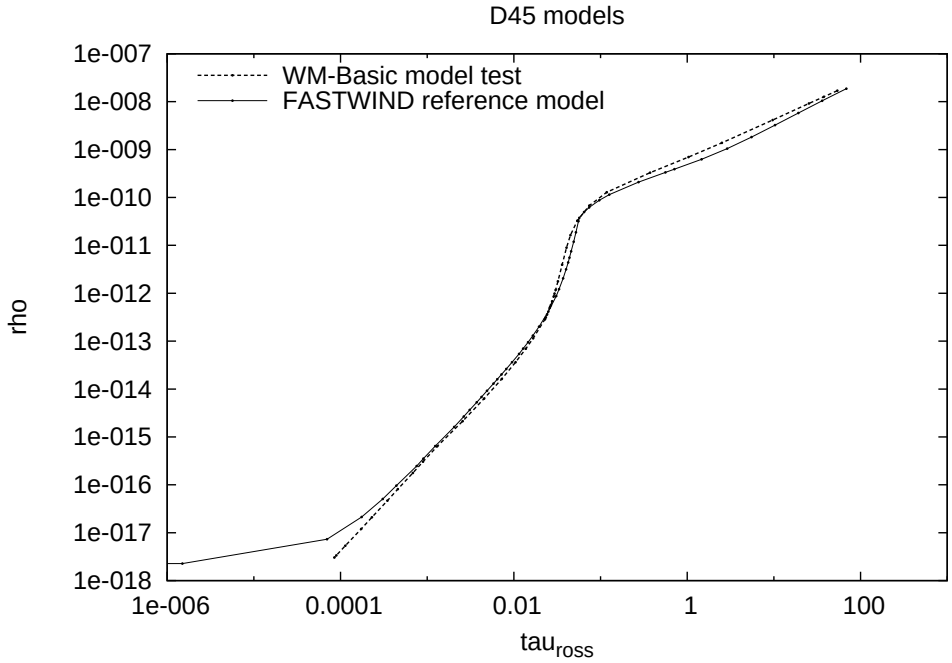

Figure 2.4: Density structure for the D45 test model. As for the D30 model, the D45 models show small differences in their density profiles compared to one another, leading to some expected differences in the line profiles.

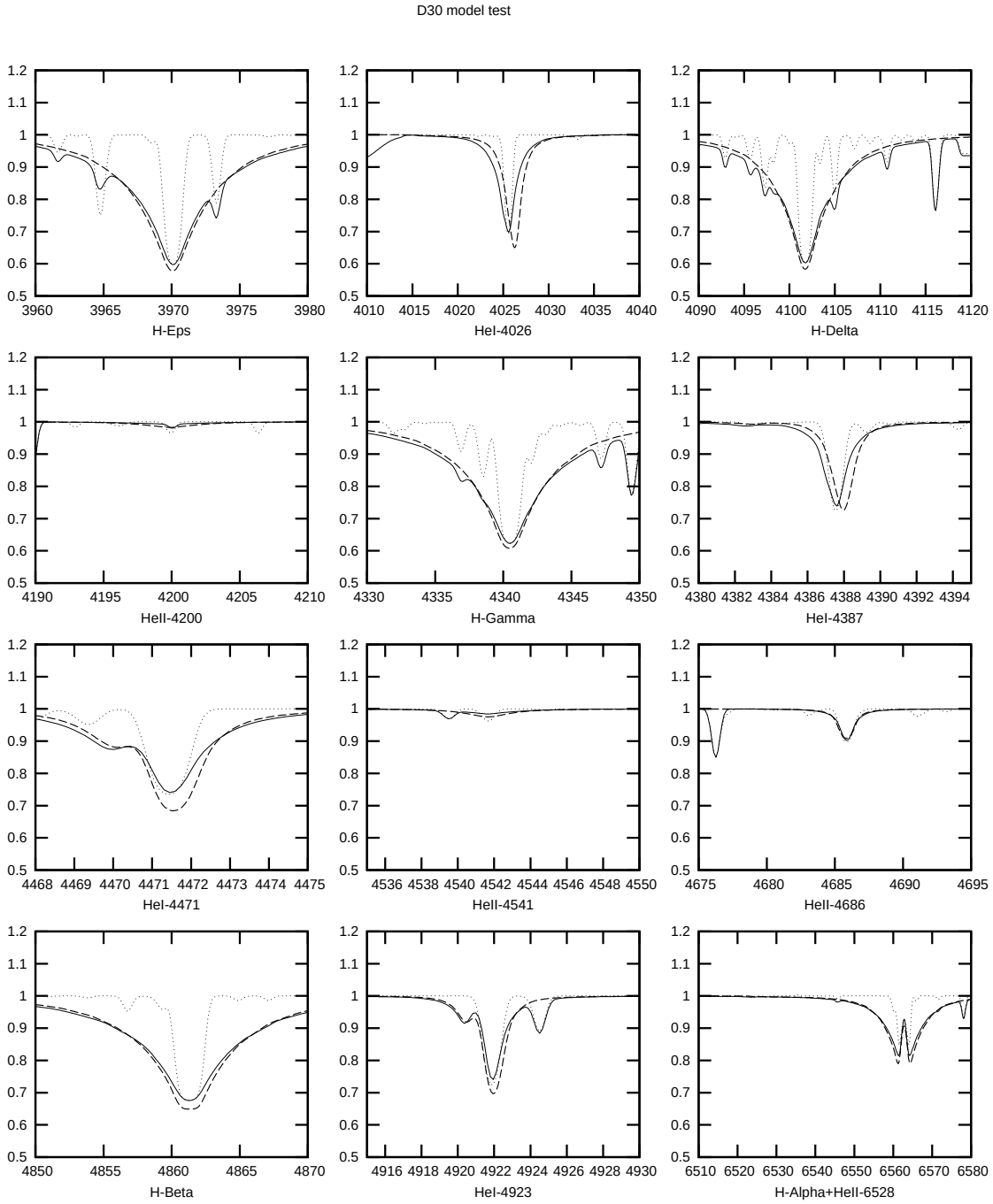

Figure 2.5: H and He lines of the D30 model calculated with our stellar atmosphere code WM-basic (solid lines) compared to the H and He lines calculated with the model atmosphere code FASTWIND (dashed lines). (The WM-basic model also contains additional metal lines not included in the FASTWIND model.) Note the big difference between the H and He line profiles of the former WM-basic code (dotted lines) missing the Stark broadening to the present profiles (solid lines). Our improved models match the reference model lines almost perfectly. Small deviations due to differences in density and occupation numbers of the two codes are to expected.

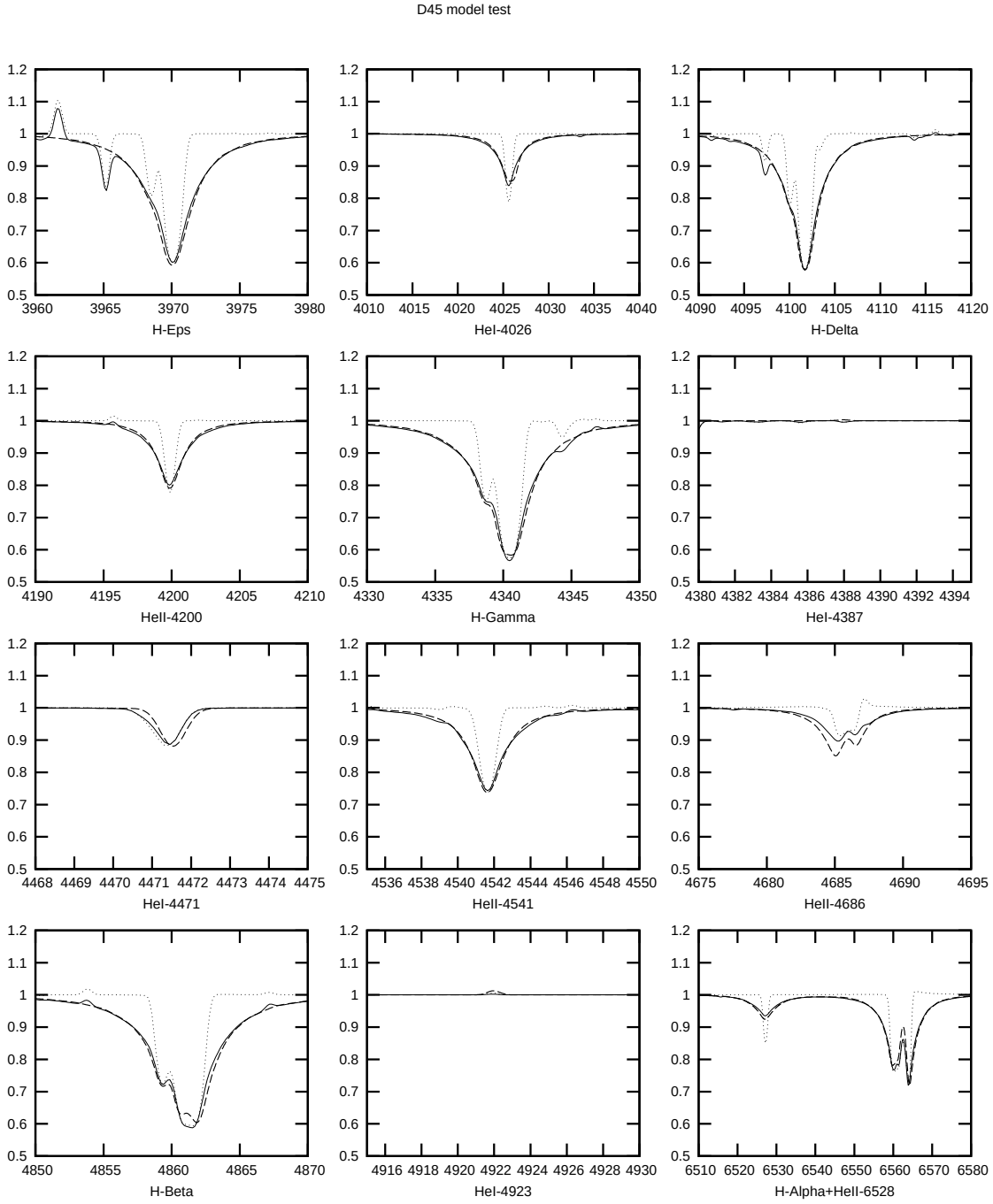

Figure 2.6: H and He lines of the D45 model calculated with our stellar atmosphere code WM-basic (solid lines) compared to the H and He lines calculated with the model atmosphere code FASTWIND (dashed lines). Note the big difference between the H and He line profiles of the former WM-basic code (dotted lines) missing the Stark broadening to the present profiles (solid lines). Again our improved models match the reference model lines almost perfectly. Small deviations due to differences in density and occupation numbers of the two codes are to expected.

Table 2.2: Stellar and wind parameters of the models used to compute the synthetic spectra presented in this work for the two CSPNs NGC 6826 and NGC 2392. P04 refers to the parameters derived by Pauldrach et al. (2004) from an analysis of the UV spectra, K97 refers to the optical analysis of Kudritzki et al. 1997, and K06 refers to the optical analysis of Kudritzki et al. 2006 (a dash in the "matches observation?" column indicates that a comparison to observations was not shown in the paper). "Consistent" means that the wind parameters are consistent with the stellar parameters as determined by our hydrodynamic calculations of the radiative driving force. We note that Kudritzki et al. 2006 obtained a much lower mass loss rate for NGC 6826 than Kudritzki et al. 1997.

$T_{\rm eff}$ (K)	R ($R_\odot$)	$\log L$ ($L_\odot$)	M ($M_\odot$)	$\log g$ (cm/s^2)	$\dot{M}$ ($10^{-6} M_\odot$/yr)	v_∞ (km/s)	parameter source stellar	wind	consistent?	matches observation?
					NGC 6826					
50000	2.0	4.4	0.92	3.8	0.26	1200	K97	K97	no	yes
〃	〃	〃	〃	〃	0.50	850	〃	this work	yes	no
46000	1.8	4.11	0.74	3.8	0.08	1200	K06	K06	no	–
44000	2.2	4.2	1.40	3.9	0.18	1200	P04	P04	**yes**	**yes**
〃	〃	〃	0.88	3.7	0.25	360	this work	this work	yes	no
					NGC 2392					
45000	2.5	4.4	0.91	3.6	≤ 0.03	400	K97	K97	no	yes
〃	〃	〃	〃	〃	0.32	400	〃	this work	yes	no
44000	2.4	4.30	0.86	3.6	≤ 0.05	400	K06	K06	no	–
40000	1.5	3.7	0.41	3.7	0.018	420	P04	P04	**yes**	**yes**

distances from the line centers. Doppler broadening, on the other hand, is always relevant and dominates the shapes close to the line center. In dense atmospheres the line shapes are also strongly influenced by interactions of radiating atoms or ions with the surrounding particles. This behavior reflects the so called pressure broadening and, as electric fields are involved, this type of broadening is also called Stark broadening. In order to include this effect in our model atmosphere code,[6] reliable profile functions for H, He I, and He II were required. For the H lines we used the data sets published by Vidal et al. (1973). Those for the He I lines have been implemented according to Griem (1964), Barnard et al. (1969) and Shamey (1964), whereas the data sets for the He II lines have been applied according to Schoening & Butler (1989).

To validate our implementation of Stark broadening, we have performed test calculations and compared our results to those obtained with the model atmosphere code FASTWIND (Puls et al. 1996, Santolaya-Rey et al. 1997, Puls et al. 2005), a well-established code for modelling the optical spectra of hot stars. Table 2.1 lists the stellar parameters for the two test models chosen.[7] Figures 2.5 and

[6] Since Stark broadening affects primarily the line wings, while the line cores are still dominated by Doppler broadening, as was shown by Herrero (1987) the inclusion of Stark broadening in the rate equations is of minor importance. (Herrero showed that the consideration of Stark broadening in both the rate equations and in the formal integral leads to results which are almost identical with results obtained for the case where Stark broadening is included just in the solution of the formal integral.) Hence, it is a common procedure to include Stark broadening only in the formal integral (cf. Santolaya-Rey et al. 1997).

[7] Stark broadening is a form of pressure broadening, and is thus only important for lines which are formed in regions of high atmospheric density, such as in the photospheres of dwarfs. In the regions where the lines go into wind emission, the density is too low for Stark broadening to show a significant effect. Thus, in a supergiant atmosphere where the absorption lines become contaminated with emission from the outer regions, a statement about the correct implementation of Stark broadening is not possible, since one would be comparing the implementation of all of the physics operating in those

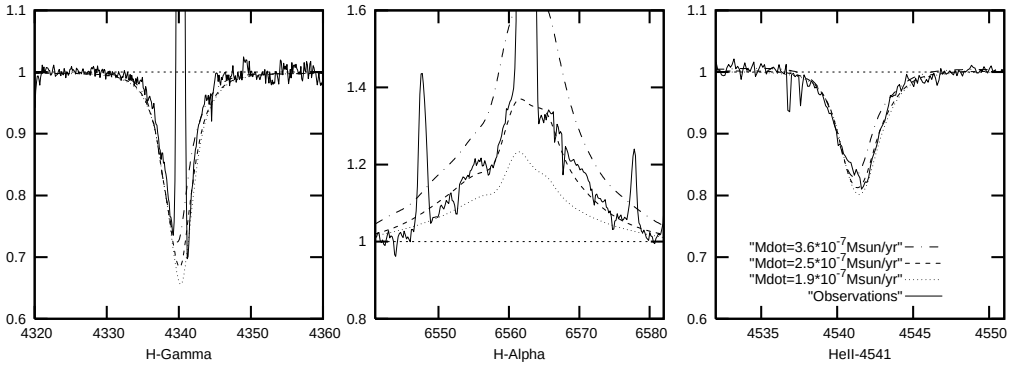

Figure 2.7: Profiles for the H_γ, H_α, and He II λ4541 lines of the CSPN NGC 6826 calculated with the model atmosphere code FASTWIND (J. Puls, priv. comm.) using the stellar parameters derived by Kudritzki et al. (1997), compared to the observed profiles. Note in particular the sensitive dependence of the emission line H_α on the mass loss rate. The different predicted line profiles correspond to mass loss rates of $\dot{M} = 1.9 \times 10^{-7} M_\odot/\mathrm{yr}$ (dotted), $\dot{M} = 2.5 \times 10^{-7} M_\odot/\mathrm{yr}$ (dashed), and $\dot{M} = 3.6 \times 10^{-7} M_\odot/\mathrm{yr}$ (dash-dotted).

2.6 show the profiles of the most important hydrogen and helium lines used in the optical analyses, computed for these two models using WM-basic (solid lines) and FASTWIND (dashed lines).

With regard to the implementation of Stark broadening in our code WM-basic, these calculated lines are expected to match their counterparts calculated with FASTWIND within errors. The lines cover a wide range of the optical spectra, starting with Hε at 3970 Å and ending with Hα at 6563 Å, including not only H lines but also He I and He II lines. As can be seen from the figure, the absorption lines match very well, with only small differences that arise from differences in the density structures. (For the purposes of this comparison the line force has not been calculated consistently but instead adapted in such a way that the computed density structure approximates the density structure used by the FASTWIND models.) Figure 2.3 shows the density profiles for the D30 model. Small deviations occur at $\tau_{\mathrm{Ross}} \approx 0.00001$ and between $\tau_{\mathrm{Ross}} = 0.0001$ and $\tau_{\mathrm{Ross}} = 0.001$. These differences contribute to small changes in the occupation numbers that lead to corresponding small differences in the computed line profiles (the fact that slightly different occupation numbers are responsible for the small differences shown is recognized by the slightly deeper cores of these lines; as the occupation numbers are calculated differently by WM-Basic and FASTWIND such small differences are to be expected and can of course not be prevented even if density and temperature were exactly the same). The behavior is similar for the D45 model for which the density structures are shown in Figure 2.4. Again some minor differences in the density structures are apparent between optical depths of $\tau_{\mathrm{Ross}} = 0.0001$ and $\tau_{\mathrm{Ross}} = 0.001$, leading to small deviations in the line profiles which are somewhat pronounced at an optical depth of $\tau_{\mathrm{Ross}} > 0.1$.

regions. We have therefore compared our Stark profiles for dwarf atmospheres, where in the regions in which Stark broadening becomes important the density structures of WM-basic and FASTWIND are in agreement.

2.4 CSPN observational material

The observed UV spectra of the two CSPNs discussed here, NGC 6826 and NGC 2392, are the same as those used by Pauldrach et al. (2004) in their UV analysis. These spectra were obtained from the INES Archive Data Server on the Web now at `http://sdc.laeff.inta.es/ines/`, providing access to IUE Final Archive data.

The optical material was collected from observations using a variety of telescopes and spectrographs: ESO 3.6 m + CASPEC, ESO NTT + EMMI, Isaac Newton 2.5 m (La Palma) + IDS, Palomar echelle, McDonald 2.1 m + Sandiford echelle. These spectrograms were kindly provided by R.-P. Kudritzki (priv. comm.).

2.5 Consistent optical and UV analysis of the CSPNs NGC 6826 and NGC 2392

In this paper we present a comparison of computed and observed optical and UV spectra for two CSPNs. We calculate optical and UV spectra using our improved WM-basic code, and we want to see if (for each CSPN) a set of stellar parameters exists for which both the predicted optical and the predicted UV spectrum simultaneously match the corresponding observations. Basis for the comparison is the analysis of the UV spectra by Pauldrach et al. (2004) and the optical analysis by Kudritzki et al. (1997), who found significantly different stellar parameters (see Table 2.2). We have chosen the two CSPNs NGC 6826 and NGC 2392 because they represent extreme examples compared to the other objects in the sample investigated by Pauldrach et al. (2004), according to which NGC 6826 has an extremely high mass of 1.4 $M_\odot$ (near the Chandrasekhar limit), whereas NGC 2392 has a mass of only 0.41 $M_\odot$, the smallest mass in the whole sample.

2.5.1 NGC 6826

Kudritzki et al. (1997) have shown their computed H_γ, H_α, and He II λ4541 line profiles for NGC 6826. Their model was calculated with a previous version of the FASTWIND model atmosphere code, but calculations (J. Puls, priv. comm.) using the current FASTWIND code yield almost identical line profiles (Figure 2.7). The Kudritzki et al. (1997) determination of the mass loss rate was based on modelling of the H_α line. As shown in Figure 2.7, a mass loss rate of around $\dot{M} = 2.5 \times 10^{-7}\, M_\odot/\mathrm{yr}$ yields the best fit to the observed H_α line profile for the stellar parameters assumed by Kudritzki et al. (1997) (which were taken to conform to the predicted mass–luminosity relation of theoretical post-AGB evolutionary models).

Figure 2.8 shows the optical lines from the corresponding WM-basic model run. For this we used the same stellar parameters, but we had to artificially adjust the line force to obtain the desired mass-loss rate of $\dot{M} = 2.6 \times 10^{-7}\, M_\odot/\mathrm{yr}$. With this mass loss rate, our calculated absorption lines are almost identical to those presented by Kudritzki et al. (1997). The small deviations in the emission lines H_α and He II λ4686 are, as already discussed above, due to the differences in the density structure. These arise from the fit parameter β (see Section 2.2.2) used in FASTWIND, which effectively allows varying the radius–density relationship in the wind, and thus allows the user to tune the amount of emission in these lines. (Remember that H_α and He II λ4686 are recombination lines and as such are strongly density-dependent.) Our WM-basic code, on the other hand, does not provide such a free

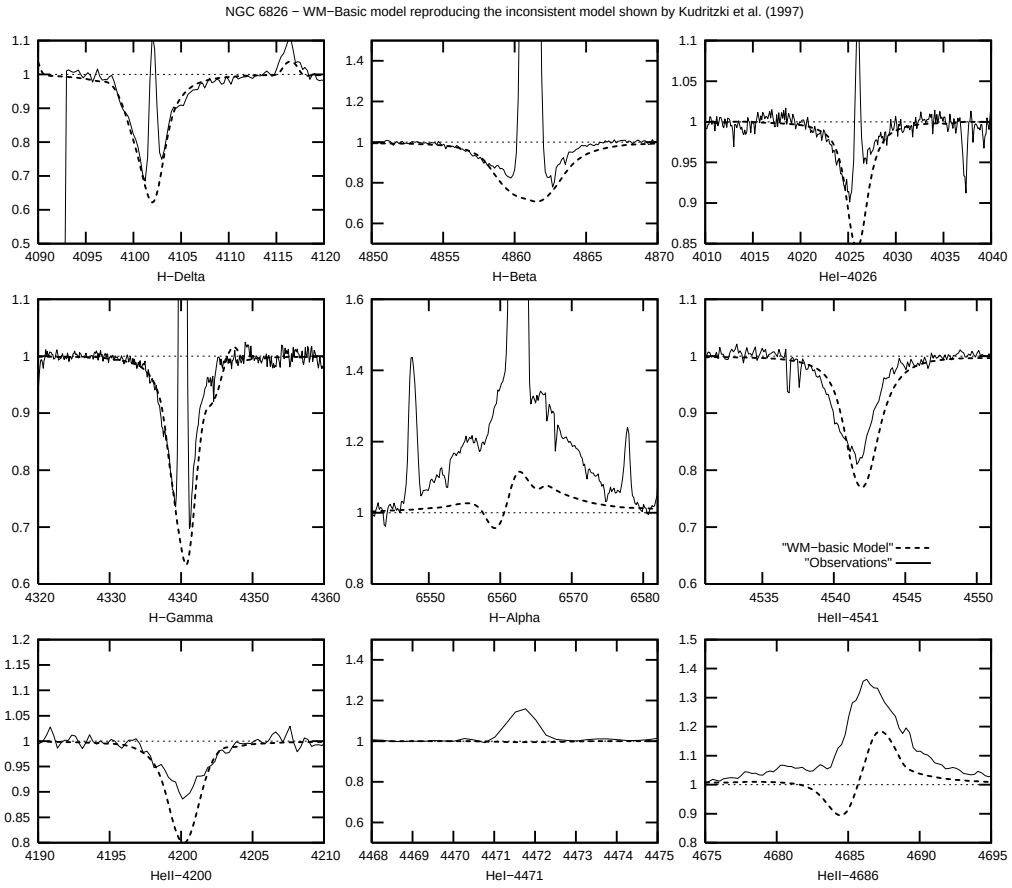

Figure 2.8: Optical line profiles from our WM-basic model of NGC 6826 with artificially adapted line force reproducing the NGC 6826 model by Kudritzki et al. (1997). Comparing our line profiles to those shown by Kudritzki et al. (their Figure 1, cf. also our Figure 2.7) we find H_γ and He II λ4541 to be almost identical, whereas our H_α line is somewhat weaker. All other absorption lines match the observations in good agreement.

parameter, since the radial run of density and velocity is not chosen by the user but computed from the hydrodynamic equations and the radiative force.[8]

Compared to the parameters obtained by Kudritzki et al. (1997), the UV analysis by Pauldrach et al. (2004) had yielded almost the same value for the mass loss rate ($\dot{M} = 1.8 \times 10^{-7}\ M_\odot/\mathrm{yr}$), but along with a consistently determined radius and mass. The latter point being the key factor in the analysis of Pauldrach et al. (2004), one of our main interests in the current work was a comparison

[8] From our point of view it is inherently dangerous to fit line profiles by simply tuning a parameter that describes an assumed velocity law, because it involves the risk of covering up intrinsic weaknesses of other parts of the model description. Thus, being able to reproduce observed line profiles by adapting such a parameter tells us nothing whatsoever about the real physics of the expanding atmosphere, and only serves to fool oneself into believing one has actually made physical progress. It should be realized that a velocity law doesn't have to be assumed for O star atmospheres, because it can be calculated from well-known physical laws. Already in 1975, Castor, Abbott, & Klein have shown the way to proceed, obtaining already reliable results as demonstrated by Pauldrach et al. (1986). An arbitrarily chosen fudge factor to describe the velocity structure has therefore not been necessary for more than 35 years.

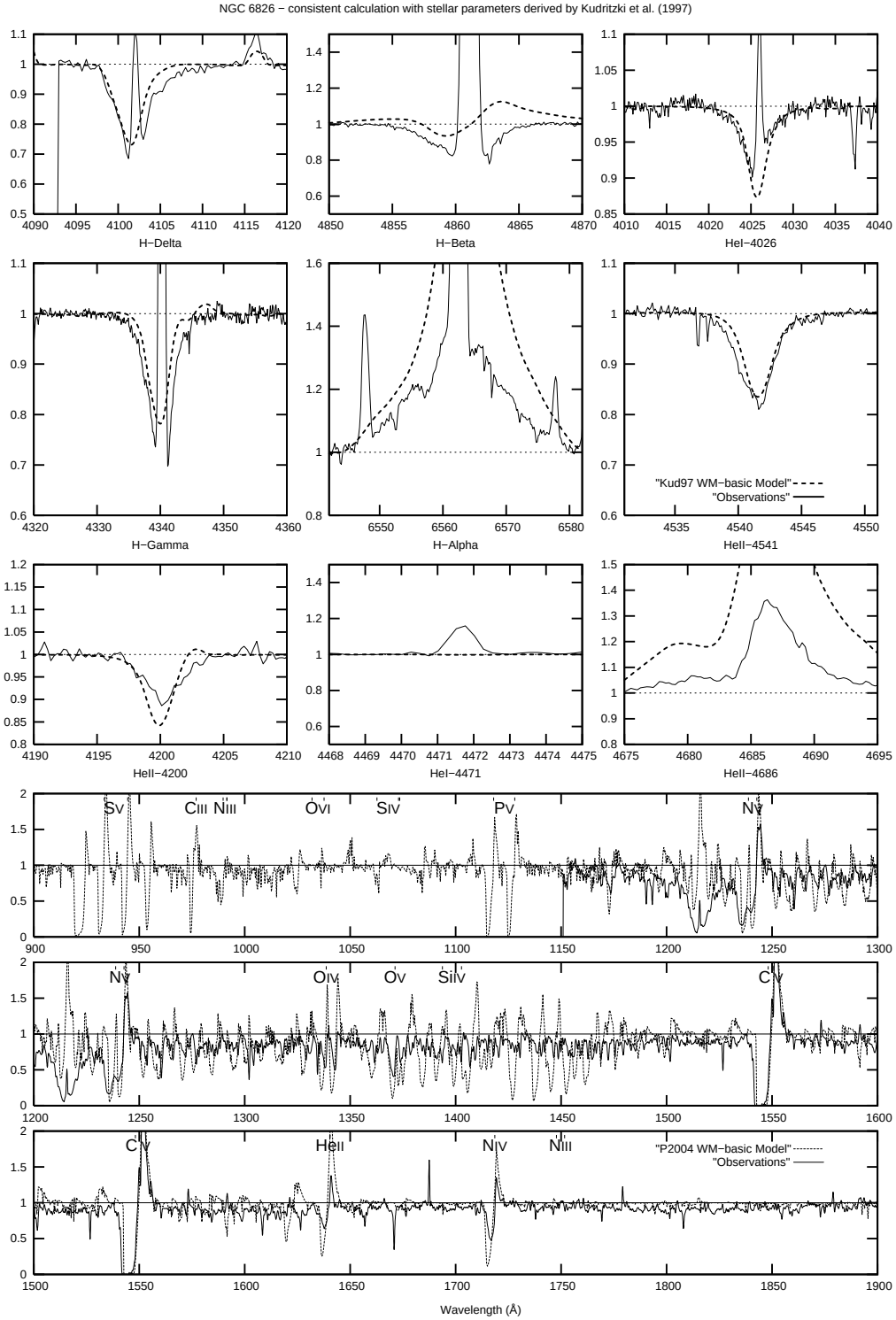

Figure 2.9: Optical and UV spectra for NGC 6826 from a model based on the stellar parameters from Kudritzki et al. (1997), but with wind parameters consistent to the stellar parameters. Compared to the observations (solid line), the model (dashed) yields far too strong emission lines in both the optical and the UV spectral ranges.

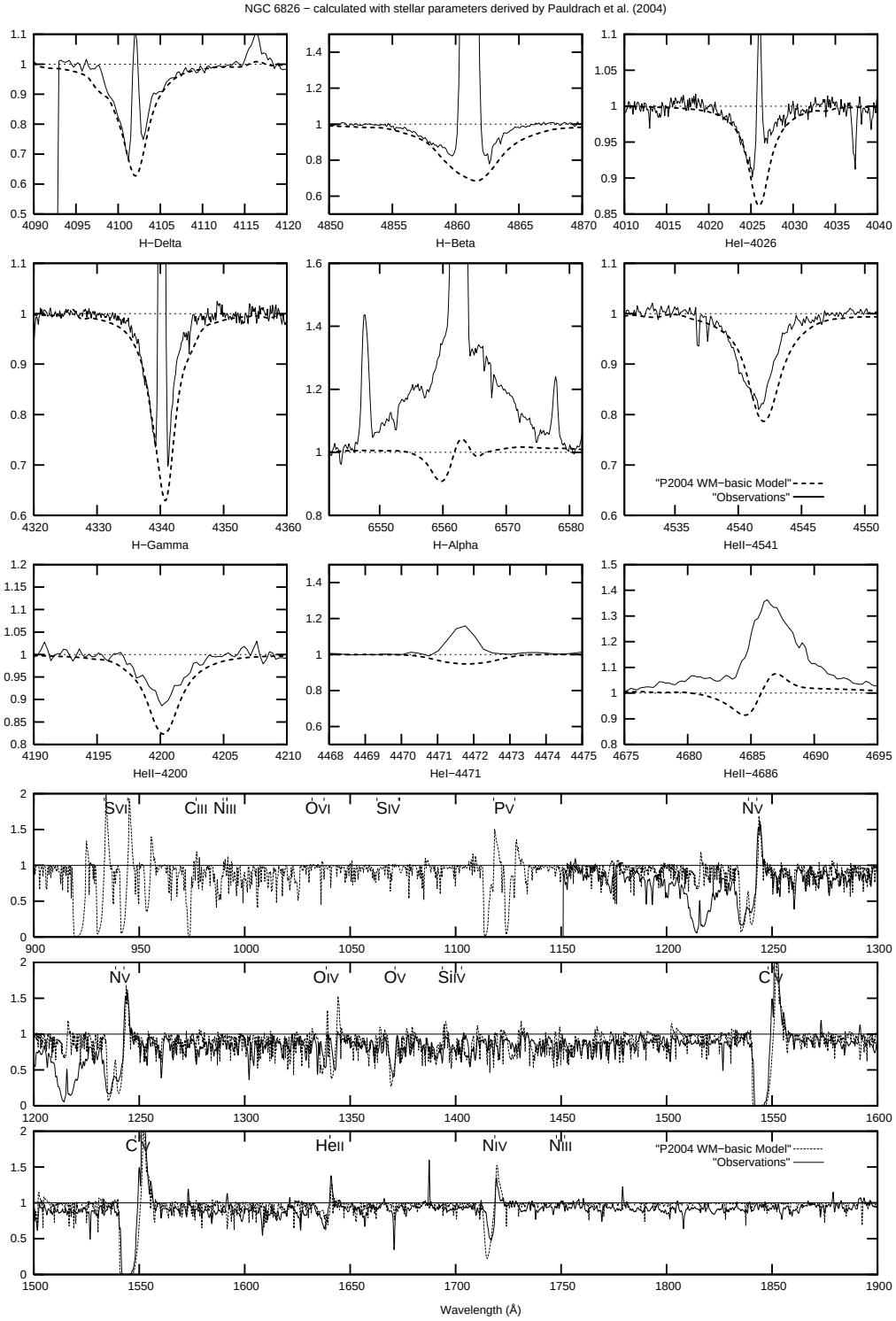

Figure 2.10: Optical and UV spectra for NGC 6826 from a model using the parameters from Pauldrach et al. (2004) (i.e., stellar parameters from Pauldrach et al. and wind parameters consistent with those stellar parameters). The predicted spectra match the observations as well as those of the model using the artificially adapted wind parameters and the stellar parameters of Kudritzki et al. (1997), but the model shown here has the merit of being hydrodynamically consistent.

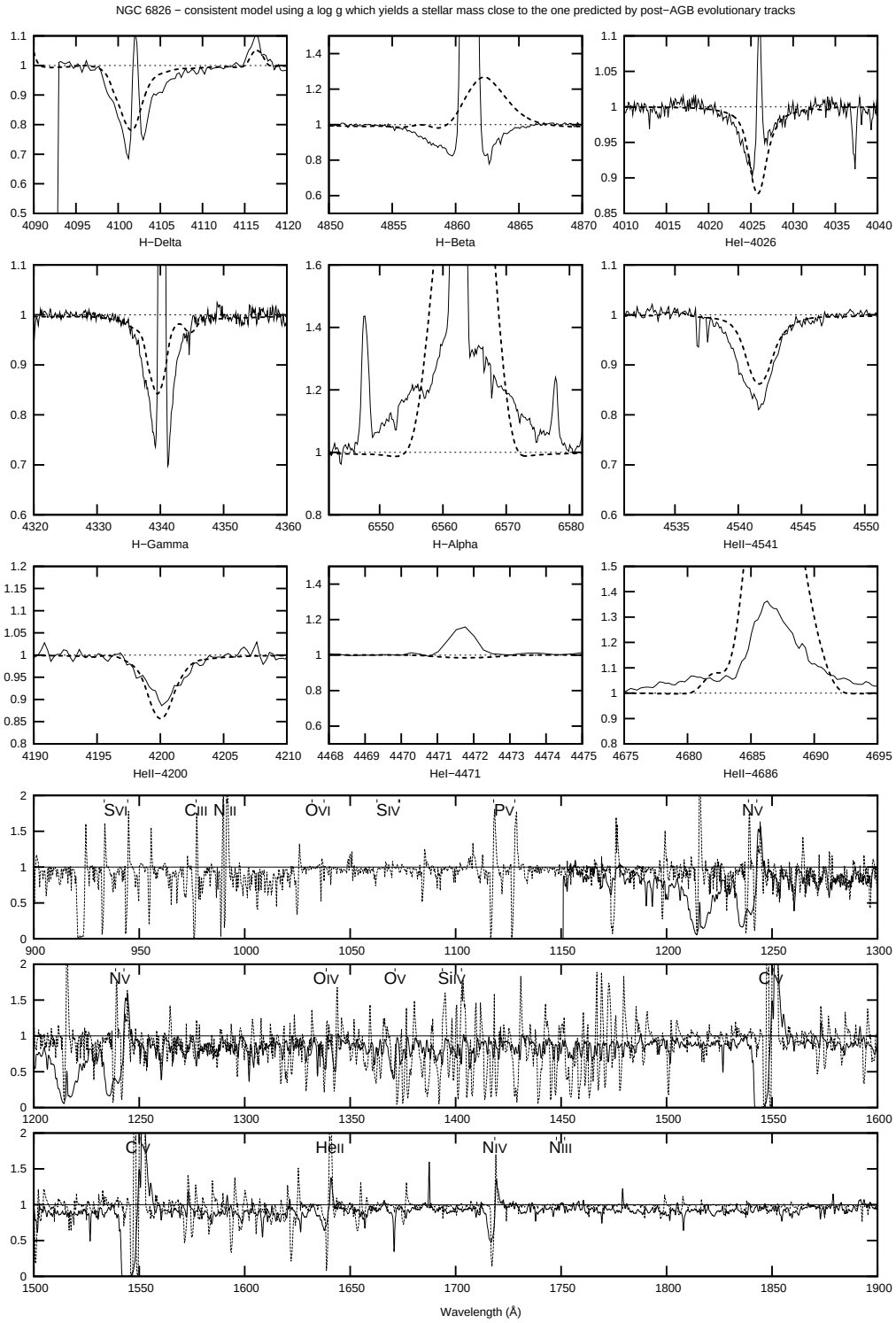

Figure 2.11: As Figure 2.10, but using a $\log g$ of 3.7, representing a consistent model with a mass very close to the one given by Kudritzki et al. (1997) (see Table 2.2). The now far too strong emission in He II λ4686 and H_α obviously does not match the observations.

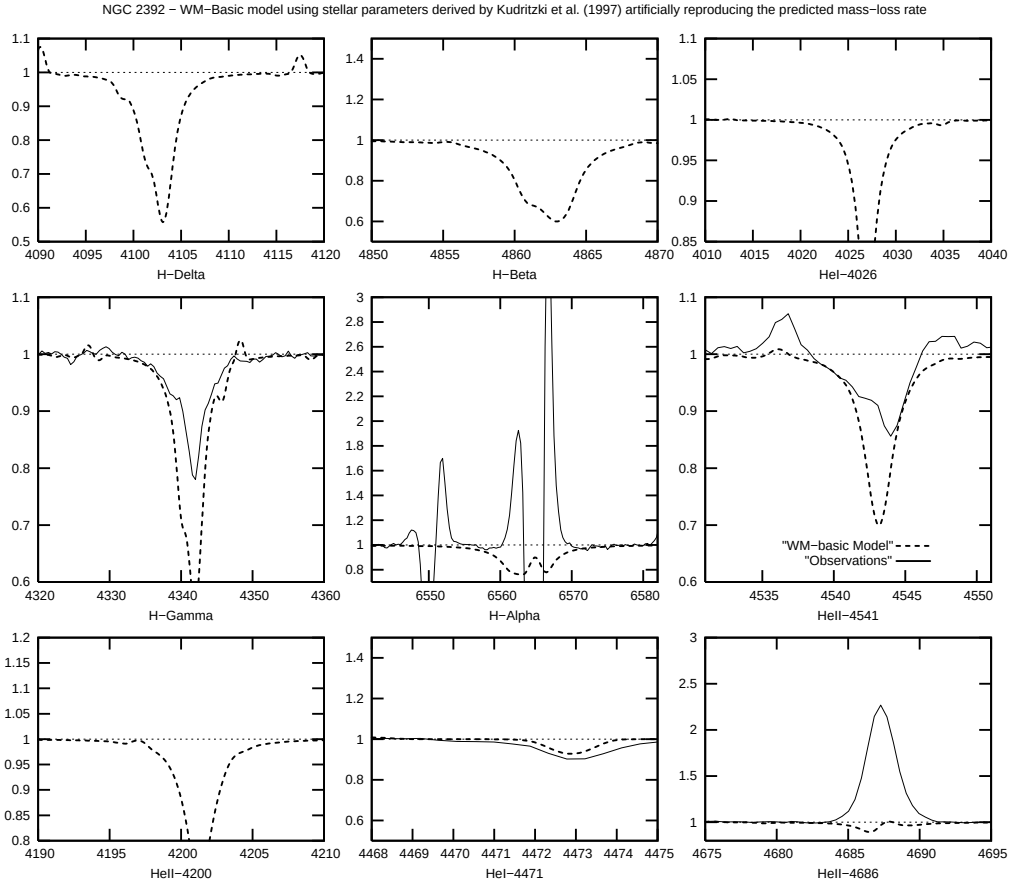

Figure 2.12: WM-basic model of NGC 2392 with artificially adapted line force reproducing the NGC 2392 model by Kudritzki et al. (1997). Given that our model for NGC 6826 adequately reproduced the line profiles shown by Kudritzki et al. (1997) for that object, we will equivalently assume the same for this CSPN. (Kudritzki et al. (1997) did not show any line profiles for NGC 2392.)

of two *consistent* models using the parameters sets of Pauldrach et al. (2004) and Kudritzki et al. (1997). The former model is of course identical to that presented by Pauldrach et al. (2004), but here we can now also compare the predicted optical line profiles (see below). For the latter model we have iterated hydrodynamics together with NLTE and line-force calculations to consistency, obtaining a (much larger) mass loss rate of $\dot{M} = 5.0 \times 10^{-7}\ M_{\odot}/\mathrm{yr}$ and a (much smaller) terminal velocity of $v_{\infty} = 850\ \mathrm{km/s}$.

Figure 2.9 shows the predicted line profiles for the selfconsistent model using the Kudritzki et al. (1997) stellar parameters. With the exception of He I λ4026, the comparison to the observed line profiles of NGC 6826 is unsatisfactory: wind emission begins to fill up the absorption lines, and the emission in H_{α} and He II λ4686 is much too strong. The bottom part of Figure 2.9 additionally shows the predicted UV spectrum, compared to the observed UV spectrum. What was already evident from the optical line profiles, namely that the stellar parameters of this model yield a much too large mass loss rate to reproduce the observations, is confirmed by the synthetic UV spectrum: the (unsaturated) P-Cygni lines He II λ1640 and N IV λ1719 are much too strong, as is the entire "forest" of Fe and Ni

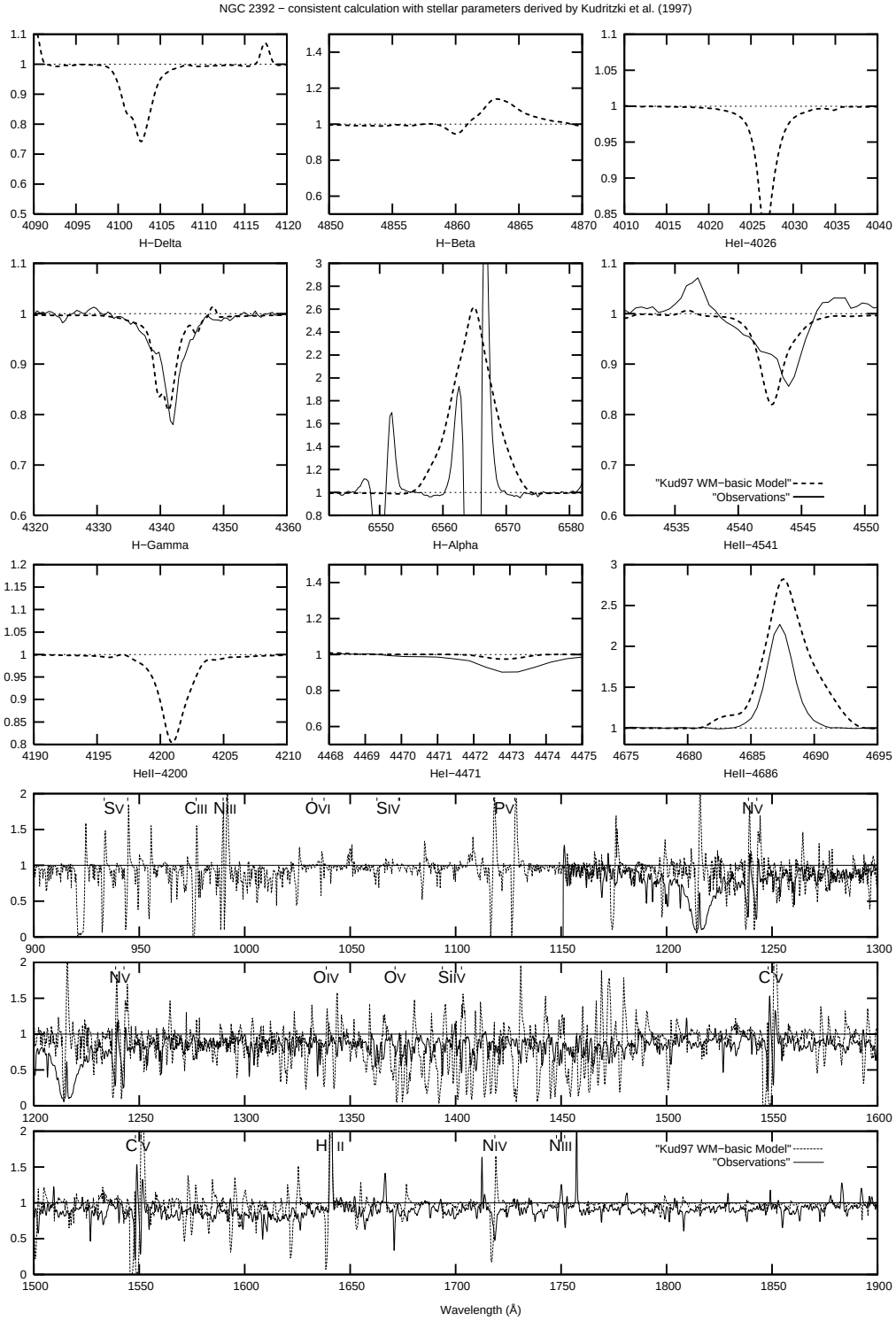

Figure 2.13: Optical and UV spectra for NGC 2392 from a model based on the stellar parameters from Kudritzki et al. (1997), but with wind parameters consistent to the stellar parameters. Compared to the observations, the model yields far too strong emission lines in both the optical and the UV spectral ranges.

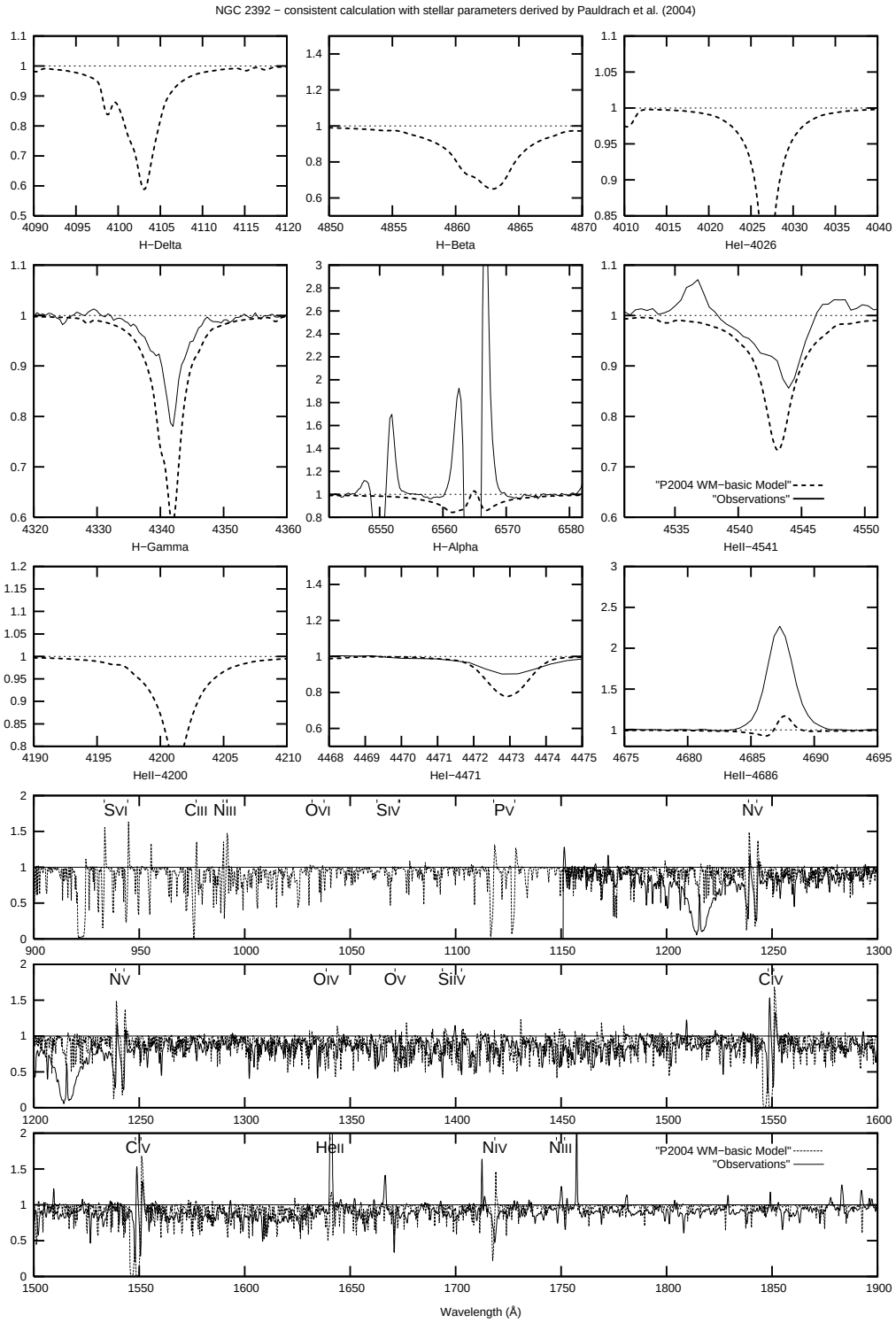

Figure 2.14: Optical and UV spectra for NGC 2392 from a model using the parameters from Pauldrach et al. (2004) (i.e., stellar parameters from Pauldrach et al. and wind parameters consistent with those stellar parameters). The predicted UV spectrum matches the observations, and the predicted optical line profiles are almost identical to those from the Kudritzki et al. (1997) model.

lines spanning the range from 1250 Å to 1500 Å.

We now turn to the model using the Pauldrach et al. (2004) parameters. As described in Section 2.2.1, these parameters were determined by varying mass and radius (and effective temperature) until the predicted UV spectrum from a *consistent* model with those parameters matched the observed UV spectrum (Figure 2.10, bottom panel). But with regard to the central question concerning the true stellar parameters of this object, the significant result of our current investigation is that the predicted optical line profiles *also* match the observed optical spectrum *as well as* those of the model using the artificial wind parameters and the Kudritzki et al. (1997) stellar parameters, whereas the *consistent* model using the Kudritzki et al. (1997) stellar parameters utterly fails to reproduce both UV and optical observations.

The conclusion to be drawn from this fact is that a match of predicted and observed spectra from any particular model does not immediately guarantee the correctness of the stellar parameters used in that model, since it is very likely that for any set of intermediate stellar parameters an (inconsistent) mass loss rate may be found that yields a similarly adequate fit to the observed spectrum. Of this series of models the singularly distinguished model is the one in which the wind parameters are consistent with the stellar parameters, and the parameters of this model must be regarded as being closest to the true parameters.

The calculated Hγ profile shown in Figure 2.10 has wings slightly broader than the observed profile, and it might thus appear that the gravity used in the model is higher than needed. In fact, the careful reader may have noticed that a drop in $\log g$ of only 0.2 (with all other parameters fixed) will bring the mass of this model very close to the mass of the Kudritzki et al. (1997) model for NGC 6826 (see Table 2.2). While the wings of Hγ from a consistent model with these stellar parameters now indeed match the observation better (see Figure 2.11), all other features in both the optical and the UV spectrum are completely ruined. The computed mass loss rate of $\dot{M} = 0.25 \times 10^{-6}\, M_{\odot}/\mathrm{yr}$ incidentally comes close to that used by Kudritzki et al. (1997), but the corresponding terminal velocity of $v_{\infty} = 360$ km/s is far too small (which can be seen in the narrow line profiles in the UV as well as the narrow optical emission lines), and the resulting higher wind density leads to far too strong emission in Hα, Hβ, and He II λ4686, as well as filling up the optical absorption lines.

Thus, although the reduction of $\log g$ achieved the goal of a better fit of the Hγ wings, the model became completely unacceptable with respect to all other spectral features. We must conclude from this that the wings of Hγ cannot by themselves be considered a reliable indicator of the surface gravity. This conclusion is underscored by a comparison of the Hγ line profiles shown in Figures 2.8 and 2.9, which result from models that have identical stellar parameters, in particular also identical $\log g$. The only difference between the two models is the density structure. Thus, while it is true that the wings of Hγ are an indicator of the density, the density structure is not determined by the surface gravity alone, but also by the radiative forces, and therefore it is inherently dangerous to base the determination of the surface gravity on a single line which is known to be also influenced by the back-reaction of thousands of other lines.

Nevertheless, the optical *emission* lines of the consistent model using the Pauldrach et al. (2004) parameters do not match the observations (though those of our model using the Kudritzki et al. (1997) stellar and wind parameters do not, either), and this detail merits discussion. Test calculations have shown that the mass loss rate needed to bring H_{α} into agreement is roughly only a factor of two larger than that of the model shown, but we cannot choose a model with a larger mass loss rate (with appropriate changes to the stellar parameters to maintain consistency) since this destroys the match of the UV spectrum. (As discussed above, Kudritzki et al. (1997) had the possibility of adjusting the

β parameter of the velocity field used in their analysis, but we do not consider this a realistic option since the computed line force does not result in a velocity field with the assumed shape used in those calculations.) Does this mismatch of the optical emission lines invalidate the parameters obtained from the consistent UV analysis? We are convinced that it does not, for the following reason:

Earlier analyses of the mass loss rates of massive O stars based on modelling the optical emission lines had seemed to indicate that the mass loss rates of supergiants were larger than those of dwarfs with similar luminosities (Puls et al., 1996), but this assessment has since been revised by the realization that the winds may be "clumped", the increased density in the clumps leading to a stronger emission of the hydrogen and helium recombination lines than in a "smooth" wind with the same mass loss rate. This revision has resulted in bringing the derived parameters into closer agreement with those predicted by radiation-driven wind theory (Puls et al., 2006), and it is likely that the winds of O-type CSPNs are similarly affected by clumping (Urbaneja et al., 2008). As we still have no consistent theory that will quantitatively predict the run and magnitude of this clumping, however, we are at the moment inclined to not rely too heavily on emission lines which are expected to be thus affected.

2.5.2 NGC 2392

The other CSPN we discuss here is NGC 2392. What makes this object so interesting is that the situation for this star is reversed compared to NGC 6826: Pauldrach et al. (2004) had to significantly decrease the luminosity to obtain a match of predicted and observed UV spectrum. They thereby derived a very small mass of only 0.41 $M_\odot$, making this the least massive CSPN of their sample.

In Figure 2.12 we show our computed line profiles for a model with the stellar parameters of Kudritzki et al. (1997) and an artificially adapted line force resulting in the same mass loss rate as fitted by Kudritzki et al. (1997). Unfortunately, the observational material available for this object is rather poor and for some of the lines no observations are available at all. Nevertheless we show our computed line profiles as reference and, since Kudritzki et al. (1997) did not show any line profiles at all for this object but our NGC 6826 model adequately reproduced theirs, we will assume that the profiles computed by Kudritzki et al. (1997) for NGC 2392 were similar to these.

In Figure 2.13 we show predicted optical line profiles and UV spectrum for a consistent model using the Kudritzki et al. (1997) stellar parameters for NGC 2392. It is evident that the consistently computed mass loss rate of 3.2×10^{-7} $M_\odot$/yr is much too large to reproduce either UV or optical spectrum. This is in contrast to the consistent model from Pauldrach et al. (2004), shown in Figure 2.14, which not only agrees much better with the observed UV spectrum, but also predicts optical line profiles which are nearly identical to those from the (inconsistent) Kudritzki et al. (1997) model shown in Figure 2.12.

In summary, the situation for NGC 2392 is similar to that for NGC 6826: the Kudritzki et al. (1997) model with the artificial mass loss rate offers no observational advantage over the Pauldrach et al. (2004) model, and the latter again has the merit of being hydrodynamically consistent. The consistent model using the Kudritzki et al. (1997) stellar parameters, on the other hand, again fails to reproduce both UV and optical observations.

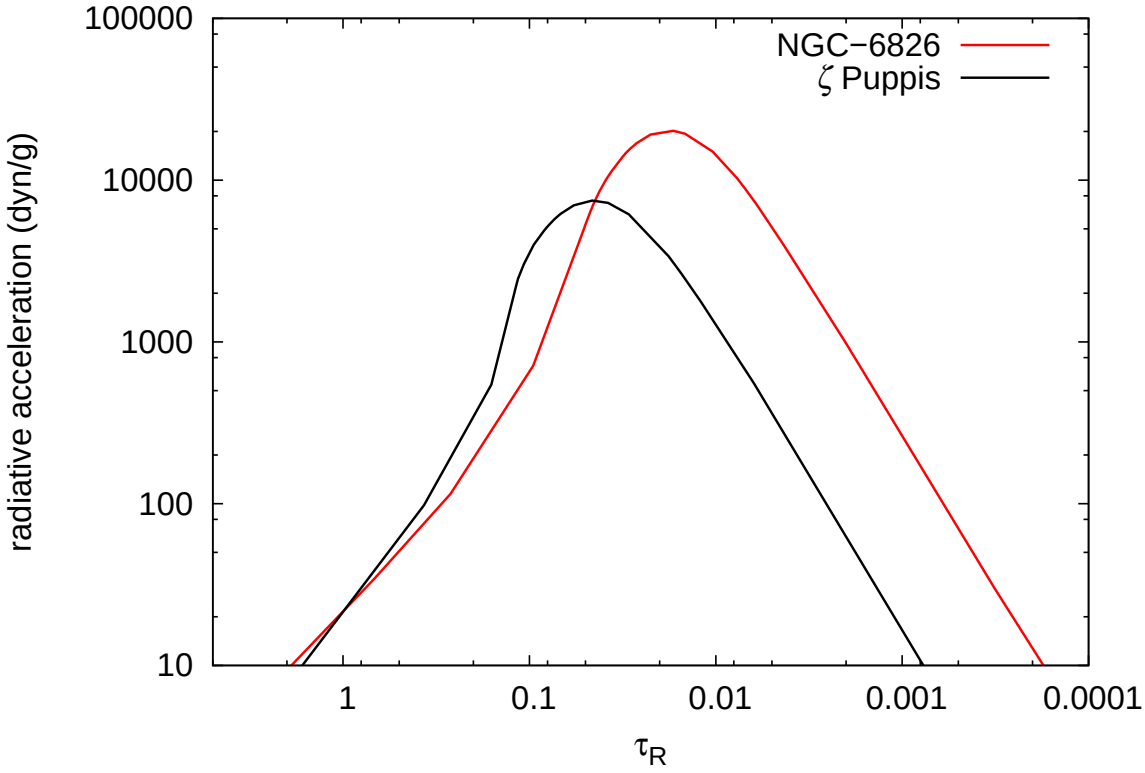

Figure 2.15: Radiative acceleration versus optical depth in the wind of the CSPN NGC 6826 (shown in red) using the parameters based on the UV analysis (model P04 in Table 2.2), compared to the radiative acceleration in a massive O star wind (ζ Puppis; shown in black).

2.5.3 Comparison of the dynamical parameters of CSPN and O star winds

The terminal velocity v_∞ and the mass loss rate $\dot{M}$ are the primary dynamical parameters of a stellar wind and the essential parameters for a consistent theoretical description. Both parameters are connected via the equation of continuity

$$\dot{M} = 4\pi r^2 \rho(r) v(r) \tag{2.1}$$

(where the outwards monotonically increasing velocity field $v(r)$ reaches its maximum value at roughly a hundred stellar radii and thus defines the terminal velocity v_∞ of the wind). Both the velocity $v(r)$ and the density $\rho(r)$ are functions of the radial coordinate r. Via the competing forces of line-driving and gravity they become unique functions of the basic stellar parameters R_*, L_*, and M_*.

Because our sample of CSPN stars shows pronounced wind features it is a natural step to examine these dynamical parameters and their relation to the basic stellar parameters as an additional and independent point of our investigation. This discussion is thus an extension of the investigation of Pauldrach et al. (1988) who already showed that the calculated terminal wind velocities are in agreement with the observations and therefore allow an independent determination of stellar masses and

radii.[9] With respect to this result, different sets of stellar masses and radii applied to our sample of stars should therefore lead at least partly to an inconsistent behavior with regard to the predictions of radiation-driven wind theory. Such an inconsistent behavior can, for example, be evident in the ratio $v_\infty/v_{\rm esc}$ of the terminal wind velocity and the escape velocity of individual stars.[10] In this investigation it is significant to not only compare the $v_\infty/v_{\rm esc}$ ratios obtained with our improved models for the CSPN sample to the corresponding "observed ratios" (which are based on the mass–luminosity relation of CSPNs), but also to the ratios of a "normal" O star sample and its corresponding observations. Because the UV-spectra of the CSPNs of our sample are very similar to those of massive O stars, the application of the theory of radiation-driven winds is expected to also yield similar results for the terminal velocity v_∞ of these CSPNs and the massive O stars. One would therefore expect the line force in the winds of our CSPNs to be of a strength comparable to that of the winds of massive O stars. In view of this expected result we have compared the computed line force from our consistent model of NGC 6826 to the corresponding one of the well known massive O star ζ Puppis, which has a similar UV spectrum. We show the radial run of the radiative forces, which include all relevant continuum and line contributions, in Fig. 2.15.

Surprisingly, the two curves of the radiative acceleration differ considerably in strength and shape, although the same sophisticated radiation-driven wind modelling has been applied in each case, and the spectra resulting from the models each match the corresponding observed spectra. The key to solving this apparent puzzle lies in understanding the basic relationships between the radiative acceleration and the density and velocity of the outflow.

Figure 2.16 shows the line acceleration along with the corresponding wind densities ρ as function of the scaled radius $r' = r/R_*$ (the x-scale chosen in Fig. 2.16 serves to emphasize the relevant radial range). In the inner (photospheric) regions the densities are similar, and this similarity in the models is supported by the fact that the optical (photospheric) spectra are also very similar (see Sect. 2.5.1 and Pauldrach et al. 2012). The similarity of the UV spectra, on the other hand, implies that the relevant wind features are formed at about the same optical depth in the wind. The optical depths in the wind are proportional to

$$\tau_R \propto \frac{\dot{M}}{v_\infty R_*^2} R_* \tag{2.2}$$

(cf. Puls & Pauldrach 1991), where

$$\frac{\dot{M}}{v_\infty R_*^2} = \overline{\rho} \tag{2.3}$$

may be unterstood as a characteristic wind density (Pauldrach et al. 1990a). Similar optical depths in the winds of both stars therefore implies

$$\overline{\rho}^{(\iota\ \mathrm{Pup})} R_*^{(\iota\ \mathrm{Pup})} \approx \overline{\rho}^{(\mathrm{NGC\ 6826})} R_*^{(\mathrm{NGC\ 6826})} \tag{2.4}$$

and thus

$$\frac{\overline{\rho}^{(\mathrm{NGC\ 6826})}}{\overline{\rho}^{(\iota\ \mathrm{Pup})}} \approx \frac{R_*^{(\iota\ \mathrm{Pup})}}{R_*^{(\mathrm{NGC\ 6826})}}. \tag{2.5}$$

[9] We note that Pauldrach et al. (1988) were also able to show that the winds of CSPNs are driven by radiation pressure and thus the insights of radiation-driven wind theory are applicable here.

[10] Investigations and interpretations of these ratios have already been performed by Pauldrach et al. 1988 (regarding CSPNs) and Pauldrach et al. 1990a (regarding massive O-stars).

Since

$$R_*^{(\text{NGC 6826})} < R_*^{(\iota \text{ Pup})} \tag{2.6}$$

this means that

$$\overline{\rho}^{(\text{NGC 6826})} > \overline{\rho}^{(\iota \text{ Pup})}. \tag{2.7}$$

This behavior is indeed also reproduced by the models (see Fig. 2.16).

As Pauldrach et al. (1990a) have shown, a higher wind density leads to a higher radiative acceleration, which explains the behavior shown in Fig. 2.16. A higher radiative acceleration in turn leads to a higher mass loss rate per unit surface element, i.e., $\dot{M}/R_*^2$ (see Pauldrach et al. 1990a), which in turn leads to a smaller terminal velocity (for comparable effective temperatures, cf. Pauldrach et al. (1988), their Figs. 10 and 6a).

The lower observed terminal velocities of CSPNs with pronounced winds thus provide evidence for the higher wind densities of these CSPNs compared to those of massive O stars (see Pauldrach et al. (1988), Pauldrach et al. (2004) and Table 2.2 of this work). The higher values of the line force for NGC 6826 compared to ζ Puppis thus follow directly from its smaller radius and the resulting consequences.

The v_∞/v_{esc} ratios of CSPNs compared to massive O stars. The observations show a dependence of v_∞ on T_{eff}, which was confirmed by the theory of radiation-driven winds. Additionally, the theory predicts a correlation of v_∞ to the other two stellar parameters, mass M_* and radius R_*, via the escape velocity v_{esc} (see Pauldrach et al. 1988),

$$v_{\text{esc}} = \left(2GM_*(1-\Gamma)/R_*\right)^{1/2} \tag{2.8}$$

(where $\Gamma = L_*/(4\pi cGM_*/(\chi_{\text{Th}}/\rho))$ is the ratio of stellar luminosity to Eddington luminosity, G is the gravitational constant, and χ_{Th} is the Thomson absorption coefficient).

Figure 2.17 shows the ratio of v_∞/v_{esc} for our CSPN sample as a function of different stellar parameters, compared to the corresponding values from a sample of massive O stars (cf. Pauldrach et al. 2011).

As is shown, the correlation of v_∞ to the escape velocity v_{esc} does not represent a strict and simple behavior. This fact was already recognized by Howarth & Prinja (1989) from a purely observational point of view. Moreover, in their comprehensive study of the wind properties of a sample of 205 O stars observed with the IUE satellite, Howarth & Prinja (1989) drew attention to a discrepancy between predictions obtained from scaling laws which were based on theoretical models (Pauldrach et al. 1986) and their interpretation of observations. This discrepancy concerned the observed dependence of the ratio of v_∞/v_{esc} on the stellar parameters T_{eff}, R_*, and M_*. This dependence was not represented by the models of Pauldrach et al. (1986), which yielded v_∞/v_{esc} ratios in a range of only $2.0 \ldots 3.0$, whereas the observations revealed ratios in a range of $2.0 \ldots 4.5$ in the same range of stellar parameters (cf. Howarth & Prinja 1989, their Fig. 10).

However, in a revised version of their procedure, Pauldrach et al. (1990a) were able to show that for certain parameter ranges of massive O stars the ratio of v_∞ to v_{esc} depends sensitively on the stellar parameters,

$$v_\infty/v_{\text{esc}} = f(T_{\text{eff}}, Z, R_*, M_*) \tag{2.9}$$

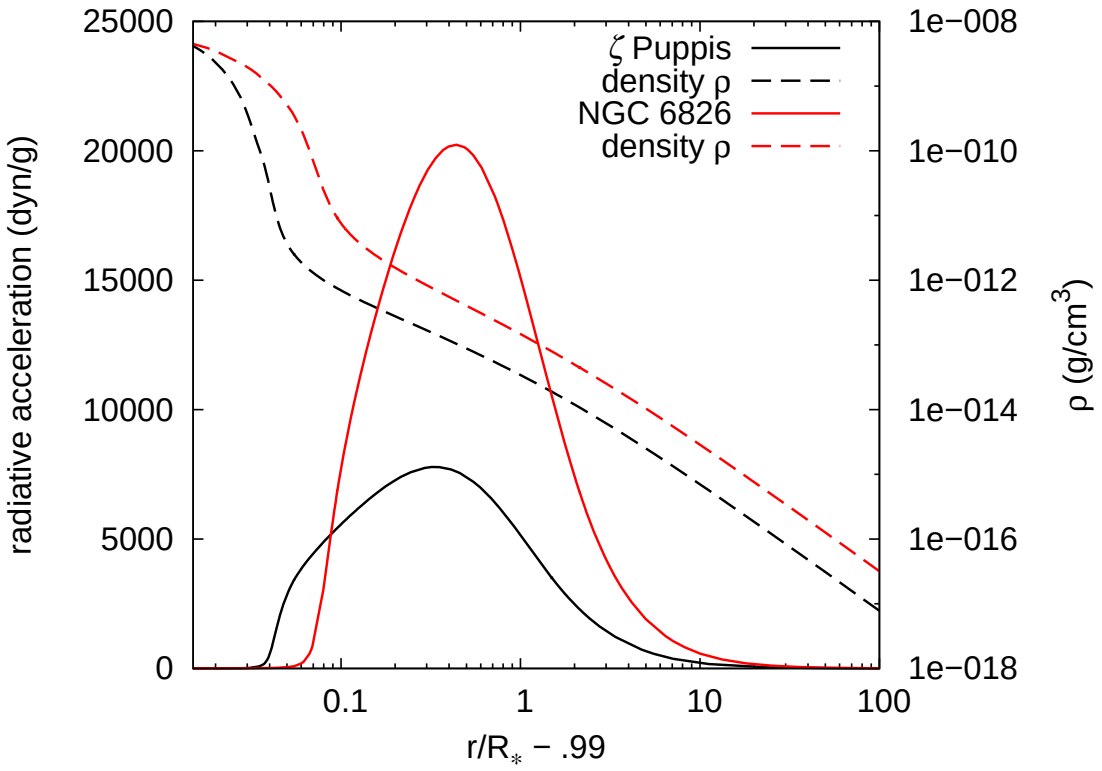

Figure 2.16: A more detailed illustration of the radiative acceleration for the CSPN NGC 6826 in comparison to the massive O star ζ Puppis. Additionally the density of both models has been plotted as well. The difference in radiative acceleration of both models shown in Fig. 2.15 can be well understood by the means of this plot (see text).

(where Z denotes the metallicity). This ratio does therefore not present a simple linear function but can vary tremendously from star to star, producing a significant overall scatter (in a range of 2.4...5.1).[11] Pauldrach et al. (1990a) explained this behavior as a result of differences in the ionization structure in the wind, which in particular causes back-reactions on the line force from changes in the level populations via the non-linear behavior of the strong UV line blocking (in particular the back-reaction on and of iron (Fe) has a strong influence in this regard).

A change of the stellar parameters therefore leads to an increase of the mass-loss rate which in turn increases the UV line blocking, which decreases the radiative temperatures in relation to the effective temperature and which thus increases the population of the lower ionization stages. As these lower ionization stages have more strong lines at the corresponding radiative flux maximum (Pauldrach 1987), the net radiative force is increased, and this behavior reinforces the increase of the UV line blocking and leads to a change of the terminal velocity even if the escape velocity $v_{\rm esc}$ has not changed.

Regarding the massive O stars, the results of our current investigation (see Fig. 2.17) are prin-

[11] We note that based on a less consistent procedure of modelling CSPN winds a similar range of the ratios of v_∞ to $v_{\rm esc}$ was also found by Pauldrach et al. (1988), albeit without the scatter.

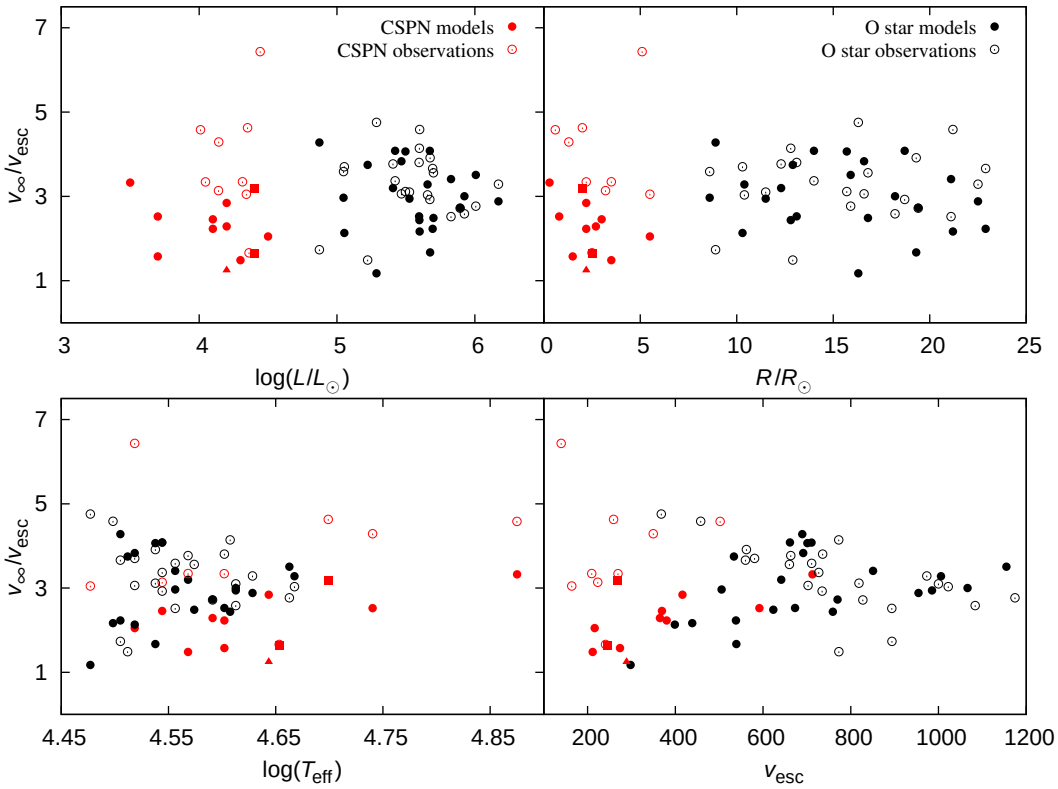

Figure 2.17: The ratio v_∞/v_{esc} as a function of the stellar parameters L_*, R_*, $T_{\rm eff}$, and $v_{\rm esc}$. Compared to the theoretical predictions of Pauldrach et al. (2004) (P04; CSPNs), this work, and Pauldrach et al. (2011) (P11; massive O stars) the values deduced from observations and theoretical relations are shown for our sample of CSPNs (Kudritzki et al. 1997; K97) and a sample of massive O stars (Repolust et al. 2004; R04). The two filled squares shown in the plots depict the two consistent CSPN models for NGC 6826 and NGC 2392 which have been computed on the basis of the parameter sets of K97. The filled triangle represents an additional consistent model for NGC 6826 where the surface gravity has been reduced to a value of $\log g = 3.7$ (the parameters of the models are listed in Table 2.2). For a discussion see the text.

cipally in accordance with those earlier analyses, and, as expected, the improved consistency of our current models does not fundamentally change this behavior, leading now to a scatter of 1.3...4.4 in $v_\infty/v_{\rm esc}$, in the same range as the observed values.

As another expected result Fig. 2.17 shows a similar spread in $v_\infty/v_{\rm esc}$ for our CSPN models (the CSPNs are clearly separated from the massive O stars in the upper two panels of Fig. 2.17 due to the very different radii of these two groups of stars). But not only is the spread roughly the same, also the mean value of the calculated $v_\infty/v_{\rm esc}$ ratios turns out to be not very different for both groups of stars (being somewhat smaller for the CSPN models). Even this is expected from our discussion above of the radiative acceleration which gives rise to considerably lower terminal velocities of CSPNs with pronounced winds because of their higher wind densities as a result of their much smaller radii. Thus, although the CSPNs of our sample have somewhat reduced escape velocities $v_{\rm esc}$ compared to the massive O stars (see below), with their range of 1.2...3.3 of the $v_\infty/v_{\rm esc}$ ratios the model calculations

behave as expected. And this is also the case for the somewhat decreased (compared to the range of O stars) lower limit of 1.2 of $v_\infty/v_{\rm esc}$.

As is shown in the bottom right panel of Fig. 2.17 the mean value of the escape velocities $v_{\rm esc}$ themselves (not the ratios) of the CSPN models and observations is slightly smaller than the ones of the massive O star observations and models. Obviously, this must be a consequence of the dependence of $v_{\rm esc}$ on the stellar mass M_* and the radius R_* of the objects (cf. Eq. 2.8). However, $v_{\rm esc}$ also depends on Γ, the ratio of stellar luminosity to Eddington luminosity. The behavior of this parameter is illustrated in Fig. 2.18, which shows the calculated mass loss rates $\dot{M}$ versus Γ for both the CSPN and the O star sample. The average Γ values are clearly smaller for the CSPNs than for the massive O stars. The interpretation of this behavior is straightforward, due to the proportionality of Γ to L_*/M_*: this ratio becomes smaller for CSPNs than for massive O stars because the difference in L_* is much larger than the difference in M_*, and therefore CSPNs are in general farther away from the Eddington limit than massive O stars are. But a decreasing value of Γ implies an increasing value of $v_{\rm esc}$, since $v_{\rm esc}$ is proportional to $(1-\Gamma)$, and this behavior may at first appear to be in contradiction with the finding that the escape velocities are on average smaller for the CSPNs than for the massive O stars (bottom right panel of Fig. 2.17). The apparent contradiction is, however, resolved by recognizing that going from massive O stars to CSPNs the M_*/R_* ratio decreases more strongly than $1/(1-\Gamma)$.

As an important result of Fig. 2.17 we thus find that, despite the reduction of the escape velocities $v_{\rm esc}$, somewhat smaller $v_\infty/v_{\rm esc}$ ratios are obtained for our CSPNs compared to massive O stars, because the lower terminal velocities v_∞ observed (and calculated) for our CSPNs dominate this effect.[12]

We are now well-prepared to draw the major conclusion of this section from Fig. 2.17. This conclusion concerns the range of the "observed" CSPN $v_\infty/v_{\rm esc}$ ratios derived from a combination of observations and theoretical relations (e.g., the post-AGB core-mass–luminosity relation, CMLR). As shown in Fig. 2.17, for the massive O star observations the range of the $v_\infty/v_{\rm esc}$ ratios is in good agreement with the range obtained for the corresponding model calculations. The CSPN model calculations also yield ratios which lie in the range of the $v_\infty/v_{\rm esc}$ spread obtained for the massive O stars (see the discussion above). Clearly at odds, however, are the CSPN "observations", yielding much too high $v_\infty/v_{\rm esc}$ ratios in general, and in particular giving values near 5 or even higher for almost half of the sample! This discrepant behavior is noticeable in all panels of Fig. 2.17, and appears conspicuously eye-catching in the upper right panel.

This result is especially interesting because such a discrepancy does not emerge when comparing observations and model calculations in regard to the wind-momentum–luminosity relation[13] (WLR), one of the most fundamental relations predicted by the theory of radiation-driven winds. No significant differences between the behavior of the observed wind momenta of massive O stars and CSPNs with pronounced winds are seen, and the computed wind momenta of both the O star models (Pauldrach

[12] In the bottom left panel of Fig. 2.17 we plot the ratio of $v_\infty/v_{\rm esc}$ versus the effective temperature $T_{\rm eff}$. As shown by Pauldrach et al. (1988) and Pauldrach et al. (1990a), the theory of radiation-driven winds predicts a mutual dependence between v_∞ and $T_{\rm eff}$. Since the range of their effective temperatures is almost the same, no significant difference between the corresponding results of both stellar groups should therefore be observed. And this is indeed the case: the characteristic values of the $v_\infty/v_{\rm esc}$ ratios and the effective temperatures $T_{\rm eff}$ differ only slightly between our CSPNs and the massive O stars.

[13] The wind-momentum–luminosity relation is a simple relation between the quantity $\dot{M}v_\infty$, which has the dimensions of a momentum loss rate, and the stellar luminosity (Lamers & Leitherer 1993, Kudritzki et al. 1995): the mechanical momentum of the wind flow ($\dot{M}v_\infty$) results from the transfer of momentum from the radiation field to the gas via photon absorption in metal lines (which defines the driving mechanism of the wind) and is thus mostly a function of photon momentum (L/c) and therefore related to the luminosity.

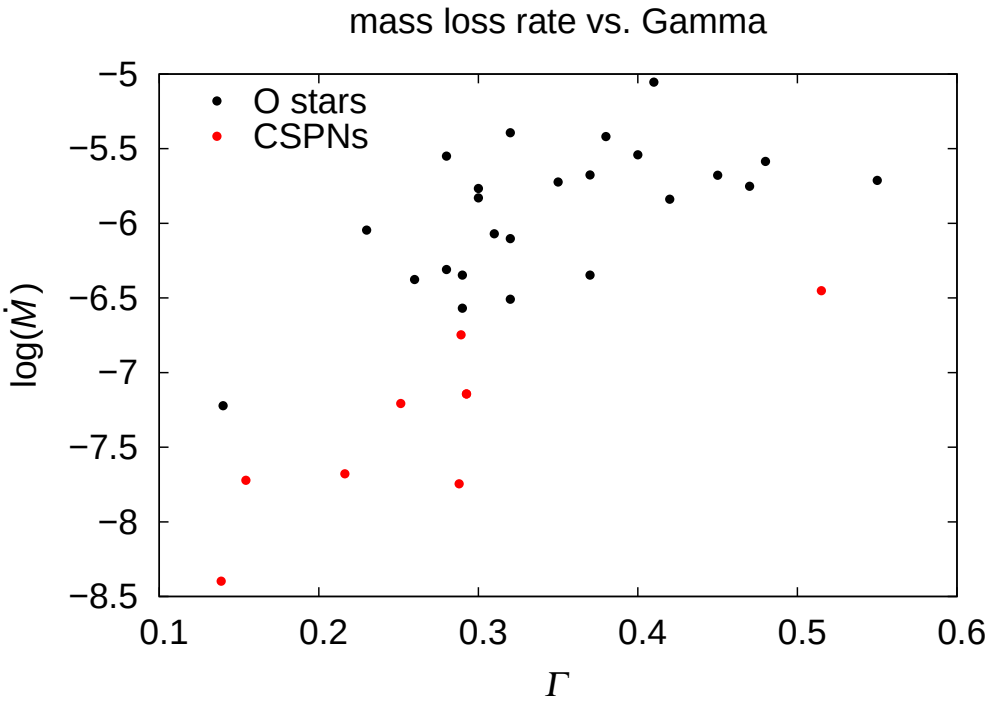

Figure 2.18: Predicted mass loss rates for our samples of CSPNs and O stars versus Γ, the ratio of stellar luminosity to Eddington luminosity.

et al. 2011) and the CSPNs (Pauldrach et al. 2004) agree well with the corresponding observations. Furthermore, the wind momenta of the CSPN models and observations lie along the line extrapolated from the massive O stars (see Pauldrach et al. 2004, their Fig. 6). This result confirms the finding of Pauldrach et al. (1988) and Kudritzki et al. (1997) that the winds of both groups of hot stars are radiation-driven.

So there is obviously an intrinsic difference between the information provided by the WLR and the information contained in the $v_\infty/v_{\rm esc}$ ratios. This difference regards the mass of the objects. The wind momenta are essentially independent of the stellar masses (a larger v_∞ coincides with a smaller $\dot{M}$ and vice versa; see Kudritzki et al. 1995 and Puls et al. 1996), so any possibly erroneous assumption about the masses made in the modelling of the objects or the interpretation of the observations does not enter into the diagnostic quantity. This is not the case, however, when considering the $v_\infty/v_{\rm esc}$ ratios, which are explicitly mass-dependent. Furthermore, we must realize that the much too high $v_\infty/v_{\rm esc}$ ratios obtained for our CSPN "observations" are not due to the numerators (v_∞), which are directly observable quantities (measurable from the blue edge of the saturated P-Cygni profiles in the UV spectra), and must therefore be due to the denominators ($v_{\rm esc}$). The high ratios are even more significant because from the discussion above we would have expected the highest $v_\infty/v_{\rm esc}$ values to occur for some massive O stars rather than for some CSPNs.

The understanding of this behavior is clearly coupled to the fact that, in contrast to the terminal velocities v_∞, the escape velocities $v_{\rm esc}$ appearing in the "observed" CSPN $v_\infty/v_{\rm esc}$ ratios are not directly observable quantities. The escape velocities are connected to the masses and the radii of

the objects, and these quantities had (as is usual) been assumed by Kudritzki et al. (1997) to conform to the theoretical CMLR. This is of course not a problem for the WLR, which shows agreement between the predictions of radiation-driven wind theory and the observations since the wind momenta are independent of the mass of the objects.

With respect to these considerations it is legitimate to conclude that there is a problem with the core-mass–luminosity relation at its high-mass end. We emphasize that we draw this conclusion purely from a comparison of the terminal velocities, independent of the behavior of $\dot{M}$ and the interpretation of either the UV or the optical spectra. We further note that consistent wind model calculations based on stellar parameters conforming to the CMLR also yield $v_\infty/v_{\rm esc}$ ratios which lie in the expected range (however, the terminal velocities obtained by these models are highly incompatible with the observations).[14] We thus conclude that the extraordinarily high values of $v_\infty/v_{\rm esc}$ appear just in cases where the numerator is disconnected from the denominator, i.e., in cases where the observed terminal velocity is not consistent with the assumed mass and radius of the star.

Taking our results of the investigation of the dynamical parameters together with our results obtained from the spectral analysis, and as a third point the assumption of the CMLR for post-AGB stars, we find that only two of these considerations are intrinsically reconcilable, whereas the third consideration is irreconcilable with this pair. For our sample of CSPN objects this means in particular:

- Analyses aiming at reproducing the observed optical and UV spectra based on masses derived from the CMLR yield dynamical wind parameters which are not consistent with the corresponding observations.
- Analyses employing a consistent treatment of the dynamical wind parameters based on masses derived from the CMLR yield optical and UV spectra which do not match the observed spectra.
- Analyses employing a consistent treatment of the dynamical wind parameters aiming at reproducing the observed optical and UV spectra yield masses which are not in accordance with the CMLR.

Moreover, for four of the CSPNs shown in Fig. 2.17 the $v_\infty/v_{\rm esc}$ ratios that follow from the parameters derived by Kudritzki et al. (1997) based on the CMLR are so extraordinary large that they are not reconcilable with the theory of radiation-driven winds, which on the other hand is strongly supported by a comparison to the WLR.

2.6 Summary and conclusions

In order to obtain further constraints on the true stellar parameters of CSPNs we have applied our stellar atmosphere code WM-basic to two objects from the sample of CSPNs investigated earlier by Kudritzki et al. (1997) and Pauldrach et al. (2004). We have chosen stars for which the two analyses yielded strongly differing parameters, namely NGC 6826 and NGC 2392, for which Pauldrach et al. (2004), comparing observed UV spectra with those predicted by hydrodynamically consistent models, had derived masses of 1.4 $M_\odot$ and 0.41 $M_\odot$, respectively, whereas Kudritzki et al. (1997), working with optical spectra and assuming that the mass–luminosity relation of theoretical post-AGB evolutionary models was valid, had obtained roughly equal masses of 0.92 $M_\odot$ and 0.91 $M_\odot$.

[14] This result has been verified by two consistently computed models for NGC 6826 and NGC 2392 using the stellar parameter sets of Kudritzki et al. (1997), shown as filled squares in Fig. 2.17; the abstruse value of the obtained terminal velocity of NGC 6826 is listed in Table 2.2.

As a prerequisite to this analysis we had extended the applicability of WM-basic to the simultaneous analysis of UV and optical lines by implementing Stark broadening and testing the improved code by comparing the computed optical line profiles with those from two reference O star models calculated with the well-known model atmosphere code FASTWIND, showing the results to be in excellent agreement, with only small differences in the predicted line profiles attributed to differences in the density structures of the two codes.

Our results regarding the stellar parameters of CSPNs confirm the conclusion tentatively drawn by Pauldrach et al. (2004), namely that the contradiction between the stellar parameters derived by Kudritzki et al. (1997) and Pauldrach et al. (2004) is not the result of using optical spectra in the former analysis and UV spectra in the latter, but is instead due to the *missing consistency* between stellar and wind parameters in the analysis of Kudritzki et al. (1997).

We arrive at this conclusion because we have now shown that the hydrodynamically consistent models of Pauldrach et al. (2004) reproduce not only the observed UV spectra but also yield optical line profiles which are nearly identical to those from models using the stellar parameters of Kudritzki et al. (1997) and the artificial (i.e., inconsistent) radiative line force necessary to reproduce the wind parameters fitted by Kudritzki et al. (1997). *Consistent* models using the Kudritzki et al. (1997) stellar parameters, on the other hand, reproduce neither the UV spectrum nor the optical line profiles.

Nevertheless, an issue of somewhat uncertain implications remains, namely the fact that we cannot at the moment match several observed optical emission lines with a hydrodynamically consistent model that can without difficulties reproduce essentially the entire observable UV range. But with regard to possible discrepancies there is no reason to assume that for modeling O-type atmospheres the optical and the UV spectral ranges carry the same diagnostic weight. The spectral lines in the optical are in general relatively weak and far in-between, compared to the lines in the UV range, and this makes the significance of the UV fit evident when drawing conclusions concerning the quality of the fit in the UV and optical parts of the spectra. Obviously, the parameters from Pauldrach et al. (2004) fit the optical spectrum *and* the UV spectrum, with the exception of Hα and He II λ4686. The currently favored explanation for such discrepancies in the strength of optical emission lines is inhomogeneities in the wind[15] (leading to stronger emission from H and He recombination lines due to the higher densities in the "clumps" compared to a smooth outflow), and an ad-hoc "clumping factor" is often employed to bring the line profiles of the model into agreement with the observed line profiles. But supposing that clumping (or some other effect with similar influence on these two lines) plays a role, then – as long as we have no consistent physical description for this effect – we have complete freedom to fit the optical emission lines without gaining any additional information about the stellar parameters.[16] Thus, a line whose model profile is determined primarily by a cosmetic clumping factor and not the underlying physics of the model completely loses its diagnostic value, and the quality of the fit of this line says nothing about the reliability of the fundamental model parameters.

A completely separate avenue of investigation is opened up by an analysis of the behavior of the dynamical wind parameters, independent of the appearance of the spectra. As the wind parameters

[15] But we note that the amplitudes of the deviations from a smooth, stationary flow are not very large in general (cf. Kudritzki 1999), and we therefore don't expect the clumping to markedly influence the hydrodynamics of the outflow (see, for instance, Pauldrach et al. 1994 and references therein, as well as Runacres & Owocki 2002). This argument is strongly supported by the fact that the hydrodynamic models based on a smooth, time-averaged density structure can indeed reproduce the multitude of UV spectral lines that are formed in the entire atmospheric depth range.

[16] Note also that without a description of clumping based on first principles, clumping is not a single fit factor but a whole number of them, one for each depth point of the model, and thus the degree of freedom is extremely large. Using these parameters it might be possible to fit the observed optical emission lines even with a wrong hydrodynamical structure.

are not free parameters but (due to the driving mechanism) functions of the stellar parameters, using sets of stellar parameters which are not realized in nature should lead at least partly to an inconsistent (i.e., not observed) behavior of the wind parameters in the analysis. Such an inconsistent behavior can, for example, be evident in the ratio $v_\infty/v_{\rm esc}$ of the terminal wind velocity and the escape velocity of individual stars.

We have therefore examined the $v_\infty/v_{\rm esc}$ ratios for our CSPN sample as a function of different stellar parameters and compared these to the corresponding ratios from a sample of massive O stars. As already found for massive O stars, the correlation of v_∞ to $v_{\rm esc}$ does not represent a strict and simple behavior for CSPNs, giving (as expected) a certain scatter about a mean value. The spread in the $v_\infty/v_{\rm esc}$ ratios for our CSPN models turned out to be comparable to that obtained from both massive O star observations and massive O star models, but (as expected from basic physics) at a slightly smaller mean value. Incompatible with all other results, however, are the CSPN "observations", which yield much too high $v_\infty/v_{\rm esc}$ ratios in general. These high $v_\infty/v_{\rm esc}$ ratios are even more significant because we would have expected the highest $v_\infty/v_{\rm esc}$ values to occur for some massive O stars rather than for some CSPNs.

This anomaly is obviously coupled to the fact that the escape velocity $v_{\rm esc}$ appearing in the "observed" CSPN $v_\infty/v_{\rm esc}$ ratios is not a directly observable quantity (whereas v_∞ can be measured directly). The escape velocity is connected to the stellar mass and radius, and these quantities had been taken from the theoretical post-AGB core-mass–luminosity relation. We thus conclude that there might be a problem with the core-mass–luminosity relation at its high-mass end. This conclusion is further supported by the finding that consistent model calculations using stellar parameters compatible with the core-mass–luminosity relation do yield $v_\infty/v_{\rm esc}$ values that lie in the expected range (however, the obtained terminal velocities v_∞ of these models are highly incompatible with the observations).

Taking these results together, we find that of the three considerations (a) consistency of the dynamical wind parameters with the stellar parameters, (b) compatibility of the model spectra with the observed spectra, and (c) conformity of the stellar parameters with the core-mass–luminosity relation, only two can be reconciled with each other, while the third is irreconcilable with the other two. Since (a) and (b) are strongly supported by both observations and models (spectral appearance, wind-momentum–luminosity relation), it is likely that the consideration that is not realized in nature is (c), the core-mass–luminosity relation, at least for the O-type CSPNs with prominent wind features as studied in this paper.

Chapter 3

Radiation-driven winds of hot luminous stars

XVIII. Wind clumpiness and the reliability of stellar and wind parameter determinations from optical and UV spectral analyses of selected central stars of planetary nebulae[1]

The contents of this chapter will be published in Kaschinski et al. (2013a), Astronomy & Astrophysics.

Abstract. The uncertainty in the degree to which radiation-driven winds of hot stars might be clumpy leads to a corresponding uncertainty in the determination of the atmospheric mass loss rates from the strength of optical recombination lines and – since the mass loss rate is not a free parameter but a function of the stellar parameters mass, radius, luminosity, and abundances – in principle also in the determination of these stellar parameters. Furthermore, the optical recombination lines also react sensitively to even small changes in the density structure resulting from the (often assumed instead of computed) velocity law of the outflow. This raises the question of how reliable the parameter determinations from such lines are.

The currently existing severe discrepancy between CSPN (central stars of planetary nebulae) stellar and wind parameters derived from model fits to the optical spectra and those derived using hydrodynamically consistent model fits to the UV spectra is to be reassessed via a simultaneous optical/UV analysis using a state-of-the-art model atmosphere code.

We have improved our model atmosphere code with the implementation of a treatment of clumping in the wind. This allows us to re-evaluate, with respect to their influence on the appearance of the UV spectra and their compatibility with the observations, the parameters determined in an earlier study that had employed clumping in its models to achieve a fit to the observed optical spectra.

The discrepancy between the optical and the UV analyses is confirmed to be the result of a missing consistency between stellar and wind parameters in the optical analysis. While clumping in the wind does significantly increase the emission in the optical hydrogen and helium recombination lines, the

[1] Based in part on observations with the Far Ultraviolet Spectroscopic Explorer (FUSE).

influence of the density (velocity field) is of the same order as that of moderate clumping factors. Moderate clumping factors leave the UV spectra mostly unaffected, indicating that the influence on the ionization balance, and thus on the radiative acceleration, is small. Instead of the erratic behavior of the clumping factors claimed from the optical analyses we find similar clumping factors for all CSPNs, with a typical value of $f_{\rm cl} = 4$. With and without clumping, wind strengths and terminal velocities consistent with the stellar parameters from the optical analysis give spectra incompatible with both optical and UV observations, whereas a model that consistently implements the physics of radiation driven winds achieves a good fit to both the optical and UV observations with a proper choice of stellar parameters. The shock temperatures and the ratios of X-ray to bolometric luminosity required to reproduce the highly ionized O VI line in the FUSE spectral range agree with those known from massive O stars, again confirming the similarity of O-type CSPN and massive O star atmospheres and further strengthening the claim that both have identical wind driving mechanisms.

The similarity of the winds of O-type CSPNs and those of massive O stars justifies using the same methods based on the dynamics of radiation-driven winds in their analysis, thus supporting the earlier result that several of the CSPNs in the sample have near-Chandrasekhar-limit masses.

3.1 Introduction

The computation of a predicted (i.e., synthetic) spectrum that can be compared to the observed spectrum is the primary and most important diagnostic tool for determining the fundamental parameters of a star. But while a photospheric model[2] will yield information about the effective temperature $T_{\rm eff}$ and the surface gravity $\log g$, the spectroscopic determination of the radius R requires an observable quantity that can be spectroscopically traced over a depth range covering an appreciable fraction of the physical size of the star. Furthermore, a physical description is required that predicts the run of this quantity as a function of the radius.

Many stars have thin, effectively plane-parallel atmospheres, for which such a procedure is not applicable. For these stars, additional information beside the stellar spectrum, for example the measured flux and the distance to the star, is required to determine the radius. In the atmospheres of O-type stars, however, the radiative intensities are large enough for the radiation pressure to drive a stellar "wind", propelled by the transfer of photon momentum to ions in the wind via absorption in spectral lines. The winds leave conspicuous, easily observable signatures in the stellar spectra, allowing individual spectral lines to be traced out to tens of stellar radii. The density and velocity of the wind can be predicted by selfconsistent hydrodynamical modelling of the outflow on the basis of the gravitational and the (computed) radiative acceleration at each point in the wind, thus providing the link to the stellar radius and allowing for a purely spectroscopic determination of the stellar mass.

Central stars of planetary nebulae (CSPNs) are valuable research objects because they represent a unique phase in the evolution of intermediate-mass stars, and accurately known stellar parameters would constitute a stringent test of evolutionary models. Unfortunately, accurate *distances* to most CSPNs are not available, and information about their sizes (and thus, via $\log g$, their masses) must therefore be derived either spectroscopically through hydrodynamic modelling of the expanding atmosphere or, supplemental to spectroscopy, with the aid of additional physical considerations and

[2] In classical photospheric models, the effective temperature $T_{\rm eff}$ is usually determined via the ionization balance, derived from the strengths of lines from successive ionization stages, and the surface gravity $\log g$ is determined via the density-dependent (and thus, pressure-dependent) Stark-broadening in the hydrogen Balmer line wings.

models.

The current dispute regarding the true stellar parameters of CSPNs has its origins in two series of analyses of (largely congruent) samples of O-type CSPNs, using different methods. One of these (Mendez et al. 1988b,a; Kudritzki et al. 1997; Kudritzki et al. 2006) used model fits to the optical hydrogen and helium lines to determine effective temperatures and surface gravities. Lacking hydrodynamical modelling of the wind, they had to use stellar evolutionary models to determine masses and radii, comparing effective temperatures and surface gravities to the theoretical evolutionary tracks in the $T_{\rm eff}$–$\log g$ plane. These analyses were therefore not an independent test of the evolutionary models, since their validity had been assumed all along. Nevertheless, a surprising result was that Kudritzki et al. (1997) found many high-mass CSPNs (with masses around $0.9\,M_{\odot}$), which was unexpected, since theory predicted them to evolve too quickly to be observed in larger numbers. Still, the mass loss rates derived from their stellar parameters and from modelling of the H_{α} emission were well in agreement with what was expected from radiation-driven wind theory, providing strong evidence that the winds of these objects are indeed driven by radiation pressure.

The other series of analyses (Pauldrach et al. 1988; Pauldrach et al. 2003, 2004; Kaschinski et al. 2012) is based on hydrodynamic modelling of the wind, using fits to the observable UV spectra. This type of analysis had been successfully applied to massive O stars (Pauldrach 1987; Pauldrach et al. 1990a; Pauldrach et al. 2001; Pauldrach et al. 2012), but its application to O-type CSPNs gave even more unexpected results: Pauldrach et al. (2004) found a number of CSPNs with masses around 1.3 to $1.4\,M_{\odot}$, near the Chandrasekhar limit for white dwarfs. These high masses, however, were not simply due to a systematic overestimate of the masses by the method. One of the stars, NGC 2392, was even found to have a surprisingly small mass of only $0.4\,M_{\odot}$, compared to the $0.9\,M_{\odot}$ that had been derived by Kudritzki et al. (1997).

Since both sets of analyses were based on different spectral regions it was not clear whether this discrepancy was due to some assumption in the modelling that was perhaps unjustified (e.g., that the winds were radiatively driven, or that the mass–luminosity relation assumed by Kudritzki et al. (1997) correctly described these objects), or whether there was something peculiar about either the optical or the UV spectra, despite the good fits both groups achieved for their spectral ranges. A first attempt to resolve the issue was made by Kaschinski et al. (2012) with combined optical and UV modelling from the same atmospheric models. For their analysis they chose NGC 2392, the least massive star, and NGC 6826, the most massive star in the sample of Pauldrach et al. (2004). These extreme cases were chosen because covering a larger spread in stellar parameters makes it more likely for the results to show real physical behavior, and not just a selection effect, in a group of stellar objects.

The results of this investigation were astounding. The synthetic spectra modeled with the stellar parameters from the optical analysis could only achieve fits to the observations because the wind parameters that had been assumed in that analysis were inconsistent with the stellar parameters. Enforcing consistency between stellar and wind parameters could yield simultaneous fits to both the UV and the optical spectra, but only with stellar parameters that were in disagreement with the theoretical CSPN mass–luminosity relation. Merely the optical emission lines H_{α} and He II λ 4686 could not be reproduced fully by Kaschinski et al., the emission predicted by their models being too weak.

In the present paper we will address this significant point. For the optical analyses, H_{α} is the primary diagnostic line for deriving mass loss rates, and reliable modelling of the H_{α} emission is

therefore crucial to obtain accurate mass loss rates in these analyses.[3] In recent years[4] evidence has accumulated that the winds might not be entirely smooth but clumpy (e.g., Repolust et al. 2004), and H_α , being a recombination line and thus proportional to the square of the density, would therefore show increased emission compared to that from a smooth wind. In other words, model fits assuming a smooth flow would overestimate the mass loss rates. In view of this fact, Kudritzki et al. (2006) reanalyzed the data of Kudritzki et al. (1997), adjusting clumping factors in the models to provide new fits to the optical emission lines and resulting in revised stellar parameters and significantly reduced mass loss rates. We will compare the results from our combined optical and UV analysis, now also taking clumping into account, to these revised parameters.

Further information about the nature of O-type CSPN winds is provided by X-ray observations (Guerrero et al. 2000; Kastner et al. 2012) that show central stars of planetary nebulae as X-ray emitters. This radiation is thought to originate, as in massive O star winds, from small packets of the gas that are accelerated[5] relative to the mean flow and collide with other gas fragments further out, resulting in small shocked regions (with a volume filling factor of around $f \simeq 10^{-3}$) of hot gas ($T \simeq 10^6$ K) that cools radiatively, emitting radiation in the X-ray regime (Lucy & White 1980; Lucy 1982). Apart from direct observation these X-rays can also be inferred from lines of highly ionized species (N V, O VI, and S VI) in the observable UV region. The presence of such highly ionized species (so-called "superionization", Snow & Morton 1976) could be readily explained by shocks being the source of the high-energy radiation required to generate these ions. Some of their lines lie in the FUSE spectral range, and corresponding observations exist for several of the CSPNs in our sample. We use these observations to ascertain whether CSPN winds differ from massive O star winds with regard to shock radiation.

In the following we will briefly review the pros and cons of the two spectral analysis techniques (UV and optical) (Section 3.2) and discuss the FUSE observations and our modelling of the shocks to provide constraints on the radiation leading to the production of O VI (Sections 3.3 and 3.4). Then we will describe our implementation of clumping, providing reference comparisons to FASTWIND, the modelling code that had been used by Kudritzki et al. (2006) (Section 3.5). Finally, we show comparisons to the observations of the synthetic spectra from our model runs, using the parameters of both Kudritzki et al. (2006) and Pauldrach et al. (2004), including and excluding clumping (Section 3.6) and discuss the implications of our findings (Section 3.7).

[3] The UV analyses are not so dependent on a single line, as an entire forest exists of lines (mainly Fe and Ni in ionization stages IV and V) that are formed at the base of the wind and react sensitively to the mass loss rate.

[4] It has long been known that the line-driving mechanism of the winds is intrinsically unstable (Milne 1926; Lucy & Solomon 1970), but it was not suspected that the fragmentation of the wind would already be significant in the lower regions where most of H_α is formed.

[5] Since the line force is proportional to the velocity *gradient*, a small localized disturbance in the velocity tends to be magnified in a runaway fashion.

3.2 Methods for the determination of stellar parameters and the investigation of CSPN winds

Although a complete set of stellar parameters (comprising the luminosity L, the mass M, the effective temperature $T_{\rm eff}$, and the abundances of a star) can be determined for stars with expanding atmospheres just from the wind-sensitive features in the UV via a comparison of consistently calculated UV spectra[6] and corresponding observations (cf. Pauldrach et al. 2004), a comparison that also includes the H and He lines of the optical spectra in a combined analysis (cf. Kaschinski et al. 2012) has a more convincing character. To establish such a procedure, Kaschinski et al. (2012) improved the stellar atmosphere code WM-basic with a description of Stark broadening in order to more realistically model the optical photospheric lines. Based on this extension they were able to apply this new procedure to the two most interesting central stars of their considered sample of CSPNs, namely NGC 2392 and NGC 6826. (The entire sample consists of nine CSPNs that have been selected because of their pronounced wind features in the UV, cf. Pauldrach et al. 2004 and Table 3.3). As a primary result, their consistent models produced not only UV spectra of high quality, but also fits to the optical H and He lines that were regarded to be of the same quality as those obtained from an analysis performed for the same sample of CSPNs using only the optical spectra (Kudritzki et al. 1997).

However, as noted in the introduction, the CSPN masses and luminosities determined by this method for this sample contradict the commonly accepted core mass–luminosity relation of central stars of planetary nebulae predicted by current stellar evolutionary models. Even more interesting was the result that five central stars of the sample were found to have masses approaching the mass limit for white dwarfs predicted by Chandrasekhar (1931). This important result raised questions about the validity of the core mass–luminosity relation of central stars of planetary nebulae.

But the consistent modeling of CSPN winds also offers other avenues of investigation. First, via a study of the behavior of the wind dynamics independent of the appearance of the spectra, and second, via modelling of the X-ray emission in the winds.

Regarding the first point it is important to keep in mind that the wind parameters are not free parameters, but are in reality functions of the stellar parameters. Thus, if the wind parameters predicted for a set of stellar parameters contradict the observations, these stellar parameters must be wrong. Such an inconsistent behavior can, for example, be evident in the ratio $v_\infty/v_{\rm esc}$ of the terminal wind velocity and the escape velocity of individual stars. We have examined the $v_\infty/v_{\rm esc}$ ratios for our CSPN sample for two sets of stellar parameters – derived (a) from an analysis of the optical lines in combination with the post-AGB core-mass–luminosity relation (set 2), and (b) from analyses of the UV spectra together with consistent modeling of the winds (set 1) – and compared these to the corresponding ratios from a sample of massive O stars. The results showed that the spread in the $v_\infty/v_{\rm esc}$ ratios for our CSPN models of set 1 turned out to be comparable to that obtained from both massive O star observations and massive O star models, whereas the $v_\infty/v_{\rm esc}$ ratios of set 2 yielded much too high values incompatible with all other results (cf. Kaschinski et al. 2012). As the latter anomaly is coupled to the fact that the escape velocity $v_{\rm esc}$ is not a directly observable quantity (in contrast to v_∞, which can be measured directly, $v_{\rm esc}$ depends on the stellar mass M and radius R, and these quantities had been taken from the theoretical post-AGB core-mass-luminosity relation), we have to conclude from this result that there is a problem with the core-mass-luminosity relation at the CSPN high-mass

[6] In this context "consistent" means that the dynamical wind parameters (the mass loss rate $\dot{M}$ and the terminal wind velocity v_∞) are not treated as free parameters, but instead are determined from a computation of the radiative pressure such that a star with the given stellar parameters can actually drive a wind with those parameters.

end.

Although this is a striking result, it might possibly be construed as an intrinsic peculiarity of CSPN winds not exhibited by massive O star winds. It is therefore of great importance that the treatment of the expanding atmospheres of O-type stars offers another, independent, path of inquiry into the driving mechanism of CSPN winds with the modeling of the wind-produced X-rays. This is based on the hydrodynamical behavior of radiation-driven winds and can therefore be used as a further test of the reliability of the calculated wind dynamics.

As the X-rays are produced by the cooling zones of shocked material within the winds, arising from the unstable, non-stationary behavior of the radiative wind driving mechanism (cf. Lucy & Solomon 1970, Owocki & Rybicki 1984), this kind of radiation can not only be observed directly, but also indirectly via its influence on the ionization balance. In particular, it leads to the production of higher ionization stages such as O VI (cf. Pauldrach 1987, Pauldrach et al. 1994), which can be observed by means of the well-known O VI resonance doublet $\lambda\lambda$ 1031, 1037. To strengthen or weaken the general finding that CSPN winds are radiatively driven it is thus important to model the O VI line in the CSPN spectra and thereby to quantify the X-ray production rate and the radial distribution of the X-ray emitting gas, as has already been done for massive O stars (cf. Pauldrach et al. 1994; Pauldrach et al. 1994, 2001; Pauldrach et al. 2012).

Another open issue concerns the optical recombination lines H_α and He II λ 4686, whose emission could not be reproduced fully by Kaschinski et al. (2012). As the current consensus appears to be that this shortcoming can be resolved by taking into consideration possible clumping in the winds (cf. Kudritzki et al. 2006 for a corresponding discussion of CSPN winds), we will reinvestigate these lines via a comparison of clumped and unclumped models for our chosen CSPN sample. The analysis techniques to be used for the points requiring clarification will now briefly be described in the following.

Method for determining an incomplete set of stellar parameters from optical H and He lines. In the analysis of the optical spectrum, the effective temperature $T_{\rm eff}$ is obtained from NLTE model fits to the optical He I and He II stellar absorption lines and the surface gravity $\log g$ is derived from fits to the Balmer lines H_α, H_β, and H_γ (cf. Kudritzki et al. 1997). The radial dependence of the outflow velocity of the expanding atmosphere is parameterized with the arbitrary parameter β in a so-called "beta velocity law," $v(r) = v_\infty (1 - R/r)^\beta$, the best-fit value of β to be fixed as part of the analysis, whereas the terminal velocity v_∞ can be measured directly from the observed blue edge of the P-Cygni profiles in the UV spectrum. The mass loss rate $\dot{M}$ is determined via a model fit to the H_α profile (cf. Kudritzki et al. 2006).[7] As already noted, the stellar mass M can not be determined with this analysis technique; instead, it is derived by comparing the measured $T_{\rm eff}$ and $\log g$ with predictions from post-AGB evolutionary tracks.

Method for determining a complete set of stellar parameters from UV spectra. In contrast to the optical spectrum, the UV spectrum in principle allows determining a complete set of stellar parameters via a model that comprises the consistent solution of the hydrodynamics with the radiative transfer and the NLTE physics. From a corresponding analysis the effective temperature $T_{\rm eff}$, the stellar mass M, the stellar luminosity L and the stellar radius R can be retrieved. Moreover, the solution

[7] Actually, only the quantity $Q \sim \dot{M}(Rv_\infty)^{-3/2}$ can be derived from the observed Hα profiles, and thus the determination of the mass loss rates requires information about the stellar radii R which can not be determined with this analysis and must be provided by other sources.

Table 3.1: Stellar and wind parameters for four selected stars of our sample of central stars of planetary nebulae. The upper part lists the parameters derived from the UV analysis (Pauldrach et al. 2004), the lower part the parameters obtained from the optical analysis (Kudritzki et al. 2006), the core mass–luminosity relation, and consistently calculated dynamics.

Object	$T_{\rm eff}$ (K)	R ($R_\odot$)	$\log L$ ($L_\odot$)	M ($M_\odot$)	$\log g$ (cm/s^2)	$\dot{M}$ ($10^{-6} M_\odot$/yr)	v_∞ (km/s)
Set 1: Parameters from a consistent UV analysis from Pauldrach et al. (2004)							
NGC 2392	40000	1.5	3.78	0.41	3.70	0.018	400
IC 4593	40000	2.2	4.08	1.12	3.80	0.061	850
IC 418	39000	2.7	4.22	1.33	3.70	0.098	800
NGC 6826	44000	2.2	4.25	1.40	3.90	0.178	1200
Set 2: Consistent wind models based on the stellar parameters from Kudritzki et al. (2006)							
NGC 2392	44000	2.4	4.36	0.84	3.60	0.471	400
IC 4593	40000	2.2	4.12	0.70	3.60	0.120	250
IC 418	36000	4.0	4.50	0.92	3.20	0.639	200
NGC 6826	46000	1.8	4.19	0.74	3.80	0.187	600

of the total system of equations also yields the hydrodynamical structure of the wind, thus providing the mass-loss rate $\dot{M}$ and the velocity field $v(r)$. Because the radiative acceleration is calculated analogously to and along with the synthetic spectrum and the accuracy of the calculation of the radiative acceleration is therefore of the same quality as that of the synthetic spectrum, the quality of the UV fit ascertains not only the quality of the determined stellar parameters, but also of the hydrodynamical structure. This means that the velocity field and the mass loss rate, which are thus direct functions of the basic stellar parameters, are as realistic as the obtained synthetic spectrum. These relations ensure that the stellar mass can be determined properly from a fit of the synthetic spectrum to the observations (cf. Pauldrach et al. 2012).

3.3 UV and optical data for the set of central stars of planetary nebulae

The UV observations redward of 1150 Å, acquired by the International Ultraviolet Explorer (IUE), were obtained from the IUE Final Archive data server (`http://sdc.laeff.inta.es/ines/`). Data for the spectral range blueward of 1150 Å, observed by the Far Ultraviolet Spectroscopic Explorer (FUSE), were obtained from the Multimission Archive (MAST) at STScI (`http://archive.stsci.edu/`). The optical observations, acquired by a variety of telescopes and spectrographs (ESO 3.6 m + CASPEC, ESO NTT + EMMI, Isaac Newton 2.5 m (La Palma) + IDS, Palomar echelle, McDonald 2.1 m + Sandiford echelle), were kindly provided by R.-P. Kudritzki (priv. comm.).

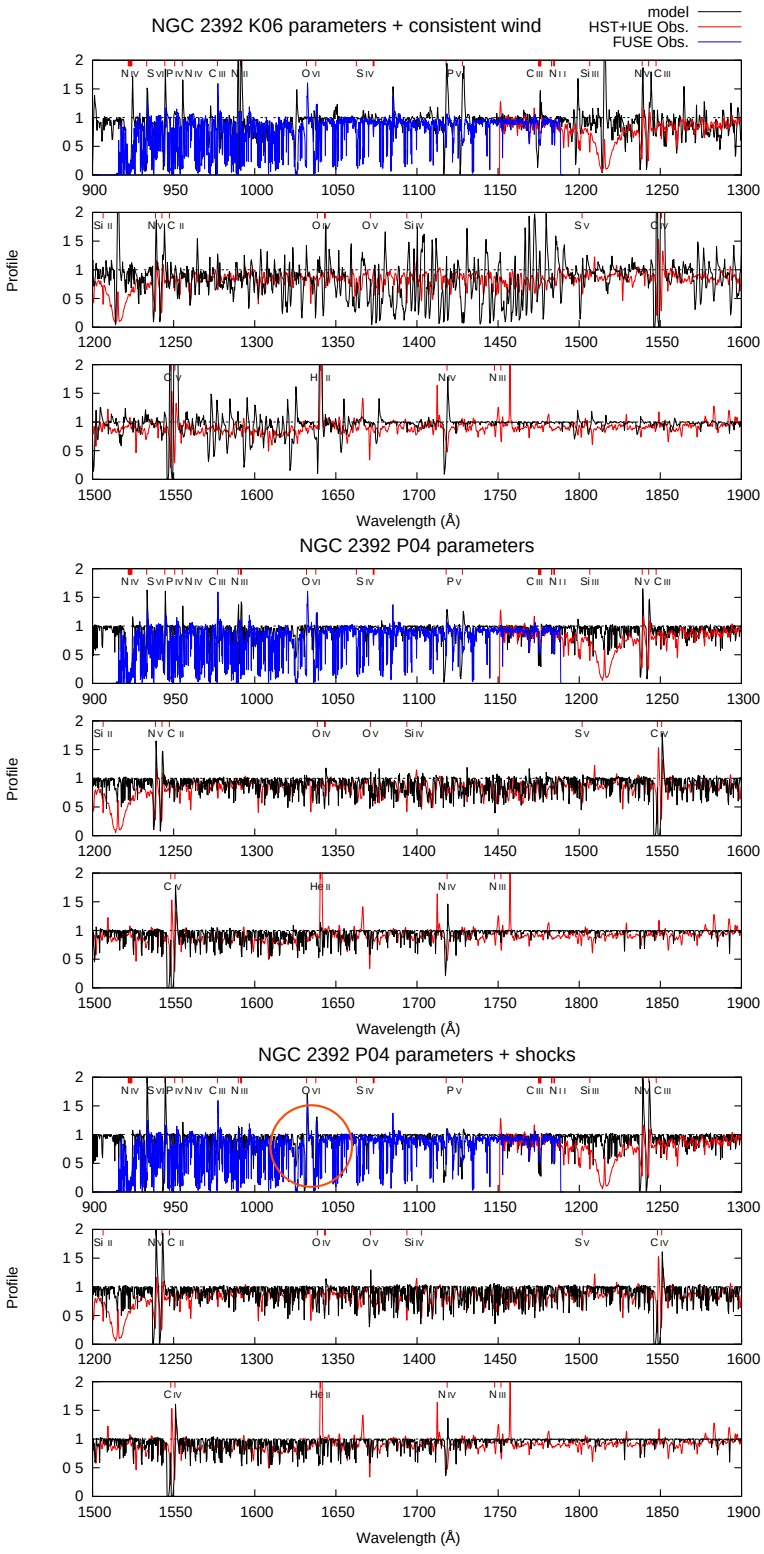

Figure 3.1: Synthetic UV spectra (black) from consistent models for NGC 2392, compared to the observed UV spectra (red and blue). The top panel show the spectrum from a model using the stellar parameters from the analysis of Kudritzki et al. (2006). The spectrum is clearly incompatible with the observations, thus ruling out this parameter set. The center panel shows the spectrum from a model using the parameters from the analysis of Pauldrach et al. (2004). The spectrum predicted by the model is generally in good agreement with the observations, but the O VI line is not reproduced. In the bottom panel, shocks in the wind have additionally been included in the modelling procedure. The small amount of high-energy radiation ($L_X/L_{bol} \sim 10^{-7}$) generated by these shocks is enough to ionize a small fraction of oxygen into O VI, sufficient to reproduce the observed line strength. This result indicates strongly that shocks and the X-ray radiation emitted by them play a role not only in the winds of massive O stars, but also in the winds of CSPNs.

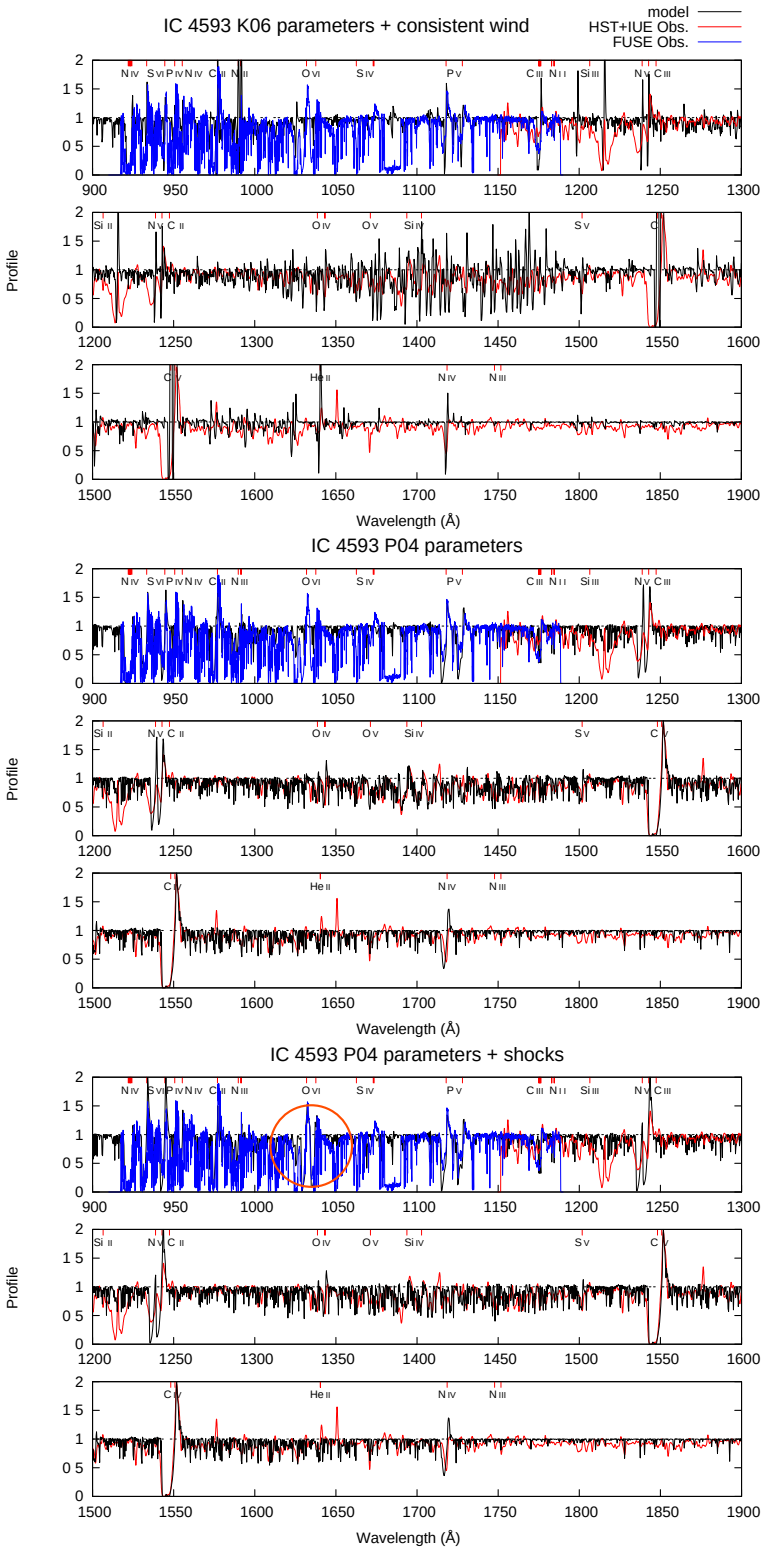

Figure 3.2: As Fig. 3.1, but for IC 4593.

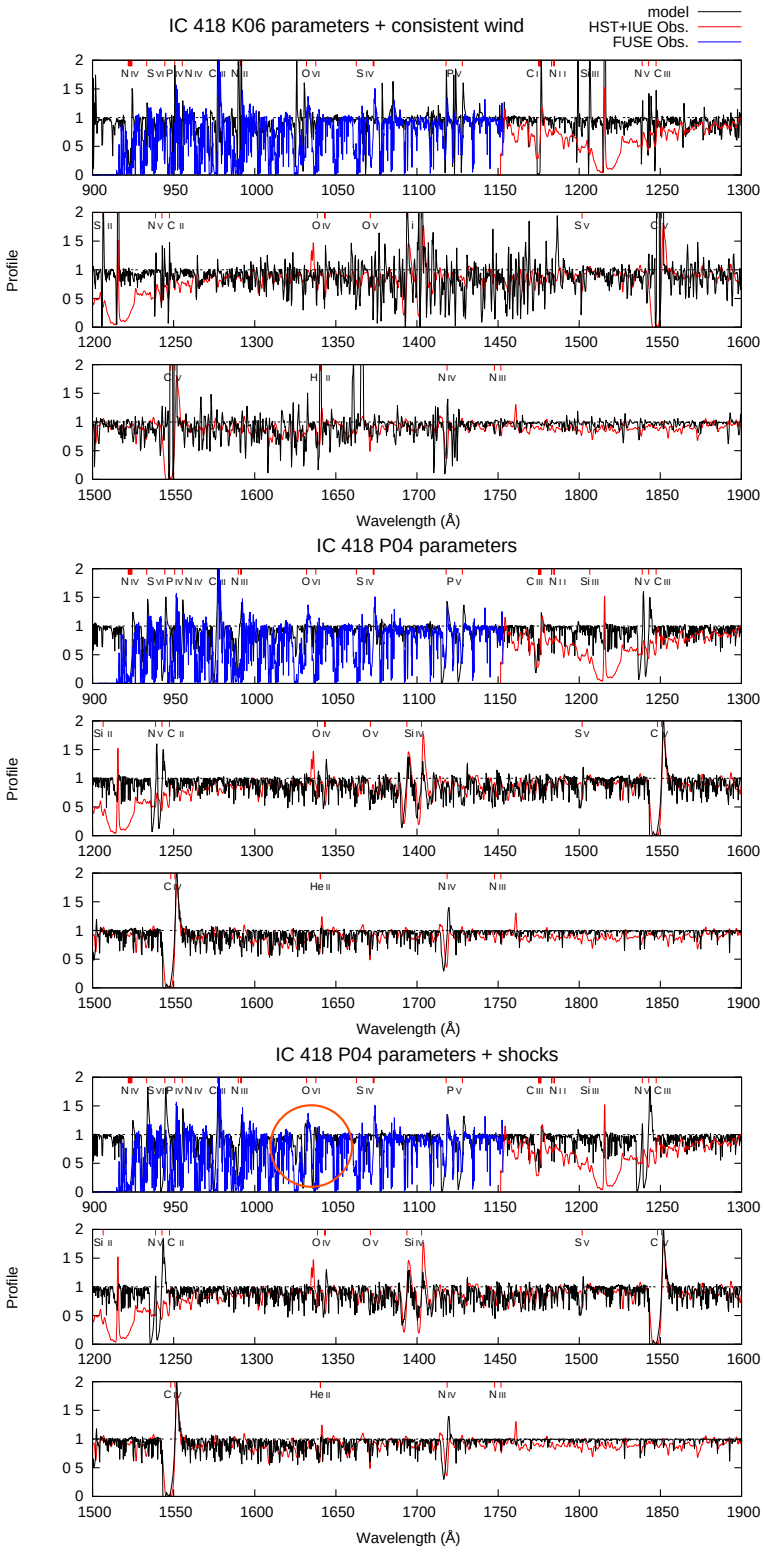

Figure 3.3: As Fig. 3.1, but for IC 418.

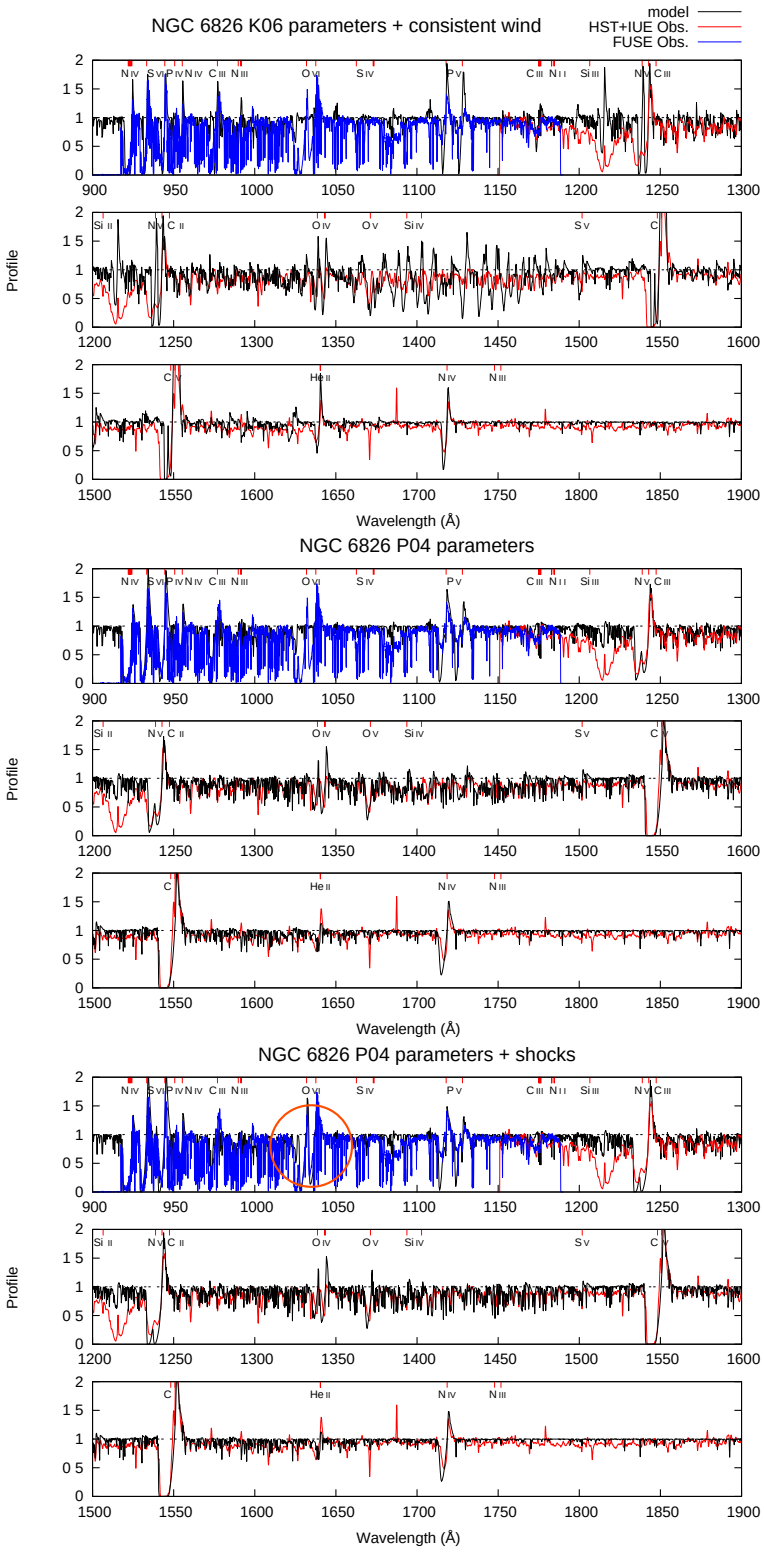

Figure 3.4: As Fig. 3.1, but for NGC 6826.

Table 3.2: Shock structures of the above four central stars. These have been determined from fits of the calculated O VI lines to the FUSE observations. The table lists the radial distributions of the maximum local shock temperatures $T_{\rm shock}^{\rm max}(r)$ and the integrated relative X-ray luminosities $L_{\rm X}/L_{\rm bol}$ emitted by the shock cooling zones embedded in the winds.

NGC 2392		IC 4593		IC 418		NGC 6826	
$\log(L_{\rm X}/L_{\rm bol}) = -6.0$		$\log(L_{\rm X}/L_{\rm bol}) = -6.3$		$\log(L_{\rm X}/L_{\rm bol}) = -6.6$		$\log(L_{\rm X}/L_{\rm bol}) = -6.4$	
r (R_*)	$T_{\rm shock}^{\rm max}(r)$ (10^6 K)	r (R_*)	$T_{\rm shock}^{\rm max}(r)$ (10^6 K)	r (R_*)	$T_{\rm shock}^{\rm max}(r)$ (10^6 K)	r (R_*)	$T_{\rm shock}^{\rm max}(r)$ (10^6 K)
1.006	0.036	1.004	0.028	1.008	0.027	1.003	0.031
1.012	0.044	1.009	0.028	1.015	0.028	1.005	0.031
1.024	0.060	1.018	0.029	1.023	0.028	1.010	0.031
1.047	0.089	1.027	0.030	1.031	0.028	1.016	0.031
1.071	0.118	1.035	0.031	1.039	0.028	1.021	0.031
1.083	0.131	1.044	0.033	1.046	0.029	1.026	0.032
1.088	0.138	1.053	0.035	1.054	0.029	1.031	0.032
1.094	0.145	1.058	0.036	1.062	0.030	1.037	0.032
1.101	0.152	1.062	0.037	1.066	0.030	1.042	0.033
1.108	0.160	1.066	0.038	1.070	0.031	1.047	0.033
1.114	0.168	1.071	0.040	1.074	0.031	1.052	0.034
1.121	0.174	1.076	0.041	1.078	0.031	1.057	0.035
1.128	0.182	1.080	0.043	1.082	0.032	1.063	0.035
1.135	0.189	1.085	0.044	1.086	0.032	1.068	0.036
1.148	0.203	1.090	0.046	1.094	0.033	1.073	0.037
1.162	0.216	1.095	0.048	1.102	0.034	1.078	0.045
1.175	0.229	1.100	0.050	1.110	0.040	1.084	0.045
1.202	0.255	1.110	0.054	1.118	0.040	1.094	0.045
1.229	0.280	1.119	0.058	1.126	0.040	1.104	0.045
1.242	0.292	1.124	0.060	1.134	0.040	1.115	0.045
1.256	0.303	1.129	0.062	1.142	0.040	1.120	0.046
1.269	0.315	1.134	0.065	1.150	0.041	1.125	0.047
1.282	0.326	1.139	0.067	1.158	0.042	1.167	0.057
1.296	0.337	1.148	0.072	1.190	0.047	1.250	0.082
1.309	0.347	1.226	0.117	1.318	0.073	1.416	0.143
1.529	0.495	1.381	0.227	1.573	0.131	1.807	0.289
1.748	0.606	1.746	0.507	1.829	0.188	2.197	0.415
2.182	0.760	2.112	0.755	2.381	0.291	3.421	0.679
2.488	0.836	3.164	1.254	2.803	0.352	4.726	0.836
2.669	0.873	4.184	1.546	3.067	0.384	5.754	0.915
2.767	0.891	4.931	1.694	3.216	0.400	6.420	0.954
4.287	1.063	5.393	1.768	4.728	0.515	9.344	1.063
5.806	1.146	8.350	2.059	6.240	0.580	12.27	1.123
8.845	1.226	11.31	2.206	9.265	0.651	18.12	1.187
14.92	1.288	17.22	2.354	15.31	0.712	29.82	1.240
27.08	1.328	29.05	2.472	27.41	0.755	41.51	1.264
51.38	1.352	52.70	2.551	51.61	0.781	53.21	1.278
75.69	1.360	76.35	2.581	75.80	0.791	76.61	1.292
95.00	1.364	95.00	2.595	95.00	0.795	95.00	1.299
100.0	1.365	100.0	2.597	100.0	0.796	100.0	1.300

3.4 An extended UV analysis of a selected sample of CSPNs

To investigate the influence of X-rays on the synthetic UV spectra of CSPNs and to analyze their characteristics we present in the following an extended UV analysis of a selected sample of CSPNs. With "extended" we mean that the UV analysis will not just be based on the comparison of our synthetic UV spectra with HST and IUE observations, but also with corresponding FUSE observations which include the wavelength range of the O VI resonance line. This spectral line is mainly produced by Auger ionization driven by X-rays emitted by the shock cooling zones resulting from the unstable, non-stationary behavior of the winds, and thus represents a special diagnostic tool for these shocks by allowing their consequences to be analyzed from observations in the UV spectral range, in particular regarding the quantity and the structure of the X-rays (Pauldrach et al. 1994, 2001; Pauldrach et al. 2012). With the FUSE data available this diagnostic potential of the O VI line can be utilized for four CSPNs of our sample: NGC 2392, IC 4593, IC 418, and NGC 6826.

For these four CSPNs we list in Table 3.1 the stellar and wind parameters obtained from the different analysis techniques (cf. Section 3.2): in the upper part the parameters deduced from the UV analyses (parameter set 1; Pauldrach et al. 2004) and in the lower part the parameters obtained from the optical analyses (Kudritzki et al. 2006), the core mass-luminosity relation, and a consistent treatment of the hydrodynamics (parameter set 2). Figures 3.1 through 3.4 show comparisons of the UV spectra from the corresponding WM-basic model runs to the observations.

The middle panel of Fig. 3.1 shows the synthetic UV spectrum of our standard model (parameter set 1) of NGC 2392. The predicted spectrum is in good agreement with not only the observed IUE spectrum, but also with the FUSE observations.[8] The observed O VI line, however, is clearly not reproduced by the synthetic spectrum, and this failure indicates strongly that – as in massive O stars – X-rays are also an important ingredient in CSPN winds. As X-rays are produced by shock cooling zones embedded in the wind, the physics that describe this phenomenon must thus be applied to CSPN models in the same manner as it has been applied to the models of massive O stars.[9]

[8] The small deviations seen in a few spectral lines (e.g., the resonance lines of P V and N V) can of course be corrected by simply adjusting the corresponding abundances slightly. Such fine-tuning is, however, beyond the scope of our present investigation.

[9] The primary effect of the EUV and X-ray radiation is its influence on the ionization equilibrium, where the enhanced direct photoionization due to the EUV shock radiation is as important as the effects of Auger ionization caused by the soft X-ray radiation (cf. Pauldrach 1987, Pauldrach et al. 1994). The radiation is explained by radiative losses of post-shock regions from shocks pushed by non-stationary features, and our modeling is based on a stationary "cool wind" with embedded randomly distributed shocks where the shock distance is much larger than the shock cooling length in the accelerating part of the wind and only a small amount of high-velocity material appears, with a filling factor not much larger than $f \approx 10^{-2}$ and jump velocities of about $u_s \approx 200 \ldots 800$ km/s which result in immediate post-shock temperatures of approximately $T_s \approx 10^6 \ldots 10^7$ K (cf. Pauldrach et al. 1994). On this basis we account for the density and temperature stratification in the shock cooling layer and the two limiting cases of radiative and adiabatic cooling layers behind shock fronts by replacing the usual volume emission coefficient $\Lambda_\nu(T_s(r), n_e)$ by integrals over the cooling zones denoted by $\hat{\Lambda}_\nu(T_s(r))$. For the shock emission coefficient $\varepsilon^s_\nu(r)$ we thus get

$$\varepsilon^s_\nu(r) = \frac{f}{4\pi} n_p n_e \hat{\Lambda}_\nu(T_s(r)),$$

where

$$\hat{\Lambda}_\nu(T_s(r)) = \pm\frac{1}{x_s}\int_r^{r\pm x_s} \hat{f}^2(r')\Lambda_\nu(T_s(r')\,\hat{g}(r'))\,\mathrm{d}r',$$

$n_p n_e$ is the product of the number densities of the ions and electrons, and r is the radial location of the shock front. The

In the lower panel of Fig. 3.1 we show the synthetic spectrum from our model of NGC 2392 in which we have included shocks in this manner. The spectrum now reproduces the profile of the O VI P-Cygni line almost perfectly, and as an integral part of the modelling procedure we obtain the emitted frequency-integrated relative X-ray luminosities[10] $L_{\rm X}/L_{\rm bol}$ as well as the radial distribution of the maximum local shock temperatures[11] $T_{\rm shock}^{\rm max}(r)$ in the cooling zones of the shock-heated matter component (cf. Table 3.2).

The finding that the complete observed UV spectrum – the IUE and HST observations along with the FUSE data – is now quite well in agreement with the synthetic spectrum of our current best model, which in turn is based on the analysis of these spectra, can however not be assigned to the model in the upper panel which has been calculated on the basis of parameter set 2 obtained from the optical analyses, the core mass–luminosity relation and a consistently calculated dynamics, since this model does not at all reproduce the observations – note that the flop of this comparison is primarily based on the consistently calculated mass loss rate which turned out to be much too high for this set of stellar parameters, whereas the consistently calculated terminal velocity is close to the observed value. As spectra computed with such stellar parameter sets – obtained from optical analyses and corresponding consistent wind parameters – showed large discrepancies when compared to observed spectra (in the optical as well as in the UV regimes) in the past, Kaschinski et al. (2012) concluded already that *the published optical analyses give good fits to the observed spectrum only because the wind parameters assumed in these analyses are inconsistent to their stellar parameters*. With regard to the comparison shown in the upper panel of Fig. 3.1 we come here to the same conclusion (compare also for the upper panels of Figs. 3.2, 3.3 and 3.4).

The findings and conclusions we have obtained from the UV analysis of NGC 2392 are also reflected in the UV analyses of the central stars IC 4593, IC 418 and NGC 6826. As is shown in the lower panels of Figs. 3.2, 3.3 and 3.4 the O VI line is along with the complete spectra also in the case of these objects quite well reproduced by our method and especially by our treatment of the shock physics (the decisive data which describe the behavior of the shocks and which are deduced from the analysis of the O VI line are presented in Table 3.2). In contrast to that the Figs. 3.2, 3.3 and 3.4 show for these CSPNs in the upper panels fits of the UV spectra which are of poor quality reflecting the weakness of the used model parameter sets 2 to represent these objects realistically. As in the case of NGC 2392 the primary reason for this behavior are the consistently determined mass loss rates which give for all of these objects too high values. But in contrast to the model of NGC 2392 the obtained terminal velocities are for these three CSPNs in addition too small (with respect to these striking mismatches it makes not much sense to apply the treatment of shocks for the case of these models). This result implies an additional strong hint that something is wrong with these parameter sets (sets 2 in Table 3.1) – and this certainly regards the stellar masses which have not been determined

plus sign corresponds to forward and the minus sign to reverse shocks, r' is the cooling length coordinate with a maximum value of $x_{\rm s}$, and $\hat{f}(r')$ and $\hat{g}(r')$ denote the normalized density and temperature structures with respect to the shock front (cf. Pauldrach et al. (2001)).

[10] As usual, the frequency-integrated X-ray luminosity $L_{\rm X}$ is normalized to the bolometric luminosity $L_{\rm bol}$; this gives the fraction of the total luminosity emitted in the X-ray regime. Note that most of the locally produced X-ray radiation is reabsorbed by the wind, but a small fraction escapes to be observed as soft X-rays with $L_{\rm X}/L_{\rm bol} \approx 10^{-7}$. Thus, the accuracy of the shock description can additionally be verified by a comparison to X-ray observations.

[11] The maximum local shock temperatures $T_{\rm shock}^{\rm max}(r)$ are given by the Rankine-Hugoniot relation as function of the immediate jump velocities $v_{\rm shock}(r)$. Normalized to the turbulent velocity $v_{\rm turb}$, which can be determined from the fit of the shape of the P-Cygni line profiles, the local values of the jump velocity $v_{\rm shock}(r)$ can be estimated via a correlation of $v_{\rm shock}(r)/v_{\rm turb}$ to the wind outflow velocity $v(r)/v_\infty$ (Pauldrach et al. 1994).

spectroscopically but assumed in this case in order to complete the sets of stellar parameters.

As a consequence of our investigation, which revealed the behavior of the X-ray emission of our sample of CSPNs and thus the structure of the underlying shock physics constrained by the quality of the fits of the O VI line, the deduced values of the integrated X-ray luminosities and the radial distribution of the maximum local shock temperatures can now also be compared with corresponding values resulting directly from observations. In this regard Kastner et al. (2012) presented results obtained from the first systematic Chandra X-ray Observatory survey of planetary nebulae (PNe) in the solar neighborhood (within $\sim$1.5 kpc). The highlights of these results include that roughly 50% of the PNe observed by Chandra harbor X-ray-luminous CSPNs, and that this fraction involves detections of diffuse X-ray emission and detections of X-ray point sources[12]. Most noticeable five objects, including NGC 2392, display both diffuse and point-like emission components in the Chandra imaging. From an observational point of view it is therefore imperative to disentangle the origin of the hot gas, since it consists of two components: the shocked fast stellar wind (diffuse source) and the emission from its central star (point source).

In this regard it is quite interesting that Guerrero et al. (2005) derived for NGC 2392 and its surrounding Eskimo Nebula at our distance of 1670 pc an X-ray luminosity of $L_{\rm X} = (2.6 \pm 1.0) \times 10^{31} \cdot (1670/1150)^2 = 5.4 \times 10^{31}$ erg s^{-1} which is almost exactly a factor of two larger than the value $L_{\rm X} = 2.3 \times 10^{31}$ erg s^{-1} we have deduced from our best-fit model for this CSPN (cf. Table 3.1 and Table 3.2). This result is not only in accordance with the observational fact of Kastner et al. (2012) (cf. their Fig. 3), but also with the interpretation of Guerrero et al. (2005) of their result: They noted that the X-ray emission of NGC 2392 has partially to be attributed to the central star and partially to the diffuse X-ray emission produced by the dynamical interaction of the fast outflow with the inner shell of the PNe. As Chandra detected relatively hard point source emission in NGC 2392 (Kastner et al. 2012), which likely explains the energy dependence of the X-ray morphology apparent in the earlier XMM data (cf. Guerrero et al. 2005), the significance of this encouraging result can certainly be improved by a comparison of the maximum shock temperatures. As shown, the best-fit model of Kastner et al., overplotted on the EPIC/pn spectrum in their Fig. 2, has a plasma temperature of $(2.0^{+0.1}_{-0.3}) \times 10^6$ K, which is compared to our value of 1.4×10^6 K (cf. Table 3.1) somewhat larger, but the highest values of the temperature of the shocked gas is definitely due to the highest Mach-number to be expected and this has to be found in the diffuse component and not the point source. We therefore regard our maximum shock temperature to be also in accord with the current observations.

Our general finding that the X-ray to bolometric luminosity ratio is for the case of CSPNs in between $L_{\rm X}/L_{\rm bol} \sim 10^{-6} \ldots 10^{-7}$ (cf. Table 3.1) is further confirmed by Guerrero (2006), who deduced for the central star NGC 6543 a value of $L_{\rm X}/L_{\rm bol} \sim 10^{-7}$ from observations. As such values of $L_{\rm X}/L_{\rm bol}$ are typical for radiation driven winds – they are of the same order as observed for the case of massive O stars (cf. Sana et al. 2005 and Sana et al. 2006) –, it is obviously the radiation pressure which determines the atmospheric structure not just of massive O stars but also of O type CSPNs; and this regards not only the primary behavior which rules the values of the mass loss rate $\dot{M}$ and the terminal velocity v_∞, but also weak and secondary effects which rule the details of the shock physics.

Our consistent procedure and the corresponding analysis is thus not only based on the high radiation flux density of CSPNs (which necessarily leads to expanding atmospheres), the wind-momentum–luminosity relation (WMLR), and the behavior of $v_\infty/v_{\rm esc}$, which can be compared to observations (cf. Pauldrach et al. 2004 and Kaschinski et al. 2012), but also on secondary effects such as the maximum

[12] The diffuse X-ray emission is thought to arise from shells where the CSPN wind rams into the previously expelled AGB envelope, producing hot shocked gas; the point-like sources are associated with the central stars themselves.

shock temperatures and the integrated X-ray luminosities which are also subject of observations. All these findings support the hypothesis that the atmospheres of CSPNs are governed by exactly the same radiative line-driving mechanism as those of massive O stars.

3.5 Accounting for clumping

To simulate the effects of clumping we consider the same basic treatment as implemented in FASTWIND (Puls et al. 2006), the model atmosphere code that had been used by Kudritzki et al. (2006) in their analysis. In this "microclumping" description the gas is considered to be swept up into small, optically thin clumps with a volume filling factor of $1/f_{\rm cl}(r)$ and void interclump regions. The density in the clumps,

$$\rho_{\rm cl}(r) = f_{\rm cl}(r)\overline{\rho}(r), \tag{3.1}$$

is then the local clumping factor $f_{\rm cl}(r)$ times the density $\overline{\rho}(r)$ of the smooth, unclumped flow given by the equation of continuity,

$$\overline{\rho}(r) = \frac{\dot{M}}{4\pi r^2 v(r)}. \tag{3.2}$$

The void interclump regions do not influence the radiative intensity, and only the fraction $1/f_{\rm cl}$ of volume that actually contains matter contributes to the opacity and emissivity along a macroscopic path element. Thus, if $\kappa = \chi/\rho$ denotes the opacity per unit mass, the optical depths

$$\tau = \int \chi_{\rm cl} \frac{1}{f_{\rm cl}}\,{\rm d}s = \int \kappa\rho_{\rm cl}\,\frac{{\rm d}s}{f_{\rm cl}} = \int \kappa f_{\rm cl}\overline{\rho}\,\frac{{\rm d}s}{f_{\rm cl}} = \int \kappa\overline{\rho}\,{\rm d}s = \int \bar{\chi}\,{\rm d}s, \tag{3.3}$$

and indeed all quantities that are linear in the density, remain unaffected by this clumping except that clumping may lead to a shift in the ionization stages, and thus a change in κ, through increased recombination in the higher-density clumps. On the other hand, quantities that are proportional to the square of the density, such as the emissivities of recombination lines, are enhanced by a factor of $f_{\rm cl}$.

To demonstrate that our clumping treatment in WM-basic produces results comparable to FASTWIND, we show in Fig. 3.5 the predicted H_α line profiles[13] for two stellar models with strong winds (in which H_α is most likely to be affected by clumping). We use, here as well as in the CSPN model calculations of Section 3.6, the same radial run of the clumping factors as used by Kudritzki et al. (2006) in their analysis (J. Puls, priv. comm.): no clumping (i.e., $f_{\rm cl}(r) = 1$) in the photosphere, up to $v = 0.05v_\infty$; a steep rise to the specified clumping factor from $v = 0.05v_\infty$ to $v = 0.1v_\infty$; and then keeping this value $f_{\rm cl}(r) = {\rm const}$ for $v > 0.1v_\infty$. To focus the comparison on the clumping and the radiative transfer we have set up the comparison runs as closely as possible, in particular we have used the density structures of the FASTWIND models in our WM-basic calculations. The remaining small differences in the predicted line profiles are due to actual differences in the modelling, such as the use

[13] We had already shown in Kaschinski et al. (2012) that the photospheric absorption lines, which are formed deep in the atmosphere where the density approaches a hydrostatic structure and is therefore independent of the density law used to describe the wind in the outer atmospheric regions, are very similar between FASTWIND and WM-basic. We therefore refrain from showing those profiles here again and instead remark only that they are also very similar for the benchmark models presented here.

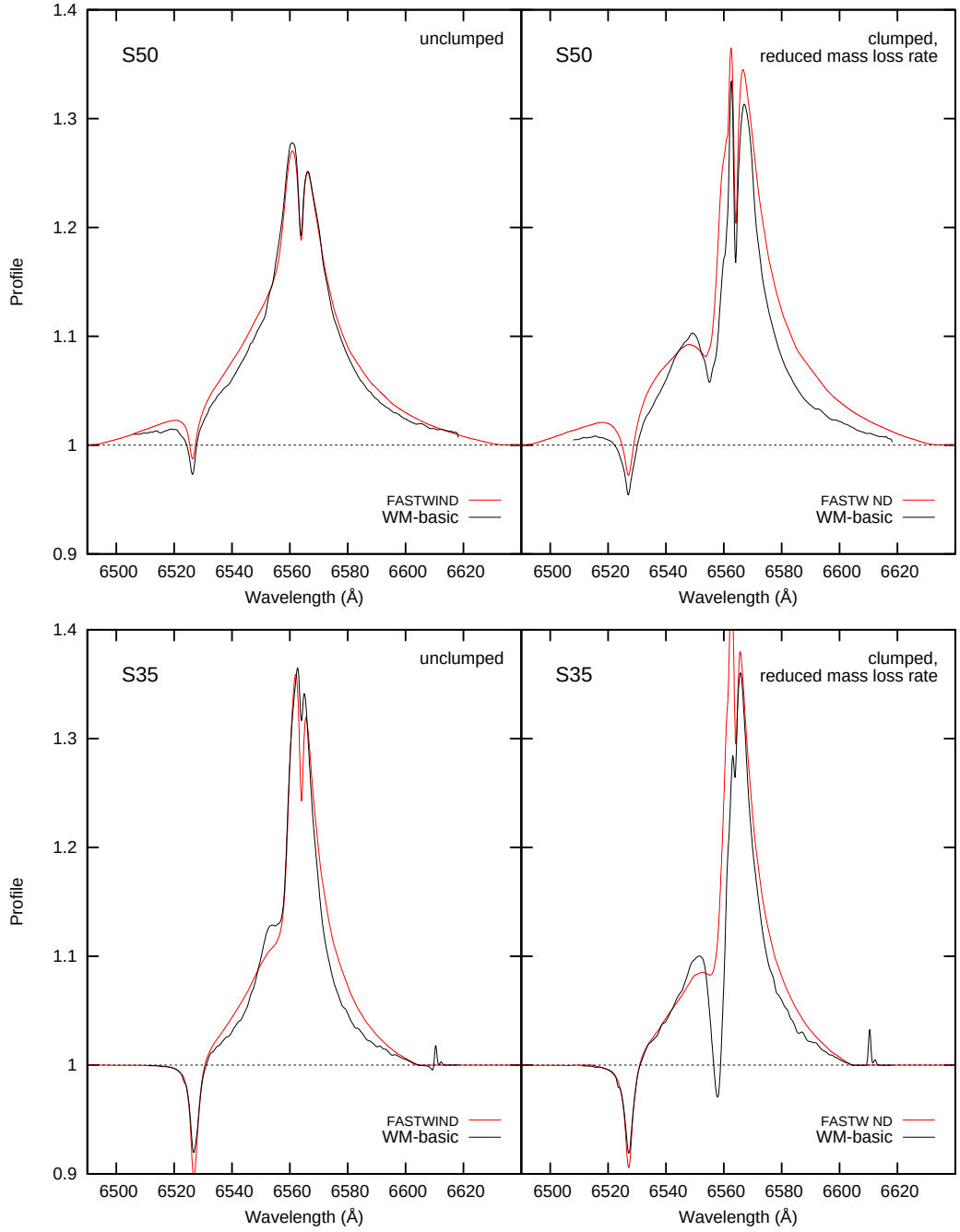

Figure 3.5: Comparison of H_α line profiles predicted by FASTWIND (red) and WM-basic (black). To focus the comparison on the NLTE modelling and the treatment of radiative transfer, these WM-basic calculations use the density structures from the FASTWIND models. The top row shows a $T_{\rm eff} = 50\,000$ K test model (S50), the bottom row a $T_{\rm eff} = 35\,000$ K test model (S35). The left panels show the profiles from a smooth, unclumped flow ($f_{\rm cl} = 1$), the right panels those from a clumped flow ($f_{\rm cl} = 81$) with a correspondingly reduced mass loss rate (by a factor of $\sqrt{f_{\rm cl}} = 9$). The differences between our WM-basic predictions and those from FASTWIND are negligible compared to the sensitive dependence of the H_α line on the clumping factor, as illustrated by Fig. 3.6.

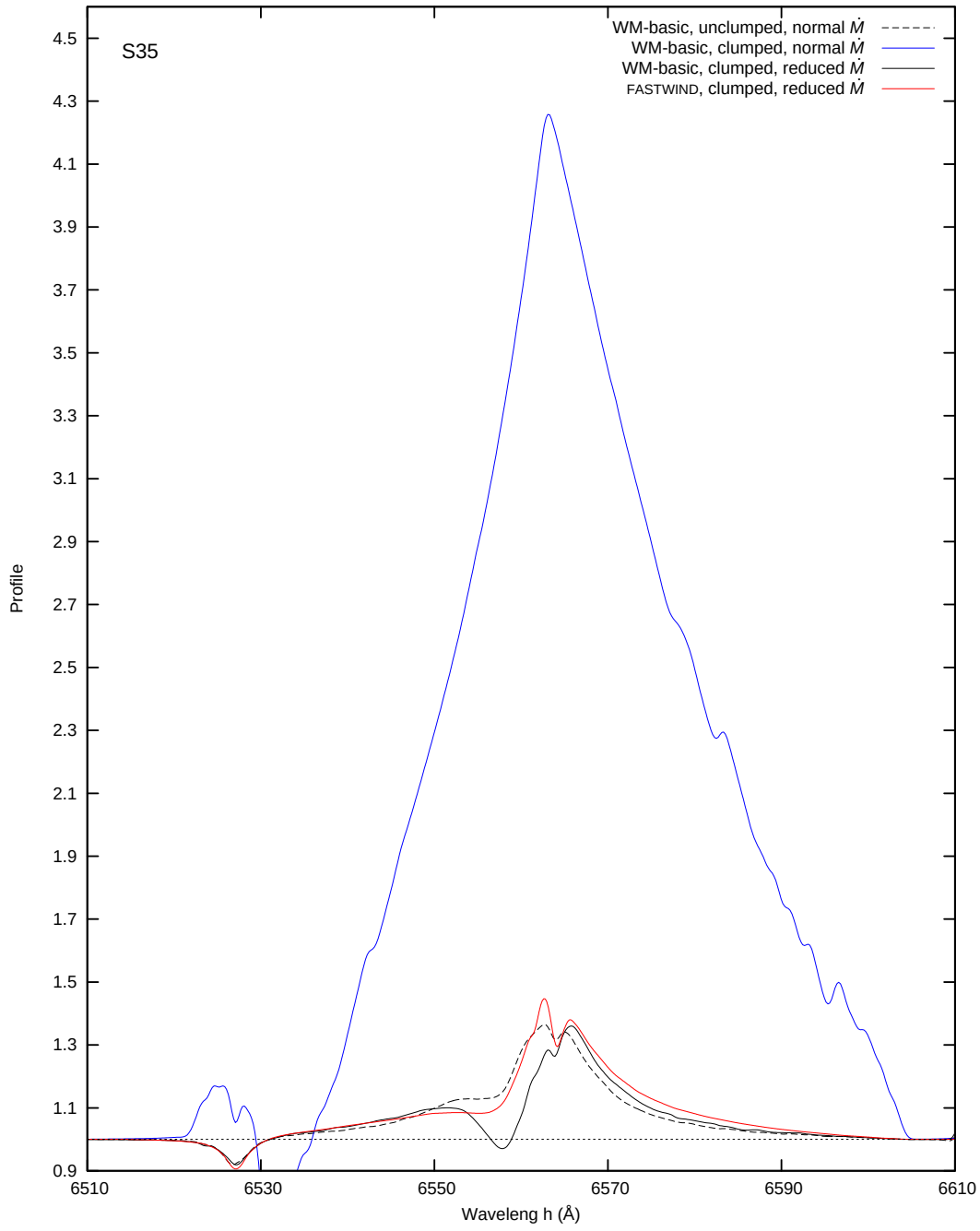

Figure 3.6: H_α line profile of the S35 test model as in Fig. 3.5, but this time also showing the case of a clumped wind ($f_{\rm cl} = 81$, as in Fig. 3.5) with the "normal" mass loss rate (blue). Compared to this strong response, the small differences between two corresponding FASTWIND (red) and WM-basic (black solid line) predictions are insignificant.

of different model atoms, or the different interpolation of the opacities and emissivities between the grid points in the radiative transfer.

These small differences in the predicted line profiles are not relevant, however, for the purposes of diagnosing mass loss rates or clumping factors from given observed profiles. This is demonstrated in Fig. 3.6 where we compare the predicted H_α line profiles from an unclumped wind and from a clumped wind ($f_{\rm cl} = 81$) with the same mass loss rate. (The latter is equivalent to an unclumped wind with a mass loss rate increased by a factor of $\sqrt{f_{\rm cl}}$.) Compared to the strong response of the profile to a change in the mass loss rate or clumping factor, the differences in the predictions of WM-basic and FASTWIND are small. In other words, for a given clumping factor one would deduce exactly the same mass loss rate from an observed H_α profile when using the WM-basic model as when using the FASTWIND model.

In these tests (and these tests only) we have used the density structures from the FASTWIND models in our WM-basic calculations. We put particular emphasis on this point, since we have shown here that both codes produce equivalent line profiles *if given the same input*. This is important to keep in mind for the model calculations for individual CSPNs below: when using the stellar parameters of Kudritzki et al. (2006), if we do not achieve as good a fit to the observed profiles as they did, *even when enforcing their mass loss rates and terminal velocities* in our models, then this is not because the codes a priori produce different results, but because a *different density structure* was used. But that is the entire point of using our modelling code in these analyses: to base the model predictions on a density structure that follows from a solution to the equation of motion of the wind, instead of simply *assuming* a certain parametrization[14] as Kudritzki et al. (2006) did. For the H_α line profile formation the differences between the assumed and the computed wind density structures play at least as important a role as the proposed clumping.

3.6 Model calculations for individual CSPNs

In the following we present a comparison of observed and computed optical line profiles for our sample of nine CSPNs. Basis for this comparison are the two sets of stellar parameters derived (a) from an analysis of the UV spectra by Pauldrach et al. (2004), hereafter labeled P04, and (b) from an analysis of the optical spectra by Kudritzki et al. (2006), labeled K06. The parameters of all objects in the sample are listed in Table 3.3.

For each CSPN we show the results from three different model runs: P04: stellar and (consistent) wind parameters from Pauldrach et al. (2004); K06f: stellar parameters from Kudritzki et al. (2006), artificially enforcing their wind parameters in our model runs; and K06c: stellar parameters from Kudritzki et al. (2006) and wind parameters consistent with those stellar parameters, as determined by our hydrodynamic calculations of the radiative driving force. For those objects where Kudritzki et al. (2006) have given a clumping factor $f_{\rm cl} \neq 1$ we show all line profiles both including and excluding clumping. Additionally we present redetermined clumping factors which have as usual been derived from a comparison of the observed optical lines to our predicted optical lines obtained from the P04 models.

[14] If we *knew* that the winds were completely smooth, a point could be made for "empirically" determining the velocity law by trying different parameter values in the prescription and choosing the one that leads to the best fit of the H_α line profile, but once we admit clumping, for which we have no theory to predict the radial run either, such reasoning becomes rather specious.

Table 3.3: Overview of models for the nine CSPNs of the investigated sample. In the parameter source column, P04 refers to the parameters derived by Pauldrach et al. (2004) from an analysis of the UV spectra, and K06 refers to the optical analysis of Kudritzki et al. 2006. "Consistent" means that the wind parameters are consistent with the stellar parameters as determined by our hydrodynamic calculations of the radiative driving force.

Object	$T_{\rm eff}$ (K)	$\log g$ (cm/s^2)	$Y_{\rm He}$	R ($R_\odot$)	$\log L$ ($L_\odot$)	M ($M_\odot$)	$\dot{M}$ ($10^{-6} M_\odot$/yr)	v_∞ (km/s)	$f_{\rm cl}$ K06	$f_{\rm cl}$ new	parameter source: stellar par.	parameter source: wind par.	parameter source: clumping	consistent?
NGC 2392	44000	3.6	.23	2.4	4.36	0.84	0.050	400	1		K06	K06	K06	no
	〃	〃	〃	〃	〃	〃	0.471	400	1		〃	this work	〃	yes
	40000	3.7	.25	1.5	3.78	0.41	0.018	400	1		P04	P04	〃	**yes**
	〃	〃	〃	〃	〃	〃	〃	〃		8	〃	〃	this work	〃
IC 4637	52000	4.2	.09	1.0	3.86	0.58	0.014	1500	4		K06	K06	K06	no
	〃	〃	〃	〃	〃	〃	0.042	700	4		〃	this work	〃	yes
	55000	4.6	.11	0.8	3.74	0.87	0.018	1500		4	P04	P04	〃	**yes**
NGC 3242	75000	4.8	.09	0.5	3.89	0.63	0.008	2300	4		K06	K06	K06	yes
	75000	5.15	.12	0.3	3.50	0.53	0.004	2400		4	P04	P04	〃	**yes**
IC 4593	40000	3.6	.09	2.2	4.12	0.70	0.042	900	4		K06	K06	K06	no
	〃	〃	〃	〃	〃	〃	0.120	250	4		〃	this work	〃	yes
	40000	3.8	.12	2.2	4.08	1.12	0.061	850		4	P04	P04	〃	**yes**
IC 418	36000	3.2	.17	4.0	4.50	0.92	0.035	700	50		K06	K06	K06	no
	〃	〃	〃	〃	〃	〃	0.639	200	50		〃	this work	〃	yes
	39000	3.7	.1	2.7	4.22	1.33	0.098	800	50		P04	P04	〃	**yes**
	〃	〃	〃	〃	〃	〃	〃	〃		4	〃	〃	this work	〃
He 2-108	34000	3.4	.09	2.6	3.99	0.62	0.136	700	1		K06	K06	K06	no
	〃	〃	〃	〃	〃	〃	0.404	300	1		〃	this work	〃	yes
	39000	3.7	.1	2.7	4.18	1.33	0.098	800	1		P04	P04	〃	**yes**
	〃	〃	〃	〃	〃	〃	〃	〃		8	〃	〃	this work	〃
Tc 1	34000	3.2	.09	3.8	4.34	0.84	0.036	950	10		K06	K06	K06	no
	〃	〃	〃	〃	〃	〃	0.605	300	10		〃	this work	〃	yes
	35000	3.6	.15	3.0	4.12	1.37	0.054	850	10		P04	P04	〃	**yes**
	〃	〃	〃	〃	〃	〃	〃	〃		4	〃	〃	this work	〃
He 2-131	32000	3.2	.33	3.5	4.13	0.71	0.131	400	8		K06	K06	K06	no
	〃	〃	〃	〃	〃	〃	0.105	300	8		〃	this work	〃	yes
	33000	3.1	.30	5.5	4.59	1.39	0.321	400	8		P04	P04	〃	**yes**
	〃	〃	〃	〃	〃	〃	〃	〃		4	〃	〃	this work	〃
NGC 6826	46000	3.8	.09	1.8	4.19	0.74	0.076	1200	4		K06	K06	K06	no
	〃	〃	〃	〃	〃	〃	0.187	600	4		〃	this work	〃	yes
	44000	3.9	.13	2.2	4.25	1.40	0.178	1200		4	P04	P04	〃	**yes**

3.6.1 NGC 2392

The central star of NGC 2392 is of particular interest as it has a mass of only $0.41\,M_{\odot}$, making it the least massive CSPN of our sample. A clumping factor of 1 was derived by Kudritzki et al. (2006), corresponding to an unclumped wind. Unfortunately we lack observations for many of the optical lines for which we show synthetic line profiles in Fig. 3.7. The computed line profiles, both in absorption and emission, for the consistent P04 and the fitted K06f models are almost identical. Both models fail to reproduce the strong H_α and He II λ 4686 emission lines but match the absorption lines equally well. The consistent K06c model has a much too high mass loss rate, reflected in a too strong emission of *all* emission lines, and even showing H_γ in emission. Table 3.3 shows this huge discrepancy in the mass loss rate which is higher by a factor of 10 in the K06c model compared to the K06f model.

As the consistent P04 and the fitted K06f model both fail to reproduce the strong H_α and He II λ 4686 emission lines, we have redetermined the clumping factor for the P04 model from a comparison of the observed optical lines to our predictions. We obtain a clumping factor of 8, a strong deviation to the result of Kudritzki et al. (2006) (cf. Table 3.3). The derived clumping factor represents a compromise between the predictions for the He II λ 4686 line and the H_α line: a higher clumping factor could have reproduced the observed height of the He II λ 4686 line better, but then the width of the predicted H_α line would have exceeded that of the observed profile (dash-dotted red line in Fig. 3.7). This is a clear indication that the physical effect that enhances the emission in these two lines and which we model with our clumping approach does not quite behave, in particular with regard to its radial run, as the simplistic description applied at the present stage.

3.6.2 IC 4637

For IC 4637 a clumping factor of 4 was derived by Kudritzki et al. (2006). The resulting synthetic optical line profiles from the P04 and the (inconsistent) K06f models match the observations for IC 4637 very well (Fig. 3.8), and both clumped and unclumped wind result in nearly the same profiles (for H_α, the unclumped P04 model even shows a better fit than the clumped one). The consistent K06c model shows a mostly equally good fit to the absorption lines, but its high emission in H_α and He II λ 4686 makes the K06 stellar parameters incompatible with the observations.

3.6.3 NGC 3242

NGC 3242 is the only CSPN of the sample for which the UV analysis of Pauldrach et al. (2004) and the optical analysis of Kudritzki et al. (2006) yield almost the same mass, and the K06f parameter set is consistent (and thus identical to the K06c model). Both the P04 and the K06f/K06c models give nearly identical, excellent fits to all observed optical line profiles. The effects of clumping are marginal, as neither H_α nor He II λ 4686 are in emission.

3.6.4 IC 4593

For IC 4593 the situation is somewhat similar to that of IC 4637: the observed optical absorption lines are matched equally well by the P04 and the (inconsistent) K06f models (Fig. 3.10). The predicted emission in H_α and He II λ 4686 is a bit too low for both models, but with some cosmetics, i.e., a slightly larger clumping factor, the P04 model would show a perfect fit to both lines. The consistent

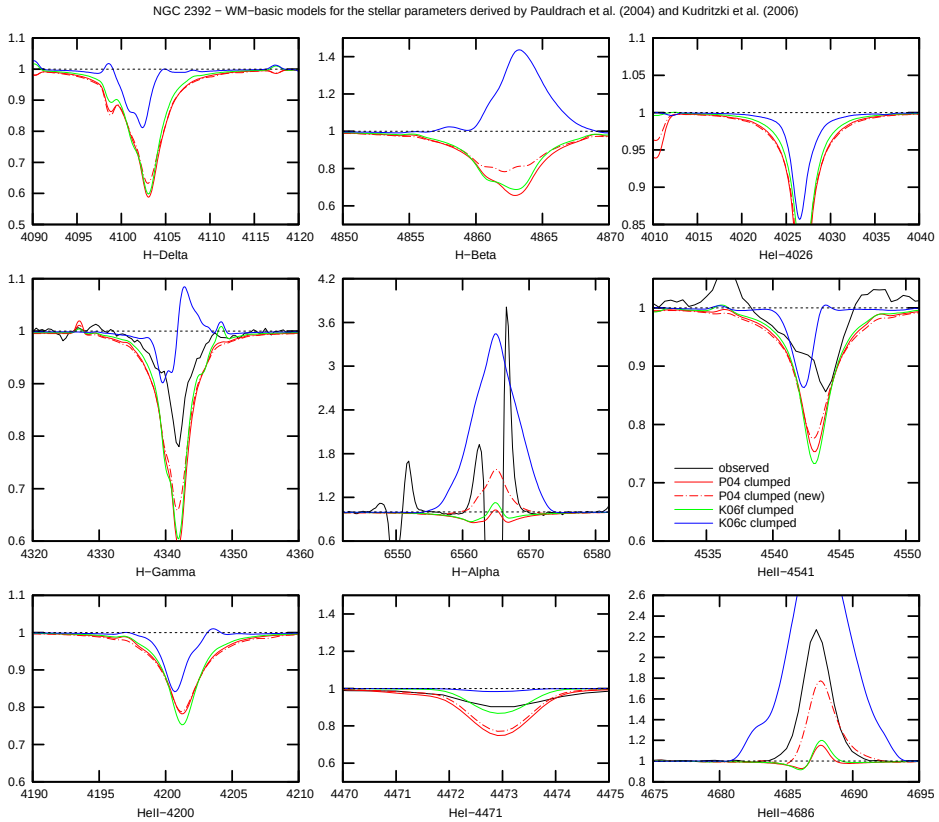

Figure 3.7: Observed optical line profiles of NGC 2392 (black) compared to predicted line profiles from four different models. Colors indicate different stellar and wind parameter sets, while dash styles indicate different clumping factors. The colors correspond to: the consistent model of Pauldrach et al. (2004) (P04, red); a model using the stellar parameters of Kudritzki et al. (2006) with mass loss rate and terminal velocity artificially set to the values given by Kudritzki et al. (K06f, green); and one using the stellar parameters of Kudritzki et al. (2006) and wind parameters consistent with those stellar parameters (K06c, blue). Solid lines indicate models using the clumping factor suggested by Kudritzki et al. (2006), the dash-dotted line indicates a model using the clumping factor redetermined in this work.

K06c model again produces too strong emission, even without clumping, and thus rules out the K06 stellar parameters.

3.6.5 IC 418

IC 418 is of special interest because Kudritzki et al. (2006) have found a clumping factor of 50 (!) for this star, which is by far the highest value, but even with this large clumping factor the K06f model fails to reproduce the observed H_α profile (Fig. 3.11). The consistent model K06c produces much too strong emission and thus gives incompatible line profiles for *all* observed lines, with and without clumping. (Additionally, it results in a terminal velocity of only 200 km/s, which is much too small compared to the observed terminal velocity of 700 km/s.) For the P04 model, this clumping factor is

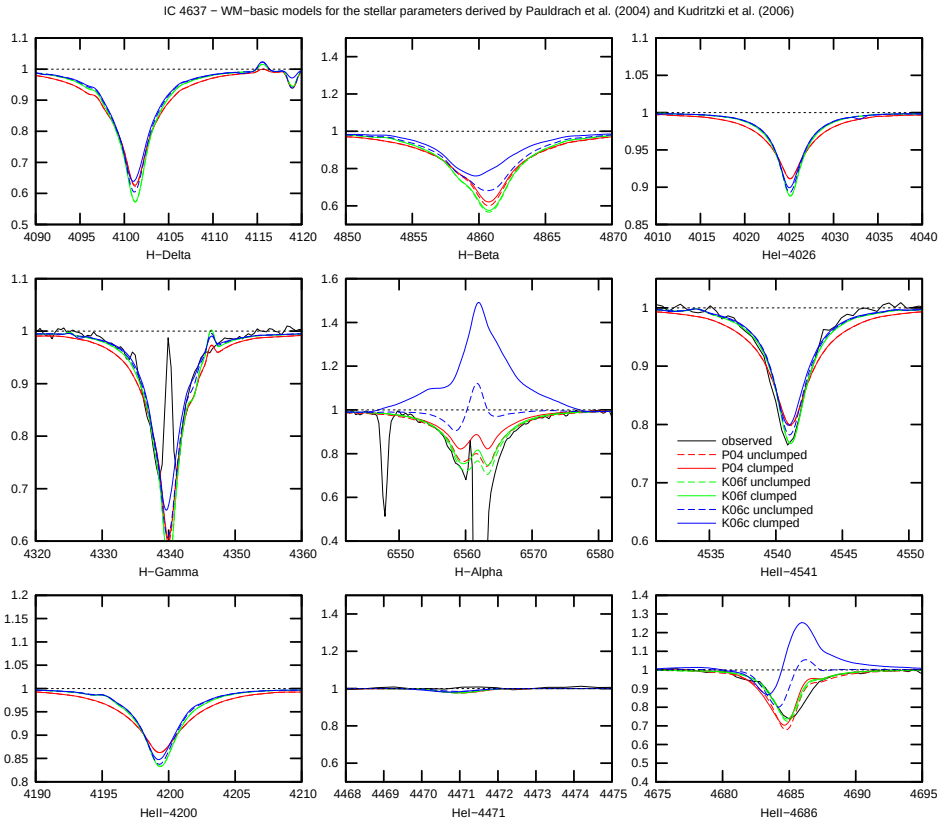

Figure 3.8: As Fig. 3.7, but for IC 4637. Profiles from unclumped models are additionally shown dashed.

also much too large, but a moderate clumping factor of 4 yields with respect to a compromise of the strength and width of the emission lines of H_α and He II λ 4686 the best fit to all lines (Fig. 3.11).

3.6.6 He 2-108

Kudritzki et al. (2006) found no evidence of clumping in the wind of He 2-108, but with our computed density structure their mass loss rate does not yield enough emission in H_α and He II λ 4686 (a situation somewhat similar to NGC 2392). A moderate clumping factor of 8, again a (slight) compromise between width and height of the profiles, yields a much improved fit (Fig. 3.12), but the same caveat from the discussion of NGC 2392 with regard to the radial run of the clumping factor applies here as well.

He 2-108 is one of the few CSPNs for which the K06c model yields fits to the optical line strength which are of the same quality as the K06f model. However, the K06c model produces a terminal velocity of only 300 km/s, which is too small compared to the observed value.

3.6.7 Tc 1

For Tc 1 Kudritzki et al. (2006) found a clumping factor of 10. In the (inconsistent) K06f model, this clumping factor yields a good fit to He II λ 4686, but the emission in H_α is still slightly low. The

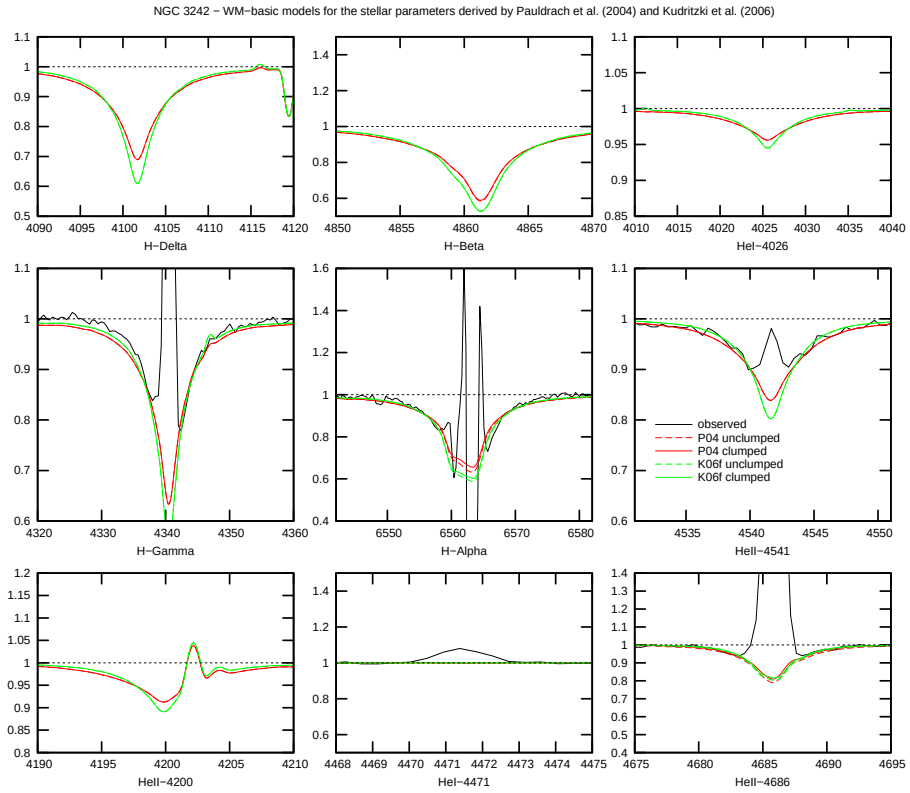

Figure 3.9: As Fig. 3.8, but for NGC 3242. This is the only CSPN for which the consistent wind calculation yields the same mass loss rate and terminal velocity as the optical analysis by Kudritzki et al. (2006) and the "green" model is thus identical to the "blue" one (which is therefore not shown).

P04 model gives too much emission in both H_α and He II λ 4686 with this clumping factor, and the somewhat lower value of $f_{\rm cl} = 4$ yields a much better fit (Fig. 3.13). The consistent K06c model has already too much emission in He II λ 4686 without clumping, and its terminal velocity of 300 km/s is also too small compared to the observed value of about 900 km/s.

3.6.8 He 2-131

For He 2-131 the consistent calculation (K06c) using the stellar parameters of Kudritzki et al. (2006) yields wind parameters similar to those used by Kudritzki et al. (K06f), and their predicted line profiles are thus also very similar (Fig. 3.14). All three model calculations yield similar profiles with too little emission in H_α, even with a clumping factor of 8, and also do not correctly reproduce He II λ 4686, P04 by yielding too much emission and K06c and K06f too little. The H_α line again shows tendencies of becoming too wide with this clumping factor, another indication that clumping should be reduced at higher outflow velocities, and a global clumping factor of 4 does not significantly change the appearance (Fig. 3.14). The P04 model, using the helium abundance determined by Kudritzki et al. (1997), shows too much emission already without clumping, indicating that the rather high helium abundance assumed might in reality be smaller, more like that of the other stars of the sample.

The absorption lines are of similar quality in all three models, and are fairly unaffected by clumping.

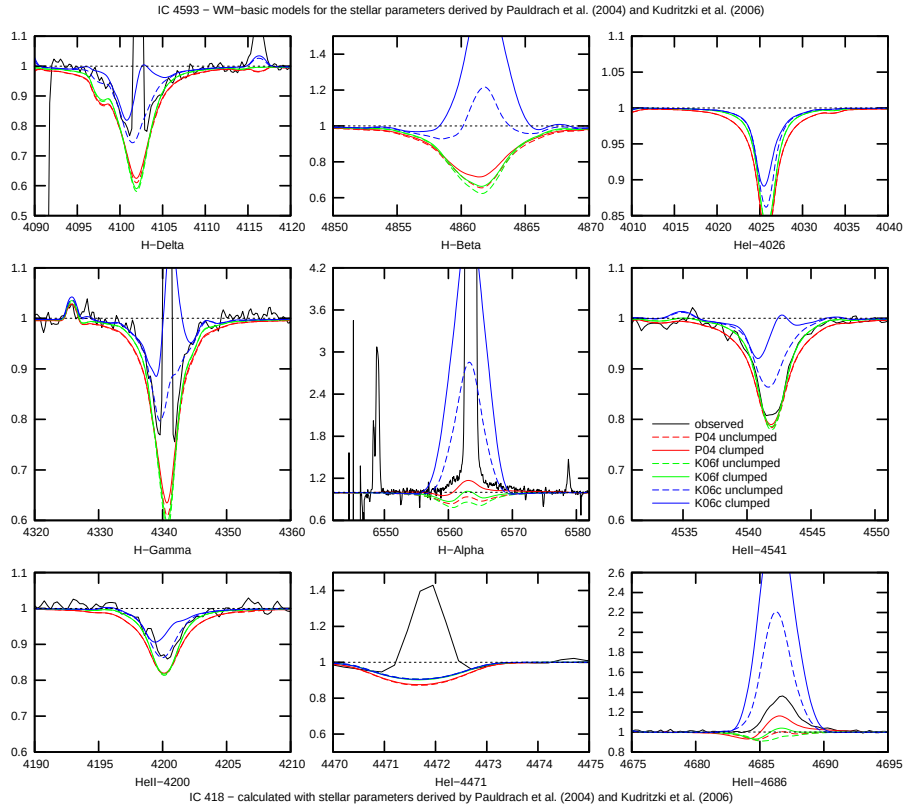

Figure 3.10: As Fig. 3.8, but for IC 4593.

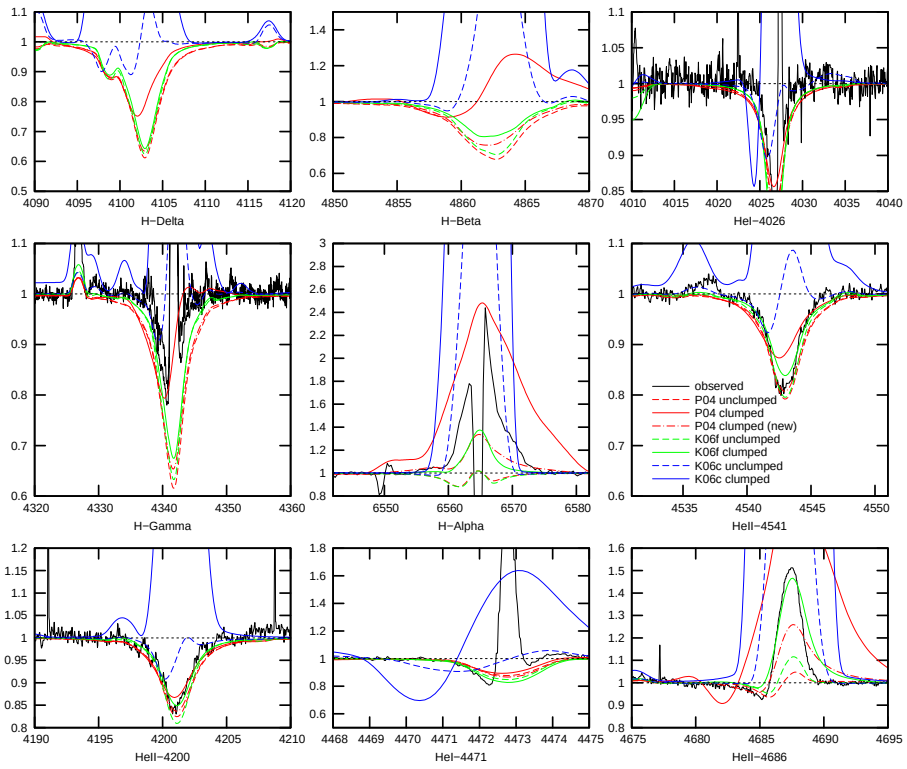

Figure 3.11: As Fig. 3.8, but for IC 418.

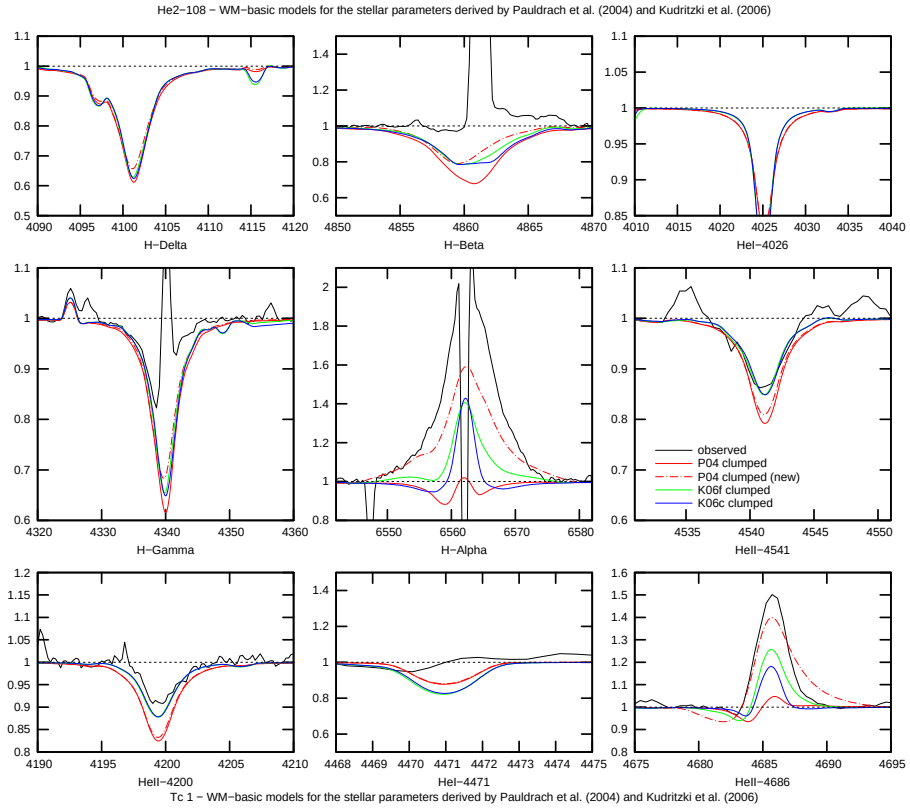

Figure 3.12: As Fig. 3.7, but for He 2-108.

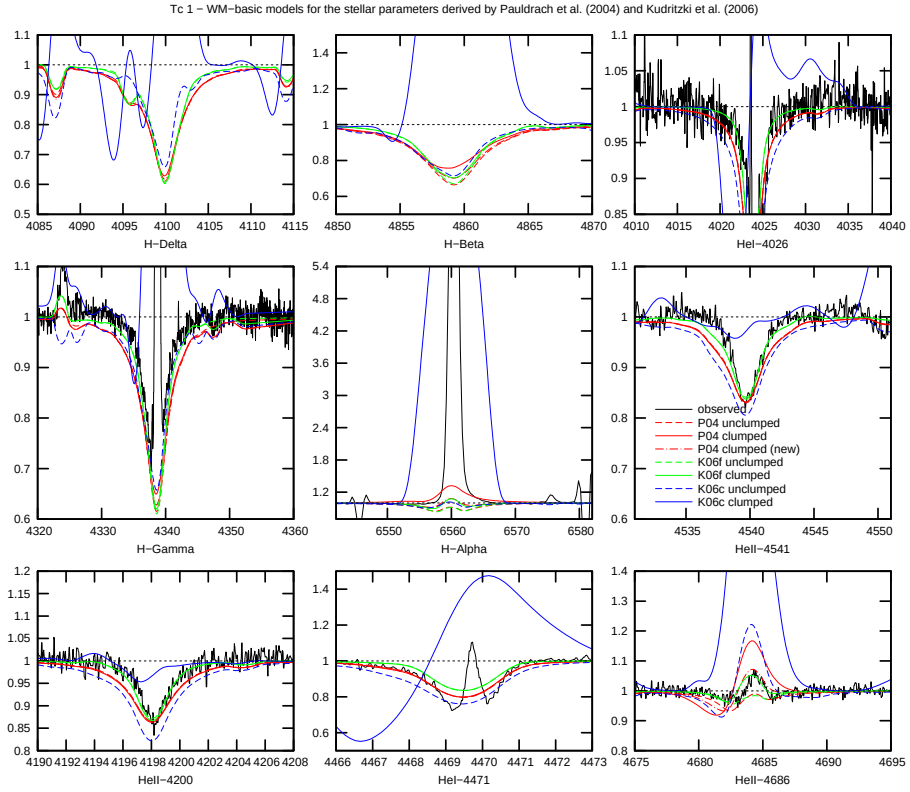

Figure 3.13: As Fig. 3.8, but for Tc 1.

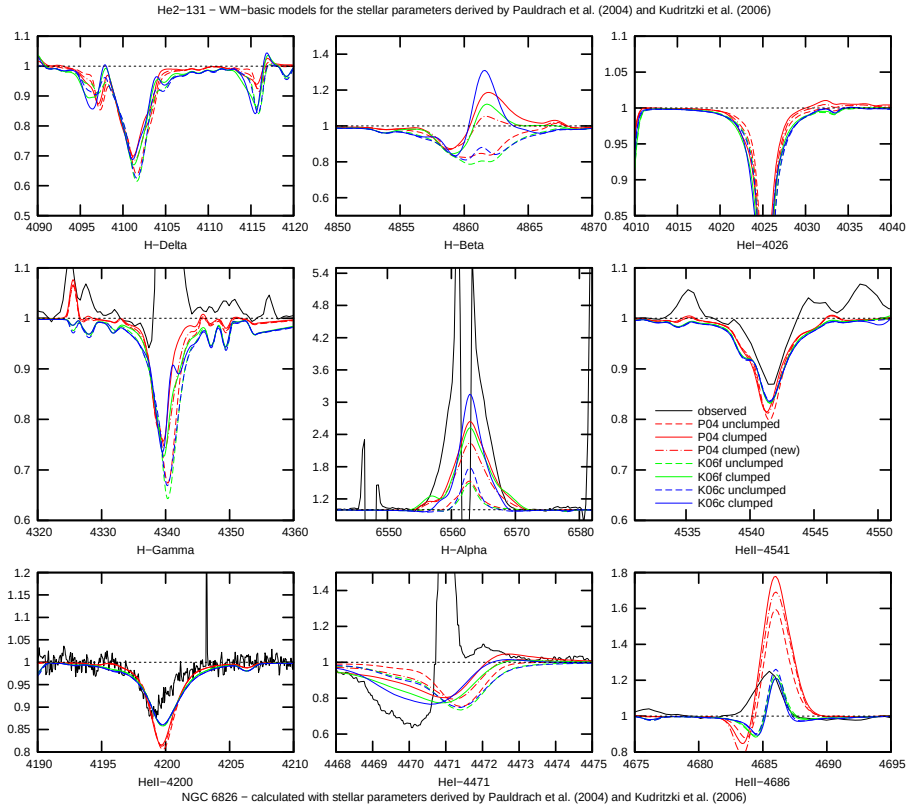

Figure 3.14: As Fig. 3.8, but for He 2-131.

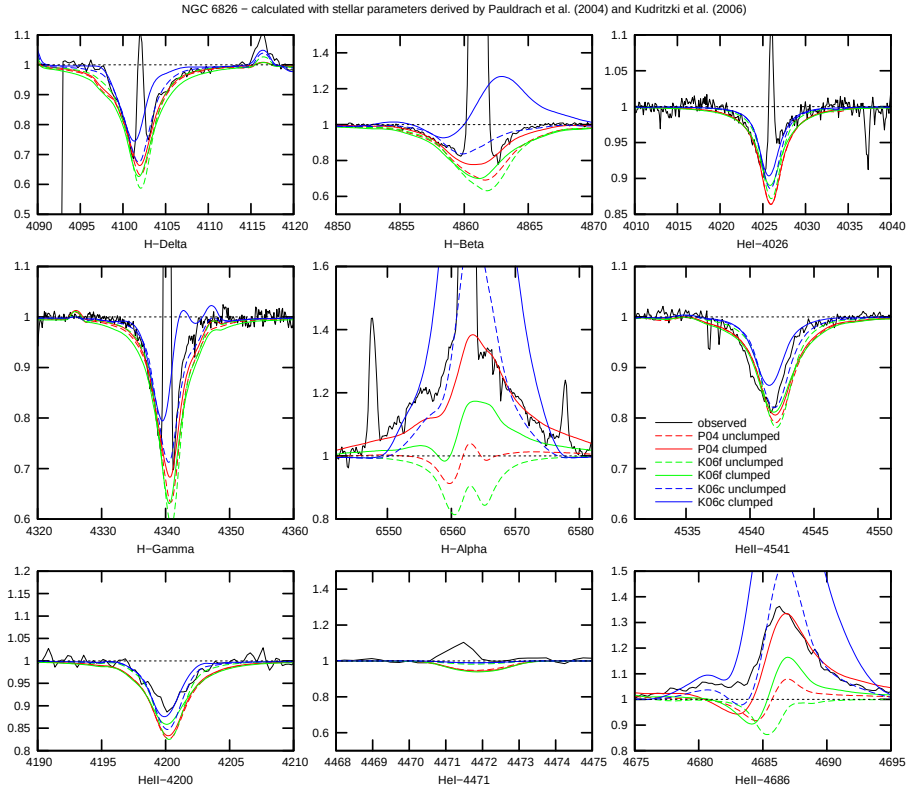

Figure 3.15: As Fig. 3.8, but for NGC 6826.

3.6.9 NGC 6826

NGC 6826 is the CSPN with the highest mass of the whole sample: for this star Pauldrach et al. (2004) derived a mass of $1.40\,M_{\odot}$, close to the Chandrasekhar limit for white dwarfs. With the clumping factor of $f_{\rm cl} = 4$ suggested by Kudritzki et al. (2006) the P04 model yields nearly perfect fits to *all* lines, including the emission lines H_{α} and He II λ 4686. This result is interesting as the *fitted* K06f model does not reproduce the strength of these emission lines (Fig. 3.15) with our computed density structure, yielding too little emission. For the absorption lines all models give equally good fits, except for the clumped K06c model, which produces too much emission in several absorption lines.

3.6.10 Clumping and the He II λ 1640 line

A number of CSPNs from our sample have a pronounced He II λ 1640 profile in the UV spectrum, which may be used to cross-check the diagnosed clumping factor from the optical He II λ 4686 line. In Fig. 3.16 (NGC 6826) and Fig. 3.17 (IC 418) we compare the observed UV spectra of two CSPNs to corresponding synthetic spectra from models including clumping. As we had already seen from the optical He II λ 4686 line profile of IC 418 that a clumping factor of $f_{\rm cl} = 50$ as suggested by Kudritzki et al. (2006) was too large to be compatible with the observations of this star, we have used a smaller clumping factor of $f_{\rm cl} = 4$ for the IC 418 model we show here.

The upper panel of each figure shows the synthetic spectrum from the unclumped model, the lower panel the synthetic spectrum from a model with identical parameters, but with clumping applied. As the plots clearly show, moderate clumping does not influence the generally good overall fit of the predicted spectra. In fact, most of the UV spectrum is unaffected by clumping, except for a few lines from subordinate ionization stages (such as P V, C III, and H I). In particular, clumping also enhances the occupation of He II (the main ionization stage of helium in the photosphere and most of the wind is He III) and leads to an almost perfect fit of the He II λ 1640 profiles.

That the UV spectrum of our stars is barely influenced by moderate clumping reflects the fact that the main ionization stages of the elements are not severely affected; the increased recombination in the denser clumps leads to a higher occupation of mostly the ionization stages below the main ionization stage, which usually have much smaller occupation numbers than the main ionization stage. As the main ionization stages, and not the subordinate ones, are the primary contributors to the line force, moderate clumping also has little influence on the hydrodynamics of the outflow, and thus on the consistency of the Pauldrach et al. (2004) stellar and wind parameters.

3.7 Summary and conclusions

Using the two mutually contradicting sets of stellar parameters published in the literature for a sample of CSPNs, we have presented new comparisons of observed and model spectra in order to provide further clues to the true parameters of the stars of this sample. Our comparisons not only include the extended spectral range of 905 to 1085 Å observed by FUSE in addition to the IUE spectral range of 1150 to 1980 Å and the optical lines, but also consider the available X-ray observations. They also include a treatment of wind clumping in the models, which in the literature has been considered to be essential to reproduce the observed optical emission lines.

The FUSE spectral range includes the wavelengths of the O VI resonance doublet. As O VI is known from massive O stars to be primarily produced by Auger ionization driven by X-rays origi-

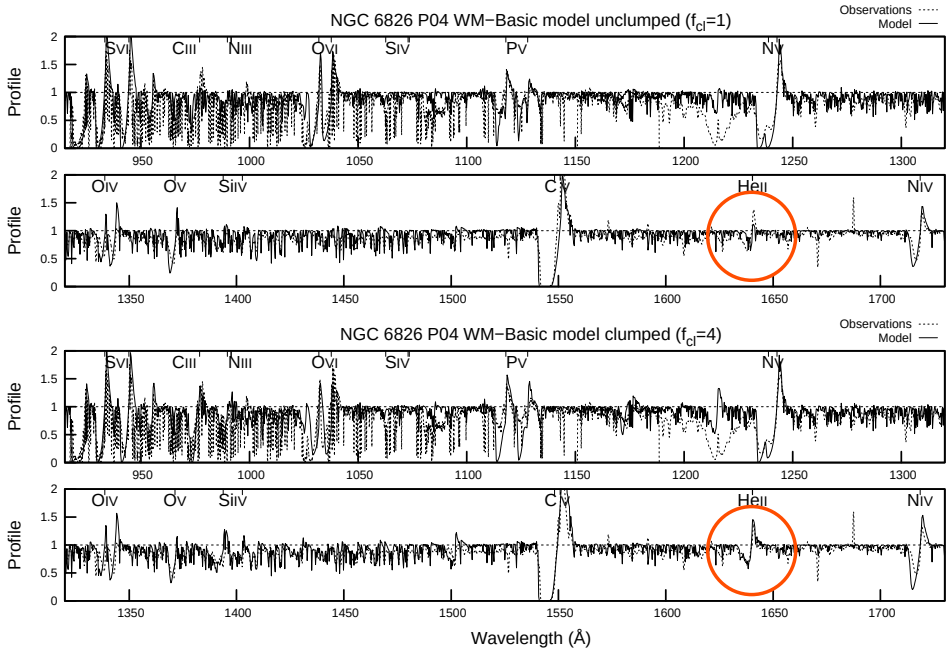

Figure 3.16: Synthetic UV spectrum of NGC 6826 calculated with the stellar parameters determined by the UV analysis, compared to the observed UV spectrum. The upper panel shows an unclumped model. The overall fit to the observed UV spectra is generally very good, although the He II λ 1640 line is not reproduced too well. The lower panel shows the same model, but with a clumping factor of $f_{\rm cl} = 4$. Most of the UV spectrum is not affected, except for a few lines from subordinate ionization stages (such as P V λ 1118, C III λ 977, and H I λ 1216). In particular the match to the observed He II λ 1640 line is now almost excellent.

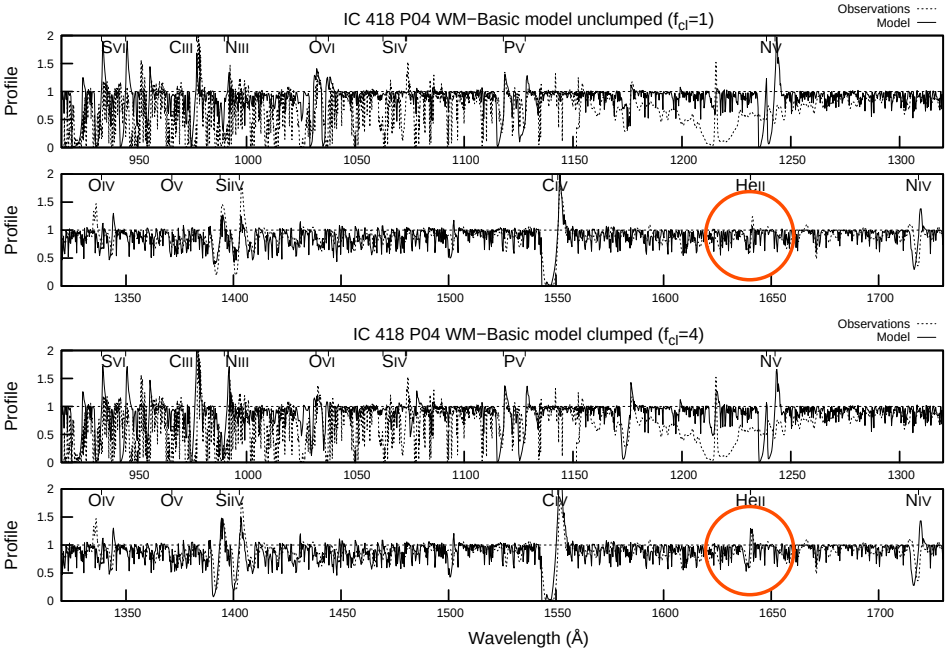

Figure 3.17: Same as Fig. 3.16, but for IC 418. The same conclusions apply.

nating from the cooling zones of shocks resulting from the unstable, non-stationary behavior of the winds, this line therefore represents a special diagnostic tool for wind-embedded shocks. The failure to reproduce the observed O VI line in the synthetic spectra of standard CSPN models strongly indicates that X-rays are an important ingredient in CSPN winds, and this information is also provided by X-ray observations that show O-type central stars of planetary nebulae as X-ray emitters. By applying the physics which describe this phenomenon in our CSPN simulations we could show that the synthetic spectra of our current best models reproduced the profile shapes of the O VI P-Cygni line almost perfectly. As an integral part of the modelling procedure we obtained the emitted frequency-integrated relative X-ray luminosities as well as the radial distribution of the maximum local shock temperatures in the cooling zones of the shock-heated matter component.

In a second step these values have been compared with those resulting directly from observations. 50% of the planetary nebulae observed by a recent Chandra survey are X-ray emitters, with both diffuse and point-like X-ray sources. A detailed measurement of the X-ray emission of one of the objects (NGC 2392) in our sample exists, which displays both a diffuse and a point-like component. The total measured X-ray emission is about a factor of two larger than the value we have deduced from our best-fit model for this CSPN. Thus our result is not only in accordance with the observations, but also with the interpretation of these observations. Moreover, the maximum shock temperatures we have derived are also in agreement with these current observations. The ratios of X-ray to bolometric luminosity we determined for the stars of our sample ($L_{\rm X}/L_{\rm bol} \sim 10^{-6} \ldots 10^{-7}$) are also typical for massive O stars, and are further confirmed by another observation which obtained a similar value for another CSPN not in our sample.

These similarities between massive O stars and O-type CSPNs justify using the same tools that had been applied successfully to the analysis of massive O star spectra also to O-type CSPNs. Indeed, the stellar parameters that had been determined from the UV analysis (Pauldrach et al. 2004) offer a consistent picture not only of the X-ray, the UV, and the optical spectral properties of CSPNs, but also of the wind-dynamical properties not directly related to the spectral appearance, such as the ratios $v_\infty/v_{\rm esc}$ of terminal wind velocity to stellar escape velocity (Kaschinski et al. 2012) and the agreement of the wind strengths with the wind-momentum–luminosity relation (WMLR).

This is in contrast to the stellar parameters that had been determined from the optical line profiles with the aid of the theoretical mass-luminosity relation of CSPNs predicted by current post-AGB evolutionary models (Kudritzki et al. 2006). The spectra from models using these parameters and consistently calculated wind dynamics reproduce the observations not at all. Furthermore, for a number of stars in the sample these stellar parameters lead to anomalously high $v_\infty/v_{\rm esc}$ ratios. From this we conclude that the published optical analyses give good fits to the observed spectra only because the wind parameters assumed in these analyses were inconsistent to their stellar parameters.

Although a complete set of stellar parameters can be determined for O-type central stars with expanding atmospheres just from the wind-sensitive features in the UV, a comparison which also includes the H and He lines of the optical spectra has, as a combined analysis, a more convincing character. To establish such a procedure, we had already improved our stellar atmosphere code WM-basic by including Stark broadening in order to describe the optical lines in a more realistic way. A still open issue, however, were the fits to the optical recombination lines H_α and He II λ 4686, whose emission could not be fully reproduced. As the current consensus appears to be that these lines are influenced by clumping in the winds, we reinvestigated these lines via a comparison of clumped and unclumped models for our chosen CSPN sample.

We have tested our implementation of clumping by a comparison with FASTWIND, the code orig-

inally used in the optical analyses to model the line profiles and determine the stellar parameters $T_{\rm eff}$ and $\log g$ as well as the mass loss rates $\dot{M}$. For the same density structure our code WM-basic yields almost identical line profiles as FASTWIND. For those CSPNs with emission lines in the optical, moderate clumping factors increase the emission and provide good fits to the observed line profiles when using the parameters of Pauldrach et al. (2004), thus supporting their parameter determination. The stellar parameters of Kudritzki et al. (2006) together with consistent wind parameters, on the other hand, gave line profiles that were not compatible with the observed line profiles.

When artificially forcing our models to use the mass loss rates of Kudritzki et al. (2006) with their stellar parameters, the fits were better than with the consistent mass loss rates and terminal velocities but not as good as those of Kudritzki et al. (2006). This is because our WM-basic code computes the density structure from a solution to the equation of motion balancing gravity and gas and radiation pressure, instead of simply parametrizing the velocity law. Thus, Kudritzki et al. (2006) could achieve good fits to the optical line profiles only by also assuming an unrealistic density structure that was not compatible with their stellar parameters. A realistic, consistent density and velocity structure with these stellar parameters yields profiles incompatible with the observations and thus rules out these stellar parameters. Thus, lines whose model profiles are determined primarily by a cosmetic clumping factor and not the underlying physics of the model completely lose their diagnostic value, and the quality of the fit of these lines says nothing about the reliability of the fundamental model parameters if the model is already based on an unrealistic density structure.

Our general finding that the observable quantities of the X-ray to bolometric luminosity ratios ($L_{\rm X}/L_{\rm bol} \sim 5 \times 10^{-7}$) and the maximum shock temperatures ($T_{\rm shock}^{\rm max} \sim 10^6$ K) have similar values for all CSPNs of the sample is consistent with our finding that the clumping factors are also similar, with a typical value of $f_{\rm cl} \sim 4$. This is an important result, since it shows that the apparently erratic character of the clumping factors seen in the optical analyses vanishes if the calculations are based on consistent sets of stellar and wind parameters. As an erratic behavior of the clumping factors is not to be expected from our knowledge of shocks arising from the radiative wind driving mechanism, this result supports the legitimate assumption that the clumping factors must be correlated with the other observables of the shock physics.

In this context we also showed that the UV spectrum of our stars is almost unaffected by moderate clumping, and the addition of clumping to the model does not worsen the generally good overall fit of our spectra previously predicted without clumping. Only a few lines from subordinate ionization stages are affected by clumping, among those the subordinate He II λ 1640 line for which we now achieve an almost perfect fit. That in this CSPN sample the UV spectrum is barely influenced by moderate clumping reflects the fact that the main ionization stages of the elements are not severely affected, and thus clumping has only a small influence on the line force and the hydrodynamics of the outflow, and therefore on the consistency of the dynamically determined stellar and wind parameters.[15] Thus, in a model that properly implements the physics of radiation driven winds a good fit to the observations can only be achieved with a proper choice of stellar parameters.

[15] The quality of the UV fit ascertains the quality of the determined stellar parameters and the hydrodynamical structure because the radiative acceleration is calculated analogously to and along with the synthetic spectrum. The accuracy of the calculation of the radiative acceleration is therefore of the same quality as that of the synthetic spectrum, and this means that the velocity field and the mass loss rate, which thus become direct functions of the basic stellar parameters, are as realistic as the obtained synthetic spectrum.

Chapter 4

Effects of shocks in stellar atmosphere models on the emission line spectrum of surrounding H II regions

The contents of this chapter will be published in Kaschinski et al. (2013b), MNRAS.

Abstract. Emission line studies from H II regions in our own and other galaxies require tools for the inversion of line ratios into desired physical properties. These tools generally come in the form of diagnostic ratios/diagrams that are based on grids of photoionisation models. An important input to the photoionisation models is the stellar atmosphere spectrum of the ionising sources. Among a number of potentially problematic biases introduced by a great deal of unknown variables in both the stellar atmosphere and nebular models, the current omission of shocks in the calculation of the former set of models could also threaten the accuracy of the physical interpretation of emission line ratios from H II regions. Current stellar atmosphere models that are crucial inputs to the grid of photoionisation models used to generate nebular emission line diagnostic diagrams might produce significant biases due to the omission of shocks. We therefore investigate whether a new generation of photoionisation model grids, taking shocks into account, is required to compensate for the biases. We make use of the WM-Basic stellar atmosphere code, which can account for the extra energetic emission in the stellar spectral energy distribution produced by shocks, in conjunction with the photoionisation code MOCASSIN to determine whether shocks produce significant biases in the determination of the physical parameters of the interstellar medium and/or ionising stellar parameters. We conclude that these effects are only important for stellar sources with effective temperatures lower than 30kK and in this case they yield artificially high stellar temperatures, electron temperatures and nebular ionisation parameters. The magnitude of the effect is also obviously dependent on the strength of the shock and is likely to be unimportant for the majority of stellar sources. Nevertheless, we find our 20kK and 30kK shock models to strongly enhance the He II λ4686 nebular emission line (next to many other lines). This result could explain previously observed He II λ4686 line emission in the spectra of H II galaxies.

4.1 Introduction

Strong emission lines in the spectra of H II regions powered by hot massive stars are a powerful tool to study the interstellar medium properties in our own and other galaxies. Numerous studies use a combination of strong lines for the determination of abundance gradients in galaxies, which are a crucial constraint for chemical evolution models. The properties of the ionising stars can also be inferred through the analysis of the nebular emission spectrum, with implications on fundamental correlations, such as the relation of stellar effective temperatures and hardness of stellar spectrum and with galactocentric distance/metallicity (e.g. Campbell et al. (1988), Martín-Hernández et al. (2002), Giveon et al. (2002), Dors & Copetti (2003)). The diagnostic potential of nebular emission lines is however somewhat limited by a number of biases and uncertainties introduced by the need of relying on photoionisation models for their interpretation (e.g. Stasińska 2010). In general, the inversion of line ratios to physical parameters is performed via diagnostic diagrams based on large grids of photoionisation models. Such diagrams exist for a number of important nebular diagnostics in the optical and in the mid-infrared (e.g. Morisset et al. 2004), but their accuracy is limited by a number of necessary assumptions used in the photoionisation models (e.g. gas geometry and spatial distributions of the ionising sources, Ercolano et al. (2007, 2008)) and on the stellar atmosphere models used as inputs in the photoionisation models. Morisset et al. (2004) and Simón-Díaz & Stasińska (2008) present extensive comparative studies of different stellar atmosphere codes and the effects on nebular emission line diagnostic diagrams, discussing also the error implied for the determination of gas and stellar parameters.

In addition to the well known biases and uncertainties already pointed out by the studies above, the neglect of shocks[1] in stellar atmosphere calculations presents a further threat to the interpretation of nebular emission lines via the application of model grids. The general effect of shocks in the calculation is the production of a somewhat harder stellar spectrum for the same nominal stellar effective temperature. Indeed, the importance of accounting for the effect of shocks in the calculations of stellar atmosphere wind models was already introduced by Lucy & Solomon (1970) who found that radiation driven winds are inherently unstable. The emergent X-rays from a star were then described by Lucy & White (1980) and Lucy (1982) as a radiative loss of post-shock regions where shocks are propelled by non-stationary features in the wind structure. The primary effect of these shocks in general affects the ionisation equilibrium in the stellar atmosphere with regard to the high ionisation stages like $N\,v$, $O\,vi$ and $S\,vi$. The detection of those high ionisation stages in wind spectra was referred to as the so called "superionisation" problem (cf. Snow & Morton 1976), which could be well accounted for by a first, simplified description of the shock theory. The implementation of shocks in the stellar atmosphere code WM-Basic and an application on one of the best known massive O stars ζ Puppis was presented by Pauldrach et al. (1994) with encouraging results concerning the modeling of the $O\,vi$ line. During their study, Pauldrach et al. (1994) also found that shock emission surprisingly has a non-negligible influence at radio (10%) and IR (30%) wavelengths. In their first approach, Pauldrach et al. (1994) assumed a simplified shock description. The characterization of the shock emission is thereby mainly based on an immediate post-shock temperature which means non-stratified, isothermal shocks are considered. An improved version of WM-Basic was published by Pauldrach et al. (2001), implementing a cooling structure with a certain range of shock temperatures. This was done by adding a spatial fragmentation of the shock structure. The inner region of the stellar wind consists of radiative shocks

[1] Shocks are understood as EUV and X-ray radiation produced by cooling zones that are based on shock heated matter which in turn is the result of the non-stationary, unstable behavior of radiation driven winds.

(cf. Chevalier & Imamura 1982) where the cooling time is shorter than the flow time. In the outer region on the other hand, the velocity structure reaches its stationary value, i.e. the terminal velocity. This leads to a negligible radiative acceleration and hence a large flow time. The cooling processes can thus be approximated by adiabatic expansion (Simon & Axford 1966). An already modified approach of isothermal wind shocks by Feldmeier et al. (1997) was used for implementation in WM-Basic. The improved code yielded again almost perfect fits of the highly ionised elements in the observed spectrum of ζ Puppis. The improved code yields a much more efficient radiation of shocks in the soft X-ray spectral band. A comparison to the observed ROSAT PSPC spectrum showed fits of at least the same quality as those obtained by Feldmeier et al. (1997). During the same study Pauldrach et al. (2001) also presented an analysis of the supergiant α Cam which was based on their improved shock method. The resulting model matched the UV observations almost perfectly. Further observational investigations regarding the detection of X-rays from O stars were performed by Sana et al. (2005) and Sana et al. (2006) for the rich O-type star cluster NGC 6231 and by Albacete Colombo et al. (2003) for the Carina nebula field. The observational data for the two studies have been both obtained by the XMM-Newton satellite. The observations revealed several hundred X-ray sources[2] for the NGC 6231 cluster and 80 discrete ones for the Carina nebula.

The shock enhanced emission of the stellar atmosphere models is also relevant for the ionisation of a number of abundant species in nebular gas surrounding hot stars. It is therefore important to ask the question of whether the current neglect of shocks in the stellar atmosphere models used as inputs to the grid of photoionisation models used by nebular emission line diagnostic diagrams would produce significant biases, and therefore whether a new generation of photoionisation model grids should be calculated.

In this paper we use the stellar atmosphere code WM-Basic (Pauldrach et al. 2001) and the photoionisation code MOCASSIN (Ercolano et al. 2003, 2004, 2005) to investigate the effects of shock-enhanced stellar spectral energy distributions on the emission line spectra of H II regions. In particular we investigate the bias introduced on the determination of gas ionisation parameters, metallicities and stellar effective temperatures from common nebular emission line diagnostics. While a subset of the stellar atmosphere calculations are discussed in this work, we have also calculated a bigger library which includes a larger range of stellar temperatures. This is provided online for use with the photoionisation code MOCASSIN.

A brief description of the methods employed in this paper, including a description of the numerical codes is given in Section 4.2. The effects on nebular diagnostics as calculated by the photoionisation models are discussed in Section 4.3. Section 4.4 consists of a brief summary of our results and main conclusions.

4.2 Methods

The unstable, non-stationary behavior of stellar atmosphere winds produces shock cooling zones. As a consequence, these cooling zones radiate X-rays which can be observed. This has been studied for a variety of objects. The massive O star ζ Puppis and the supergiant α Cam have been investigated by Pauldrach et al. (2001) who obtained values for the total X-ray luminosity of $log(L_X/L_{bol}) = -7.1$ and $log(L_X/L_{bol}) = -6.5$, respectively. Sana et al. (2005) and Sana et al. (2006) presented an analysis of the young open cluster NGC 6231 and derived for the contained O stars an X-ray luminosity value of

[2] A smaller fraction of which are O stars.

$log(L_X/L_{bol}) \approx -7.0$. They also reviewed the Carina nebula field observations presented by Albacete Colombo et al. (2003). On the bases of their analysis, Sana et al. (2006) rederived for the observed O stars a value of $log(L_X/L_{bol}) \approx -6.2$ for the integrated X-ray luminosity. For our computed models we have therefore chosen similar parameter values which are thus representative of the real situations. We have run a grid of 16 stellar atmosphere models using the WM-Basic code in shock and no-shock mode for stellar effective temperatures in the range of 20kK to 50kK in steps of 10kK for a surface gravity of log g = 3.9 and a temperature range of 60kK to 90kK also in steps of 10kK for a surface gravity of log g = 4.9. All models, i.e. shock as well as no-shock, use solar abundances. The parameters for the shock models are:

- v_t/v_∞: The jump velocity v_t is the immediate post-shock temperature normalized to the terminal velocity v_∞. v_t was set to 0.25 in units of the terminal velocity v_∞.
- *X-ray luminosity*: The X-ray luminosity is normalized to the bolometric luminosity ($log(L_X/L_{bol})$). We used a value of -6.5.
- *Parameter m*: The parameter m controls the onset of shocks. It is defined as the ratio of outflow to sound velocity where shocks start to form. A direct correlation of jump velocity to outflow velocity reflects a dependency to the radius. This means via this parameter it can be controlled where shocks start to form in the wind, e.g. higher values for m enables shocks for outer regions but leaves inner regions mainly undisturbed. m = 1 was adopted enabling shocks in the whole atmosphere.
- *Stratification exponent* γ: γ controls the strength of the shocks depending on the local velocity $v(r)$. It is set to 1 for all simulations, which means a linear dependency on the local velocity.

The models were formatted for easy use in the MOCASSIN code and are freely downloadable from www.3d-mocassin.net. For our grid of effective temperatures and surface gravities a radius of 2.2 solar radii $R_\odot$ was assumed for all shock and no-shock models. The models were used as input to the MOCASSIN photoionisation code. The photoionisation models were set up as to simplify the configuration as much as possible in order to easily isolate the effects of shocks on the physical conditions in the nebular gas. The set up is very similar to that employed in the Meudon-Lexington benchmark models (Péquignot et al. 2001) and assume spherical geometry and homogeneous gas distributions. The input ionising flux is set to the output of the stellar atmosphere calculations and is given in Table 4.1. This corresponds to models with mean ionisation parameters log (U) = -2.6, -2.4 and -2.2 respectively for $T_{\rm eff}$ = 20, 30 and 40kK. The outer radius of the photoionisation models were adjusted to the nebular Strömgren radius. The set up parameters are as follows:

- *Formatted WM-Basic spectrum*: Emergent synthetic spectrum (Flux of the star [$\AA$]) up to a wavelength of 1×10^5 $\AA$.
- $T_{\rm eff}$: The effective stellar temperature of the WM-Basic model in Kelvin.
- L_{phot}: The number of ionising photons of the central star computed in a range up to a wavelength of 1×10^5 $\AA$.

A list of all the MOCASSIN model input parameter values for the shock and no-shock models in the temperature range of 20kK to 40kK is shown in Table 4.1. The models with higher temperatures

Input Parameter	20 $[10^3K]$		30 $[10^3K]$		40 $[10^3K]$	
	ns	s	ns	s	ns	s
Temperature [K]	20000		30000		40000	
log(U)	-2.6		-2.4		-2.2	
$Q_{13.6}$	$3.0e^{47}$	$3.0e^{47}$	$1.2e^{48}$	$1.2e^{48}$	$3.0e^{48}$	$3.0e^{48}$
r_{stroem} [cm]	$3.1e^{17}$	$3.1e^{17}$	$5.0e^{17}$	$5.0e^{17}$	$6.7e^{17}$	$6.7e^{17}$

Table 4.1: MOCASSIN input parameter values. $r_{stroemgren}$ is the Strömgren radius and $Q_{13.6}$ the number of ionising photons of the model. Both quantities have been calculated using the ionising flux of the corresponding WM-Basic model up to a wavelength of 1×10^5 $\AA$. The ionisiation parameters log(U) (see section 4.3) have been calculated according to the corresponding temperatures, ionising photons $Q_{13.6}$ and Strömgren radii r_{stroem} of each model.

than 40kK of our calculated grid are not listed since the effects of shocks are only of significance for low temperature stars. All models use a hydrogen density of 3000 $[cm^{-3}]$.

4.2.1 WM-Basic

In this manuscript we will only give a short overview of the general concept and computational steps which are performed by WM-Basic. A more detailed description of the concept and all its contained fundamental methods are shown in the corresponding code publications by Pauldrach et al. (1994), Pauldrach et al. (1994), Pauldrach et al. (1998) and Pauldrach et al. (2001).

WM-Basic provides the diagnostic tool to construct detailed atmospheric models and synthetic spectra for hot luminous stars. The concept is based on homogeneous, stationary and spherically symmetric radiation driven winds. The driving mechanism of the expanding atmospheres lies in the line absorption and scattering of Doppler-shifted metal lines (Lucy & Solomon (1970)). The model code is constituted by three main blocks:

i) *The hydrodynamics*: In a first step the hydrodynamics is solved. The input values are the effective temperature $T_{\rm eff}$, the logarithm of the photospheric gravitational acceleration $log\ g$, the photospheric radius R_* and the abundances Z in units of the corresponding solar values. For each line the oscillator strength f_{lu}, the statistical weights g_l, g_u and the occupation numbers n_l, n_u of the lower and upper levers have to be computed. The hydrodynamics is then solved by iterating the complete continuum force $g_c(r)$, the temperature structure (assuming in both cases a spherical grey model), the density structure $\rho(r)$ and the velocity structure $v(r)$.

ii) *NLTE-model*: During this step the radiation field $H_\nu(r) = 4\pi F_\nu(r)$, the mean intensity $J_\nu(r)$ and the final NLTE temperature structure $T(r)$ (determined by the energy equation and line blanketing effect which reflects the influence of line blocking on the temperature structure) are calculated. All opacities χ_ν and emissivities η_ν using detailed atomic models are computed along with the occupation numbers for all relevant levels. Solving the spherical-transfer equation correctly for all total opacities (κ_ν) and source functions (S_ν) yields the radiation field. A revised treatment of shocks is included and expressed by the shock source function (S_ν^S).

iii) *Solution of the formal integral and computation of the synthetic spectrum*: in a final step the synthetic spectrum is computed. This is done by performing a formal integral solution of the

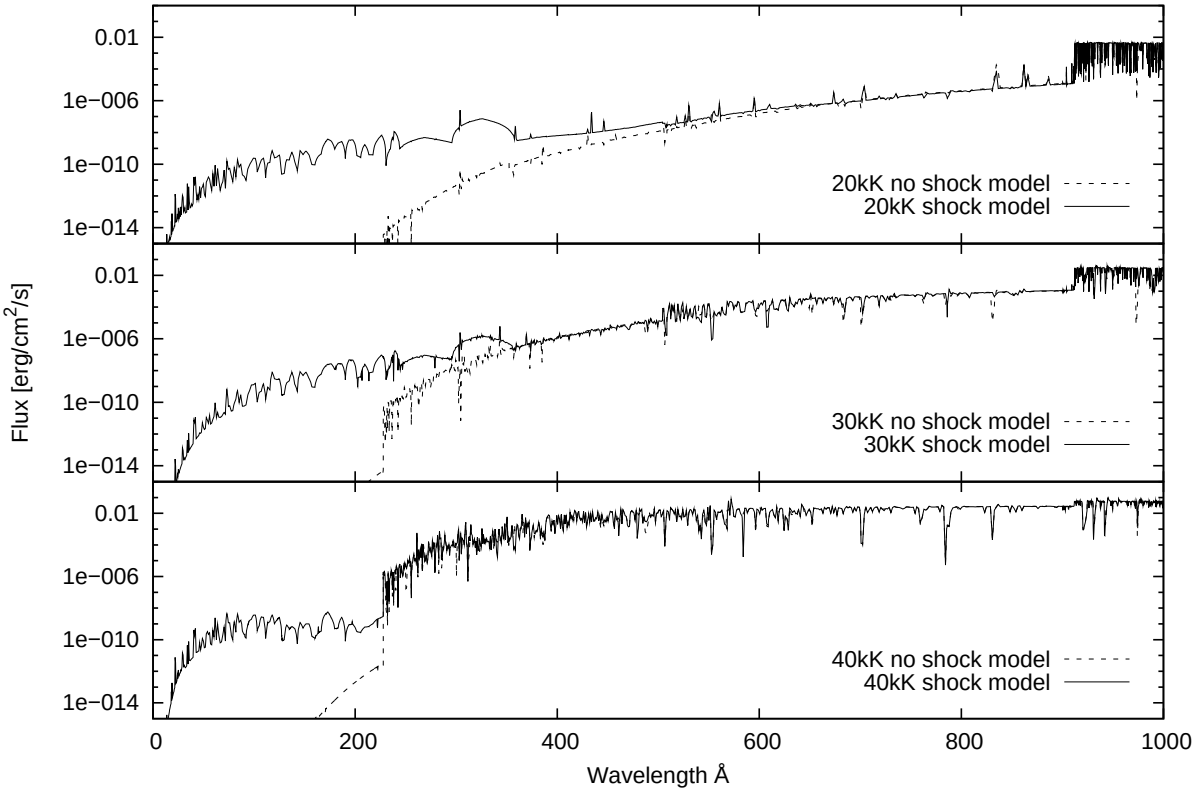

Figure 4.1: Ionising flux of our three models ranging in the effective temperatures from 20kK (top panel) to 40kK (bottom panel). Each panel shows one of the three models, computed once including shocks (solid line) and once neglecting shocks (dashed line). The comparison shows the non-negligible influence of shocks on the ionising flux.

transfer equation in the observer's frame. The synthetic spectrum is then compared to the observations, if available.

The three blocks form a coupled system and therefore an iterative solution is required. Next to a synthetic model spectrum, the ionising fluxes and a hydrodynamical structure of the wind are calculated enabling the derivation of the mass-loss rate $\dot{M}$ and the velocity field $v(r)$ which characterize the wind features.

4.2.2 MOCASSIN

The 3-dimensional Monte Carlo photoionisation code Mocassin (version 2.02.67), employed for the calculation of the nebular electron temperature, ionisation structure and emission line spectrum, is described in detail by Ercolano et al. (2003, 2005, 2008). The basic structure of the code is summarised briefly here. MOCASSIN employs a Monte Carlo approach to the transfer of radiation allowing the treatment of primary and secondary diffuse fields exactly for arbitrary geometries and density distri-

butions. The code includes all the major microphysical processes that influence the gas ionisation balance and the thermal balance of dust and gas, including processes that couple the gas and dust phases. In the case of H II regions ionised by OB stars the dominant heating process for typical gas abundances is hydrogen photoionisation, balanced by cooling by collisionally excited (generally forbidden) line emission (dominant), recombination line emission, free-bound and free-free continuum emission. The atomic database includes opacities from Verner et al. (1993) and Verner & Yakovlev (1995), energy levels, collision strengths and transition probabilities from Version 5.2 of the CHIANTI database (Landi et al. 2006, and references therein) and hydrogen and helium free-bound continuous emission data of Ercolano & Storey (2006). Arbitrary ionising spectra can be used as well as multiple ionisation sources whose ionised volumes may or may not overlap, with the overlap region being self-consistently treated by the code.

4.3 Results

We compared the resulting lines for our no-shock to shock models for the stellar atmosphere models of temperatures ranging from 20kK to 50kK in steps of 10kK. Tables 4.2 and 4.4 show all lines of He I, He II and the heavier elements of these runs where the differences in the line strengthes between the no-shock and shock runs are larger then 20%. As can be seen from the table only models with a temperature of 20kK and 30kK show differences. Models for higher temperatures do only show differences between no-shock to shock models which are smaller than 20% and are therefore not listed. In what follows, we used these lines to deduce physical properties of the ionising stellar source and of the nebular gas.

Table 4.2: He I and He II nebular line strengthes corresponding to the stellar source models with effective temperatures of 20kK and 30kK. Both models have been calculated in no-shock 'ns' and shock 's' mode. Only lines which show differences larger than 20% are shown. The dash '-' appearing for some lines means differences in the line strength which are smaller than 20% for this particular line and are not listed. For stellar atmosphere models with a temperature of 30kK only the He II λ1640 and He II λ4686 lines show a large enough difference in the line strength between the no-shock and shock model. There are no differences in the line strength larger than 20% for models with higher temperatures than 30kK which are therefore not listed.

Line	20 $[10^3 K]$		30 $[10^3 K]$	
	ns	s	ns	s
[He I] 4473 Å	1.501×10^{-4}	2.249×10^{-3}	-	-
[He I] 2946 Å	5.348×10^{-5}	8.204×10^{-4}	-	-
[He I] 3189 Å	1.121×10^{-4}	1.715×10^{-3}	-	-
[He I] 3615 Å	1.407×10^{-5}	2.153×10^{-4}	-	-
[He I] 3890 Å	2.813×10^{-4}	4.308×10^{-3}	-	-
[He I] 3966 Å	2.900×10^{-5}	4.428×10^{-4}	-	-
[He I] 4027 Å	6.741×10^{-5}	1.020×10^{-3}	-	-
[He I] 4122 Å	$< 1 \times 10^{-5}$	6.593×10^{-5}	-	-

continued on next page

continued from previous page

Line	20 $[10^3 K]$		30 $[10^3 K]$	
	ns	s	ns	s
[He I] 4389 $\AA$	1.794×10^{-5}	2.713×10^{-4}	-	-
[He I] 4439 $\AA$	$< 1 \times 10^{-5}$	2.985×10^{-5}	-	-
[He I] 4473 $\AA$	1.501×10^{-4}	2.249×10^{-3}	-	-
[He I] 4715 $\AA$	1.134×10^{-5}	1.760×10^{-4}	-	-
[He I] 4923 $\AA$	4.021×10^{-5}	6.043×10^{-4}	-	-
[He I] 5017 $\AA$	7.453×10^{-5}	1.136×10^{-3}	-	-
[He I] 5049 $\AA$	$< 1 \times 10^{-5}$	7.198×10^{-5}	-	-
[He I] 5877 $\AA$	4.460×10^{-4}	6.625×10^{-3}	-	-
[He I] 6680 $\AA$	1.277×10^{-4}	1.904×10^{-3}	-	-
[He I] 7067 $\AA$	5.592×10^{-5}	8.816×10^{-4}	-	-
[He I] 7283 $\AA$	1.731×10^{-5}	2.687×10^{-4}	-	-
[He I] 9466 $\AA$	$< 1 \times 10^{-5}$	4.539×10^{-5}	-	-
[He I] 1.08 μm	1.072×10^{-3}	0.017	-	-
[He I] 1.20 μm	$< 1 \times 10^{-5}$	1.029×10^{-4}	-	-
[He I] 1.25 μm	$< 1 \times 10^{-5}$	5.491×10^{-5}	-	-
[He I] 1.28 μm	2.597×10^{-5}	3.867×10^{-4}	-	-
[He I] 1.28 μm	$< 1 \times 10^{-5}$	1.291×10^{-4}	-	-
[He I] 1.30 μm	$< 1 \times 10^{-5}$	3.443×10^{-5}	-	-
[He I] 1.51 μm	$< 1 \times 10^{-5}$	2.353×10^{-5}	-	-
[He I] 1.70 μm	$< 1 \times 10^{-5}$	1.487×10^{-4}	-	-
[He I] 1.87 μm	6.520×10^{-5}	9.608×10^{-4}	-	-
[He I] 1.90 μm	2.169×10^{-5}	3.205×10^{-4}	-	-
[He I] 1.91 μm	$< 1 \times 10^{-5}$	5.587×10^{-5}	-	-
[He I] 1.96 μm	$< 1 \times 10^{-5}$	3.201×10^{-5}	-	-
[He I] 2.06 μm	1.005×10^{-4}	1.541×10^{-3}	-	-
[He I] 2.11 μm	$< 1 \times 10^{-5}$	2.687×10^{-5}	-	-
[He II] 1025 $\AA$	$< 1 \times 10^{-5}$	2.312×10^{-4}	-	-
[He II] 1084 $\AA$	$< 1 \times 10^{-5}$	4.259×10^{-4}	-	-
[He II] 1215 $\AA$	$< 1 \times 10^{-5}$	9.554×10^{-4}	-	-
[He II] 1640 $\AA$	$< 1 \times 10^{-5}$	3.160×10^{-3}	$< 1 \times 10^{-5}$	2.380×10^{-4}
[He II] 2734 $\AA$	$< 1 \times 10^{-5}$	1.018×10^{-4}	-	-
[He II] 3204 $\AA$	$< 1 \times 10^{-5}$	1.976×10^{-4}	-	-
[He II] 4686 $\AA$	$< 1 \times 10^{-5}$	4.880×10^{-4}	$< 1 \times 10^{-5}$	3.676×10^{-5}
[He II] 10126 $\AA$	$< 1 \times 10^{-5}$	1.344×10^{-4}	-	-

4.3.1 Effects of shocks on the stellar spectral energy distribution

Figure 4.1, compares shock (solid line) and no-shock models (dashed line) for stellar atmosphere models of temperatures 20kK (upper panel), 30kK (middle panel) and a 40kK (lower panel) with a log g of 3.9. Shock parameters are as discussed in section 4.2.

As shown in Fig. 4.1, shocks produce extra emission in the range short of approximately 500 $\AA$ for all models. However, stars with temperatures in excess of 30kK already radiate a significant fraction of their bolometric luminosity in this range thus diminishing the effects of shocks. For hotter stars the shock effects are completely washed away.

The computed spectral energy distribution of stars with temperatures of 20kK is however visibly affected by the inclusion of shocks, providing an excess of photons at energies able to ionise some common ionic species found in H II regions. As a consequence, for these lower temperature stars, one would expect a different nebular ionisation structure resulting for photoionisation models that employ shock stellar atmosphere models as energy sources. This would also be reflected in the nebular emission line spectrum from the different models as will be discussed in the next section.

4.3.2 Implications for nebular line diagnostics of stellar effective temperature

The ionisation parameter of an ionised nebular gas can be defined as $U = Q_{13.6}/(n_H \cdot 4\pi r^2 c)$ (where $Q_{13.6}$ is the number of ionising photons per second produced by the central star, n_H is the hydrogen number density, r is the Strömgren radius and c is the speed of light) and effectively provides a measure for the number of photons that are available to ionise a given pocket of gas at a given location in the nebula. Evans & Dopita (1985) define a mean $\overline{U} = U(\bar{r})$ where $\bar{r}$ is a mean distance from the ionising source. This quantity can be useful to get a handle on the level of ionisation of the gas. A number of empirical methods have been developed to estimate $\overline{U}$ and T_{eff} from ratios of strong nebular emission lines, and one of the most commonly employed ones is based on a combination of ratios of the infrared lines [S IV]λ10.5μm/[S III]λ18.7μm and the [Ne III]λ15.5μm/[Ne II]λ12.8μm, via the η_{S-Ne} parameter as used by Morisset et al. (2004) based on the original definition by Vilchez & Pagel (1988). The η_{S-Ne} parameter is defined as

$$\eta_{S-Ne} = [S\,IV/III]/[Ne\,III/II] \tag{4.1}$$

where [S IV/III] =[S IV]λ10.5μm/[S III]λ18.7μm and [Ne III/II] = [Ne III]λ15.5μm/[Ne II]λ12.8μm.

Table 4.3 shows the ratios computed by our photoionisation models for input stellar atmospheres with and without shocks labeled 's' and 'ns', respectively. These ratios and the resulting η_{S-Ne} parameter are then shown in Figure 4.2 and compared with the grid of photoionisation models presented by Morisset et al. (2004) (black solid and dashed lines), for log(U) = -1, -2 and -3 at stellar effective temperatures T_{eff} = 35kK (circles), 40kK (triangles) and 45kK (diamonds).

Before we move on to the interpretation of the effect of shocks on these diagnostics it is perhaps worth noticing here that the difference between the location of our non-shock 40kK point from that of the Morisset et al. (2004) model with similar ionisation parameter is understandable due to the different input parameters used in this work for the stellar atmosphere code and for the photoionisation code. We stress that the aim here is not to benchmark our models to this previous work, rather the Morisset et al. (2004) tracks are only shown in order to illustrate the direction in which changes in the ionisation parameter and effective temperature affect the diagnostic diagram.

The net effect of shocks is to simulate a star of higher effective temperature and a higher ionisation parameter in the nebular gas as shown in Figure 4.2. These effects are however only important for

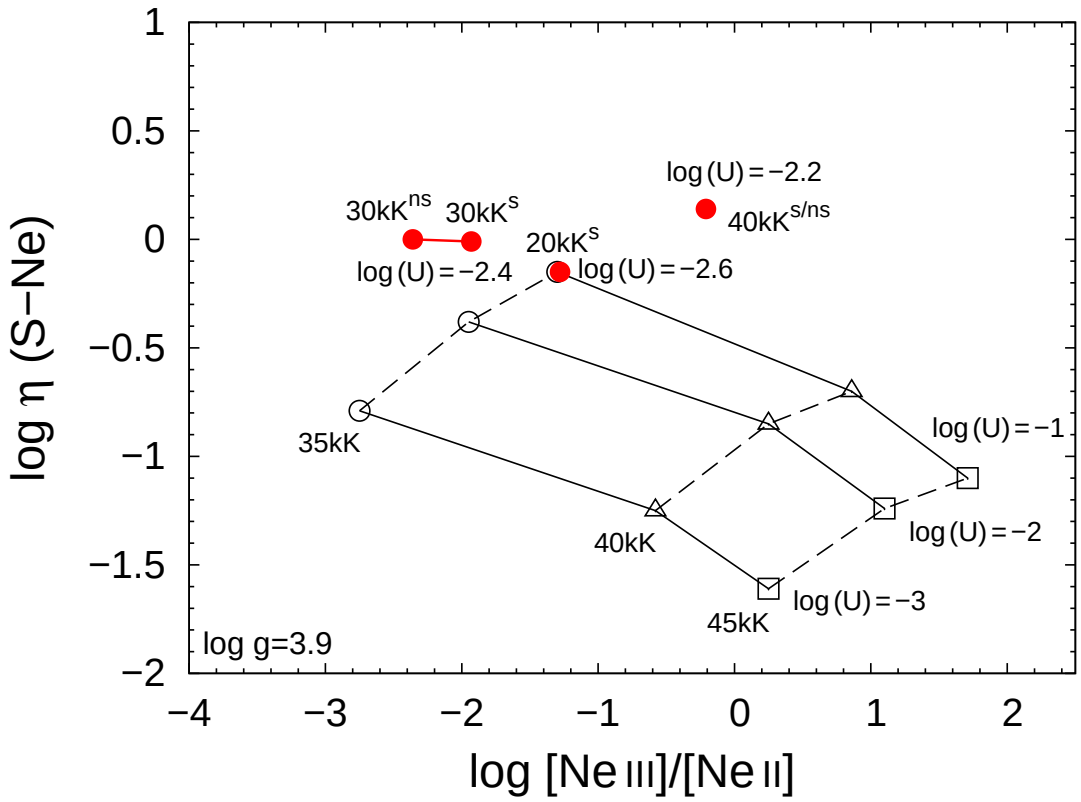

Figure 4.2: Resulting $\eta_{\mathrm{S-Ne}}$ parameter derived for the MOCCASIN models compared to the grid of photoionisation models presented by Morisset et al. (2004). Shown are the position of the corresponding parameter values for the shock and no-shock models labeled by the 's' and 'ns' exponent. Obviously there are no differences between the 40kK shock and no-shock model. The 30kK shock model compared to the 30kK no-shock model shows already small deviations. The 20kK no-shock model is not even depicted in the plot since the spectrum of a 20kK star is not hot enough to produce a significant population of doubly ionised neon or triply ionised sulfur. The 20kK shock model is located in a region expected to be populated by systems with roughly 30-35kK ionising stars.

cooler stars, indeed the 30kK shock case only shows a small deviation from the non-shock case, and no change at all is visible for the 40kK case. The effects on the 20kK case are, on the other hand, dramatic. The 20kK non-shock case is in fact not even shown on the diagram, since the spectrum of a 20kK star is not hot enough to produce a significant population of doubly ionised neon or triply ionised sulfur. The addition of shocks, however, does produce ionising photons in the required wavelength range, placing the 20kK shock model in a region of the diagnostic diagram expected to be populated by systems with roughly 30-35kK ionising stars and approximately a decade higher ionisation parameter.

Ratio	20 $[10^3K]$		30 $[10^3K]$	
	ns	s	ns	s
log([Ne III]/[Ne II])	-	-1.286	-2.365	-1.935
log([S IV]/[S III])	-	-0.896	-2.375	-1.881
log η	-	-0.157	0.002	-0.012

Table 4.3: MOCASSIN logarithmic ion ratios.

Line	20 $[10^3K]$		30 $[10^3K]$	
	ns	s	ns	s
[C II] 2325 $\AA$	4.654×10^{-4}	5.969×10^{-4}	2.337×10^{-3}	2.318×10^{-3}
[C II] 2324 $\AA$	4.924×10^{-4}	6.315×10^{-4}	2.337×10^{-3}	2.318×10^{-3}
[C II] 2329 $\AA$	5.504×10^{-4}	7.059×10^{-4}	2.337×10^{-3}	2.318×10^{-3}
[C II] 2328 $\AA$	1.507×10^{-3}	1.932×10^{-3}	2.337×10^{-3}	2.318×10^{-3}
[C II] 2326 $\AA$	2.969×10^{-3}	3.810×10^{-3}	2.337×10^{-3}	2.318×10^{-3}
[C III] 1909 $\AA$	$< 1 \times 10^{-5}$	1.742×10^{-5}	3.210×10^{-3}	2.437×10^{-3}
[C III] 1907 $\AA$	$< 1 \times 10^{-5}$	2.277×10^{-5}	2.422×10^{-3}	1.842×10^{-3}
[N I] 5199 $\AA$	3.745×10^{-5}	5.843×10^{-5}	-	-
[N I] 5202 $\AA$	1.532×10^{-5}	2.403×10^{-5}	-	-
[N II] 2140 $\AA$	7.093×10^{-5}	9.330×10^{-5}	-	-
[N II] 2143 $\AA$	1.749×10^{-4}	2.300×10^{-4}	-	-
[N III] 1750 $\AA$	-	-	1.857×10^{-5}	1.290×10^{-5}
[N III] 57.3 μm	$< 1 \times 10^{-5}$	4.020×10^{-3}	-	-
[O I] 6302 $\AA$	4.324×10^{-3}	6.569×10^{-3}	-	-
[O I] 6366 $\AA$	1.383×10^{-3}	2.101×10^{-3}	-	-
[O I] 5579 $\AA$	1.088×10^{-5}	2.200×10^{-5}	-	-
[O III] 88.3 μm	$< 1 \times 10^{-5}$	6.919×10^{-3}	2.109×10^{-3}	4.980×10^{-3}
[O III] 51.8 μm	$< 1 \times 10^{-5}$	0.039	0.011	0.027
[O III] 4960 $\AA$	$< 1 \times 10^{-5}$	0.012	9.150×10^{-3}	0.019
[O III] 2322 $\AA$	-	-	$< 1 \times 10^{-5}$	1.581×10^{-5}
[O III] 5008 $\AA$	$< 1 \times 10^{-5}$	3.500	0.027	0.056
[O III] 1666 $\AA$	-	-	$< 1 \times 10^{-5}$	1.296×10^{-5}
[O III] 4363 $\AA$	$< 1 \times 10^{-5}$	1.592×10^{-5}	3.623×10^{-5}	6.283×10^{-5}
[O IV] 25.9 μm	$< 1 \times 10^{-5}$	2.564×10^{-3}	$< 1 \times 10^{-5}$	2.274×10^{-4}
[Ne II] 12.8 μm	0.497	0.616	-	-

continued on next page

continued from previous page

Line	20 $[10^3 K]$		30 $[10^3 K]$	
	ns	s	ns	s
[Ne III] 15.5 μm	$< 1 \times 10^{-5}$	0.032	3.664×10^{-3}	9.804×10^{-3}
[Ne III] 3870 $\AA$	$< 1 \times 10^{-5}$	8.971×10^{-4}	3.651×10^{-4}	8.213×10^{-4}
[Ne III] 36.0 μm	$< 1 \times 10^{-5}$	2.566×10^{-3}	3.004×10^{-4}	8.021×10^{-4}
[Ne III] 3969 $\AA$	$< 1 \times 10^{-5}$	2.703×10^{-4}	1.100×10^{-4}	2.474×10^{-4}
[Mg IV] 4.5 μm	-	-	$< 1 \times 10^{-5}$	1.737×10^{-5}
[Si II] 2335 $\AA$	8.767×10^{-5}	1.276×10^{-4}	-	-
[Si II] 2351 $\AA$	5.742×10^{-5}	8.355×10^{-5}	-	-
[Si II] 2345 $\AA$	2.642×10^{-4}	3.836×10^{-4}	-	-
[Si II] 2335 $\AA$	3.417×10^{-4}	4.942×10^{-4}	-	-
[S III] 33.5 μm	0.085	0.147	-	-
[S III] 12.0 μm	$< 1 \times 10^{-5}$	1.152×10^{-5}	-	-
[S III] 8831 $\AA$	1.264×10^{-4}	2.290×10^{-4}	-	-
[S III] 18.7 μm	0.160	0.277	-	-
[S III] 9070 $\AA$	0.015	0.027	-	-
[S III] 3722 $\AA$	1.121×10^{-4}	2.287×10^{-4}	-	-
[S III] 9532 $\AA$	0.085	0.153	-	-
[S III] 6314 $\AA$	1.982×10^{-4}	4.041×10^{-4}	-	-
[S IV] 10.5 μm	$< 1 \times 10^{-5}$	0.035	4.031×10^{-3}	0.012

Table 4.4: Resulting nebular line strengthes for all higher elements of the stellar source models with effective temperatures of 20kK and 30kK. Both models have been calculated in no-shock 'ns' and shock 's' mode. Only lines which show differences larger than 20% are shown. The dash '-' appearing for some lines means differences in the line strength which are smaller than 20% for this particular line and are not listed. This is also true for all lines of stellar atmosphere models for temperatures higher than 30kK which are therefore also not shown.

4.3.3 Implications for line diagnostics of electron temperature and density

The energy-level structure of some ions leads to the formation of emission lines from two different upper levels which have considerably different excitation energies. The relative rates of excitation to these levels depend strongly on the temperature and thus emission lines originating from them may be used to measure the electron temperature. We used the line ratios of the four lines [O III], [N II], [Ne III] and [S III] to deduce the electron temperatures for the no-shock and shock runs of our 20kK, 30kK and 40kK models. The line ratios are connected to the electron temperature via the following equations (see Osterbrock & Ferland 2006):

Line Ratio	20 $[10^3K]$		30 $[10^3K]$		40 $[10^3K]$	
	Derived electron temperatures [K]					
	ns	s	ns	s	ns	s
[O III]	5334.72	5544.08	6764.84	6529.89	7571.73	7578.90
[N II]	5415.73	5542.92	6671.09	6664.40	8324.86	8328.70
[Ne III]	5401.27	5635.36	6805.02	6572.95	7597.79	7602.95
[S III]	5022.46	5157.55	6465.15	6449.19	7919.35	7919.24

Table 4.5: Values obtained by the graphical solution of the line ratio equations (Eq. 4.2-4.5) for the no-shock and shock models of our 20kK, 30kK, and 40kK models.

$$[\text{O III}]\frac{j_{\lambda 4959}+j_{\lambda 5007}}{j_{\lambda 4363}} = \frac{7.90exp(3.29\times 10^4/T)}{1+4.5\times 10^{-4}n_e/\sqrt{T}} \tag{4.2}$$

$$[\text{N II}]\frac{j_{\lambda 6548}+j_{\lambda 6583}}{j_{\lambda 5755}} = \frac{8.23exp(2.50\times 10^4/T)}{1+4.4\times 10^{-3}n_e/\sqrt{T}} \tag{4.3}$$

$$[\text{Ne III}]\frac{j_{\lambda 3869}+j_{\lambda 3968}}{j_{\lambda 3343}} = \frac{13.7exp(4.30\times 10^4/T)}{1+3.8\times 10^{-5}n_e/\sqrt{T}} \tag{4.4}$$

$$[\text{S III}]\frac{j_{\lambda 9532}+j_{\lambda 9069}}{j_{\lambda 6312}} = \frac{5.44exp(2.28\times 10^4/T)}{1+3.5\times 10^{-4}n_e/\sqrt{T}} \tag{4.5}$$

j is the strength of the stated line, n_e is the electron density and T the electron temperature. Figure 4.3 shows the graphical solution of the line ratio equations for [O III] (red), [N II] (green), [Ne III] (blue) and [S III] (magenta) for our 20kK (upper panel), 30kK (intermediate panel) and 40kK models (lower panel). The dashed line always depicts the derived temperature for the no-shock model whereas the solid line represents the temperature derived for the shock model. The electron temperatures are slightly higher for the shock model for the case of the 20kK model. Interestingly are the temperatures for the 30kK shock model slightly lower than for the no-shock model. This is to be understood in the context of the thermal balance in the two cases. In the 20kK case the extra heating due to the ionising radiation coming from the shock region causes the increase in the nebular gas temperature. In the case of the 30kK star however the increase in the heating by photoionisation is less in proportion (the star already radiates in this wavelength region), and this effect is overpowered slightly by the enhancement of some of the cooling emission lines, causing a slight net decrease in the nebular gas temperature. For the 40kK model, as expected, the differences between the no-shock and shock model are again almost negligible.

As expected, the line diagnostics of the electron density yielded no differences whatsoever between the no-shock and shock models. Using the graphical solution presented in Osterbrock & Ferland (2006) for the [O II]λ3729/λ3726 and the [S II]λ6716/λ6731 line ratio, we deduce an electron density of roughly $3700cm^{-3}$, $3400cm^{-3}$ and $2800cm^{-3}$ for our 20kK, 30kK and 40kK models, which are the values used in the electron temperature equations above.

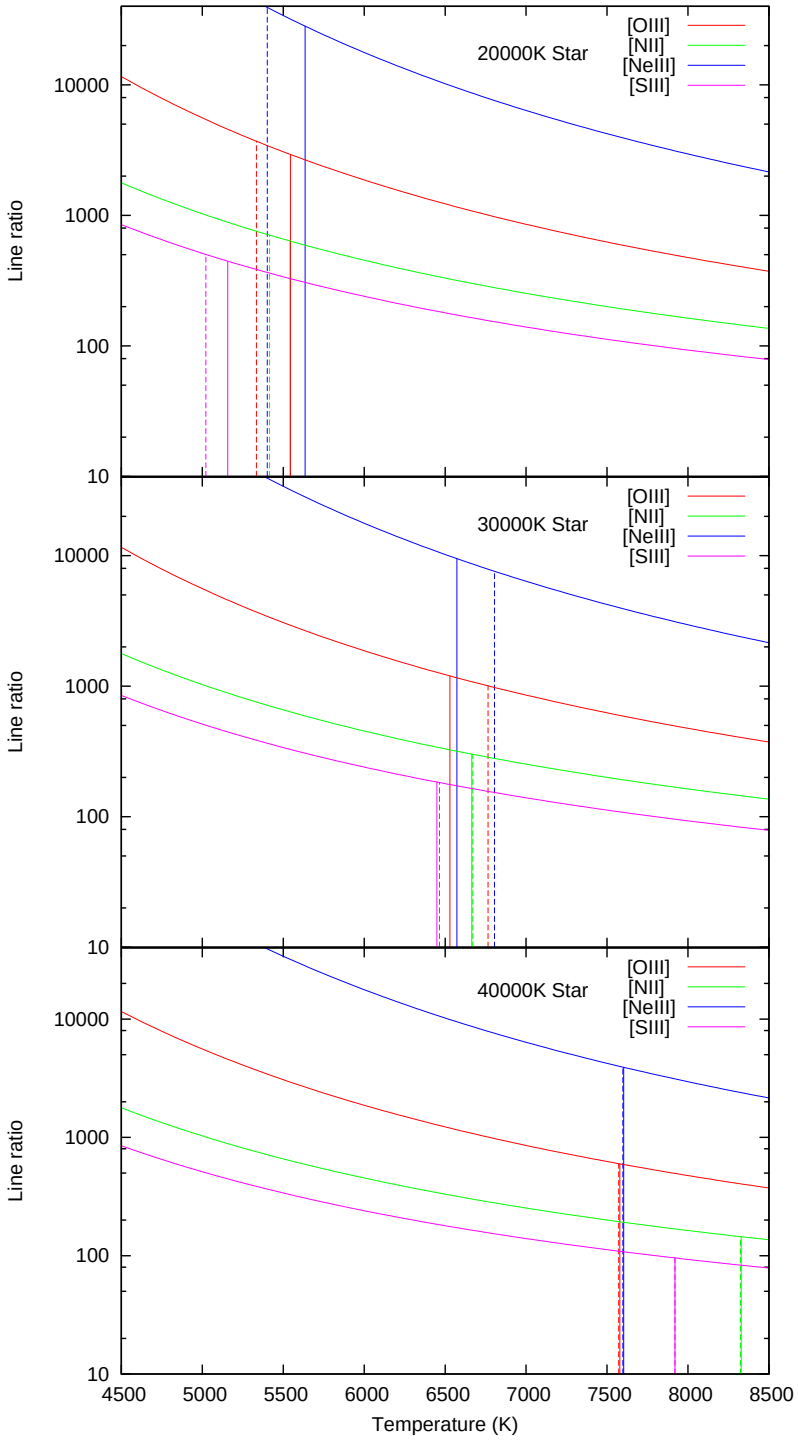

Figure 4.3: Graphical solution for the electron temperature line diagnostic equations (see Sec. 4.3.3) for the 20kK (upper panel), the 30kK (intermediate panel) and the 40kk model (lower panel). The calculated line ratios for the four investigated lines [O III] (red), [N II] (green), [Ne III] (blue) and [S III] (magenta) yield for the no-shock and shock model different temperatures. Each vertical dashed line points out the electron temperature obtained by the corresponding line ratio in case of the no-shock model whereas the vertical solid line points out the electron temperature obtained by the corresponding line ratio of the shock model.

4.3.4 The effect of shocks on strong lines in giant H II regions

An interesting question was to estimate the effect of shocks in stellar atmospheres on giant H II regions. The question was if the 20kK stars in a stellar cluster do significantly influence the overall ionising spectrum under the consideration of shocked stellar atmospheres.

We however found that the extra-emission produced by shocks in the atmospheres of 20kK stars is completely washed out by the emission of higher mass stars that photospherically emit in the same wavelength region. This effect would be only noticeable in a cluster where the largest star is indeed a 20kK star. Nevertheless we found in this context an interesting result concerning the He II λ1640 and He II λ4686 nebular lines. Table 4.2 shows only these two lines with a significant enhancement by shocks in the stellar atmosphere of a 30kK stars, all other lines show, compared to the 20kK model, already no differences. This is especially of interest since Stasińska & Izotov (2003) pointed out that the He II λ4686 nebular emission line of their sample of investigated H II galaxies occurred too frequently. The observed He II $\lambda 4686/H_\beta$ ratios could only be explained by assuming an additional X-ray radiation from a roughly 10^6K hot thermal plasma. This finding goes perfectly along with the emission of high energy radiation produced by shocks in the atmospheres of the ionising star. Moreover, our derived shock structure results in maximum shock temperatures of $1.1 \times 10^6 K$ for the 20kK model and $1.2 \times 10^6 K$ for the 30kK model, respectively, which is in almost perfect agreement with the finding of Stasińska & Izotov (2003). The effect of shocks in stellar atmospheres might therefore be a reasonable explanation for the observed He II λ4686 nebular emission line produced by the extra emission of X-rays resulting from shock cooling zones.

4.4 Summary and conclusions

In this paper we have used the stellar atmosphere code WM-Basic (Pauldrach et al. 2001) and the photoionisation code MOCASSIN (Ercolano et al. 2003, 2005, 2008) to investigate whether or not the shock enhanced ionising flux from stellar atmospheres has a non-negligible influence on the emission line spectra of H II regions. A possible influence would lead to an impact on the determination of stellar and electron effective temperatures as well as electron densities. The question was if current stellar atmosphere models, which do not take shocks into account, and are used as inputs to the grid of photoionisation models in currently employed nebular emission line diagnostic diagrams would produce significant biases, and therefore whether a new generation of photoionisation model grids is required to solve the problem.

To answer this question we have run a grid of stellar atmosphere models using the WM-Basic code in shock and no-shock mode to generate input spectra for the MOCASSIN photoionisation code. The calculated WM-Basic grid ranged from 20kK to 50kK (60kK to 90kK) in steps of 10kK in the effective temperature for a surface gravity of log g = 3.9 (log g = 4.9) and solar abundances. The emergent ionisiong flux was then used to derive the corresponding number of ionising photons as well as the model's Strömgren radius. The derived quantities were used as an input in the MOCASSIN code. Based on these input parameters each MOCASSIN model yielded a corresponding ionisation parameter U. We used the η_{S-Ne} parameter which is one of the most commonly employed method to estimate the mean $\overline{U}$ and $T_{\rm eff}$ from ratios of strong nebular emission lines. The net effect of shocks is to simulate a star of higher effective temperature and thus a higher ionisation parameter in the nebular gas. Our results showed no change at all for the 40kK case. For cooler stars we indeed found small deviations for the 30kK non-shock case to the 30kK shock case. The effects on the 20kK case are

dramatic, placing the 20kK shock model in a region of the diagnostic diagram (Fig. 4.2) expected to be populated by systems with roughly 30-35kK ionising stars and approximately a decade higher ionisation parameter U.

We also investigated a possible influence on the electron temperatures and densities for the no-shock and shock cases of our models. We used line ratio equations for the electron temperature and density determination as presented by Osterbrock & Ferland (2006). A graphical solution of the line ratios equations (see Fig. 4.3) yielded in the shock case for all temperatures values which are roughly 200K higher than for the 20kK no-shock model and showed again almost no differences between the no-shock and shock models in the 40kK case. Interestingly the obtained electron temperatures for the 30K case were all a bit lower in the shock case compared to the no-shock case. This is understood in the context of the thermal balance for each model. In the 20kK case the extra heating due to the ionising radiation coming from the shock region causes the increase in the nebular gas temperature. The 30kK star however already radiates in this wavelength region and therefore is the increase in the heating by photoionisation less in proportion. This effect is overpowered slightly by the enhancement of some of the cooling emission lines, causing a slight net decrease in the nebular gas temperature.

For the empirically derived electron densities we found no differences between the no-shock and shock models.

As an additional result we found our shock models to show a very strong enhancement of the He II λ4686 line which could explain observations by Stasińska & Izotov (2003) of an unusually frequent occurrence of the He II λ4686 nebular emission line in their sample of investigated H II galaxies.

Overall we conclude that shock effects are only important for stellar sources with effective temperatures equal or lower than 30kK. The magnitude of the effect is also obviously dependent on the strength of the shock (which can be determined by modelling fits to the stellar emission lines, e.g. the *O vi* line, if observations are available for appropriate stellar objects) and thus might only show dramatic effects for a chosen sample of stellar sources and be likely unimportant for the majority of stellar sources.

Chapter 5

Spectroscopic Constraints on the Form of the Stellar Cluster Mass Function

The contents of this chapter was published in Bastian et al. (2012b), Astronomy & Astrophysics, 541A, 25B.

Abstract. This contribution addresses the question of whether the initial cluster mass function (ICMF) has a fundamental limit (or truncation) at high masses. The shape of the ICMF at high masses can be studied using the most massive young ($<$10 Myr) clusters, however this has proven difficult due to low-number statistics. In this contribution we use an alternative method based on the luminosities of the brightest clusters, combined with their ages. The advantages are that more clusters can be used and that the ICMF leaves a distinct pattern on the global relation between the cluster luminosity and median age within a population. If a truncation is present, a generic prediction (nearly independent of the cluster disruption law adopted) is that the median age of bright clusters should be younger than that of fainter clusters. In the case of an non-truncated ICMF, the median age should be independent of cluster luminosity. Here, we present optical spectroscopy of twelve young stellar clusters in the face-on spiral galaxy NGC 2997. The spectra are used to estimate the age of each cluster, and the brightness of the clusters is taken from the literature. The observations are compared with the model expectations of Larsen (2009) for various ICMF forms and both mass dependent and mass independent cluster disruption. While there exists some degeneracy between the truncation mass and the amount of mass independent disruption, the observations favour a truncated ICMF. For low or modest amounts of mass independent disruption, a truncation mass of $5-6\times10^5 M_\odot$ is estimated, consistent with previous determinations. Additionally, we investigate possible truncations in the ICMF in the spiral galaxy M83, the interacting Antennae galaxies, and the collection of spiral and dwarf galaxies present in Larsen (2009) based on photometric catalogues taken from the literature, and find that all catalogues are consistent with having a truncation in the cluster mass functions. However for the case of the Antennae, we find a truncation mass of a few $\times10^6 M_\odot$, suggesting a dependence on the environment, as has been previously suggested.

5.1 Introduction

Since their discovery in starburst and merging galaxies (e.g., Schweizer 1987, Holtzman et al. 1992), young massive stellar clusters (YMCs, a.k.a. young globular clusters or super star clusters) have been the focus of a plethora of studies (c.f. Portegies Zwart, McMillan, & Gieles 2010). These studies have focused on individual clusters (e.g., Smith & Gallagher 2001; Larsen et al. 2008) as well as full cluster populations (e.g., Konstantopoulos et al. 2009; Adamo et al. 2010) in a variety of galaxy types. Some characteristics of YMC populations appear to be related to the properties of the host galaxy, with high star-formation rate galaxies (i.e., starbursts) producing more massive clusters (e.g., Larsen 2002, Bastian 2008), and there are indications that the cluster formation efficiency (i.e., the fraction of stars that form in clusters) increases with increasing star-formation rate surface density of the host galaxy (e.g., Meurer et al. 1995; Zepf et al. 1999; Larsen 2004; Goddard et al. 2010; Adamo et al. 2011, Silva-Villa & Larsen 2011). Additionally, the form of the cluster luminosity or mass distributions appears to be well described by a power-law with index ~ -2, at least on the low mass end (e.g., de Grijs et al. 2003).

Despite these intensive studies, there is still ongoing debate in the literature on some of the basic properties of cluster populations. Is the mass function of clusters truncated at high masses (e.g., Gieles et al. 2006a,b; Bastian 2008; Larsen 2009; Gieles 2009; Bastian et al. 2012a) or does the power-law continue to the highest mass clusters (e.g., Chandar et al. 2010; Whitmore et al. 2010)? How long do clusters live, and how does disruption affect the cluster population? Is cluster disruption dependent on the mass of the cluster and its environment? Or is cluster disruption independent of environment, being dominated by internal processes (see Bastian 2011 for a recent review)? Here, we focus on the form of the initial mass function of clusters, paying particular attention to whether it is truncated at the high mass end.

Whether the initial mass function of stellar clusters (ICMF) has a truncation at the high mass end is important for a number of reasons. In particular, if there is a truncation, and the truncation varies as a function of environment (e.g., Gieles et al. 2006b; Bastian et al. 2012a) this may be reflecting important physics in the star/cluster formation process, or about the distribution of the ISM within galaxies (i.e, size scale of GMCs). Additionally, a truncation of the ICMF would have important implications for the globular cluster specific frequency problem (e.g., Kruijssen & Cooper 2012), with the number of clusters surviving after a Hubble time being strongly dependent on whether a truncation occurs at $\sim 10^5\ M_\odot$ or $\sim 10^6\ M_\odot$. Finally, knowing the form of the ICMF allows for tighter constraints to be placed on the role of disruption in shaping cluster populations (e.g, Gieles & Bastian 2008; Chandar et al. 2010; Bastian et al. 2012a).

The form of the ICMF and the mechanism of cluster disruption leaves a characteristic imprint on the relation between the age and absolute magnitude of ensembles of clusters (Larsen 2009). For example, if cluster disruption is strong (i.e., the timescale of disruption is short) and independent of environment (a mass-independent dissolution time scale, e.g., all clusters lose 90% of their mass every decade in age - Fall et al. 2009), then few old (> 50 Myr) bright clusters are expected to exist within the population. Additionally, if the cluster mass function is truncated at the upper end (i.e., the mass function is described by a Schechter function), this also limits the likelihood of finding a bright, old cluster.

Larsen (2009) derived the expected relations between the median age vs. absolute magnitude of a cluster population, assuming a range of ICMFs and disruption laws. He used published catalogues of the brightest and 5th brightest clusters in a sample of spiral and dwarf galaxies, and found evi-

dence that the mass function was indeed truncated at a value of $\sim 2 \times 10^5\ M_\odot$, and that strong mass independent disruption (90% per decade in age) scenarios were not favoured.

In the present work, we apply the Larsen (2009) analysis to a single galaxy, NGC 2997, and use Gemini spectroscopy to derive the age of the individual clusters, eliminating the age/extinction/metallicity degeneracies known to hamper photometric studies.

5.2 Observations

NGC 2997 is a face on spiral galaxy, located at a distance of ~ 9.5 Mpc (distance modulus of 29.9 - de Vaucouleurs 1979). It hosts a relatively rich young cluster population (Larsen & Richtler 1999), including one of the brightest YMCs known in a spiral galaxy ($M_V \sim -12.9$; Larsen 2009). The face on orientation of NGC 2997, as well as its relatively large distance, allows us to sample the full galaxy with a single pointing of GMOS (discussed in more detail in § 5.2.2), mitigating any potential selection biases of focussing on the central regions of the galaxy, giving a more global picture.

5.2.1 NGC 2997 cluster sample

The sample of clusters was taken from the catalogue of Larsen (2004), which is based on ground-based U, B, V, Hα and I-band imaging. We refer to Larsen & Richtler (1999) and Larsen (1999) for details of the cluster selection process and derivation of the completeness limits, and only summarise here. Cluster candidates were selected through DAOFIND routine in IRAF, and a colour cut of $B-V < 0.45$ was applied to remove foreground stars. Additionally, magnitude cuts were applied in order to remove individual bright stars within NGC 2997, namely $M_V < -9.5$ for blue sources ($U-B \leq -0.4$) and $M_V < -8.5$ for red sources ($U-B > -0.4$). Artificial star and cluster tests resulted in approximately 80% completeness at $M_V = -9.5$. All candidates were visually inspected and large diffuse sources (likely background galaxies or extended high-surface brightness regions within spiral arms) were removed.

Additionally, sources that had significant Hα emission associated with them were removed, which has two benefits. The first is that it is often difficult to distinguish a stellar cluster from an unbound association at young ages (e.g., Larsen 2004; Gieles & Portegies Zwart 2011; Bastian et al. 2011). However, once a stellar group has had time to dynamically evolve, it is easier to distinguish between clusters and associations (Gieles & Portegies Zwart 2011), so restricting to candidates older than $5-7$ Myr helps in removing many spurious sources (i.e., unbound associations). Secondly, it has been suggested that the rapid removal of gas from a young cluster can disrupt a large fraction of clusters or can lead to significant stellar mass loss within clusters (e.g., Goodwin & Bastian 2006; Goodwin 2009). However, within a few crossing times, the clusters should stabilise (e.g., Portegies Zwart et al. 2010), so limiting our sample to older clusters lessens the impact that infant mortality or infant weight loss may have on the population.

5.2.2 Spectroscopy

The brightest 30 candidates were chosen, and a multi-slit spectroscopic mask was made that maximised the number of clusters that could be observed in a single pointing. When the dispersion axis of two potential targets overlapped, the brighter cluster was chosen. This resulted in 12 clusters that

Larsen ID	RA	Dec	Ranking	log (age/yr)	σ(log age)	M_V (mag)	S/N
679	09 45 47.01	−31 11 05.3	1	7.2	0.1	-12.92	26
453	09 45 30.98	−31 12 43.6	2	6.9	0.1	-12.77	58
693	09 45 48.92	−31 10 54.9	3	7.1	0.1	-12.63	35
518	09 45 48.44	−31 12 17.2	4	6.7	0.1	-12.28	45
715	09 45 40.63	−31 10 50.8	5	7.2	0.1	-12.23	30
519	09 45 32.20	−31 12 20.9	7	6.7	0.1	-12.08	50
836	09 45 33.80	−31 10 01.8	8	7.62	0.05	-11.94	25
645	09 45 33.40	−31 11 20.9	10	7.9	0.2	-11.62	8
405	09 45 35.12	−31 13 10.1	11	7.12	0.05	-11.33	25
696	09 45 28.50	−31 10 59.8	17	7.5	0.2	-10.64	8
648	09 45 44.18	−31 11 14.6	18	7.8	0.2	-10.59	5
690	09 45 51.34	−31 10 56.3	30	7.4	0.2	-9.86	10

Table 5.1: The ID, location, ranking (in terms of V-band absolute brightness in the population), spectroscopically determined age and error, and absolute V-band magnitude of the clusters in NGC 2997 presented in the current work.

could be observed in a single pointing. The absolute V-band magnitudes of these clusters were taken from the Larsen catalogue and the basic properties of the clusters are given in Table 5.1.

We obtained spectra of 12 sources in NGC 2997 using the Multi-Object Spectroscopy (MOS) mode of the Gemini Multi-Object Spectrograph (GMOS) on Gemini South. The data were obtained as part of Queue program GS-2009B-Q-29 (PI N. Bastian). We used the B600 grating and a slit width of 0.75 arcsec, resulting in an instrumental resolution of 110 kms^{-1} at 5000 Å. The spectroscopic observations were obtained as four individual exposures with an exposure time of 1800 s each (for a total on-target integration time of 7200 s). No atmospheric dispersion corrector (ADC) was available on Gemini South at the time of the observations, causing wavelength-dependent slit losses. We corrected each exposure for this effect using the method of Filippenko (1982).

The basic reductions of the data were done using a combination of the Gemini IRAF package and custom reduction techniques, as described in Appendix A in Trancho et al. (2007).

The age of each cluster was derived using the method presented in Trancho et al. (2007). In brief, a template is built for each cluster (avoiding lines affected by nebular emission) using simple stellar population (SSP) models (González Delgado et al. 2005) and the PPxF method (Cappellari & Emsellem 2004). Spectral indices are measured from the template spectra ($H+He$, K, $H8$, $\mathrm{H}\gamma_\mathrm{A}$, $Mgb5177$,$Fe5270$, $Fe5335$; see Trancho et al. 2007 for the full definitions), along with error estimates, which are then compared to SSP models (measured in the same way) in a least χ^2 sense in order to choose the best fitting model. The uncertainty in age is derived by running 2000 monte carlo simulations for each cluster, adding random noise to the measured indices, sampled from the estimated errors. The age uncertainty is then taken as the standard deviation of a log-normal fit to the resulting age distribution. This method has been shown to be largely independent of the signal-to-noise ratio of the data (Trancho et al. 2007).

The observed spectra are shown in Fig. 5.1, along with the estimated age of each cluster. Additionally, the cluster properties are given in Table 1. Only the 12 clusters with spectroscopic age determinations are used for determining the cluster mass function.

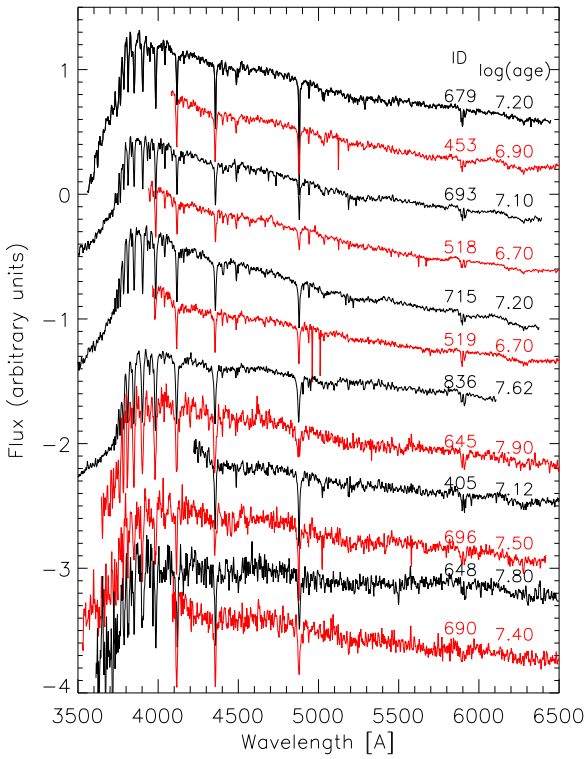

Figure 5.1: The observed spectra of the 12 observed clusters in NGC 2997 presented in this work. The ID (following L04) and derived spectroscopic (logarithmic) age (in yr) are given for each target.

5.3 Comparison with Models

The underlying initial cluster mass function (ICMF) and type of disruption strongly affect the relation between the observed age and absolute magnitude of a cluster population. Larsen (2009) presented an analytic representation of the $d^2N/(dtdL)$ distribution, i.e., the number of clusters with an age between t and $t+dt$ and luminosity between L and $L+dL$, that considers functional forms for the ICMF and the mass evolution of the stellar population due to disruption. From this it is possible to derive the median age (as well as the mean and the standard deviation) as a function of M_V. He considered various ICMF types (truncated or untruncated) and different disruption laws (mass/environment dependent or independent).

If disruption does not influence the population, and the mass function has an exponential cutoff (i.e., is described by a Schechter (1976) type function - $dN/dM_i \sim M_i^{-2}\exp(-M_i/M\star)$) then the brightest clusters in a population are preferentially young (see also Bastian 2008). The exact relation between median age and M_V depends on the truncation mass, $M\star$, with lower $M\star$ values resulting in the brightest clusters being younger. If cluster disruption is included, in particular if cluster disruption is dependent on the cluster mass, as expected from N-body and analytic considerations (see e.g., Portegies Zwart, McMillan, & Gieles 2010) then the older clusters and lower mass clusters are most affected. This results in a turn-around in the relation between age and M_V with fainter clusters also

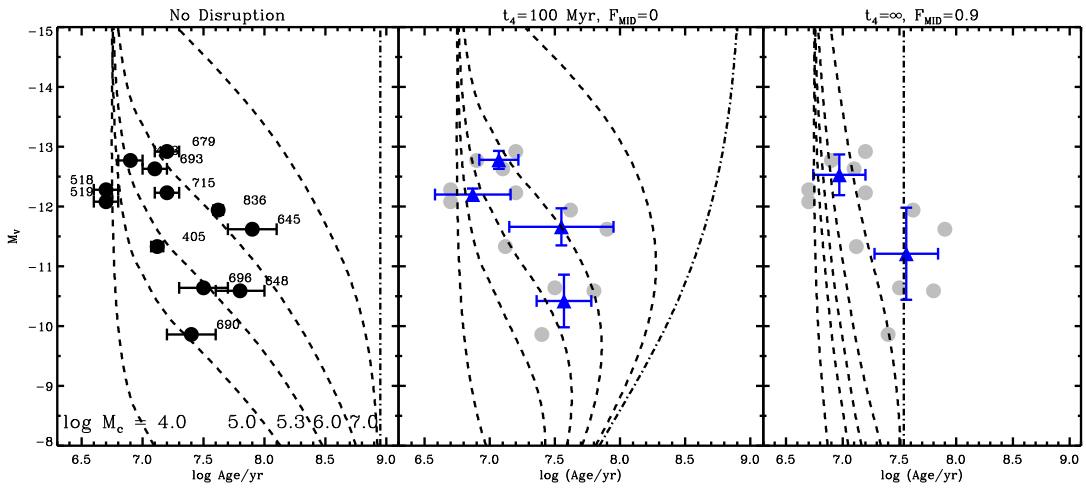

Figure 5.2: Age vs. M_V for the twelve clusters in the present study. In each panel, we also show the expectations of the median M_V, for a given age, following the results of Larsen (2009). The model disruption parameters are given at the top of each panel, where $\widehat{4}$ is the disruption timescale of a 10^4 $M_\odot$ cluster in the mass dependent cluster disruption scenario, and F_{MID} is the fraction of clusters destroyed every decade in age. The dashed lines represent models with different values of the Schechter truncation mass, and the dashed-dot lines in each panel represents the case without truncation (i.e., a pure power-law). In the middle and right panels, the original data are shown in grey, while the binned data (the mean in flux and age, with the error bars representing the standard deviation) are shown as solid (blue) triangles. Two different bin sizes are shown.

being preferentially young. Alternatively, if the ICMF does not have a truncation and there is no mass dependent disruption, then the median age of a cluster population should be independent of M_V (the vertical dash-dotted line in the first panel of Fig. 5.2). Including strong mass independent disruption (where a large and constant fraction of the population disappears every decade of age[1]) also results in the median age being independent of M_V.

Three characteristic cases are shown in Fig. 5.2 (after Larsen 2009). In each of the panels six models are shown. In all models a constant star/cluster formation rate is assumed. The dashed lines represent models that adopt a Schechter ICMF with M$\star$ values of 1×10^4, 1×10^5, 2×10^5,1×10^6, and $1\times10^7 M_\odot$, from left to right, respectively. In all cases we adopted an index of -2 for the ICMF at the low mass end. The dash-dotted lines represent the results of models that have a pure power-law ICMF (untruncated). The left panel shows models that have no disruption, while the middle panel shows models with mass dependent disruption (adopting the formalism of Lamers et al. (2005), with $t_4 = 100$ Myr), and the right panel adopts no mass dependent disruption but instead strong mass independent disruption (a long duration infant mortality rate of 90% - see Whitmore et al. 2007). The models explicitly include the effects of stochasticity in the cluster population and do not require a fully sampled mass function at young ages.

[1] There is a subtle difference between all clusters losing a fraction of their mass every decade in age, and a constant fraction of clusters are completely disrupted. If the mass function is a pure untruncated power-law (with an index of -2), then there is no difference in terms of the method used here. If there is any structure in the ICMF (such as a truncation), in the case of all clusters losing a fraction of their mass, then this structure will shift towards lower masses with time.

In all cases, the models represent the *median* age of the clusters for a given magnitude. Hence if the model is a good representation of the data, half of the clusters should lie to the left and half to the right of the curve, at all magnitudes. From Fig. 5.2 it is clear that certain models do not represent the observed data well. Low or high truncation values (i.e., $\sim 10^4$ or $\sim 10^7 M_{\odot}$) are not favoured if there is little or no mass dependent disruption, and low truncation values are also not favoured in the case of strong mass independent disruption.

The data presented in Fig. 5.2 show on overall tendency for younger clusters to be brighter than older ones (Spearman's rank correlation coefficient of 0.58, meaning that there is $\sim 5\%$ chance of log(age) and M_V to show such a relation by chance). This is a generic prediction for any cluster population that displays a truncation in the upper end of the mass function (e.g., Gieles et al. 2006a, Bastian 2008, Larsen 2009). If no cluster disruption is assumed, then the data points are most consistent with a truncation mass of a few times $10^5 M_{\odot}$. Additionally, while the impact of mass dependent disruption is largely negligible for the observed sample (due to the fact that the brightest clusters tend to be young and massive), strong mass independent disruption models are not favoured by the data.

5.3.1 Statistical measures

In order to place the above conclusions on a more statistically robust footing, we have also carried out maximum likelihood tests, comparing the observations to a wide range of models. For the models, we use the Larsen (2009) analytic prescriptions, and vary M$\star$ from 1×10^4 to $1 \times 10^7 M_{\odot}$, $\widehat{4}$ from 100 to 10^9 Myr, and F_{MID} from 0 to 0.9.

To assess the likelihood of our data for a given model, we assume that the uncertainties on both age and M_V follow a Gaussian distribution. From this assumption, we can then write down the likelihood function to be:

$$\mathscr{L} \propto e^{\frac{-\chi^2}{2}} \tag{5.1}$$

where

$$\chi^2 = \sum_{i=1}^{N} \frac{(\log(age)_{i,obs} - \log(age)_{i,mod})^2}{\sigma^2_{\log(age)_{i,obs}}} + \frac{(M_{V,i,obs} - M_{V,i,mod})^2}{\sigma^2_{M_{V,i,obs}}} \tag{5.2}$$

and N is the number of observed data points. Because we are only interested in relative likelihoods, we do not compute the normalisation term for the likelihood function in Equation 5.1. For this analysis we limit the comparison between observations and models to the range of magnitudes of the observations.

Using this framework, we sampled the likelihood function for 6300 models described in Larsen (2009). The ensemble of models that maximise the likelihood function are deemed to represent a set of the most likely model parameters (e.g., truncation mass, $\widehat{4}$, etc).

5.3.2 NGC 2997 results

As expected from visual inspection of Fig. 5.2, the results of the maximum likelihood fitting were largely independent of the mass dependent disruption timescale, $\widehat{4}$. However, for all values of $\widehat{4}$, a truncation in the mass function was favoured by the fitting procedure. In order to judge the importance of mass independent disruption (i.e., long duration infant mortality) we set the mass dependent

disruption timescale to 10^9 Myr (i.e., essentially infinite). Doing this, we are left with only two free parameters in the model, M$\star$ and F_{MID}.

The results from this two dimensional maximum likelihood analysis are shown in Fig. 5.3. The darker the shading the higher likelihood (also shown in coarser steps as dashed contour lines). A clear maximum in this space is seen, a largely horizontal "valley" with a truncation at $5 \times 10^5 M_\odot$ that increases slightly as a function of F_{MID}. The solid (white) circles denote the models with the maximum likelihood (i.e., with the same likelihood). While eleven of the models have M$\star$ between $5-6 \times 10^5 M_\odot$ and $F_{MID} \leq 0.2$, two of the models had significantly higher F_{MID} values (0.5 and 0.7) and somewhat larger M$\star$ values ($1-2 \times 10^6 M_\odot$). These models are shown in Fig. 5.4.

Hence, we find that a truncation in the cluster mass function is favoured independent of the disruption law adopted. If disruption is dependent on mass and the surrounding environment of a cluster, then a truncation of $\sim 5 \times 10^5 M_\odot$ is strongly preferred. A similar conclusion is reached, that a truncation of $\sim 5-10 \times 10^5 M_\odot$ is required, if the fraction of clusters disrupted every decade in, F_{MID}, is less or equal to 0.5. For higher values of F_{MID} a truncation is still preferred, although at higher M$\star$ values.

The largest uncertainty in the value of M$\star$ is due to the disruption law adopted. If we adopt a mass and environmentally dependent disruption scenario, as found for M83 (Bastian et al. 2011, 2012a) and dwarf galaxies (Cook et al. 2012), then the uncertainties are drastically reduced, and instead are due to the limitations of age dating clusters, resulting in an uncertainty in M$\star$ within a factor of two.

5.4 Other cluster catalogues

Additionally, we have run our maximum likelihood method over the data presented in Larsen (2009). This catalogue contains the brightest and 5$^{\rm th}$ brightest cluster in a photometrically determined sample of cluster populations in spiral and dwarf galaxies. The fits result in a very similar picture, with M$\star$ slightly lower, $2 \times 10^5 M_\odot$.

Finally, we can look at the photometrically determined properties of cluster populations, taken from the literature. For this, we use the 50 brightest clusters in the Antennea galaxies as determined by Whitmore et al. (2010) and the sample of clusters in M83 taken from Bastian et al. (2011). For each dataset, we removed sources with ages less than 6 Myr (see § 5.2.1 for a discussion on this point) and then looked at the median age and brightness of the population in bins of 4 and 10 clusters in the Antennae and M83, respectively. The data are shown in Fig. 5.5. Additionally, for the M83 results, we have overplotted the expected model as derived from the full population study of Bastian et al. (2012a). These are models with M$\star$= $1.6 \times 10^5 M_\odot$ and $\widehat{4}$= 130 Myr for the inner field and M$\star$= $5 \times 10^4 M_\odot$ and $\widehat{4}$= 600 Myr for the outer field.

Both galaxies are consistent with having a truncated mass function, with the Antennae having an M$\star$ value of a few $\times 10^6 M_\odot$, while M$\star$ is $\sim 10^5 M_\odot$ in M83. The value of $\sim 10^6 M_\odot$ found for the Antennae galaxies is similar to that suggested by Zhang & Fall (1999) and Gieles et al. (2006a) based on the observed luminosity function of the cluster population. As expected, the cluster mass function extends to higher mass than seen in spiral or dwarf galaxies, however it still appears to be truncated.

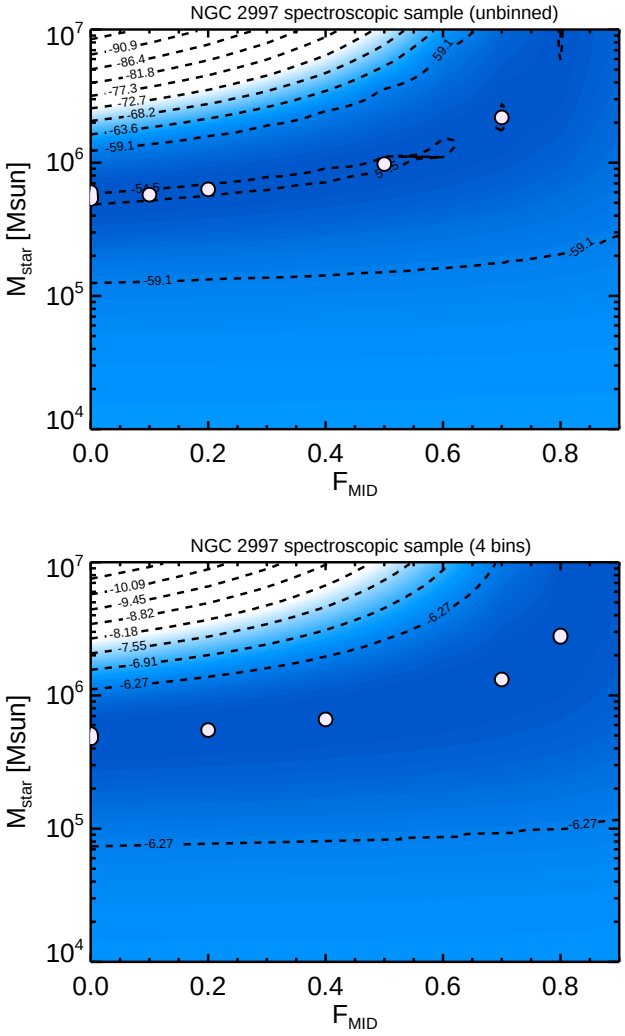

Figure 5.3: Results from the two dimensional statistical analysis (i.e., adopting no mass dependent disruption, and determining the likelihood for the models only varying M⋆ and F_{MID}). The shaded region/contour lines denote the logarithm of the likelihood of the model for the combination of M⋆ and F_{MID}, and the filled (white) points denote the maximum likelihood models. **Top:** The analysis carried out on the unbinned dataset. **Bottom:** The same analysis, but now carried out on the binned dataset (four bins, each with the mean age/flux of three clusters). The white points from the upper panel denote models that are shown in Fig. 5.4.

5.5 Conclusions

We confirm the findings of Larsen (2009) that the cluster mass function in spiral galaxies is consistent with a Schechter mass function with a truncation near $2-5\times10^5 M_\odot$. Additionally, strong mass independent disruption ($>80-90\%$ per decade in age) is not supported by the current observations. Comparing the age-M_V method to that derived with full population studies in M83 leads to largely consistent results (i.e., that a truncation in the ICMF is needed and that strong mass independent disruption is disfavoured). Applying this method to the cluster population of the Antennae galaxies

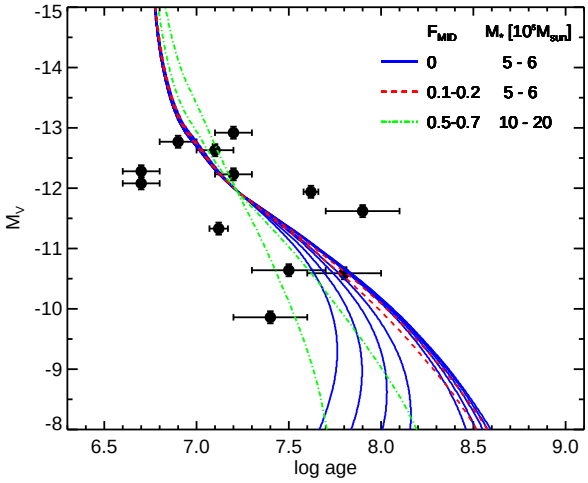

Figure 5.4: The observed age vs. M_V relation along with the maximum likelihood models from § 5.3.2. The solid (blue curves) represent models that have F_{MID}=0, and from left to right have $\widehat{4}$ values ranging from 100 Myr (left) to 10 Gyr (right). All these models have M⋆ values between 5 and $6\times10^5 M_\odot$. The dashed (red) lines have similar M⋆ values, but no mass dependent disruption and a small amount of mass independent disruption. The dash-dotted (green) lines also represent models with a truncation mass ($\gtrsim 10^6 M_\odot$) but have higher mass independent disruption rates.

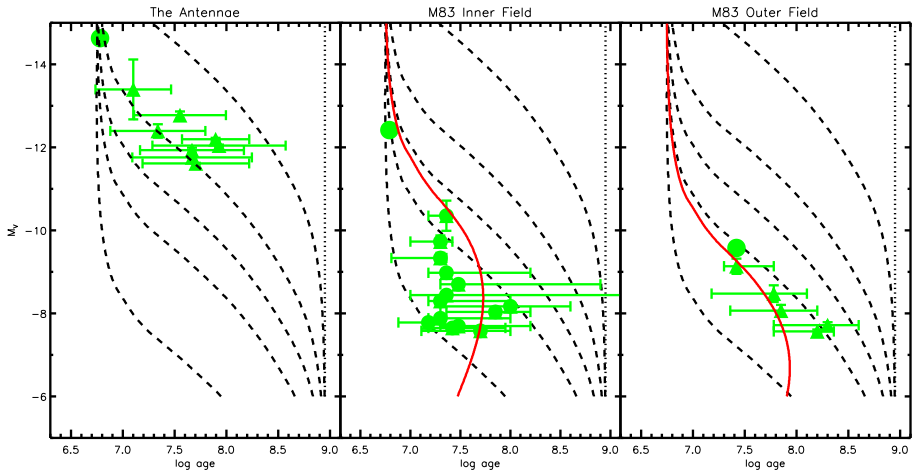

Figure 5.5: Age vs. M_V for clusters in the Antennae (left panel - Whitmore et al. 2010), M83 inner region (middle panel - Bastian et al. 2011) and M83 outer region (right panel - Bastian et al. 2011). Only clusters with ages greater than 6 Myr were used. In all panels the brightest cluster in the sample is shown as a (green) filled circle. For the Antennae, the triangles represent the median of the age and M_V of clusters in the rest of the catalogue (in bins of four clusters). For M83, each bin contains 10 clusters. In the middle/right panels, the model corresponding to the best fit results of Bastian et al. (2012a) are shown as solid (red) lines. They have been corrected the a Salpeter stellar IMF adopted by the Larsen (2009) models in M⋆. For the Antennae data, the error bars represent the standard deviation for each bin. For the M83 data, the error bars represent the region where 60% of the data in that bin lie. We note that the models also show such scatter, i.e. only the median of the models is shown.

shows that it is also consistent with a truncated ICMF, however the truncation mass is significantly higher, a few $\times 10^6 M_\odot$.

Chapter 6

The Role of Environment in Stellar Clustering in Galaxies

The contents of this chapter will appear in Kruijssen et al. (2013), Astronomy & Astrophysics.

Abstract. We investigate the radial distribution of young massive clusters (YMCs) in a sample of nearby spiral galaxies. In particular, we search for characteristic galactocentric radii that are conducive to the formation (and/or survival) of the most massive YMCs. We use the Larsen (2004) catalogue of YMCs in a sample of nine nearby, relatively face-on, spiral galaxies, and select the five most massive clusters per galaxy, as determined through fitting each cluster's SED to simple stellar population models. We find that the radial distribution of YMCs has a pronounced peak at 0.05 to 0.2 times the major axis and an exponential drop off beyond this radius. A simple model is developed which adopts a radial distribution of molecular gas in spiral galaxies, a Schmidt-Kennicutt star-formation rate law to convert the surface density of gas to a star-formation rate surface density, and a size-of-sample effect to convert the total SFR to a distribution of cluster masses. We find that such a model is able to reproduce the observed YMC radial distribution without the need to include preferential cluster formation (i.e. higher cluster formation rate in the central regions of galaxies due to a higher pressure) or dissolution due to the increased density of giant molecular clouds near galactic centres.

6.1 Introduction

Our knowledge of the stellar cluster population of the Milky Way is extremely incomplete. The main causes of this incompleteness are the extinction in the disk of the Galaxy and crowding/source confusion due to foreground and background stars. Our current census of the cluster population of Galaxy is only complete to approximately 800 pc (Piskunov et al. 2006; Röser et al. 2010) from the sun, and while we are complete for higher mass clusters to greater distances, relatively nearby, massive clusters are still being discovered (e.g., Glimpse-C01 at a distance of ~ 5 kpc, an age of 400-800 Myr, and a mass of $\sim 10^5 M_{\odot}$; Davies et al. 2011). Hence, in order to gain a full understanding of the cluster population in spiral galaxies, it is necessary to search in nearby galaxies, where extinction and source confusion is significantly reduced.

Larsen (1999) and Larsen & Richtler (1999, 2000) were the first to systematically search nearby, relatively face-on, spiral galaxies for young massive stellar clusters, using deep ground based multi-

filter optical/UV imaging. They found that young clusters were ubiquitous in star-forming galaxies, with luminosities ranging from $M_V = \sim -8.5$ to ~ -13, rivalling that of clusters found in starburst and merging galaxies. Using this dataset, Larsen (2002) found that the luminosity of the brightest cluster correlated with the star-formation rate (SFR) of the galaxy, with higher SFR galaxies producing brighter clusters. This correlation has been explained as a result of a size-of-sample effect, with higher SFR galaxies forming more stars and star clusters, which allows the population to be sampled to higher masses and luminosities (Bastian 2008).

These pioneering studies have been followed up with Hubble Space Telescope based imaging studies of other spiral galaxies (e.g. M81 - Chandar et al. 2001; M51 - Bastian et al. 2005; M83 - Bastian et al. 2012b) which have confirmed the ubiquity of young massive clusters in spirals and allowed for more detailed studies of individual clusters (e.g., Larsen & Richtler 2004) and cluster populations (e.g., Gieles et al. 2005). While many aspects of massive cluster populations (e.g., their evolution and destruction) in spiral galaxies are now relatively well understood (c.f., Portegies Zwart, McMillan, and Gieles 2010), the location of the most massive clusters, specifically their radial distribution, has not been investigated to date.

The detailed process of cluster formation (as well as early evolution) is not well understood, in particular, the role of the ambient environment. High pressure environments are suspected to preferentially form bound clusters (e.g., Elmegreen 2008), hence we may expect the inner regions of galaxies to form more, and potentially higher mass clusters. We also may expect a size-of-sample effect, with regions that have a higher star-formation rate forming more massive clusters. Alternatively, the environment may negatively effect cluster formation and early evolution. In dense environments the interstellar medium (ISM), in particular, massive giant molecular clouds (GMCs), may disrupt young clusters very rapidly (within the first few Myr of their lives), resulting in more clusters surviving in the outer regions of galaxies (Elmegreen & Hunter 2010; Kruijssen et al. 2011).

In the present work we investigate whether there is a characteristic galactocentric radius where young massive clusters are more likely to reside. Given the uncertainties in the Galactic cluster population, we will use a survey of YMCs in nearby spiral galaxies presented in Larsen (2004). Additionally, we will compare observed distribution of the most massive YMCs to expectations of various models, in order to attempt to constrain cluster formation and early evolution.

This paper is organised in the following way. In § 6.2 we will present the cluster populations used, along with a brief description on how the cluster parameters have been estimated. In § 6.3 we will present some basic models giving the expectation of the galactocentric radius distribution of the massive clusters for different assumptions. Finally, in § 6.4 we will discuss our results and present our conclusions.

6.2 Observations

6.2.1 The cluster sample

The sample of clusters was taken from the catalogue presented in Larsen (2004), which is based on ground-based U, B, V, Hα and I-band imaging of 17 nearby, largely face-on, spiral galaxies. The images and original cluster selection is discussed in detail in Larsen & Richtler (1999, 2000) and Larsen (1999). Candidate clusters were selected to be semi-resolved on the ground based images (half-light radii larger than a 1-2 pc) and to have colours consistent with young (< 500 Myr) simple stellar population models ($B-V < 0.45$).

Since young clusters are not found uniformly distributed across galaxies (e.g., Scheepmaker et al. 2009) and the background flux level in spirals varies significantly, it is not sufficient to define a single completeness level for the entire galaxy. Larsen (1999) derived completeness estimates by adding artificial clusters with sizes between 1 and 20 parsecs, near detected cluster candidates (within 20-70 pixels). For compact sources (expected for clusters), he found that for nearly all galaxies the catalogues were complete at the $> 85\%$ level for clusters brighter than $M_V = -10$ mag. Additionally, in the current study we will only use the most massive or the five most massive clusters per galaxy, which, on average, are the brightest, meaning that our sample should be nearly complete.

Additionally, candidate clusters that have significant Hα emission have been removed from the sample. This has had two benefits. The first is that it is often difficult to distinguish a stellar cluster from an unbound association at young ages (e.g. Larsen 2004; Gieles & Portegies Zwart 2011; Bastian et al. 2012b). However, once a stellar group has had time to dynamically evolve, it is easier to distinguish between clusters and associations (Gieles & Portegies Zwart 2011), so restricting the sample to candidates older than $5-7$ Myr helps in removing many spurious unbound sources. Secondly, it has been suggested that the rapid removal of gas from a young cluster can disrupt a large fraction of clusters or can lead to significant stellar mass loss within clusters (e.g. Goodwin & Bastian 2006; Goodwin 2009). However, within a few crossing times, the clusters should stabilise (e.g. Portegies Zwart et al. 2010), so limiting our sample to older clusters lessens the impact that infant mortality or infant weight loss may have on the population.

The ages and masses for all clusters in the sample have been estimated through comparison of the cluster colours and magnitudes to simple stellar population (SSP) models (Larsen 2009). Comparison between the derived ages and masses using different SSP models have shown that the typical errors in deriving the age/mass of a cluster are approximately 0.3 dex (Anders et al. 2004). This cluster sample has previously been used to study the relation between clusters and their host galaxies (Larsen & Richtler 1999, 2000), derive the mass function of clusters (Larsen 2009) as well as to test whether there is a truncation in the mass function of clusters at the high mass end (Larsen 2009, Bastian et al. 2012b).

The galactocentric distance of each cluster was then calculated by comparing the coordinates of the cluster to the galaxy centre, taken from the *NASA Extragalactic Database* (*NED*). We adopt the same distance to each galaxy as that of Larsen (1999, 2004, 2009) in order to convert the angular distance to a physical distance. Finally, since the galaxies have different physical sizes, we normalised the measured galactocentric distances by the major axis radius of each galaxy, also taken from *NED*. We did not attempt to correct for the orientation of each galaxy, as they are mostly face-on, and the corrections were estimated to be small.

The normalised galactocentric distance distribution of the five most massive clusters in our sample is shown as a histogram in Fig. 6.1. Note the strong peak at a normalised distance of 0.05 - 0.2. Inspection of the inner regions of the galaxies (with the completeness tests) shows that the lack of massive clusters at small radii is real and not caused by an observational bias. We have also looked at the distribution of the most massive cluster in each galaxy and find that it is consistent with the five most massive, although with more noise due to the lower number of objects.

Galaxy	Distance [Mpc]	Radius [kpc]
NGC 45	4.8	10.1
NGC 247	2.5	10.3
NGC 300	2.2	11.7
NGC 628	8.3	12.3
NGC 2403	3.2	7.3
NGC 2835	6.1	9.8
NGC 3184	7.9	16.5
NGC 3521	11.8	13.9
NGC 4395	4.2	14.7
NGC 5055	8.9	14.1
NGC 5204	4.8	5.6
NGC 5236	3.7	5.9
NGC 5585	6.9	9.6
NGC 6744	5.0	24.0
NGC 6946	5.5	8.6
NGC 7424	12.6	32.2
NGC 7793	3.3	7.5

Table 6.1: Sample of investigated galaxies with their calculated distances and radii.

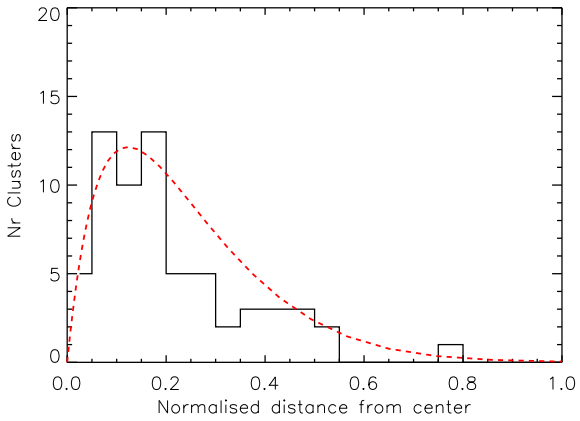

Figure 6.1: The galactocentric distance distribution (normalised to the major axis of each galaxy) of the five most massive clusters per galaxy in our sample. The peak at $0.05 - 0.2$ appears to be real and not caused by selection effects. The dashed (red) line is the best fitting model (discussed in § 6.3) based on the expected cluster formation rate of a spiral galaxy. No additional disruption or environmentally dependent cluster formation law is needed to fit the distribution.

6.3 Comparison with Models

We derive the expected cluster formation rate (CFR) as a function of galactocentric radius as follows. First, we adopt a general gas surface density profile $\Sigma_{\rm g}(R)$ that obeys a modified exponential and which is characteristic of the Milky Way (Dehnen & Binney 1998):

$$\Sigma_{\rm g} = f_{\rm d}\Sigma_{\rm g,0}\exp\left[-\frac{R_{\rm m}}{2R_{\rm d}} - \frac{R}{2R_{\rm d}} - 0.1\cos\left(\frac{R}{2R_{\rm d}}\right)\right] \tag{6.1}$$

where $f_{\rm d} = 0.25$ is the gas fraction, $\Sigma_{\rm g,0} = 52.8$ M$_\odot$ pc^{-2} is the central gas surface density, $R_{\rm m} = 4$ kpc is the characteristic radius of a central density depression, and $R_{\rm d}$ is the scale radius of the exponential. For the Milky Way, $R_{\rm d} = 2.4$ kpc, but this is adjusted to match the observed galaxies. This is converted into a star formation rate density profile $\Sigma_{\rm SFR}(R)$ using the Kennicutt (1998) formulation of the Schmidt law:

$$\frac{\Sigma_{\rm SFR}}{\rm M_\odot\ yr^{-1}\ kpc^{-2}} = 2.5\times10^{-4}\left(\frac{\Sigma_{\rm g}}{\rm M_\odot\ pc^{-2}}\right)^{1.4}. \tag{6.2}$$

By assuming that a certain, fixed fraction of star formation occurs in bound stellar clusters, the cluster formation rate density is taken to be proportional to the star formation rate density at each radius, i.e. $\Sigma_{\rm CFR} \propto \Sigma_{\rm SFR}$. The radial profile d$\rm CFR$/d$R$ is then obtained by multiplying the $\Sigma_{\rm CFR}(R)$ profile with $2\pi R$, which accounts for the increase of the surface area with radius. The size-of-sample effect (e.g., Larsen 2004; Bastian 2008) then dictates that the most massive cluster that is sampled from a power law cluster initial mass function should be located statistically at the galactocentric radius where d$\rm CFR$/dR peaks, i.e. d$^2\rm CFR$/d$R^2 = 0$. In effect, this model predicts the probability density function for the distribution of all clusters, which should also hold for the most massive clusters.

The best fitting model (CFR) is shown as the dashed (red) line in Fig. 6.1. We note that the overall fit of the model is quite good (a KS test gives a probability that the observations were drawn from the parent distribution of the model of $\sim 40\%$) although it does predict a marginally wider peak than observed.

The model described above does not include any additional components beyond adopting a standard star-formation rate law, a distribution of molecular gas in spirals, and assuming that cluster formation traces star formation. We take this as our basic model. As noted in the introduction, we were looking for deviations from this model that may be caused by 1) cluster formation being enhanced in regions of higher pressure (i.e., the inner regions of galaxies) or 2) early cluster disruption due to a denser ISM. Neither effect appears to be required, although they both may be present and simply cancel each other out. In a future work (Kriujssen et al., in prep.) further models will be considered and compared to the data.

6.4 Conclusions

We have presented an analysis of the radial distribution of young massive clusters in spiral galaxies. Focussing on just the five most massive clusters per galaxy, we find that the number distribution peaks at radii between 0.05 and 0.2 times the major axis radius of the galaxies. This peak appears to be real and not due to observational selection effects, as it is similar to that of the single most massive cluster per galaxy and different from the full cluster sample which is known to be incomplete.

Comparison of the observed distribution with simple models shows that the distribution can be understood in relatively simple terms without resorting to environmental effects to enhance or inhibit cluster formation as a function of environment. Instead, we have shown that adopting a model of the Galactic distribution of molecular gas (Dehnen & Binney 1998), assuming the Schmidt-Kennicutt relation (Kennicutt 1998) between gas surface density and star-formation rate, and a size-of-sample effect where areas of higher total star-formation rate (i.e., multiplying the star-formation rate surface density by the area of annular rings) form more clusters and hence more massive clusters (e.g., Bastian 2008) can satisfactorily reproduce the observed distribution.

Chapter 7

Summary and Conclusions

The main part of this thesis concerns a detailed investigation of a sample of selected Central Stars of Planetary Nebulae (CSPNs) for which a severe discrepancy between (a) the masses (and radii) derived from optical observations with the help of theoretical post-AGB[1] evolutionary tracks and (b) the masses determined from UV observations with self-consistent, hydrodynamical NLTE[2] models of CSPNs. This discrepancy first became apparent in a study by Pauldrach et al. (2004) of this sample of selected central stars. The masses derived by means of the self-consistent, hydrodynamical models deviated severely from those obtained from an analysis of the same sample of CSPNs by Kudritzki et al. (1997) based on optical hydrogen and helium lines by assuming the core mass-luminosity relation from theoretical post-AGB evolutionary tracks. This was surprising because both methods earlier derived masses of several massive O-stars that were almost identical.

The code used by Pauldrach et al. (2004) used for their UV analysis was at that time not able to compute optical lines. The optical analyses had so far to be performed with a different code. It was important to resolve this conflict thus to be able to use the code for the computation of both, the optical and the UV lines simultaneously. A successful analysis of such an investigation that includes H and He lines has, as a combined analysis, a more convincing character. Lacking hydrodynamical models, the optical analysis could only derive effective temperatures and surface gravities. To determine masses and radii, they had to compare the effective temperatures and surface gravities to the theoretical evolutionary tracks in the $T_{\rm eff} - \log g$ plane, assuming the evolutionary models to be valid all along. The hydrodynamical self-consistent UV models on the other hand could determine the masses consistently and in accordance to the wind parameters. In the case of CSPNs this led to two contradictory sets of stellar parameters $T_{\rm eff}$, log g, and R_* with their corresponding mass loss rates $\dot{M}$ and derived stellar masses M_*. This raised questions about either the correctness of the theoretical post-AGB evolutionary models or the applicability of the radiation driven wind models on CSPNs. The main goal of this thesis is to contribute with the obtained results to the further clarification of this question.

In this respect, to model the UV and optical wavelength range with the use of the hydrodynamical code WM-basicwe had to improve the modeling of the optical line formation. In the following, we summarize the work necessary and our most important findings and results achieved within the scope of this thesis.

[1] Asymptotic Giant Branch
[2] Non local thermodynamic equilibrium

Implementation of Stark broadening and a combined analysis of optical absorption and UV lines

As a prerequisite to the combined analysis of UV and optical lines with WM-basic we had to extend the applicability of the code to optical absorption lines by implementing Stark broadening which plays a role for the pressure broadened line wings of hydrogen Balmer and helium lines. Testing the improved code by comparing the computed optical line profiles with those from two reference O star models calculated with the well-known model atmosphere code FASTWIND resulted in excellent agreement. Only small differences in the predicted line profiles were visible which we found to be attributed to differences in the density structures of the two codes.

In order to obtain further constraints on the true stellar parameters of CSPNs we have applied our improved stellar atmosphere code WM-basic to two objects from the sample of CSPNs investigated earlier by Kudritzki et al. (1997) and Pauldrach et al. (2004). For this sample, Kudritzki et al. (1997) derived masses which showed only a small scatter around roughly 0.8 solar masses ($M_{\odot}$) whereas the self-consistent, hydrodynamical models by Pauldrach et al. (2004) derived massed ranging from 0.41 $M_{\odot}$ to 1.4 $M_{\odot}$. We therefore chose for our analysis the two stars having the smallest and largest masses of the sample: NGC 2392 and NGC 6826. For these stars, the optical analysis derived strongly different masses using the theoretical post-AGB evolutionary tracks which predict masses of 0.92 $M_{\odot}$ and 0.91 $M_{\odot}$, respectively.

Our combined UV and optical analysis of the two CSPN confirmed the conclusion tentatively drawn by Pauldrach et al. (2004) regarding the stellar parameters of CSPNs, namely that the contradiction between the stellar parameters derived by Kudritzki et al. (1997) and Pauldrach et al. (2004) is not the result of using optical spectra in the former analysis and UV spectra in the latter, but is instead due to the *missing consistency* between stellar and wind parameters in the analysis of Kudritzki et al. (1997). This conclusion is based on the fact that we were not only able to reproduce the observed UV spectrum in excellent agreement but also achieve fits to the optical absorption lines which were in excellent agreement to the observations. We calculated three models, one based on the UV parameters from Pauldrach et al. (2004) (P04), one using the optical parameters from Kudritzki et al. (1997) with an artificial (i.e., inconsistent) radiative line force necessary to reproduce their adopted wind parameters ($K97_f$) and one that was also based on the optical parameters from Kudritzki et al. (1997) but this time with consistent wind parameters ($K97_c$). Our predicted optical lines for both CSPNs based on the P04 model were of the same quality than the predicted lines from the $K97_f$ model although both models did not as good reproduce the line profiles of the H_α and He II λ 4686 emission lines of both CSPNs as shown in Kudritzki et al. (1997) since they were a bit too weak. The $K97_c$ model yielded line profiles that neither matched the observed UV nor to the optical spectra for both CSPNs.

Implementation of clumping for a combined optical and UV analysis of our sample of selected CSPNs

An open issue remained concerning the strength of the H_α and He II λ 4686 emission lines which could not entirely be reproduced for both stellar parameter sets. In recent years, evidence has accumulated that winds are not smooth but rather clumped. This might be relevant for our analysis because of the ρ^2 dependency of the emission lines on the density. A clumped wind would therefore show increased emission compared to a smooth wind with the same mass loss rate. We used the same approach as implemented in the model code used by Kudritzki et al. (2006) in a follow up analysis of their earlier analysis of Kudritzki et al. (1997). In this approach the gas is considered to be swept up

into small, optically thin clumps with a volume filling factor of $1/f_{\rm cl}(r)$ ($f_{\rm cl}(r)$ is the local clumping factor) and void interclump regions. We tested the improved code by comparing the computed optical absorption and emission line profiles of two O star models to the ones predicted by the FASTWIND code. For these tests we artificially adopted the FASTWIND density, velocity and temperature structure thus eliminating the small differences in our earlier tests. The line profiles computed with the two codes were in excellent agreement both times, with and without clumping. The minor differences remaining are based on the extreme sensitivity of the emission lines in respect to slight deviations in the ionization balances and occupation numbers. We could show that these differences were however not relevant for the analysis of the mass loss rate.

With our improved code we re-analyzed the complete sample of CSPNs. As before we considered three models for each star: one based on the UV parameters from Pauldrach et al. (2004) (P04), one using the optical parameters from Kudritzki et al. (2006) with an artificial (i.e., inconsistent) radiative line force necessary to reproduce their adopted wind parameters ($\mathrm{K06}_f$) and one that was also based on the optical parameters from Kudritzki et al. (2006) but this time with consistent wind parameters ($\mathrm{K06}_c$). For all models we used the clumping factor values suggested by Kudritzki et al. (2006). But in a number of cases the models using this clumping factor showed unsatisfactory fits. For these stars we derived our own values for which a resulting fourth P04 model using the new values predicted line profiles that were in better agreement to the observations.

As expected, the consideration of clumping in the models led to an increase in H_α and He II λ4686. The P04 models showed an increase in the strength of their emission lines and could provide good fits to the observed lines (this also affected the He II λ1640 line in the UV spectral range which resulted in an almost perfect fit). In general, the $\mathrm{K06}_c$ models on the other hand predicted line profiles that were not compatible with the observations. The $\mathrm{K06}_f$ models could indeed fit the observations better than the $\mathrm{K06}_c$ models but still not as good as the original line profiles presented by Kudritzki et al. (2006). This is understood to be the result of their unrealistic density structure that was used in their code to compute their models. They used a simplified velocity law controlled by a free parameter adopted to provide a good fit to their observed lines. Because our WM-basic code computes the density structure from a solution to the equation of motion balancing gravity, gas and radiation pressure, our $\mathrm{K06}_f$ line profiles look slightly different even though using the same stellar and wind parameters. This result means that model profiles predicted by a cosmetic clumping factor rather than the underlying physics lose their diagnostic value. The fit quality of such a synthetic spectrum is thus not a reliable tool to determine fundamental parameters since the model is already based on physical conditions that are not realized by nature.

An important result regards our derived clumping factors. We obtain similar values for the clumping factor for almost all CSPNs with a typical value of $f_{cl} = 4$. This is true for both those CSPNs for which Kudritzki et al. (2006) determined a clumping factor of one, i.e., a smooth, unclumped wind as well as those for which they derive unrealistically high clumping factors. This erratic character of the clumping factors does not exist for our models that are based on a consistent set of stellar and wind parameters.

Modeling of the O VI line by means of shock produced X-rays

A common property of massive O stars is the presence of highly ionized species in the wind such as O VI observable at 1031$\mathring{A}$ and 1037$\mathring{A}$. If CSPN winds are driven by the same mechanism as massive O star winds we can expect similar behavior in CSPN winds.

We therefore further extended our investigation of the CSPN sample by augmenting our existing HST (Hubble Space Telescope) and IUE (International Ultraviolet Explorer) observations with newly obtained FUSE (Far Ultraviolet Spectroscopic Explorer) data which exists for four of our CSPNs. The FUSE spectral range covers the wavelength range of the O VI $\lambda\lambda$1031 and 1037 line. O VI is primarily produced by Auger-ionization by X-rays that are understood to arise from shocks embedded in the wind due to the intrinsic unstable behavior of the line driving mechanism. With these observations we could derive shock parameters which reproduced the observed O VI line. Thus we obtained the integrated X-ray luminosities and radial distribution of the maximum local shock temperatures in the shock cooling zones. These obtained values for the X-ray luminosity to bolometric luminosity $log(L_X/L_{bol})$ are those typical of massive O stars, thus supporting that CSPN winds are indeed radiation driven.

Furthermore, direct X-ray observations of CSPNs show that our derived X-ray luminosities are in agreement with the observations. A recent Chandra survey revealed 50% of the planetary nebulae observed to be X-ray emitters. For one CSPN (NGC 2392) of our sample a detailed measurement of the X-ray emission shows both a diffuse and a point-like component[3]. Our derived X-ray luminosity, which only regards the central star itself, is about a factor of two smaller than the total observed value from both the star and its nebular and thus was in accordance with the observations and the interpretation. This result was confirmed by another observation of the CSPN NGC 6543 which is not in our sample but where a similar value was obtained. That the $log(L_X/L_{bol})$ ratios and the maximum shock temperatures we find for our four observed CSPNs all have similar values is in full agreement to our finding that our clumping factors are very similar since they are all expected to result from the same line driving instability. Thus this further supports the legitimate assumption that the winds of O-type CSPNs are radiation driven like those of massive O stars.

Comparison of the dynamical parameters of CSPN and O star winds

Further evidence that the winds of O-type CSPNs are radiation driven is provided by a comparison of the dynamical parameters of CSPN and massive O star winds independent of the appearance of the spectra. One of these is the (modified) wind–momentum ($\dot{M}v_\infty\sqrt{(r)}$) which the theory of radiation driven winds predicts to be a function of stellar luminosity. This wind–momentum luminosity relation is indeed followed by massive O stars but also by our CSPNs. Another one is the behavior of the wind terminal velocity v_∞. As the wind parameters are not free parameters but (due to the driving mechanism) functions of the stellar parameters, using sets of stellar parameters which are not realized by nature should lead at least partly to an inconsistent (i.e., not observed) behavior of the wind parameters in the analysis. Such an inconsistent behavior can, for example, be evident in the ratio $v_\infty/v_{\rm esc}$ of the terminal wind velocity and the escape velocity of individual stars.

We have therefore examined the $v_\infty/v_{\rm esc}$ ratios for our CSPN sample as a function for the two different stellar parameter sets and compared these to the corresponding ratios from a sample of massive O stars. As found by other authors for massive O stars, the correlation of v_∞ to $v_{\rm esc}$ does not represent a strict and simple behavior for CSPNs, giving (as expected) a certain scatter about a mean value. The spread in the $v_\infty/v_{\rm esc}$ ratios for our CSPN models turned out to be comparable to that obtained from both massive O star observations and massive O star models, but (as expected from basic physics) at a slightly smaller mean value. Incompatible with all other results where the $v_\infty/v_{\rm esc}$ ratios based

[3] The diffuse X-ray emission is thought to arise from shells where the CSPN wind rams into the previously expelled AGB envelope, producing hot shocked gas; the point-like sources are associated with the central stars themselves.

on the stellar parameters derived from the optical analysis which yield much too high $v_\infty/v_{\rm esc}$ ratios in general. These high $v_\infty/v_{\rm esc}$ ratios are even more significant because we would have expected the highest $v_\infty/v_{\rm esc}$ values to occur for some massive O stars rather than for some CSPNs.

This anomaly is obviously coupled to the fact that the escape velocity $v_{\rm esc}$ appearing in the CSPN $v_\infty/v_{\rm esc}$ ratios is not a directly observable quantity (whereas v_∞ can be measured directly). The escape velocity is connected to the stellar mass and radius, and in the optical analysis these quantities had been taken from the theoretical post-AGB core mass–luminosity relation. This supports the conclusion that there might be a problem with the core mass–luminosity relation at its high-mass end. This conclusion is further supported by the finding that *consistent* model calculations using stellar parameters compatible with the core mass–luminosity relation do yield $v_\infty/v_{\rm esc}$ values that lie in the expected range (however, the obtained terminal velocities v_∞ of these models are highly incompatible with the observations).

Taking these results together, we find that of the three considerations (a) consistency of the dynamical wind parameters with the stellar parameters, (b) compatibility of the model spectra with the observed spectra, and (c) conformity of the stellar parameters with the core mass–luminosity relation, only two can be reconciled with each other, while the third is irreconcilable with the other two. Since (a) and (b) are strongly supported by both observations and models (spectral appearance, wind-momentum–luminosity relation), it is likely that the consideration that is not realized in nature is (c), the theoretical core mass–luminosity relation, at least for the O-type CSPNs with prominent wind features as studied in this work.

Implications for nebular line diagnostics due to shock enhanced ionizing fluxes of the central source

In a related investigation we considered the influence of shock emission (which we have shown to be vital for the ionization of higher species such as O VI in the stellar spectrum) also on the interstellar gas surrounding stars. We thus extended our analysis on H II regions using shock enhanced fluxes produced by the central source to see whether this has an effect on some of the derived physical properties of H II regions. To accomplish this we calculated a grid of fluxes based on our derived UV stellar and shock parameters of CSPNs. The resulting fluxes have then been used as an input to the photoionization code MOCASSIN. Based on these input parameters each MOCASSIN model yielded a corresponding ionization parameter U. Our results showed no change at all for a model using a 40kK ionizing source. For cooler stars we indeed found small deviations for the 30kK non-shock case to the 30kK shock case. The effects on the 20kK case are dramatic, placing the 20kK shock model in a region of the diagnostic diagram (Fig. 4.2) expected to be populated by systems with roughly 30-35kK ionizing stars and approximately a decade higher ionization parameter U. Overall we conclude that shock effects are only important for stellar sources with effective temperatures equal or lower than 30kK. The magnitude of the effect is also obviously dependent on the strength of the shock and thus might only show dramatic effects for a chosen sample of stellar sources.

Limit of the initial cluster mass function

In the context of stellar feedback on the environment we also addressed the question of a fundamental limit of the initial mass function (ICMF) at high masses by studying the twelve most massive young clusters in the face-on spiral galaxy NGC 2997. The method was based on the luminosities combined

with their age of these clusters. We confirmed the findings of Larsen (2009), who showed a truncation near $2-5\times10^5 M_\odot$ although with some degeneracy with the fraction of clusters disrupted due to mass independent effects. Our results based on our age-M_V method are largely consistent to the ones derived with full population studies. An application to the cluster population of the Antennae galaxy showed that the method is also consistent with a truncated ICMF, but with a truncation at a higher mass of a few $\times10^6 M_\odot$.

Radial galactocentric distances of massive stellar clusters in spiral galaxies

In a in a photometric, observational study we investigated the radial distribution of young massive clusters (YMCs) in a sample of nearby spiral galaxies. In particular, we searched for characteristic galactocentric radii that are conducive to the formation (and/or survival) of the most massive YMCs. We used the Larsen (2004) catalogue of YMCs in a sample of nine nearby, relatively face-on, spiral galaxies, and selected the five most massive clusters per galaxy. We found that the radial distribution of YMCs has a pronounced peak at 0.05 to 0.2 times the major axis and an exponential drop off beyond this radius. We compared the observed data to a simple theoretical model which provides a distribution of cluster distances. We found that such a model is able to reproduce the observed YMC radial distribution without the need to include preferential cluster formation or dissolution due to the increased density of giant molecular clouds near galactic centres to enhance or inhibit cluster formation as a function of the environment. Instead, we demonstrated that the observed distribution can be satisfactorily reproduced by a model of the galactic distribution of molecular gas, assuming the Schmidt-Kennicutt relation between gas surface density and star-formation rate.

Bibliography

Adamo, A., Östlin, G., & Zackrisson, E. 2011: *Probing cluster formation under extreme conditions: massive star clusters in blue compact galaxies*, mnras, 417, 1904

Adamo, A., Östlin, G., Zackrisson, E., Hayes, M., Cumming, R. J., & Micheva, G. 2010: *Super star clusters in Haro 11: properties of a very young starburst and evidence for a near-infrared flux excess*, mnras, 407, 870

Albacete Colombo, J. F., Méndez, M., & Morrell, N. I. 2003: *XMM-Newton X-ray observations of the Carina nebula*, mnras, 346, 704

Anders, P., Bissantz, N., Fritze-v. Alvensleben, U., & de Grijs, R. 2004: *Analysing observed star cluster SEDs with evolutionary synthesis models: systematic uncertainties*, mnras, 347, 196

Barnard, A. J., Cooper, J., & Shamey, L. J. 1969: *Calculated Profiles of He I 4471 and 4922 A and their Forbidden Components*, aap, 1, 28

Bastian, N. 2008: *On the star formation rate - brightest cluster relation: estimating the peak star formation rate in post-merger galaxies*, mnras, 390, 759

Bastian, N. 2011: *Cluster Disruption: From Infant Mortality to Long Term Survival*, in Stellar Clusters amp Associations: A RIA Workshop on Gaia, 85–97

Bastian, N., Adamo, A., Gieles, M., Lamers, H. J. G. L. M., Larsen, S. S., Silva-Villa, E., Smith, L. J., Kotulla, R., Konstantopoulos, I. S., Trancho, G., & Zackrisson, E. 2011: *Evidence for environmentally dependent cluster disruption in M83*, mnras, 417, L6

Bastian, N., Adamo, A., Gieles, M., Silva-Villa, E., Lamers, H. J. G. L. M., Larsen, S. S., Smith, L. J., Konstantopoulos, I. S., & Zackrisson, E. 2012a: *Stellar clusters in M83: formation, evolution, disruption and the influence of the environment*, mnras, 419, 2606

Bastian, N., Gieles, M., Lamers, H. J. G. L. M., Scheepmaker, R. A., & de Grijs, R. 2005: *The star cluster population of M 51. II. Age distribution and relations among the derived parameters*, aap, 431, 905

Bastian, N., Konstantopoulos, I. S., Trancho, G., Weisz, D. R., Larsen, S. S., Fouesneau, M., Kaschinski, C. B., & Gieles, M. 2012b: *Spectroscopic constraints on the form of the stellar cluster mass function*, aap, 541, A25

Blöcker, T. 1995: *Stellar evolution of low- and intermediate-mass stars. II. Post-AGB evolution.*, aap, 299, 755

Brodie, J. P. & Strader, J. 2006: *Extragalactic Globular Clusters and Galaxy Formation*, araa, 44, 193

Campbell, B., Asbell-Clarke, J. E., Weiler, J., Deblasi, C., & Persson, S. E. 1988: *Survey of New Young Stellar Objects Found by IRAS: Centimeter-wave Detections and Dust Emission*, in Bulletin of the American Astronomical Society, Vol. 20, Bulletin of the American Astronomical Society, 956

Cappellari, M. & Emsellem, E. 2004: *Parametric Recovery of Line-of-Sight Velocity Distributions from Absorption-Line Spectra of Galaxies via Penalized Likelihood*, pasp, 116, 138

Castor, J. I., Abbott, D. C., & Klein, R. I. 1975: *Radiation-driven winds in Of stars*, ApJ, 195, 157

Chandar, R., Tsvetanov, Z., & Ford, H. C. 2001: *Compact Star Clusters in M81. II. Two Populations*, aj, 122, 1342

Chandar, R., Whitmore, B. C., Kim, H., Kaleida, C., Mutchler, M., Calzetti, D., Saha, A., O'Connell, R., Balick, B., Bond, H., Carollo, M., et al. 2010: *The Luminosity, Mass, and Age Distributions of Compact Star Clusters in M83 Based on Hubble Space Telescope/Wide Field Camera 3 Observations*, apj, 719, 966

Chandrasekhar, S. 1931: *The Maximum Mass of Ideal White Dwarfs*, apj, 74, 81

Chevalier, R. A. & Imamura, J. N. 1982: *Linear analysis of an oscillatory instability of radiative shock waves*, apj, 261, 543

Conti, P. S., Leitherer, C., & Vacca, W. D. 1996: *Hubble Space Telescope Ultraviolet Spectroscopy of NGC 1741: A Nearby Template for Distant Energetic Starbursts*, apjl, 461, L87

Cook, D. O., Seth, A. C., Dale, D. A., Johnson, L. C., Weisz, D. R., Fouesneau, M., Olsen, K. A. G., Engelbracht, C. W., & Dalcanton, J. J. 2012: *The ACS Nearby Galaxy Survey Treasury. X. Quantifying the Star Cluster Formation Efficiency of nearby Dwarf Galaxies*, apj, 751, 100

Crowther, P. A., Schnurr, O., Hirschi, R., Yusof, N., Parker, R. J., Goodwin, S. P., & Kassim, H. A. 2010: *The R136 star cluster hosts several stars whose individual masses greatly exceed the accepted 150M_{solar} stellar mass limit*, mnras, 408, 731

Davies, B., Bastian, N., Gieles, M., Seth, A. C., Mengel, S., & Konstantopoulos, I. S. 2011: *GLIMPSE-CO1: the most massive intermediate-age stellar cluster in the Galaxy*, mnras, 411, 1386

de Grijs, R., Anders, P., Bastian, N., Lynds, R., Lamers, H. J. G. L. M., & O'Neil, E. J. 2003: *Star cluster formation and evolution in nearby starburst galaxies - II. Initial conditions*, mnras, 343, 1285

de Vaucouleurs, G. 1979: *The extragalactic distance scale. VI - Distances of 458 spiral galaxies from tertiary indicators*, apj, 227, 729

Dehnen, W. & Binney, J. 1998: *Mass models of the Milky Way*, mnras, 294, 429

Dors, Jr., O. L. & Copetti, M. V. F. 2003: *Determination of temperature of the ionizing stars of H II regions*, aap, 404, 969

Elmegreen, B. G. 2008: *Variations in Stellar Clustering with Environment: Dispersed Star Formation and the Origin of Faint Fuzzies*, apj, 672, 1006

Elmegreen, B. G. & Hunter, D. A. 2010: *On the Disruption of Star Clusters in a Hierarchical Interstellar Medium*, apj, 712, 604

Ercolano, B., Barlow, M. J., & Storey, P. J. 2005: *The dusty MOCASSIN: fully self-consistent 3D photoionization and dust radiative transfer models*, mnras, 362, 1038

Ercolano, B., Barlow, M. J., Storey, P. J., & Liu, X. . 2004: *MOCASSIN: 3D photoionisation and dust radiative transfer modelling of PNe*, ArXiv Astrophysics e-prints

Ercolano, B., Barlow, M. J., Storey, P. J., & Liu, X.-W. 2003: *MOCASSIN: a fully three-dimensional Monte Carlo photoionization code*, mnras, 340, 1136

Ercolano, B., Bastian, N., & Stasińska, G. 2007: *The effects of spatially distributed ionization sources on the temperature structure of HII regions*, mnras, 379, 945

Ercolano, B. & Storey, P. J. 2006: *Theoretical calculations of the HI, HeI and HeII free-bound continuous emission spectra*, mnras, 372, 1875

Ercolano, B., Young, P. R., Drake, J. J., & Raymond, J. C. 2008: *X-Ray Enabled MOCASSIN: A Three-dimensional Code for Photoionized Media*, apjs, 175, 534

Evans, I. N. & Dopita, M. A. 1985: *Theoretical models for H II regions. I - Diagnostic diagrams*, apjs, 58, 125

Fall, S. M., Chandar, R., & Whitmore, B. C. 2009: *New Tests for Disruption Mechanisms of Star Clusters: Methods and Application to the Antennae Galaxies*, apj, 704, 453

Feibelman, W. A. 1996: *An O VIII Sequence for Planetary Nebula Nuclei*, pasp, 108, 664

Feldmeier, A., Kudritzki, R.-P., Palsa, R., Pauldrach, A. W. A., & Puls, J. 1997: *The X-ray emission from shock cooling zones in O star winds.*, A&A, 320, 899

Fierro, C. R., Peimbert, A., Georgiev, L., Morisset, C., & Arrieta, A. 2011: *NGC 6826: a unified study of the planetary nebula and its central stars*, in Revista Mexicana de Astronomia y Astrofisica, vol. 27, Vol. 40, Revista Mexicana de Astronomia y Astrofisica Conference Series, 167–168

Filippenko, A. V. 1982: *The importance of atmospheric differential refraction in spectrophotometry*, pasp, 94, 715

Gieles, M. 2009: *The early evolution of the star cluster mass function*, mnras, 394, 2113

Gieles, M. & Bastian, N. 2008: *An alternative method to study star cluster disruption*, aap, 482, 165

Gieles, M., Bastian, N., Lamers, H. J. G. L. M., & Mout, J. N. 2005: *The star cluster population of M 51. III. Cluster disruption and formation history*, aap, 441, 949

Gieles, M., Larsen, S. S., Bastian, N., & Stein, I. T. 2006a: *The luminosity function of young star clusters: implications for the maximum mass and luminosity of clusters*, aap, 450, 129

Gieles, M., Larsen, S. S., Scheepmaker, R. A., Bastian, N., Haas, M. R., & Lamers, H. J. G. L. M. 2006b: *Observational evidence for a truncation of the star cluster initial mass function at the high mass end*, aap, 446, L9

Gieles, M. & Portegies Zwart, S. F. 2011: *The distinction between star clusters and associations*, mnras, 410, L6

Giveon, U., Sternberg, A., Lutz, D., Feuchtgruber, H., & Pauldrach, A. W. A. 2002: *The Excitation and Metallicity of Galactic H II Regions from Infrared Space Observatory SWS Observations of Mid-Infrared Fine-Structure Lines*, apj, 566, 880

Goddard, Q. E., Bastian, N., & Kennicutt, R. C. 2010: *On the fraction of star clusters surviving the embedded phase*, mnras, 405, 857

González Delgado, R. M., Cerviño, M., Martins, L. P., Leitherer, C., & Hauschildt, P. H. 2005: *Evolutionary stellar population synthesis at high spectral resolution: optical wavelengths*, mnras, 357, 945

Goodwin, S. P. 2009: *The effect of the dynamical state of clusters on gas expulsion and infant mortality*, apss, 324, 259

Goodwin, S. P. & Bastian, N. 2006: *Gas expulsion and the destruction of massive young clusters*, mnras, 373, 752

Griem, H. R. 1964, Plasma spectroscopy

Guerrero, M. A. 2006: *Planetary Nebulae and Their Central Stars in the X-ray and EUV Regions*, in IAU Symposium, Vol. 234, Planetary Nebulae in our Galaxy and Beyond, ed. M. J. Barlow & R. H. Méndez, 153–160

Guerrero, M. A., Chu, Y.-H., & Gruendl, R. A. 2000: *ROSAT Observations of X-Ray Emission from Planetary Nebulae*, apjs, 129, 295

Guerrero, M. A., Chu, Y.-H., Gruendl, R. A., & Meixner, M. 2005: *XMM-Newton detection of hot gas in the Eskimo Nebula: Shocked stellar wind or collimated outflows?*, aap, 430, L69

Heap, S. R. 1982: *Subluminous Wolf-Rayet stars - Observations*, in IAU Symposium, Vol. 99, Wolf-Rayet Stars: Observations, Physics, Evolution, ed. C. W. H. De Loore & A. J. Willis, 423–445

Heap, S. R. 1997: *Observations of CSPN (Invited Review)*, in IAU Symposium, Vol. 180, Planetary Nebulae, ed. H. J. Habing & H. J. G. L. M. Lamers, 55

Herrero, A. 1987: *Improved NLTE profiles of He II lines in hot stars including their overlap with hydrogen*, aap, 186, 231

Hertzsprung, E. 1911: *Ueber die Verwendung photographischer effektiver Wellenlaengen zur Bestimmung von Farbenaequivalenten*, Publikationen des Astrophysikalischen Observatoriums zu Potsdam, 63

Herwig, F., Freytag, B., & Werner, K. 2006: *The Evolution of Central Stars of Planetary Nebulae*, in IAU Symposium, Vol. 234, Planetary Nebulae in our Galaxy and Beyond, ed. M. J. Barlow & R. H. Méndez, 103–110

Hodges, S. E. 2012: *A Multi-Wavelength Study Of Fast Winds From Central Stars Of Planetary Nebulae*, PhD thesis, University College London, (2012)

Hoffmann, T. L. & Pauldrach, A. W. A. 2003: *Wind Models for O-type Stars*, in Planetary Nebulae: Their Evolution and Role in the Universe, Proceedings of the 209th Symposium of the International Astronomical Union held at Canberra, Australia, 19-23 November, 2001. Edited by S. Kwok, M. Dopita, and R. Sutherland, Vol. 209th IAU Symposium, 189

Holtzman, J. A., Faber, S. M., Shaya, E. J., Lauer, T. R., Groth, J., Hunter, D. A., Baum, W. A., Ewald, S. P., Hester, J. J., Light, R. M., Lynds, C. R., et al. 1992: *Planetary Camera observations of NGC 1275 - Discovery of a central population of compact massive blue star clusters*, aj, 103, 691

Howarth, I. D. & Prinja, R. K. 1989: *The stellar winds of 203 Galactic O stars – A quantitative ultraviolet survey*, ApJS, 69, 527

Kaschinski, C. B., Pauldrach, A. W. A., & Hoffmann, T. L. 2012: *Radiation-driven winds of hot luminous stars. XVII. Parameters of selected central stars of PN from consistent optical and UV spectral analysis and the universality of the mass-luminosity relation*, aap, 542, A45

Kastner, J. H., Montez, Jr., R., Balick, B., Frew, D. J., Miszalski, B., Sahai, R., Blackman, E., Chu, Y.-H., De Marco, O., Frank, A., Guerrero, M. A., et al. 2012: *The Chandra X-Ray Survey of Planetary Nebulae (CHANPLANS): Probing Binarity, Magnetic Fields, and Wind Collisions*, aj, 144, 58

Kennicutt, Jr., R. C. 1998: *The Global Schmidt Law in Star-forming Galaxies*, apj, 498, 541

Konstantopoulos, I. S., Bastian, N., Smith, L. J., Westmoquette, M. S., Trancho, G., & Gallagher, III, J. S. 2009: *A Spectroscopic Census of the M82 Stellar Cluster Population*, apj, 701, 1015

Kruijssen, J. M. D. & Cooper, A. P. 2012: *The initial mass spectrum of old globular clusters in dwarf galaxies*, mnras, 420, 340

Kruijssen, J. M. D., Pelupessy, F. I., Lamers, H. J. G. L. M., Portegies Zwart, S. F., & Icke, V. 2011: *Modelling the formation and evolution of star cluster populations in galaxy simulations*, mnras, 414, 1339

Kudritzki, R.-P. 1999: *The Wind Momentum - Luminosity Relationship of Blue Supergiants*, in Lecture Notes in Physics, Berlin Springer Verlag, Vol. 523, IAU Colloq. 169: Variable and Non-spherical Stellar Winds in Luminous Hot Stars, ed. B. Wolf, O. Stahl, & A. W. Fullerton, 405

Kudritzki, R.-P., Lennon, D. J., & Puls, J. 1995: *Quantitative Spectroscopy of Luminous Blue Stars in Distant Galaxies*, in Science with the VLT, 246

Kudritzki, R. P., Mendez, R. H., Puls, J., & McCarthy, J. K. 1997: *Winds in the atmospheres of central stars of Planetary Nebulae (Invited Review)*, in IAU Symposium, Vol. 180, Planetary Nebulae, ed. H. J. Habing & H. J. G. L. M. Lamers, 64

Kudritzki, R. P., Urbaneja, M. A., & Puls, J. 2006: *Atmospheres and Winds of PN Central Stars*, in IAU Symposium, Vol. 234, Planetary Nebulae in our Galaxy and Beyond, ed. M. J. Barlow & R. H. Méndez, 119

Lamers, H. J. G. L. M., Gieles, M., Bastian, N., Baumgardt, H., Kharchenko, N. V., & Portegies Zwart, S. 2005: *An analytical description of the disruption of star clusters in tidal fields with an application to Galactic open clusters*, aap, 441, 117

Lamers, H. J. G. L. M. & Leitherer, C. 1993: *What are the mass-loss rates of O stars?*, ApJ, 412, 771

Larsen, S. S. 1999: *Young massive star clusters in nearby galaxies. II. Software tools, data reductions and cluster sizes*, aaps, 139, 393

Larsen, S. S. 2002: *The Luminosity Function of Star Clusters in Spiral Galaxies*, aj, 124, 1393

Larsen, S. S. 2004: *The structure and environment of young stellar clusters in spiral galaxies*, aap, 416, 537

Larsen, S. S. 2009: *The mass function of young star clusters in spiral galaxies*, aap, 494, 539

Larsen, S. S., Origlia, L., Brodie, J., & Gallagher, J. S. 2008: *Anatomy of a young massive star cluster: NGC 1569-B*, mnras, 383, 263

Larsen, S. S. & Richtler, T. 1999: *Young massive star clusters in nearby galaxies . I. Identification and general properties of the cluster systems*, aap, 345, 59

Larsen, S. S. & Richtler, T. 2000: *Young massive star clusters in nearby spiral galaxies. III. Correlations between cluster populations and host galaxy properties*, aap, 354, 836

Larsen, S. S. & Richtler, T. 2004: *Dynamical mass estimates for two luminous young stellar clusters in ¡ASTROBJ¿Messier 83¡/ASTROBJ¿*, aap, 427, 495

Lucy, L. B. 1982: *X-ray emission from the winds of hot stars. II*, ApJ, 255, 286

Lucy, L. B. & Solomon, P. M. 1970: *Mass Loss by Hot Stars*, ApJ, 159, 879

Lucy, L. B. & White, R. L. 1980: *X-ray emission from the winds of hot stars*, ApJ, 241, 300

Maciel, W. J., Costa, R. D. D., & Idiart, T. E. P. 2011a: *Age Distribution of AGB Stars and Central Stars of Planetary Nebulae*, in Astronomical Society of the Pacific Conference Series, Vol. 445, Why Galaxies Care about AGB Stars II: Shining Examples and Common Inhabitants, ed. F. Kerschbaum, T. Lebzelter, & R. F. Wing, 343

Maciel, W. J., Rodrigues, T. S., & Costa, R. D. D. 2011b: *Kinematic ages of the central stars of planetary nebulae*, rmxaa, 47, 401

Martín-Hernández, N. L., Vermeij, R., Tielens, A. G. G. M., van der Hulst, J. M., & Peeters, E. 2002: *The stellar content, metallicity and ionization structure of H II regions*, aap, 389, 286

Mendez, R. H. 1991: *Photospheric Abundances in Central Stars of Planeteray Nebulae, and Evolutionary Implications*, in IAU Symposium, Vol. 145, Evolution of Stars: the Photospheric Abundance Connection, ed. G. Michaud & A. V. Tutukov, 375

Mendez, R. H., Kudritzki, R. P., Groth, H. G., Husfeld, D., & Herrero, A. 1988a: *PHL 932 - Another non-post-AGB central star of planetary nebula*, aap, 197, L25

Mendez, R. H., Kudritzki, R. P., Herrero, A., Husfeld, D., & Groth, H. G. 1988b: *High resolution spectroscopy of central stars of planetary nebulae. I - Basic atmospheric parameters and their interpretation*, aap, 190, 113

Meurer, G. R., Heckman, T. M., Leitherer, C., Kinney, A., Robert, C., & Garnett, D. R. 1995: *Starbursts and Star Clusters in the Ultraviolet*, aj, 110, 2665

Meynet, G., Maeder, A., Schaller, G., Schaerer, D., & Charbonnel, C. 1994: *Grids of massive stars with high mass loss rates. V. From 12 to 120 M_{sun} at Z=0.001, 0.004, 0.008, 0.020 and 0.040*, aaps, 103, 97

Milne, E. A. 1926: *On the possibility of the emission of high-speed atoms from the sun and stars*, mnras, 86, 459

Morisset, C., Schaerer, D., Bouret, J.-C., & Martins, F. 2004: *Mid-IR observations of Galactic H II regions: Constraining ionizing spectra of massive stars and the nature of the observed excitation sequences*, aap, 415, 577

Napiwotzki, R. 2006: *On near Chandrasekhar mass central stars of planetary nebulae*, aap, 451, L27

Napiwotzki, R., Green, P. J., & Saffer, R. A. 1999: *A Comparative Study of the Mass Distribution of Extreme-Ultraviolet-selected White Dwarfs*, apj, 517, 399

Osterbrock, D. E. & Ferland, G. J. 2006, Astrophysics of gaseous nebulae and active galactic nuclei

Owocki, S. P. & Rybicki, G. B. 1984: *Instabilities in line-driven stellar winds. I. Dependence on perturbation wavelength*, ApJ, 284, 337

Pauldrach, A. 1987: *Radiation driven winds of hot luminous stars. III. Detailed statistical equilibrium calculations for hydrogen to zinc*, A&A, 183, 295

Pauldrach, A., Puls, J., & Kudritzki, R.-P. 1986: *Radiation-driven winds of hot luminous stars – Improvements of the theory and first results*, A&A, 164, 86

Pauldrach, A., Puls, J., Kudritzki, R.-P., Méndez, R. H., & Heap, S. R. 1988: *Radiation-driven winds of hot stars. V. Wind models for central stars of planetary nebulae*, A&A, 207, 123

Pauldrach, A. W. A. 2003: *Hot Stars: Old-Fashioned or Trendy? (With 24 Figures)*, in Reviews in Modern Astronomy, Vol. 16, Reviews in Modern Astronomy, ed. R. E. Schielicke, 133

Pauldrach, A. W. A. 2005: *Radiation Driven Atmospheres of O-type Stars – Synthetic UV-spectra of Consistent Atmospheric Models as a Spectroscopic Tool*, in Planetary Nebulae as Astronomical Tools, ed. R. Szczerba, G. Stasiska, & S. K. Gorny, Vol. 804 (San Francisco: AIP Conf. Proc.), 105–116

Pauldrach, A. W. A., Feldmeier, A., Puls, J., & Kudritzki, R. P. 1994: *Radiation driven winds of hot stars: theory of O-Star atmospheres as a spectroscopic tool.*, in Evolution of Massive Stars, ed. D. Vanbeveren, W. van Rensbergen, & C. De Loore, 105–125

Pauldrach, A. W. A., Hoffmann, T. L., & Lennon, M. 2001: *Radiation-driven winds of hot luminous stars. XIII. A description of NLTE line blocking and blanketing towards realistic models for expanding atmospheres*, A&A, 375, 161

Pauldrach, A. W. A., Hoffmann, T. L., & Méndez, R. H. 2003: *Radiation Driven Atmospheres of O-type stars: Constraints on the Mass-Luminosity Relation of Central Stars of Planetary Nebulae (invited review)*, in IAU Symposium, Vol. 209, Planetary Nebulae: Their Evolution and Role in the Universe, ed. S. Kwok, M. Dopita, & R. Sutherland, 177

Pauldrach, A. W. A., Hoffmann, T. L., & Méndez, R. H. 2004: *Radiation-driven winds of hot luminous stars. XV. Constraints on the mass-luminosity relation of central stars of planetary nebulae*, aap, 419, 1111

Pauldrach, A. W. A., Kudritzki, R.-P., Puls, J., & Butler, K. 1990a: *Radiation driven winds of hot luminous stars. VII. The evolution of massive stars and the morphology of stellar wind spectra*, A&A, 228, 125

Pauldrach, A. W. A., Kudritzki, R.-P., Puls, J., Butler, K., & Hunsinger, J. 1994: *Radiation-driven winds of hot luminous stars. XII: A first step towards detailed UV-line diagnostics of O-stars*, A&A, 283, 525

Pauldrach, A. W. A., Lennon, M., Hoffmann, T. L., Sellmaier, F., Kudritzki, R.-P., & Puls, J. 1998: *Realistic Models for Expanding Atmospheres*, in Astronomical Society of the Pacific Conference Series, Vol. 131, Properties of Hot Luminous Stars, ed. I. Howarth, 258

Pauldrach, A. W. A. & Puls, J. 1990a: *Radiation Driven Winds of Hot Luminous Stars. Applications of Stationary Wind Models.*, Reviews of Modern Astronomy, 3, 124

Pauldrach, A. W. A. & Puls, J. 1990b: *Radiation-driven winds of hot stars. VIII. The bistable wind of the luminous blue variable P Cygni (B1 Ia$^+$)*, A&A, 237, 409

Pauldrach, A. W. A., Puls, J., Gabler, R., & Gabler, A. 1990b: *Radiation driven winds of hot luminous stars. IX. Constraints on the wind temperature of O-stars*, in Properties of hot luminous stars, Boulder-Munich workshop, ed. C.D. Garmany, Vol. PASPC 7, 171–188

Pauldrach, A. W. A., Vanbeveren, D., & Hoffmann, T. L. 2011: *Radiation-driven winds of hot luminous stars. XVI. Expanding atmospheres of massive and very massive stars and the evolution of dense stellar clusters*, aap, ArXiv e-prints 1107.0654v2

Pauldrach, A. W. A., Vanbeveren, D., & Hoffmann, T. L. 2012: *Radiation-driven winds of hot luminous stars XVI. Expanding atmospheres of massive and very massive stars and the evolution of dense stellar clusters*, aap, 538, A75

Péquignot, D., Ferland, G., Netzer, H., Kallman, T., Ballantyne, D. R., Dumont, A.-M., Ercolano, B., Harrington, P., Kraemer, S., Morisset, C., Nayakshin, S., et al. 2001: *Photoionization Model Nebulae*, in Astronomical Society of the Pacific Conference Series, Vol. 247, Spectroscopic Challenges of Photoionized Plasmas, ed. G. Ferland & D. W. Savin, 533

Pettini, M., Steidel, C. C., Adelberger, K. L., Dickinson, M., & Giavalisco, M. 2000: *The Ultraviolet Spectrum of MS 1512-CB58: An Insight into Lyman-Break Galaxies*, apj, 528, 96

Piskunov, A. E., Kharchenko, N. V., Röser, S., Schilbach, E., & Scholz, R.-D. 2006: *Revisiting the population of Galactic open clusters*, aap, 445, 545

Portegies Zwart, S. F., McMillan, S. L. W., & Gieles, M. 2010: *Young Massive Star Clusters*, araa, 48, 431

Puls, J. & Hummer, D. G. 1988: *The Sobolev approximation for the line force and line source function in a spherically-symmetrical stellar wind with continuum opacity*, A&A, 191, 87

Puls, J., Kudritzki, R., Herrero, A., Pauldrach, A. W. A., Haser, S. M., Lennon, D. J., Gabler, R., Voels, S. A., Vilchez, J. M., Wachter, S., & Feldmeier, A. 1996: *O-star mass-loss and wind momentum rates in the Galaxy and the Magellanic Clouds Observations and theoretical predictions.*, aap, 305, 171

Puls, J., Markova, N., Scuderi, S., Stanghellini, C., Taranova, O. G., Burnley, A. W., & Howarth, I. D. 2006: *Bright OB stars in the Galaxy. III. Constraints on the radial stratification of the clumping factor in hot star winds from a combined H_α, IR and radio analysis*, aap, 454, 625

Puls, J. & Pauldrach, A. W. A. 1991: *Radiative Transfer in Expanding Atmospheres - Radiative Acceleration of Wolf-Rayet Envelopes*, in NATO ASIC Proc. 341: Stellar Atmospheres - Beyond Classical Models, ed. L. Crivellari, I. Hubeny, & D. G. Hummer, 175

Puls, J., Urbaneja, M. A., Venero, R., Repolust, T., Springmann, U., Jokuthy, A., & Mokiem, M. R. 2005: *Atmospheric NLTE-models for the spectroscopic analysis of blue stars with winds. II. Line-blanketed models*, aap, 435, 669

Repolust, T., Puls, J., & Herrero, A. 2004: *Stellar and wind parameters of Galactic O-stars. The influence of line-blocking/blanketing*, A&A, 415, 349

Rivero González, J. G. 2012: *Nitrogen line spectroscopy in O-stars*, PhD thesis, , Universitäts-Sternwarte der Ludwig-Maximillian Universität, München, (2012)

Rose, W. K. 1998, Advanced Stellar Astrophysics (Cambrigde University Press, 1998)

Röser, S., Kharchenko, N. V., Piskunov, A. E., Schilbach, E., Scholz, R.-D., & Zinnecker, H. 2010: *Open clusters and the galactic disk*, Astronomische Nachrichten, 331, 519

Runacres, M. C. & Owocki, S. P. 2002: *The outer evolution of instability-generated structure in radiatively driven stellar winds*, aap, 381, 1015

Russell, H. N. 1913: *"Giant" and "dwarf" stars*, The Observatory, 36, 324

Sana, H., Rauw, G., & Gosset, E. 2005: *The young open cluster NGC 6231: five years of investigations*, in Massive Stars and High-Energy Emission in OB Associations, ed. G. Rauw, Y. Nazé, R. Blomme, & E. Gosset, 107–110

Sana, H., Rauw, G., Nazé, Y., Gosset, E., & Vreux, J.-M. 2006: *An XMM-Newton view of the young open cluster NGC 6231 - II. The OB star population*, mnras, 372, 661

Santolaya-Rey, A. E., Puls, J., & Herrero, A. 1997: *Atmospheric NLTE-models for the spectroscopic analysis of luminous blue stars with winds.*, aap, 323, 488

Schechter, P. 1976: *An analytic expression for the luminosity function for galaxies.*, apj, 203, 297

Scheepmaker, R. A., Lamers, H. J. G. L. M., Anders, P., & Larsen, S. S. 2009: *The spatial distribution of star and cluster formation in M 51*, aap, 494, 81

Schoening, T. & Butler, K. 1989: *Stark broadening of He II lines*, aaps, 78, 51

Schweizer, F. 1987: *Star formation in colliding and merging galaxies*, in Nearly Normal Galaxies. From the Planck Time to the Present, ed. S. M. Faber, 18–25

Shamey, L. J. 1964PhD thesis, , B. S. Loyola University of Los Angeles, (1964)

Silva-Villa, E. & Larsen, S. S. 2011: *The star cluster - field star connection in nearby spiral galaxies. II. Field star and cluster formation histories and their relation*, aap, 529, A25

Simon, M. & Axford, W. I. 1966: *Shock waves in the interplanetary medium*, Planet. Space Sci., 14, 901

Simón-Díaz, S. & Stasińska, G. 2008: *The ionizing radiation from massive stars and its impact on HII regions: results from modern model atmospheres*, mnras, 389, 1009

Smith, L. J. & Gallagher, J. S. 2001: *M82-F: a doomed super star cluster?*, mnras, 326, 1027

Snow, T. P. & Morton, D. C. 1976: *Copernicus ultraviolet observations of mass-loss effects in O and B stars*, ApJS, 32, 429

Stasińska, G. 2010: *Nebular abundances in galaxies: Beware of biases*, in IAU Symposium, Vol. 262, IAU Symposium, ed. G. Bruzual & S. Charlot, 93–96

Stasińska, G. & Izotov, Y. 2003: *Modeling the emission line sequence of H II galaxies*, aap, 397, 71

Tinkler, C. M. & Lamers, H. J. G. L. M. 2002: *Mass-loss rates of H-rich central stars of planetary nebulae as distance indicators?*, aap, 384, 987

Todt, H., Peña, M., Hamann, W.-R., & Gräfener, G. 2010: *[WN] central stars of planetary nebulae*, in American Institute of Physics Conference Series, Vol. 1273, American Institute of Physics Conference Series, ed. K. Werner & T. Rauch, 219–224

Trancho, G., Bastian, N., Miller, B. W., & Schweizer, F. 2007: *Gemini Spectroscopic Survey of Young Star Clusters in Merging/Interacting Galaxies. II. NGC 3256 Clusters*, apj, 664, 284

Traulsen, I., Hoffmann, A. I. D., Rauch, T., Werner, K., Dreizler, S., & Kruk, J. W. 2005: *HST and FUSE Spectroscopy of Hot Hydrogen-Rich Central Stars of Planetary Nebulae*, in Astronomical Society of the Pacific Conference Series, Vol. 334, 14th European Workshop on White Dwarfs, ed. D. Koester & S. Moehler, 325

Urbaneja, M. A., Kudritzki, R., & Puls, J. 2008: *Clumping in the winds of O-type CSPNs*, in Clumping in Hot-Star Winds, ed. W.-R. Hamann, A. Feldmeier, & L. M. Oskinova, 67

Verner, D. A. & Yakovlev, D. G. 1995: *Analytic FITS for partial photoionization cross sections.*, aaps, 109, 125

Verner, D. A., Yakovlev, D. G., Band, I. M., & Trzhaskovskaya, M. B. 1993: *Subshell Photoionization Cross Sections and Ionization Energies of Atoms and Ions from He to Zn*, Atomic Data and Nuclear Data Tables, 55, 233

Vidal, C. R., Cooper, J., & Smith, E. W. 1973: *Hydrogen Stark-Broadening Tables*, apjs, 25, 37

Vilchez, J. M. & Pagel, B. E. J. 1988: *On the determination of temperatures of ionizing stars in H II regions*, mnras, 231, 257

Villaver, E., Stanghellini, L., & Shaw, R. A. 2007: *The Mass Distribution of the Central Stars of Planetary Nebulae in the Large Magellanic Cloud*, apj, 656, 831

Weidmann, W. A. & Gamen, R. 2011: *Central stars of planetary nebulae. II. New OB-type and emission-line stars*, aap, 531, A172

Whitmore, B. C., Chandar, R., & Fall, S. M. 2007: *Star Cluster Demographics. I. A General Framework and Application to the Antennae Galaxies*, aj, 133, 1067

Whitmore, B. C., Chandar, R., Schweizer, F., Rothberg, B., Leitherer, C., Rieke, M., Rieke, G., Blair, W. P., Mengel, S., & Alonso-Herrero, A. 2010: *The Antennae Galaxies (NGC 4038/4039) Revisited: Advanced Camera for Surveys and NICMOS Observations of a Prototypical Merger*, aj, 140, 75

Zepf, S. E., Ashman, K. M., English, J., Freeman, K. C., & Sharples, R. M. 1999: *The Formation and Evolution of Candidate Young Globular Clusters in NGC 3256*, aj, 118, 752

Zhang, Q. & Fall, S. M. 1999: *The Mass Function of Young Star Clusters in the "Antennae" Galaxies*, apjl, 527, L81

Danksagung

Nachdem ich kein begnadeter Schreiber bin, weiss ich nicht, wie sehr ich meine Gedanken und Gefühle ausdrücken kann, die ich gerade beim Schreiben dieser Zeilen empfinde. Noch vor einem Jahr hätte ich nicht gedacht, dass ich es jemals schaffen werde, an diesem Punkt anzukommen. Gerade durch den Kontakt zu meinen Feuerwehrkollegen habe ich doch sehr oft mitbekommen, auf wieviel man eigentlich während der Promotion verzichten muss, was für andere selbstverständlich ist. Als bestes Beispiel dafür sind das Finanzielle und der sehr stark ausgeprägte Druck, den man gerade im letzten Jahr der Promotion spührt, zu erwähnen. Als Doktorand "bezahlt" man für seine Promotion nicht nur mit viel Arbeit, sondern gerade in den genannten (und auch anderen) "Waren". In so einer Zeit ist jegliche Unterstützung mehr Wert als Geld. Deshalb möchte ich, dass meine Danksagung an die Menschen gerichtet ist, die mir durch diese schwierige Zeit halfen und die zu meiner Persönlichkeitsentwicklung beigetragen haben:

Ein spezieller Dank geht an Tadziu Hoffmann. Ohne ihn wäre ich sicherlich erst viel später, wenn überhaupt, mit meiner Arbeit fertig geworden. An unzähligen, langen Abenden war er stets geduldig und bereit, jedes Problem anzugehen. Egal ob computertechnischer Natur oder theoretischen Fachwissens, er war von Anfang bis Ende einer der wichtigsten Personen während meiner Arbeit am Institut. Auch wenn ich meinen Dank auf diese Weise sicherlich nicht richtig ausdrücken kann, er ist da!

Danke natürlich auch an meinen Dr. Vater Adi Pauldrach. Er hat mir sicherlich keine einfache Zeit beschert, aber ich bin davon überzeugt, dass auch ich ihm kein einfacher Doktorand war. Es war definitiv nicht einfach, meine positiven Seiten als Doktorand heraus zu finden, dennoch hat er es geschafft und mich das auch immer wissen lassen. Die langen Nachmittage in seinem Büro haben mir vieles für meinen zukünftigen beruflichen Werdegang dargelegt, wofür ich ihm sehr dankbar bin und was mich sicherlich sehr geprägt und weitergebracht hat. Adi hat vor allem immer versucht, das Maximum des Möglichen aus mir heraus zu holen wobei ich meine Grenzen überschreiten musste. All dies sind Lernprozesse, die sicherlich wenige Menschen in ihrem Leben erfahren können, wofür ich sehr dankbar bin.

Der nächste Dank geht an drei nicht deutschsprachige, Menschen weswegen ich für sie ins Englische wechseln werde, nachdem ich möchte, dass mein Dank sie erreicht, sollten sie meine Arbeit mal in die Finger bekommen:

Nate Bastian: thank you my good man for all the time we spent together in the last two years. Your help regarding my thesis, the two papers we did together, your support and corrections on my work were so important to me. Without them i would not have been able to finish in that time. For that and much more you have my deepest gratitude! I wish you all the best for your future career and time in Liverpool. May our pathes cross again somewhere in the future.

Barbara Ercolano: thank you also so much for all your help! The paper with you was very interesting and gave me more than just the much needed first author paper. Also all your backup during the last months of my thesis will not be forgotten.

Tomer Czaczkes: thanks to you too dude for reading my whole thesis over during just one weekend and giving me a shit load of corrections and stuff to think about! Very much appreciated and will be repayed accordingly.

Nachdem ich nicht langatmig werden möchte, kann ich jetzt leider nicht jeden aufzählen, dem ich zu verdanken habe, dass ich es geschafft habe, die Arbeit fertig zu stellen. Deshalb möchte ich an dieser Stelle allen Leuten an der Uni-Sternwarte, mit denen ich näheren Kontakt hatte, für die Zeit mit ihnen danken. Es war immer eine ruhige und entspannte Arbeitsatmosphäre, was für mich sehr wichtig ist. Drei meiner langjährigen Freunde seien doch noch erwähnt, Thomas Eichner, Martin Höfling und Wolfgang von Glasow, mit denen ich tatsächlich vor 11 Jahren angefangen habe, Physik zu studieren. Wir vier haben uns all die Jahre lang immer gegenseitig motiviert und sind durch Dick und Dünn gegangen. Gentlemen, es war mir ein Vergnügen und die Zeit mit euch wird mir immer in Erinnerung bleiben!

Von meinem privaten Freundeskreis möchte ich vor allem meinem "Moon Of My Life" - Agnieszka Chrobok, sowie Dominik Birgel, Eva und Obi Obermüller danken, die mir in den letzten Jahren immer eine mentale Stütze waren. Vor allem Eva und Obi haben mir unfassbar viel geholfen, nachdem mein Privatleben im letzten Jahr ziemlich mies war und die Arbeit an der Promotion für Wahr nicht leichter gemacht hat. Dafür habt ihr zwei einen speziellen Dank verdient!

Das Wichtigste kommt meistens zum Schluss: ich möchte meinen Eltern danken, dass sie mich, in der langen Zeit in der ich nicht finanziert war, finanziell unterstützt haben. Vor allem meiner Mama ist es sicherlich nicht einfach gefallen, alles Finanzielle so auf die Reihe zu bekommen, was nur ihrem Geschick in diesem Bereich zu verdanken ist.

An dieser Stelle muss ich auch erwähnen, womit ich auch meine Danksagung schliessen werde, dass es im Prinzip nur meiner Mama zu verdanken ist, dass ich den Weg gehen konnte, den ich gegangen bin. Sie war es, die immer versucht hat, mir den Rücken frei zu halten und allen Lehrern und Personen zum Trotz steif und fest behauptet hat, dass ich nicht zu dumm bin für eine Hochschullaufbahn!

What we do in life echoes in eternity.